Integration of Utility-Scale Variable Generation into Resistive Networks

by

Sina Sadeghi Baghsorkhi

A dissertation submitted in partial fulfillment
of the requirements for the degree of
Doctor of Philosophy
(Electrical Engineering: Systems)
in the University of Michigan
2015

Doctoral Committee:

Professor Ian A. Hiskens, Chair
Professor Duncan S. Callaway
Professor Marina A. Epelman
Professor Johanna L. Mathieu

2015

TABLE OF CONTENTS

LIST OF FIGURES

LIST OF TABLES

ABSTRACT

Integration of Utility-Scale Variable Generation into Resistive Networks

by

Sina Sadeghi Baghsorkhi

Wind and solar power account for half of newly installed electricity generation capacity worldwide. Due to falling technology costs, this trend is expected to continue despite the global economic turmoil and uncertainty over policy incentives for these fledgling sectors. A sizable portion of this capacity is connected to sub-transmission networks that typically have mesh configurations and are characterized by resistive lines (i.e. lines with $X/R \leq 4$). The resistivity of sub-transmission networks creates a strong coupling between power flows and voltage magnitudes that is atypical in high-voltage transmission systems. In the presence of generation variability, this can lead to extreme voltages, unacceptable voltage fluctuations, unusual (active and reactive) power flow patterns throughout the network, line congestions and increased losses. This can also cause excessive tap-changing operation of transformers with On-Load Tap Changers (OLTCs). These issues can be substantially mitigated with flexible methods of network operation and control. This dissertation examines the impact of variable embedded generation on the voltage profile, structural stability and the OLTC operation of the DTE/ITC network serving Eastern Michigan. It introduces a number of tools and methods to analyze the impact of variable generation in meshed resistive networks. It investigates how network resistivity transforms the impact of the reactive compensation, associated with variable generation, on the structural stability of the system. Finally an optimal voltage control scheme is presented to better coordinate the voltage regulation of variable generation with OLTCs, reduce network losses and enhance the structural stability of the system. The scheme is a model predictive control with an equivalent mixed integer formulation which models the hybrid dynamics of OLTC tap operations.

CHAPTER 1

Introduction

Wind and solar power accounts for slightly less than half of newly installed electricity generation capacity worldwide. Due to falling technology costs, this trend is expected to continue despite the global economic turmoil and uncertainty over policy incentives for these fledgling sectors [1]. A sizable portion of this capacity is connected to weak sub-transmission networks that typically have mesh configurations and are characterized by medium voltage levels (40-120kV) and resistive lines ($X/R \leq 4$). This is either due to the unavailability of high voltage transmission lines or the cost of connection assets (mainly transformers) which rises sharply with the voltage level and makes it uneconomical to connect wind and solar farms below a certain capacity directly to higher voltage networks even when the option exists [2]. Variable generation connected at multiple nodes can create unanticipated power flow patterns within a meshed network. This may result in line congestion at power production levels that are far below the rated capacity of the wind or solar farms. Furthermore, the resistivity of subtransmission networks creates a strong coupling between active power flows and voltage magnitudes that is atypical in high-voltage transmission systems. In the presence of generation variability, this can lead to extreme voltages, unusual reactive flow patterns throughout the network and increased active power losses. Figure 1.1 shows a simplified diagram of a legacy power system with centralized conventional generation. Bulk power is transported from a central power plant through transmission system to sub-transmission network which typically has a meshed structure. In proximity to consumers, power is delivered in radial distribution feeders and the voltage magnitude is successively reduced by transformers at a number of substations.

When significant variable generation is introduced into this legacy structure, particularly at sub-transmission levels, the following problems may arise:

1. Voltage magnitudes fluctuate significantly as generation varies.

2. OLTC transformers that are used for voltage regulation experience higher frequency of operation.

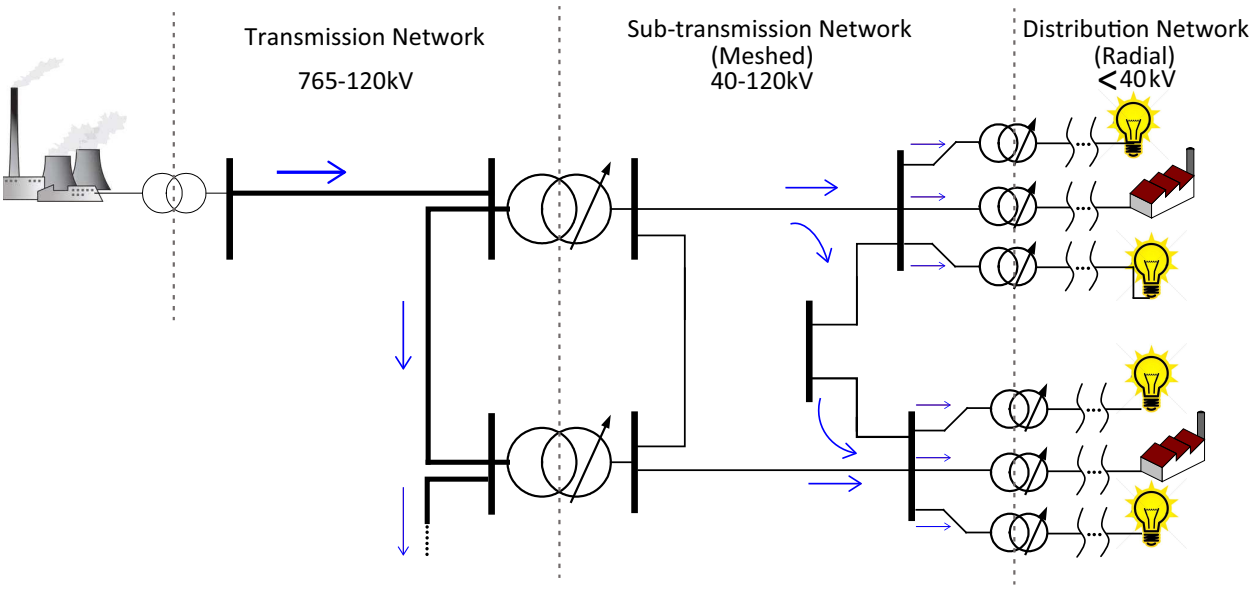

Figure 1.1: Conventional Power Grid

3. Reactive power flow patterns change depending on the voltage control mode of wind and solar farms.

4. Voltage stability of the system may be negatively affected.

5. Network losses are more likely to increase.

6. Lines are more likely to experience congestion.

The first problem is rooted in the legacy voltage control schemes. Power grids (with either radial or meshed configurations or a combination of both as depicted in Figure 1.1) have been historically designed so that voltage magnitudes near the bulk power transmission systems are higher compared to voltage magnitudes near the load. This is in anticipation of the fact that voltages tend to drop as current is drawn by network loads [3]. When generation is connected to resistive feeders (Figure 1.2), the feeders draw smaller currents and thus the voltage drop is mitigated. When generation exceeds network load, the reverse flow of current can cause voltage rise. This phenomenon was first noticed and analyzed in the context of an 11kV radial feeder with embedded generation in 2002 [4]. A number of case studies since then have observed and investigated this phenomenon in radial distribution feeders [5] and meshed sub-transmission networks [6].

The second problem is essentially the reflection of the first problem on the key voltage regulators of the network. These switching devices control the voltage magnitudes at a number of substations starting from the bulk power system and ending at the customer. On-load tap-changing (OLTC) transformers are the most prevalent type of these

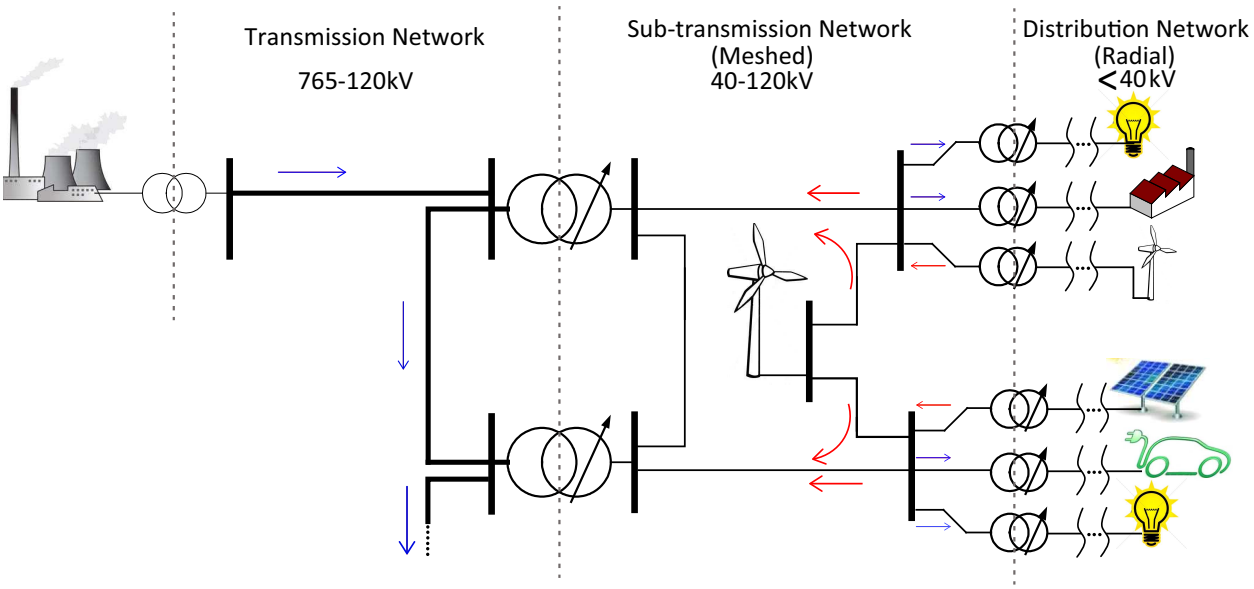

Figure 1.2: Modern Power Grid with Variable Generation

voltage regulators. A common practice to compensate for transmission system voltage variations and adjust voltage levels across distribution/subtransmission networks is to use OLTC transformers. The OLTC mechanism effectively decouples the voltages of the two networks and act as buffers against the impact of higher voltage network disturbances on the lower voltage network. This is achieved by adjusting the transformer's effective turn ratio through the tapping mechanism as to maintain the secondary side voltage constant. OLTCs are indispensable where there are sensitive (customer) nodes in the lower voltage network whose voltage profile should be maintained under all loading conditions. It is a well established fact that as the number of switching (tap) operations increases, the life-time of these expensive devices shortens [7, 8, 9] and the risk of substation failures and maintenance costs increase [10, 11, 12]. Despite the indispensable role of OLTCs in voltage regulation, it is not uncommon to see off-circuit tap-changing (fixed tap) transformers especially at distribution levels [7]. The fixed tap transformer has also a tap changer that can be manually adjusted only when the transformer is de-energized and thus while the transformer is in operation the tap is considered fixed. These transformers are significantly less costly, more reliable and have a simpler maintenance [7, 10].

In recent years a number of studies have examined the impact of variable generation, specifically wind power, on the OLTC operations [6, 13, 14, 15, 16]. These studies are all based on simulation of voltage profile and OLTC operations for specific networks. There is a general consensus that generation variability affects OLTC operations but the specific conclusions from these studies are inconsistent with one another. A detailed discussion

of these conclusions which primarily focus on the simulation of the impact of different voltage control modes at the POI on the OLTC operations is presented later in this thesis. In the wake of such inconsistencies, clarification is need on the precise relationship between generation variability and OLTC operations.

The legacy voltage control schemes may change the reactive requirement of the resistive networks creating reactive sinks at the point of interconnection (POI) of wind and solar farms. These reactive sinks absorb substantial amount of reactive power which has to be provided by the transmission reactive reserves, i.e. the available reactive supply (such as the free reactive capacity of synchronous generators) that can be utilized in response to reactive demands in the system. This problem is closely related to the voltage rise phenomenon and is a direct consequence of the new grid codes. As the active power injection into a resistive feeder increases, the voltage at the point of injection tends to rise when the voltage on the receiving end of the feeder is held fixed, for example, regulated by an OLTC transformer [4]. To remedy this voltage rise, reactive power is absorbed at the point of injection of active power. As the penetration of variable generation has increased in recent years and with the emergence of voltage fluctuation issues, utilities have adopted new grid codes requiring the voltage magnitudes at the POI to be strictly regulated [2, 17]. This requires absorbtion of reactive power at the POI which may lead to significant flow of reactive power in meshed resistive networks substantially increasing active power losses. Furthermore, the new reactive requirement may strain the reactive reserves of the transmission system and negatively impact the voltage security of the network, i.e. the ability of the network to keep voltages within their acceptable range. It can also bring the system closer to the point of voltage instability where the combined capability of generation and transmission system is no longer adequate to support a given level of power consumption [18] and the attempt by load dynamics to restore the power consumption leads to voltage collapse [19]. The distance to voltage instability in a given parameter space (load and/or generation) is generally defined as the voltage stability margin. Hence the integration of embedded generation under the new grid codes may negatively affect the voltage stability margin of the system. These issues have not yet been investigated or reported by the industry. This thesis explores these issues in the context of the DTE/ITC system. It is expected that as the penetration of variable generation increases and wind and solar farms are increasingly required to absorb reactive power to control voltage magnitudes, these issues will be noticed by utilities in the near future.

The last problem, line congestion, is the primary reason for wind curtailment which has become a well-established practice in industry [20, 21] and has resulted in substantial loss of revenue for wind and solar farm operators [21, 22]. Line congestion is defined as

the condition where the power flow through the line exceeds certain reliability limits [23]. For resistive feeders these limits are generally determined in terms of the thermal ratings of line conductors whereas in higher-voltage transmission lines these limits are determined by voltage or angular stability criteria [24]. Line congestion becomes even more pertinent in meshed resistive networks such as the DTE-owned 42kV sub-transmission network where variable generation at multiple injection nodes creates unforseen flow patterns causing certain resistive feeders to reach their thermal ratings at wind generation levels that may be far below the rated capacity of wind farms [25]. Reactive requirement of resistive networks and lack of coordination between voltage regulators, discussed in the previous paragraph, can further exacerbate line congestion problem especially in meshed networks.

These problems can be substantially mitigated with flexible methods of network operation and control where the control setpoints, primarily the voltage setpoints of reactive compensation devices, are not fixed but rather adjusted at short time intervals in response to variation of wind or solar power output. Thus the central task of such methods should be to coordinate the voltage regulation of the network by anticipating short-term variations of wind and solar generation throughout the network. The prerequisite for designing such a coordinated control scheme is the theoretical understanding of the underlying causes of OLTC operation, network losses and the complicated relationship between voltage regulation and the structural stability in resistive networks.

1.1 Overview of the Dissertation

This dissertation is organized as follows:

Chapter 2 introduces a set of tools that are used in later chapters to analyze the impact of generation variability on a typical sub-transmission network with resistive feeders that are connected in mesh. These include sensitivity analysis and continuation power flow for the impact on voltage profile and OLTC tap operations, quadratic optimization for line congestion studies and an efficient and exact method for computing power flow feasibility boundary which is used later to investigate the impact of reactive compensation on the structural stability of power systems with sub-transmission wind injection. The chapter concludes by formulating the rectangular power flow as a special case of the semi-definite relaxation of optimal power flow which is central to the exact formulation of optimal variable generation capacity allocation problem.

Chapter 3 applies these tools to investigate the impact of wind generation on the DTE/ITC system serving Eastern Michigan. Here certain patterns regarding voltage regulation, reactive compensation, tap sensitivity, losses and voltage stability margin are high-

lighted. These patterns are explained through analytical investigations in the next two chapters.

Chapter 4 analyzes the impact of voltage control mode of embedded (wind and solar) generation in resistive networks on the structural stability of the power system. It is shown in this chapter that network resistivity transforms the typical paradigm of reactive compensation and voltage stability. Whereas in inductive transmission systems enhancing the reactive compensation capability always improves the voltage stability margin, in resistive networks this can reduce the stability margin and negatively impact the structural stability of the system.

Chapter 5 focuses on the operation of OLTCs in relation to variable generation in resistive networks. It explores the real cause of tap change by analyzing the generic model of an OLTC and the active and reactive power that flow through the transformer. This chapter also shows how active power losses can be minimized in the presence of OLTCs and FACTs devices which regulate voltages and indirectly control the flow of reactive power through the network. Later the chapter presents the evolution of a coordinated voltage control scheme that controls the voltage setpoints at POIs based on the short-term forecast of variation of wind or solar power with the objective of reducing sub-transmission and distribution OLTC operations, network losses and the reactive flow into the sub-transmission network. Finally it introduces a mixed-integer formulation that captures the hybrid dynamics of the tap change mechanism and solves for the voltage setpoint(s) that minimizes the above objectives. The chapter concludes with the results of the implementation of the voltage control scheme on the DTE/ITC system.

Chapter 6 summarizes the major conclusions of the dissertation and sketches an outline for future research.

The results of a number of simulations involving wind and solar generation and load data are presented in this dissertation. All these simulations are based on codes that were developed in Matlab by the author and verified with commercial solvers (PSLF and PowerWorld). Annual wind generation and load data with a one-minute resolution was provided by DTE energy which owns and operates the sub-transmission and distribution networks in Eastern Michigan as well as multiple sub-transmission wind farms connected at the 42kV level. PV data with a one-minute resolution was provided by Dr. Leith Elder and belongs to the Atlantic City Convention Center solar PV project in Atlantic City, New Jersey.

Figure 1.3 shows wind and solar PV output for a 24-hour period that is atypical in terms of generation variability. The wind output indicates that there were wind gusts at the beginning of the day which abate later. This scale of wind output variation is extreme and is chosen to show the scope of wind power variability that can realize over the course of a

day. The PV power output is also quite variable and one can infer from the patterns that the output corresponds to a rainy or cloudy day. The standard to mean ratio for wind data depicted in Figure 1.3 is 0.70 whereas the same ratio for PV output is 1.40. However it is difficult to conclude any statistical feature that can distinguish wind from PV output other than the obvious diurnal pattern in PV output. The variability of wind and solar PV output is determined by many factors such as the geographic location, dominant weather patterns and the scale of wind or solar farms (i.e. output aggregation). The PV data is from the East Coast of the United States with more rainy and cloudy days than the US Southwest where solar PV has a much more rapid pace of development and utilities are already grappling with the issues caused by generation variability [70]. Therefore the variability of the PV data may not be representative of the output variability in more sunny regions. Also the PV data is only based on a 2.4 MW project and it is expected that utility-scale PV generation exhibits less variability than the present data. The smoothing effect of aggregation is a factor that needs to be examined for both wind and PV output, a task that lies outside the scope of this thesis. Among the key tasks of this thesis is to highlight how generation variability in resistive networks can impact voltage regulation and the operation of OLTC devices and how these effects can be remedied by a coordinated control scheme. The approach has been mainly theoretical and the key findings and the proposed control scheme that flows from this analysis is independent of generation data.

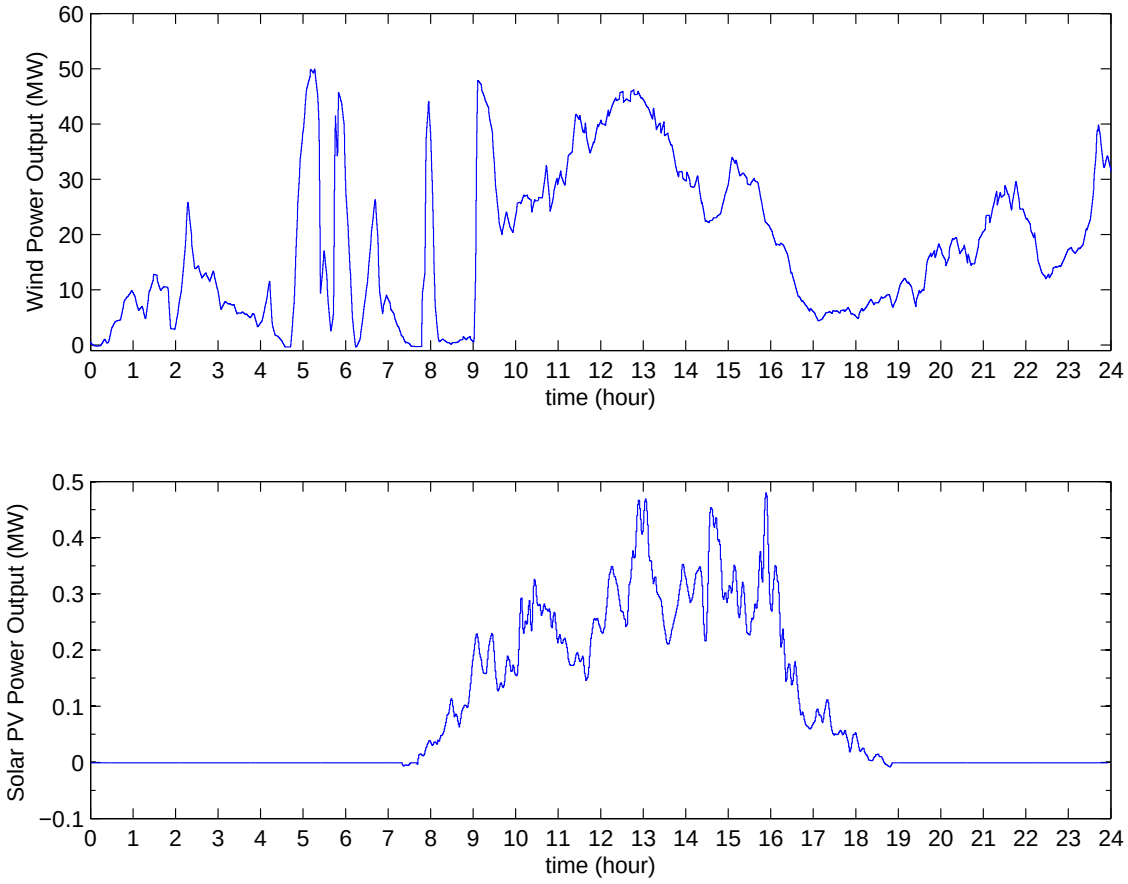

Figure 1.3: Wind and Solar PV Variability

CHAPTER 2

Tools for Assessing the Impact of Variable Generation in Resistive Networks

2.1 Introduction

Wind and solar generation introduce high variability into sub-transmission networks (40-120 kV), significantly influencing the statistical characteristics of voltages and power flows. High penetration of wind and solar power also often lead to bi-directional flows in network configurations that were historically evolved for uni-directional operation. Meshed interconnections within sub-transmission networks further complicate power flow patterns induced by variable generation, particularly when wind or solar farms are connected through multiple nodes of a meshed network.

The variability inherent in the power produced by distributed variable generation can lead to reactive power requirements that may adversely affect bus voltages and OLTC transformers. In particular, legacy voltage regulation schemes may be ill-equipped to cope with the variations in power flow. Wind and solar farm operators are often required to regulate the voltage at the point-of-interconnection. However that requirement does not ensure that voltages throughout the network are not adversely affected. In fact, if voltage controls are not carefully coordinated, voltage regulating transformers may undergo excessive tap-changing operations, leading to a significant increase in maintenance and reduced lifetime. Furthermore, variable generation connected at multiple nodes can create unanticipated power flow patterns within the sub-transmission network. This may result in line congestion at power production levels that are far below the rated capacity of the wind or solar farms.

The effects of variable generation on the grid are often not obvious *a priori*. Standard power flow simulations provide limited insights, with few systematic methods available for analyzing the impact of wind on network voltages, OLTC operation and line flows. In this chapter a range of analysis tools for assessing the impact of generation variability

on voltage regulation, line flows and structural stability is considered. These tools have been used to study the ITC/DTE power grid in Michigan where significant growth in wind generation is expected. It is anticipated that this increased wind generation will cause operational difficulties, including voltage variability and line overloading. These issues have been explored further in Chapter 3.

The chapter is organized as follows. Sensitivity analysis is presented in Section 2.2. Continuation power flow method is considered in Section 2.3. An optimization formulation for assessing line congestion is developed in Section 2.4. A method for obtaining saddle-node bifurcation (critical) boundary is presented in Section 2.5.

2.2 Sensitivity Analysis

The power flow is fundamental to power system analysis, underpinning studies from contingency analysis to system planning. The power flow problem consists of a set of nonlinear algebraic equations that can be expressed as,

$$P_i(\theta, V) = |V_i| \sum_{k \in \mathcal{N}[i]} |V_k|(G_{ik} \cos\theta_{ik} + B_{ik} \sin\theta_{ik}) \qquad \forall i \in \mathcal{N} \tag{2.1a}$$

$$Q_i(\theta, V) = |V_i| \sum_{k \in \mathcal{N}[i]} |V_k|(G_{ik} \sin\theta_{ik} - B_{ik} \cos\theta_{ik}) \qquad \forall i \in \mathcal{N} \tag{2.1b}$$

where (2.1a) describes the active power balance at PV and PQ buses, (2.1b) describes the reactive power balance at PQ buses, θ is the vector of voltage angles (relative to the slack bus) at all PV and PQ buses, and V is the vector of voltage magnitudes at PQ buses and $\mathcal{N}$ is the set of all nodes in the network [26]. It follows that P and θ have the same dimensions, and likewise the dimensions of Q and V are equal.

Transformer taps can be incorporated into the power flow equations by assuming tap positions a_i are continuous variables, and noting that each transformer regulates a particular bus voltage. That bus voltage magnitude V_i takes on a known fixed value, and so it can be replaced in (2.1a)-(2.1b) by the new variable a_i. The power flow equations can be generalized accordingly by replacing the voltage vector V with $\mathcal{V} = \begin{bmatrix} \tilde{V} \\ a \end{bmatrix}$ where $\tilde{V}$ is the vector of voltage magnitudes at non-regulated buses, and a is the vector of tap positions associated with the transformers that are regulating bus voltages. Note that Q and $\mathcal{V}$ still have equal dimensions.

Taking partial derivatives of P and Q with respect to θ and $\mathcal{V}$ gives the linearized

relationship,

$$\begin{bmatrix} \Delta P \\ \Delta Q \end{bmatrix} = \begin{bmatrix} P_\theta & P_\mathcal{V} \\ Q_\theta & Q_\mathcal{V} \end{bmatrix} \begin{bmatrix} \Delta\theta \\ \Delta\mathcal{V} \end{bmatrix} \tag{2.2}$$

where $P_\theta \equiv \frac{\partial P}{\partial \theta}$, and likewise for the other sub-matrices. We are interested in how variations ΔP in the injected active power at wind-farm locations affect voltage magnitudes and tap positions, which are given by $\Delta\mathcal{V} = \begin{bmatrix} \Delta\tilde{V} \\ \Delta a \end{bmatrix}$. For transmission systems, where resistance is negligible, the off-diagonal blocks in (2.2) are almost zero, and so are normally neglected. This decouples ΔP from $\Delta\mathcal{V}$. However in sub-transmission and distribution networks, where resistance is non-negligible, the off-diagonal blocks become important. To understand how $\Delta\mathcal{V}$ varies with ΔP, we can use the Matrix Inversion Lemma [27] to give,

$$\begin{aligned} \Delta\mathcal{V} = &- \left[Q_\mathcal{V} - Q_\theta P_\theta^{-1} P_\mathcal{V}\right]^{-1} Q_\theta P_\theta^{-1} \Delta P \\ &+ \left[Q_\mathcal{V} - Q_\theta P_\theta^{-1} P_\mathcal{V}\right]^{-1} \Delta Q. \end{aligned} \tag{2.3}$$

Here it is assumed that reactive power remains unchanged at PQ buses, so $\Delta Q = 0$. It follows that the desired sensitivities are given by,

$$\begin{aligned} \Delta\mathcal{V} &= - \left[Q_\mathcal{V} - Q_\theta P_\theta^{-1} P_\mathcal{V}\right]^{-1} Q_\theta P_\theta^{-1} \Delta P \\ &= S_\mathcal{V}\, \Delta P \end{aligned} \tag{2.4}$$

where $S_\mathcal{V} = \begin{bmatrix} S_{\tilde{V}} \\ S_a \end{bmatrix}$, and

$$\begin{aligned} \Delta\tilde{V} &= S_{\tilde{V}} \Delta P \quad \text{for buses where voltages are not regulated,} \\ \Delta a &= S_a \Delta P \quad \text{for transformer taps.} \end{aligned}$$

Later, in Section 2.4 the following identity is also used,

$$\begin{aligned} \Delta\theta &= \left[P_\theta - P_\mathcal{V} Q_\mathcal{V}^{-1} Q_\theta\right]^{-1} \Delta P \\ &= S_\theta\, \Delta P. \end{aligned} \tag{2.5}$$

It should be remarked that the use of the power flow Jacobian for sensitivity analysis is not new, with applications dating back to the late 1960s [28]. Since then, sensitivity analysis has been applied in a wide range of power system studies, from voltage stability [29, 30, 31] to assessing the impact of distributed generation on line losses [32].

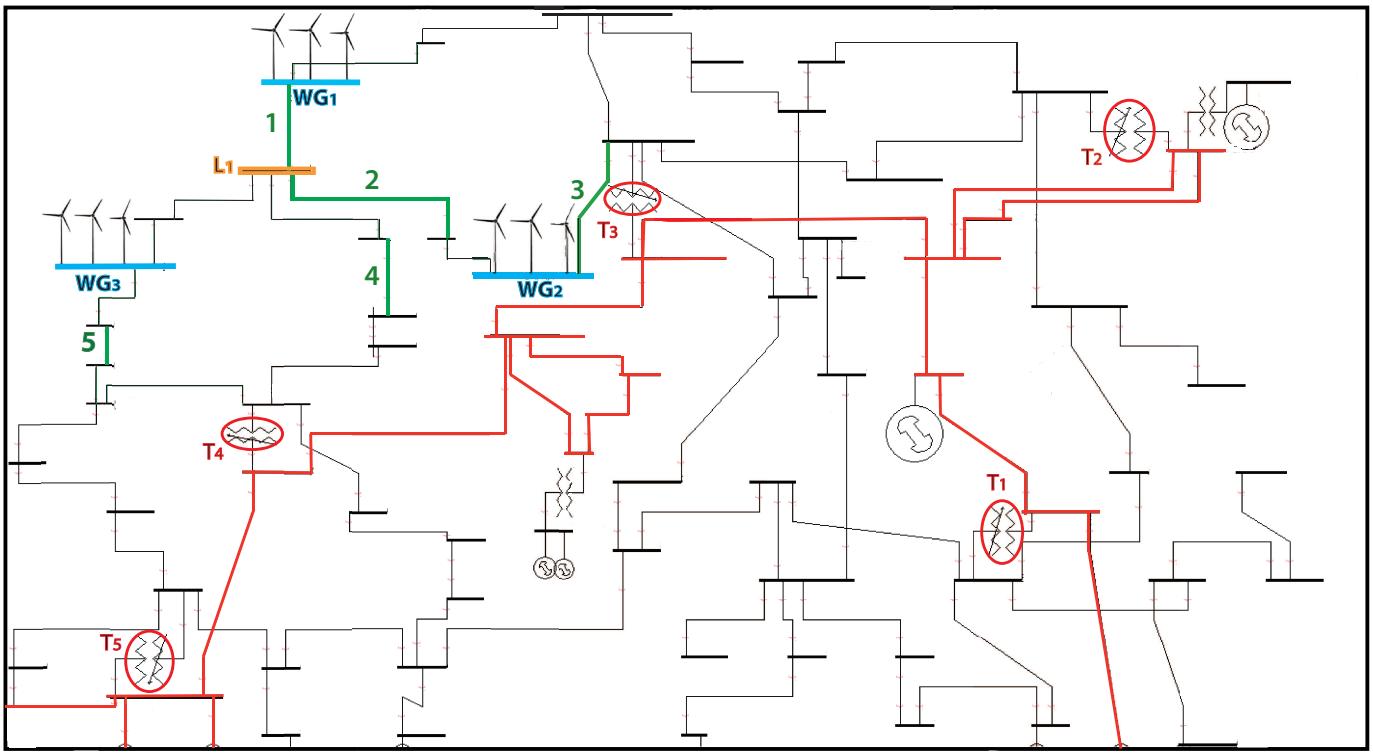

Figure 2.1: DTE sub-transmission wind development network

Table 2.1 lists the sensitivity values of transformer tap-ratio to wind injection at WG_1 and WG_2 in the 42 kV sub-transmission network shown in Figure 2.1. Note that wind injection nodes are highlighted in blue, load bus L_1 in yellow, the 120 kV transmission system and the 120/42 kV tap-changing transformers in red, the 42 kV sub-transmission network black and the lines of interest in the later congestion study in green. According to these values, transformers are most likely to undergo tap-changing operations at low to medium wind injections. Transformer T_3 is the most sensitive transformer to wind injection, followed by T_4 and T_5. Furthermore, the sensitivity analysis indicates that T_3 is extremely sensitive to wind injection at WG_2.

In the next section, the continuation power flow will be used to explore key parameters of the system, with the goal of reducing the impact of wind injection at WG_2 on the tap position of transformer T_3.

2.3 Continuation Power Flow

Sensitivity values only provide local information around a single operating point. This can be helpful in identifying bus voltages and transformer taps that are highly sensitive to

Transformer Tap-Ratio Sensitivities ($\frac{\text{tap-ratio}}{\text{MW injection}}$)						
Operating Point	Inject. Node	Transformer				
		T_1	T_2	T_3	T_4	T_5
Low wind injection	WG_1	0.04	0.04	0.10	0.11	0.07
	WG_2	0.05	0.04	0.14	0.09	0.06
Medium wind injection	WG_1	0.04	0.04	0.09	0.05	0.05
	WG_2	0.08	0.07	0.20	0.18	0.14
High wind injection	WG_1	0.03	0.01	0.02	0.03	0.05
	WG_2	0.03	0.01	0.02	0.03	0.06

Table 2.1: Tap step sensitivities for the transformers highlighted in Figure 2.1.

wind injection at a certain operating point. However sensitivity analysis may not accurately capture the behavior of these variables in response to large changes in the system.

The power flow equations (2.1a)-(2.1b) can be written in generalized form as $f(x) = 0$, where f and x have the same dimension. This problem is fully determined, so solutions will be points. If a single parameter is allowed to vary, for example the active power at a PV or PQ bus, or the voltage setpoint at a voltage regulated bus, the problem takes the form,

$$f(x, \lambda) = 0, \tag{2.6}$$

where λ is the single free parameter. Now the problem has one more variable than constraint, so is under-determined. In this case, the solution is no longer a single point, but rather defines a curve. Freeing a second parameter results in a surface which can be shown as a collection of curves, i.e. contour diagram, similar to a topographic map with contours of elevation. This concept underlies the continuation power flow.

Continuation methods for solving problems of the form (2.6) are well documented [33, 34]. Predictor-corrector algorithms, such as the Euler homotopy method, provide a robust process for obtaining a sequence of points along the desired curve. These methods first found application in power system studies in the early 1980s, see for example [35]. Subsequent power system applications of continuation methods include voltage stability studies [36] and solution space investigations [37].

The continuation power flow enables a range of studies that assist in assessing the impact of wind power in weak grids, including:

A. Exploring parametric influences in the relationship between variable wind and solar power injection and bus voltages, tap positions and line flows, and

B. Extending those studies to consider interactions between multiple injection nodes.

2.3.1 Parametric effects

The continuation power flow can be used to show how certain network parameters can be adjusted to reduce the impact of generation variability. In the previous section it was observed that at low to medium levels of wind-power injection, wind-power variability at WG_2 (in Figure 2.1) has a detrimental effect on the tap-changing operation of transformer T_3. It is important to determine actions that minimize the number of tap-change operations as wind injection at WG_2 varies, thereby extending transformer life. Let us consider the setpoint of the transformer voltage regulator, as that parameter has a significant impact on the tap position. Figure 2.2(a) shows a collection of contour curves, with each curve obtained by fixing the tap at a discrete value and freeing the two power-flow parameters, 1) wind injection at WG_2, and 2) voltage setpoint of T_3. Each curve corresponds to a discrete tap position, with adjacent curves corresponding to the next higher and lower taps.

Power systems incorporate numerous devices that regulate voltages, with an overall voltage profile achieved through coordination of generators, tap-changing transformers, and FACTS devices such as Statcoms and SVCs. Under normal operation these devices regulate to specified setpoints. However significant changes, such as large variations in wind-power or deviations in load, can drive these regulating devices to their limits. Regulation can no longer be achieved when a limit is encountered, so the controlled quantity will deviate from its setpoint value. The resulting change in the system description introduces discontinuities into the contours.

Two such discontinuities are apparent in Figure 2.2(b), where the contour lines corresponding to the inductive limits of WG_1 and WG_2 have been superimposed on the tap-position contours. As the voltage setpoint for T_3 is lowered and the WG_2 discontinuity is crossed, the slope of the tap contours increases. As a consequence, deviations in wind injection will induce greater tap variation. It may be concluded that increasing the voltage setpoint of T_3 tends to lower the impact of WG_2 output variability on T_3 tap changing.

It should be noted that contour curves may pass through turning points where the Jacobian of the power-flow equations is singular [34]. The power flow equations generically have multiple solutions, but usually only one solution is stable. Extraneous solutions can be easily recognized by checking the eigenvalues of the Jacobian matrix. Each time the contour curve passes through a turning point, one eigenvalue of the Jacobian changes sign. The red dotted branches in Figure 2.2(a) identify cases where eigenvalues have changed sign.

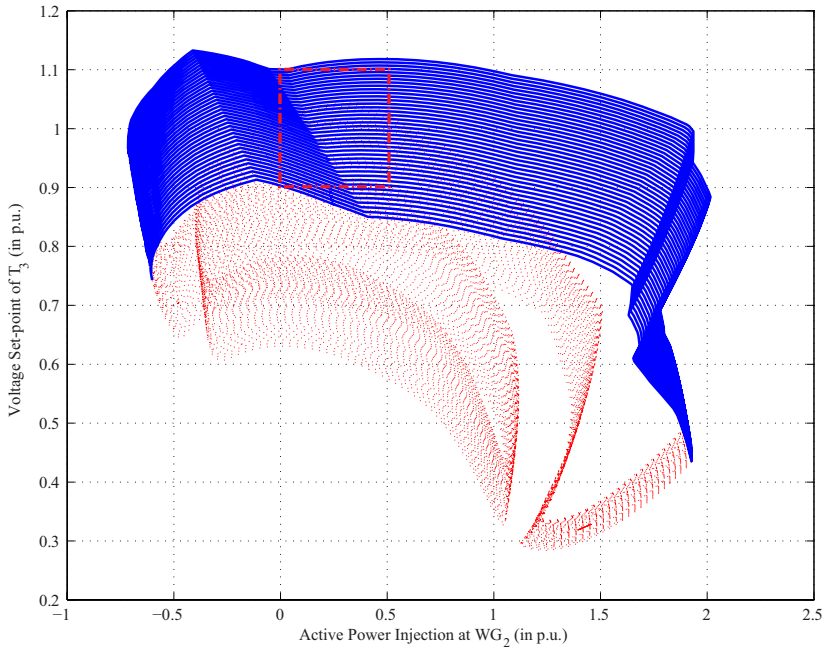

(a) Global View

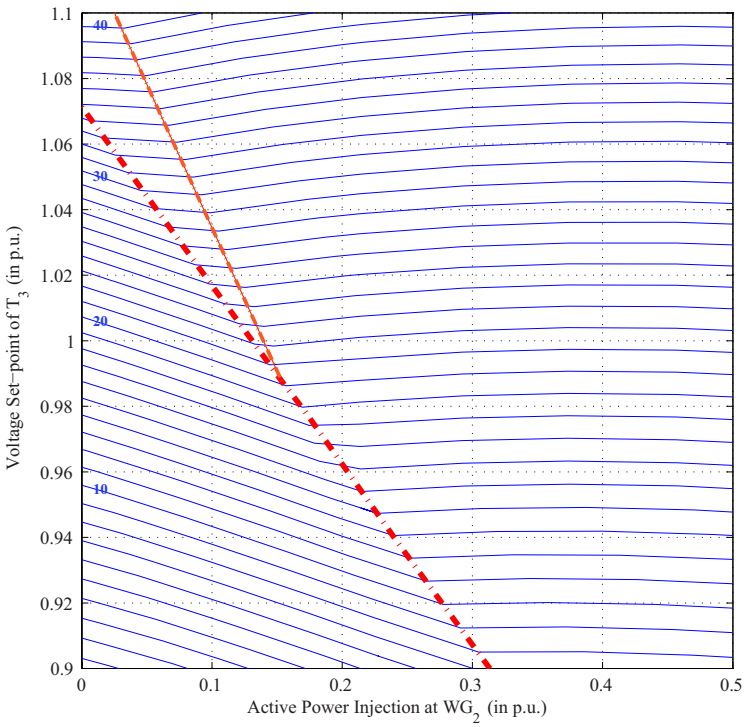

(b) Region of Interest

Figure 2.2: Contour diagrams of T_3 tap position for varying active power injection at WG_2 and T_3 voltage setpoint.

2.3.2 Interactions due to wind or solar power injection at multiple nodes

Wind and solar power injections at multiple nodes may interact to affect the voltage profile and tap positions in unexpected ways. The continuation power flow provides a means of exploring such phenomena. Figure 2.3(a) shows the contours of voltage at load bus L_1 (highlighted in yellow in Figure 2.1), which is in the vicinity of wind injection nodes WG_1 and WG_2. The region of the contour diagram corresponding to the feasible range of wind power injections is highlighted by the red box in Figure 2.3(a), and an enlargement of that region is provided in Figure 2.3(c).

Discontinuities induced by reactive power limits at the two wind farms WG_1 and WG_2 are evident in Figure 2.3(a). They introduce a roughly symmetric pattern, corresponding to wind power being high at one wind farm and low at the other. Figure 3.5 shows the contour lines for the inductive limits of WG_1 and WG_2 superimposed on the contour diagram of Figure 2.3(a). As wind power injection increases, the wind farm must absorb more reactive power to prevent the voltage from rising. This continues until its inductive limit is encountered. As wind power continues to increase, the voltage magnitude at the wind farm and adjacent nodes will rise. The solution space in Figure 3.5 is divided into four regions labeled A, B, C and D. In region A, both WG_1 and WG_2 are regulating voltage. In region C, WG_2 has reached its inductive limit but WG_1 is still regulating, whereas in region D the situation is the reverse. In region B both WG_1 and WG_2 have reached their inductive limits, so no voltage regulation is possible.

2.4 Quadratic Optimization for Line Congestion

In order to minimize the cost of sub-transmission and distribution networks, line designs are usually closely tied to the load profile of the network and its growth projections. The addition of substantial variable generation to such networks is, therefore, likely to cause overloading of line segments.

In a meshed network with multiple points of connection to the transmission system, as in Figure 2.1, wind and solar generation patterns may cause line flows to vary in ways that are not always obvious. Consequently, line segments that are not even necessarily near injection nodes may be driven to their limits as the power production of wind or solar farms change. On the other hand, maximum generation at all farms may not cause any congestion. It is therefore challenging to discover potential line overload vulnerabilities using conventional power-flow methods. To circumvent this difficulty, it would be useful

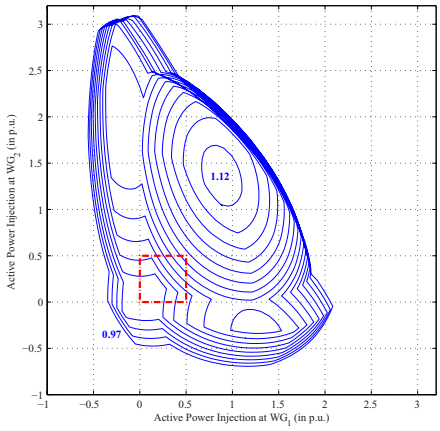

(a) Global view.

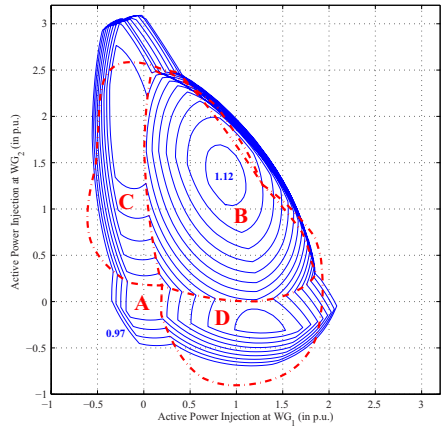

(b) Global view, including reactive limit curves.

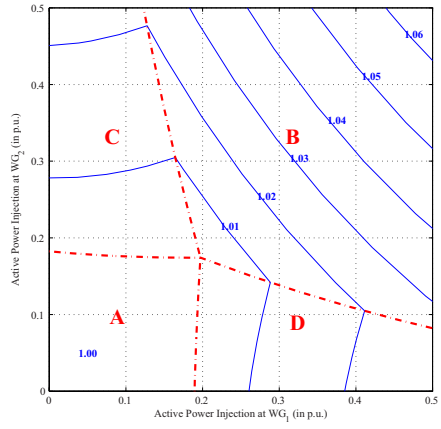

(c) Region of Interest.

Figure 2.3: Contour diagrams of voltage magnitude at load bus L_1 for varying active power injections at wind nodes (± 15 MVAr compensation).

Line	DC Flow (%)	AC Flow (%)
1	66	55
2	45	43
3	82	84
4	107	95
5	114	90

Table 2.2: DC approximation of actual line flows, for lines highlighted in green in Figure 2.1.

to know the smallest change in the generation pattern that would cause any line segment to encounter its limit. This would immediately identify the most vulnerable line, as well as the most troublesome generation pattern.

Two optimization methods have been proposed for determining that information for any given operating point. Both are based on a convex quadratic optimization formulation, with the first using a DC power-flow approximation, and the second using AC sensitivities. The first of these methods shares some similarities with the instanton formulation developed in [38]. The DC method is more efficient computationally whereas the AC sensitivity-based method is more accurate. The AC approach may, however, require multiple iterations to achieve convergence, with each iteration solving a power flow and computing sensitivities. The AC formulation also does not provide any guarantee of a globally optimal solution, though these investigations have not found this to be an issue. Both methods take into account correlation between power production at different nodes that naturally arises as a results of temporal and spatial correlation between wind (or solar) energy.

2.4.1 DC quadratic optimization

At the core of the DC quadratic optimization is the DC power flow. The usefulness of this optimization approach therefore depends on how accurately the DC power flow approximates actual line flows. It has been argued that the DC power flow may yield inaccurate approximations for networks where resistance is non-negligible ($\frac{X}{R} < 4$) [39]. However, for the power system of Figure 2.1, where $\frac{X}{R} \approx 1$, the DC power flow approximation is still quite accurate. Table 2.2 compares the DC approximation with the accurate AC power flow for the lines highlighted in green in Figure 2.1. The values in the table are given as a percentage of the line rating, and correspond to the case where each of the wind farms in Figure 2.1 is producing 30 MW.

Let the power generated at m wind-farms be described by the vector $\rho \in \mathbb{R}^m$. The wind power generation pattern ρ that is closest (in a weighted 2-norm sense) to base-case

generation ρ_0, and that causes line i to encounter its flow limit ℓ_i, is given by the DC quadratic optimization problem,

$$\bar{\rho}_i = \underset{\rho}{\operatorname{argmin}} \ \frac{1}{2}(\rho - \rho_0)^\top W(\rho - \rho_0) \tag{2.7}$$

subject to

$$\begin{bmatrix} A_\rho \\ A_b \end{bmatrix} \theta - \begin{bmatrix} \rho \\ b \end{bmatrix} = 0 \tag{2.8}$$

$$s_i^\top \theta - \ell_i = 0 \tag{2.9}$$

$$0 \leq \rho \leq \rho_{max} \tag{2.10}$$

where W is a symmetric, positive definite weighting matrix that captures the correlation between generation at the m wind (or solar) farms. For an n-bus network, bus phase angles are given by $\theta \in \mathbb{R}^{n-1}$, and non-wind power injections/loads by $b \in \mathbb{R}^{n-1-m}$. The admittance matrix $\begin{bmatrix} A_\rho \\ A_b \end{bmatrix}$ establishes a linear mapping between phase angles and power injections. Eq. (2.9) forces the flow on a single chosen line i to equal its limit value, given by the scalar ℓ_i.

The Lagrangian [40] for this problem is given by,

$$\begin{aligned} \mathcal{L}(\rho, \theta, \lambda_\rho, \lambda_b, \gamma) =& \frac{1}{2}(\rho - \rho_0)^\top W(\rho - \rho_0) + \lambda_\rho^\top (A_\rho \theta - \rho) \\ &+ \lambda_b^\top (A_b \theta - b) + \gamma(s_i^\top \theta - \ell_i) \end{aligned} \tag{2.11}$$

with the Karush-Kuhn-Tucker conditions [40] yielding the set of linear equations,

$$\frac{\partial \mathcal{L}}{\partial \rho} = (\rho - \rho_0)^\top W - \lambda_\rho^\top \qquad = 0 \tag{2.12}$$

$$\frac{\partial \mathcal{L}}{\partial \theta} = \begin{bmatrix} \lambda_\rho^\top & \lambda_b^\top \end{bmatrix} \begin{bmatrix} A_\rho \\ A_b \end{bmatrix} + \gamma s^\top = 0 \tag{2.13}$$

$$\frac{\partial \mathcal{L}}{\partial \lambda_\rho} = A_\rho \theta - \rho \qquad = 0 \tag{2.14}$$

$$\frac{\partial \mathcal{L}}{\partial \lambda_b} = A_b \theta - b \qquad = 0 \tag{2.15}$$

$$\frac{\partial \mathcal{L}}{\partial \gamma} = s_i^\top \theta - \ell_i \qquad = 0 \tag{2.16}$$

which can be expressed in matrix form as,

$$\begin{bmatrix} W & 0 & -I & 0 & 0 \\ 0 & 0 & A_\rho^\top & A_b^\top & s_i \\ -I & A_\rho & 0 & 0 & 0 \\ 0 & A_b & 0 & 0 & 0 \\ 0 & s_i^\top & 0 & 0 & 0 \end{bmatrix} \begin{bmatrix} \rho \\ \theta \\ \lambda_\rho \\ \lambda_b \\ \gamma \end{bmatrix} = \begin{bmatrix} W\rho_0 \\ 0 \\ 0 \\ b \\ \ell_i \end{bmatrix}. \tag{2.17}$$

This problem can be efficiently solved for large systems using standard sparse linear solvers. Note that the base-case generation ρ_0 appears only in the right hand side of (2.17). Therefore a range of base-case conditions can be evaluated efficiently through forward and backward substitution.

Because (2.17) considers only one line limit at a time, determining the most restrictive case from a set of candidate lines requires repeated solutions, with different line parameters (s_i, ℓ_i) for each case. The modifications required in (2.17) for each new case are minimal though, allowing efficient partial refactorization techniques [41] to be used to reduce the computational burden. Collecting the minima for all the candidate lines into the set $P = \{\bar{\rho}_1, \bar{\rho}_2, \dots\}$, the most restrictive case is given by,

$$\rho^* = \underset{\rho \in P}{\operatorname{argmin}} \ \frac{1}{2}(\rho - \rho_0)^\top W(\rho - \rho_0). \tag{2.18}$$

The network presented in Figure 2.1 provides a realistic test case for illustrating the DC optimization. The three wind farms WG_1, WG_2 and WG_3 have the potential to overload the five feeders that are labeled and highlighted in green in the network diagram. For this initial case, it was assumed the outputs of the wind farms were not correlated, so the weighting matrix W was set to the identity matrix. Table 2.3 presents the minimal (in the norm-2 sense) wind generation that will drive each line to its limit. These results were obtained for $\rho_0 = 0$ corresponding to absolute generation levels rather than changes from pre-existing loading conditions.

The insights provided by the results are helpful in understanding the influence of generation on feeder loadings. Line 1, for example, reaches its maximum loading when the flow is towards the south from WG_1, in the general direction of WG_2 and WG_3. When the other wind farms generate, they produce a counter-flow on line 1, allowing WG_1 to further increase its output. Hence line 1 in most vulnerable to overload when WG_2 and WG_3 are out of service. Similarly, line 2 reaches its limit when flow is towards the west, from WG_2 in the direction of WG_1 and WG_3. In this case, generation at WG_1 and WG_3 will produce counter-flows on line 2, so this line is most vulnerable to overloading when

Line	WG_1	WG_2	WG_3
1	37	0	0
2	0	27	0
3	19	46	18
4	31	23	22
5	13	10	36

Table 2.3: Minimal wind injection needed to cause line congestion.

No.	Operating point			Congested line / $\Delta\rho$	
	WG_1	WG_2	WG_3	No Correlation	Correlation
1[a]	30	30	30	–	–
2	30	30	10	4 / [5,3,3]	4 / [4,4,4]
3	30	10	30	5 / [0,0,2]	5 / [1,1,1]
4	10	30	30	5 / [1,1,1]	5 / [1,1,1]
5	30	10	10	1 / [9 -1 -1]	1 / [10,4,4]
6	10	30	10	2 / [-3,5,-3]	2 / [-4,4,-4]
7	10	10	30	5 / [2,2,6]	5 / [4,4,5]
8	10	10	10	2 / [-10,17,-10]	5 / [14,13,19]

[a] Lines 4 and 5 are already congested according to the DC power flow approximation.

Table 2.4: Most vulnerable lines at each operating points, DC optimization.

those generators are not producing power. In the other cases, all generators contribute to line overloading, though typically the generator that is electrically closest has the greatest influence.

The value of the DC optimization can be further illustrated by considering vulnerability of lines when the wind-farms are operating at various different output levels. Table 2.4 lists operating points obtained from all combinations of low (10 MW) and high (30 MW) wind generation. Each case identifies the line that would reach its limit first as wind generation was increased, along with the corresponding change in wind-power production $\Delta\rho$ that causes this congestion. The effect of correlation between wind-farms was explored by first assuming no correlation, so W in (2.7) was simply the identity matrix. Secondly, it was assumed the three wind-farms tended to increase/decrease output in unison. In this latter case, the desired correlation matrix W was obtained by shaping the axes of the ellipsoids given by level-sets of the cost function (2.7). The axis in the direction $[1\ 1\ 1]^\top$ was scaled by a factor of 4 relative to the axes in the orthogonal directions. This scaling is illustrated in Figure 2.4, which shows a 2-dimensional projection of the level-sets. The resulting

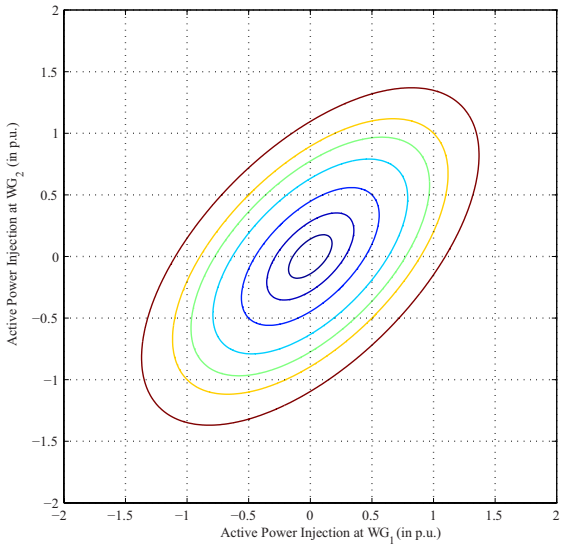

Figure 2.4: Ellipsoids generated by correlation matrix (2.19).

correlation matrix was

$$W = \begin{bmatrix} 3 & -1 & -1 \\ -1 & 3 & -1 \\ -1 & -1 & 3 \end{bmatrix}. \tag{2.19}$$

The results of Table 2.4 again reveal interesting trends in the relationships between generation patterns and line overloads. It can be seen that whenever WG_3 is heavily loaded, line 5 is the first to become congested. This is consistent with the findings of Table 2.3. Line 1 becomes limiting when WG_1 is heavily loaded, and the other wind-farms are not, which is again consistent with Table 2.3. There is a similar connection between WG_2 and line 2.

The eighth case is interesting in that correlation between wind farms clearly affects the outcome. With no correlation, the most vulnerable loading direction $\Delta\rho = [-10\ 17\ -10]^\top$ has WG_2 increasing its output, while WG_1 and WG_3 reduce theirs. This would be unlikely if the outputs of all three wind-farms tended to change in unison. With correlation taken into account, the optimization has identified the more likely scenario of $\Delta\rho = [14\ 13\ 19]^\top$, where all wind farms undergo a similar change.

2.4.2 AC sensitivity-based quadratic optimization

The DC quadratic optimization of (2.18) is guaranteed to give the globally optimal solution for the approximate DC system [40]. However, because of the approximation inherent in the DC formulation, there is no guarantee that the line limits discovered are in fact the most

restrictive. The AC sensitivity-based quadratic optimization provides increased accuracy over the DC method, though at an increased computational cost, and with no guarantee of achieving global optimality.

The magnitude of the current flow over a line between two nodes i and k can be written as the function,

$$I_{ik} = I_{ik}(\theta_i, \theta_k, V_i, V_k). \tag{2.20}$$

Linearizing gives

$$\Delta I_{ik} = \begin{bmatrix} \frac{\partial I_{ik}}{\partial \theta_i} & \frac{\partial I_{ik}}{\partial \theta_k} & \frac{\partial I_{ik}}{\partial V_i} & \frac{\partial I_{ik}}{\partial V_k} \end{bmatrix} \begin{bmatrix} \Delta\theta_i \\ \Delta\theta_k \\ \Delta V_i \\ \Delta V_k \end{bmatrix} \tag{2.21}$$

where the partial derivatives are evaluated at the operating point. Also, linearizing the power flow equations, as in (2.2), and inverting provides an approximate linear relationship between perturbations in power injection ΔP and ΔQ, and the corresponding perturbations in the state variables $\Delta\theta$ and $\Delta\mathcal{V}$. Assuming all perturbations in power injections are zero except for $\Delta\rho$ at wind farms, perturbations in the states associated with nodes i and k are given by,

$$\begin{bmatrix} \Delta\theta_i \\ \Delta\theta_k \\ \Delta V_i \\ \Delta V_k \end{bmatrix} = \begin{bmatrix} S_{\theta[i,\rho]} \\ S_{\theta[k,\rho]} \\ S_{V[i,\rho]} \\ S_{V[k,\rho]} \end{bmatrix} \begin{bmatrix} \Delta\rho_1 \\ \vdots \\ \Delta\rho_m \end{bmatrix} \tag{2.22}$$

where S_V and S_θ follow from (2.4) and (2.5) respectively, and subscript $[i, \rho]$ refers to the i-th row and the subset of columns that correspond to ρ. Combining (2.21) and (2.22) allows the change in line current ΔI_{ik} to be related directly to changes in wind generation $\Delta\rho$ through,

$$\Delta I_{ik} = S_{I\rho}\Delta\rho. \tag{2.23}$$

If the line current limit of I_{ik}^{lim} and operating point value I_{ik}^0 are sufficiently close, the linearization (2.23) can be used to establish a first-order approximation to the minimum change in wind power that would force the line to its limit. The resulting formulation is,

$$\Delta\bar{\rho}_{ik} = \underset{\Delta\rho}{\operatorname{argmin}} \ \frac{1}{2}\Delta\rho^\top W \Delta\rho \tag{2.24}$$

subject to

$$I_{ik}^{lim} - I_{ik}^0 = \Delta I_{ik} = S_{I\rho}\Delta\rho. \tag{2.25}$$

The Lagrangian for this problem can be written as,

$$\mathcal{L}(\Delta\rho, \lambda) = \frac{1}{2}\Delta\rho^\top W \Delta\rho + \lambda\big(S_{I\rho}\Delta\rho - \Delta I_{ik}\big) \tag{2.26}$$

with the Karush-Kuhn-Tucker conditions yielding,

$$\frac{\partial\mathcal{L}}{\partial\Delta\rho} = \Delta\rho^\top W + \lambda S_{I\rho} = 0 \tag{2.27}$$

$$\frac{\partial\mathcal{L}}{\partial\lambda} = S_{I\rho}\Delta\rho - \Delta I_{ik} \ = 0 \tag{2.28}$$

or more compactly,

$$\begin{bmatrix} W & S_{I\rho}^\top \\ S_{I\rho} & 0 \end{bmatrix} \begin{bmatrix} \Delta\rho \\ \lambda \end{bmatrix} = \begin{bmatrix} 0 \\ \Delta I_{ik} \end{bmatrix}. \tag{2.29}$$

Solving (2.29) is straightforward, and yields an estimate $\Delta\bar{\rho}_{ik}$ of the change in wind power output that is most likely to drive line i-k to its limit. That estimate can be used in an iterative scheme:

A. Update wind-power production $\rho + \Delta\bar{\rho}_{ik}$,

B. Solve the AC power flow for the new operating point,

C. Calculate new sensitivities, and

D. Repeat the optimization.

This method converges reliably within 1-2 iterations and the iterative solution process is then repeated for each line in a specified set of candidate lines. The line that is most restrictive, in the W-norm sense of (2.18), establishes the most vulnerable loading direction for the wind farms.

Table 2.5 lists the lines identified as the most vulnerable for the same set of operating points as in Table 2.4. Again, the influence of correlation between wind farms has been considered.

There is generally strong qualitative agreement between the DC and AC optimization results presented in Tables 2.4 and 2.5 respectively. This is particularly so for the operating points that are more heavily loaded. In cases where the two methods identified different lines, the DC results were investigated further. It was found that the difference in cost (2.18) between the two most vulnerable lines was small. In such cases, typically the second ranked line matched the line selected by the AC optimization.

No.	Operating point			Congested line / $\Delta\rho$	
	WG_1	WG_2	WG_3	No Correlation	Correlation
1	30	30	30	4 / [1,1,1]	4 / [1,1,1]
2	30	30	10	4 / [9,6,6]	4 / [8,7,7]
3	30	10	30	5 / [2,2,8]	5 / [5,5,6]
4	10	30	30	5 / [3,2,9]	5 / [5,5,7]
5	30	10	10	1 / [14,-5,-6]	4 / [14,13,13]
6	10	30	10	2 / [-8,3,-8]	3 / [12,15,12]
7	10	10	30	5 / [4,3,13]	5 / [8,8,11]
8	10	10	10	5 / [10,7,31]	4 / [22,21,20]

Table 2.5: Most vulnerable lines at each operating points, AC optimization.

Computationally, the efficiency of the DC optimization provides a significant advantage when analyzing systems with large numbers of wind and solar injection nodes and numerous lines that are susceptible to overloading.

2.5 Computing the Power Flow Feasibility Boundary of Large Networks

Although many criteria and proximity indices for steady-state voltage instability have been proposed over the past few decades, all are related to the maximum power transfer capability which is rooted in the feasibility boundary of the power flow algebraic equations. Equating power flow feasibility and the steady-state voltage stability boundaries has its origin in the influential works of Zhdanov, Venikov and their colleagues in the former USSR [42].

Power system dynamics can be modeled mathematically by a system of autonomous nonlinear differential-algebraic equations (DAEs):

$$\dot{x} = f(x, y, z, \lambda) \tag{2.30a}$$

$$0 = g(x, y, z, \lambda) \tag{2.30b}$$

$$0 = h(z, \lambda) \tag{2.30c}$$

where x and y are the dynamical and algebraic states associated with electromechanical devices in the network such as synchronous and doubly-fed induction generators and their (AVR, rotor speed, pitch-angle) controllers, z the set of power flow variables and λ the set of parameters. As demonstrated by Sauer and Pai [43], the standard set of power flow

equations or its variants represented in (2.30c), can always be solved for the multi-valued z_0 independent of initial conditions of dynamical states and other algebraic variables. Once a particular z_0 is obtained, (2.30a)-(2.30b) can be solved for the corresponding equilibrium point $E_0 = (x_0, y_0, z_0)$. It has been shown that under certain assumptions on the power flow and dynamical models, the differential-algebraic system of (2.30) can experience bifurcation if and only if h_z is singular [42, 43]. Note that the singularity of the power flow Jacobian h_z implies that the obtained solution of z_0 is on the solution space boundary. From a geometric point of view this is a branch point in the parameter space of (2.30c) where at least two algebraic sheets coalesce. As the power flow parameters are perturbed there is a structural change in the set of equilibria containing E_0 where at least two equilibria coalesce into a single equilibrium and disappear. In other words, at a bifurcation (branch) point "two solutions are born or two solutions annihilate each other" [34]. More precisely at the saddle-node bifurcation point the following conditions hold between $z_0 \in \mathbb{R}^n$ and a given bifurcation parameter value $\alpha_0 \in \mathbb{R}$ where $\alpha \subset \lambda$ [34]:

(1) $h(z_0, \alpha_0) = 0$

(2) $rank\ h_z(z_0, \alpha_0) = n - 1$

(3) $h_\alpha(z_0, \alpha_0) \notin range\ h_z(z_0, \alpha_0)$, that is, $rank\ (h_\alpha(z_0, \alpha_0) | h_z(z_0, \alpha_0)) = n$

(4) there exists a parametrization $z(\sigma)$, $\alpha(\sigma)$ with $z(\sigma_0) = z_0$, $\alpha(\sigma_0) = \alpha_0$ where $\mathrm{d}^2\alpha(\sigma_0)/\mathrm{d}\sigma^2 \neq 0$

2.5.1 The Concept of Structural Stability and its relation to Power Flow Feasibility Boundary

The dynamical system of (2.30) is called structurally stable if for a given value of the parameter set $\lambda = \overline{\lambda}$, there exists an $\epsilon > 0$ such that (2.30) is topologically equivalent to the dynamical system of (2.31) for all values of λ satisfying $||\lambda - \overline{\lambda}|| < \epsilon$ and there is no qualitative change in the set of solutions to the algebraic manifold defined by (2.30b) and (2.30c) .

$$\dot{x} = f(x, y, z, \overline{\lambda}) \tag{2.31a}$$

$$0 = g(x, y, z, \overline{\lambda}) \tag{2.31b}$$

$$0 = h(z, \overline{\lambda}) \tag{2.31c}$$

Two systems are topologically equivalent if there exists a homeomorphism of the phase space of the first system onto the phase space of the second, which converts the phase flow of the first system into the phase flow of the second [45]. Hence a dynamical system is structurally stable if it can preserve its topology following small perturbations of the system and structurally unstable if there is a qualitative change in the flows of the system. It should be noted that for DAE systems solution trajectory lies on an algebraic manifold [46] and the branch points of this algebraic manifold are where two or more (solution) branches coalesce and disappear. At these branch points as the parameter set λ is perturbed the sensitivities of the algebraic states and as a result the trajectories of the dynamical states may reverse and the topological equivalence of the perturbed system flows does not hold. In the case of power systems, the power flow Jacobian h_z is singular at the branch points corresponding to the algebraic system of (2.30c) which characterizes the saddle-node bifurcation. Reference [47] presents a more detailed discussion of the dynamical model and response of a similar generator-load system.

The concept of structural stability was introduced by Andronov and Pontryagin [48]. Reference [49] discusses, at great detail, the concept of structural stability in the context of dynamical systems characterized by ordinary differential equations. There it is shown that for such systems modeled as $\dot{x} = f(x, \lambda)$ the structural stability is lost whenever $\det f_x = 0$ and the set of solutions merge and annihilate each other. This corresponds to the singularity of h_z for the differential algebraic system of (2.30). Hence on the power flow feasibility boundary where $\det h_z = 0$ (assuming that the other two conditions of saddle-node bifurcation hold) the system loses structural stability. This correspondence between the feasibility boundary of power flow algebraic equations and the structural stability is central to the discussion presented in Chapter 4 where the impact of embedded generation connected to resistive feeders on the structural stability of the power system is studied.

2.5.2 An Algorithm for Computing the Saddle-Node and Limit-Induced Bifurcation Boundary

The feasibility boundary, also referred to as the critical boundary [34] is generally characterized by the singularity of the power flow Jacobian. A typical predictor-corrector method as the one proposed in [37] would start from any given point on the boundary enforcing the power flow and Jacobian singularity conditions to find the successive points of the boundary curve. The computation of the singular segments of the boundary as proposed in [37] requires augmenting the Jacobian matrix to include elements of the Hessian. Unfortunately, it is extremely difficult and inefficient to compute and work with the Hessian matrix of large

networks. What further complicates the computation of the Hessian matrix is the existence of multiple types of FACTS devices each appearing with their own unique variables in power flow equations. Apart for computational challenges, the boundary curves *may* have segments that are characterized by reactive devices reaching their limits where the Jacobian is no longer singular.

In this section a method is proposed that has the following advantages compared to the Hessian-based methods,

- eliminates the need to construct the "cumbersome" Hessian matrix
- significantly boosts the computational speed as it works with the Jacobian matrix
- calculates the non-singular segments of the boundary characterized by reactive limits

These advantages make the method scalable to realistic large networks. The power flow feasibility boundary and its geometry have been explored previously [37, 50, 51]. Reference [37] introduces a method to obtain the saddle-node bifurcation boundary based on continuation method that involves the power flow Hessian. Reference [50] shows that the boundary is generally non-convex. Reference [51] presents an exhaustive discussion of the feasibility boundary and its relation to saddle-node bifurcation and much rarer Hopf and singularity-induced bifurcations. However, there are very few works that have examined the reactive limit-induced instability [52, 53]. Reference [52] examines the dynamic of voltage collapse when the reactive limit of a generator under study is encountered. Reference [53] examines the relationship between non-smoothness of the boundary and reactive limits. What is missing from the literature is a methodology for efficiently obtaining both the singular and limit-induced segments of the feasibility boundary for large networks.

2.5.2.1 Singular Segment

Suppose $\lambda_p \subset \lambda$ is a subset of parameters that are set free to vary and z is the set of variables. The power flow and the singularity equations can be expressed as:

$$h(z, \lambda_p) = 0 \tag{2.32}$$

$$\det h_z(z, \lambda_p) = 0 \tag{2.33}$$

Here $z \in \mathbb{R}^n$, $\lambda_p \in \mathbb{R}^p$ and $h : \mathbb{R}^{n+p} \to \mathbb{R}^n$. Assuming that $p = 2$, there are $n + 1$ equations and $n + 2$ unknowns and the solution is a 1-manifold in the parameter space of λ_p.

To obtain this manifold, the first step is to find an initial point. This is easily done by the continuation method to reach a turning point where $\det(h_z)$ changes sign. It can then back-step to the point immediately before the singularity and approach the singular manifold with arbitrarily small step sizes. Clearly the smaller the step size is the higher the precision with which the singular manifold can be approached. The is essentially a bisection method that repeatedly bisects an interval between two adjacent points that contains the turning point. Once the initial point is obtained homotopy methods can be used to solve (2.32)-(2.33) for the successive points on the singularity manifold. This, however, involves computing the Hessian matrix of $h(z, \lambda_p)$.

Alternatively the vector that is normal to the singular manifold in the λ_p parameter space can be exploited to estimate the successive points with much less computational effort. The following relation can be deduced from (2.32).

$$\frac{\partial h}{\partial \lambda_p}\Delta\lambda_p + \frac{\partial h}{\partial z}\Delta z = 0 \tag{2.34}$$

Finding the normal vector requires a knowledge of the left eigenvector that corresponds to the zero-approaching eigenvalue of the Jacobian.

Multiplying (2.34) by ${w^\star}^\top$, the left eigenvector corresponding to the smallest eigenvalue which is effectively zero gives the following relation: (Note ${w^\star}^\top \frac{\partial h}{\partial z} \approx 0$)

$${w^\star}^\top \frac{\partial h}{\partial \lambda_p}\Delta\lambda_p \approx 0 \tag{2.35}$$

Therefore the normal vector, at the initial point on the manifold, is ${w^\star}^\top \dfrac{\partial h}{\partial \lambda_p}$ which can be used to find the vector that is tangent to the manifold at that point. Moving along the tangent from the initial point, with arbitrarily chosen step sizes (as shown in Figure 2.5 for two different step sizes in red and green), gives an initial prediction of (z, λ_p) for the second point on the manifold. The initial prediction of free parameters, λ_p^0 is directly given by the tangent vector and z_0, the initial prediction for the states, is given as,

$$z_0 = z_f + (\frac{\partial h}{\partial z})^{-1} h(z_f, \lambda_p^0) \tag{2.36}$$

where z_f is the set of states at the first point on the boundary, $(\frac{\partial h}{\partial z})^{-1}$ is the inverse of Jacobian at the first point and $h(z_f, \lambda_p^0)$ is the mismatch in power flow equations caused by λ_p^0. It should be noted that in the realm of computation, Jacobian can never be truly

singular. It can only approach singularity as the boundary is approached but can never reach singularity. Thus in the realm of numerical analysis there does not exists a single point in the parameter space of λ_p where the Jacobian is singular. A close-to-singularity Jacobian matrix can still be exploited within the default arithmetic precision of numerical computing environments [54] which is more than sufficient for the type of computation discussed in this section.

The initial prediction, λ_p^0, as can be seen in Figure 2.5, is infeasible if the manifold is convex. However by formulating the problem as a nonlinear least squares state estimation (see (2.40)-(2.41)), the point on the boundary that is closest (in a 2-norm sense) to the predicted value λ_p^0 can be obtained through a number of iterations. Figure 2.5 shows the procedure of finding the second point. The sequence $\lambda_p^1, \lambda_p^2, \lambda_p^3, ...$ approaches to the second point on the boundary. Given that the initially predicted values of (z, λ_p) are typically very close to the actual values, the second point can be obtained by monitoring the smallest eigenvalue of the Jacobian and with only a few iterations. Figure 2.5 also highlights the robustness of the method in obtaining the second point on the high curvature region of the boundary with an exaggerated choice of tangent vector length (green arrow).

Once the second point is obtained, secant method can be used in the following way to find the successive points,

$$z_0 = z_i + \tau \frac{(z_i - z_{i-1})}{\| z_i - z_{i-1} \|} \tag{2.37}$$

where z_i and z_{i-1} are the states corresponding to consecutive points on the boundary and τ is the step size.

Most parameters of interest, such as active or reactive power injections and loads can be explicitly expressed as functions of the state variables,

$$\hat{h}(z, \lambda_p) = \lambda_p - \hat{k}(z) = 0 \tag{2.38}$$

.

where $\hat{h}(z, \lambda_p) : \mathbb{R}^{n+p} \rightarrow \mathbb{R}^p$ is a subset of $h(z, \lambda_p)$ and $\hat{k}(z) : \mathbb{R}^n \rightarrow \mathbb{R}^p$ corresponds to the p free parameters. Hence λ_p can be predicted as $\hat{k}(z_0)$ where z_0 is given by the secant method in (2.37). Fixing λ_p at its predicted value and solving for (2.32) gives an estimate z_1 where (z_1, λ_p) is usually a solution for (2.32)-(2.33) eventhough the secant method does not actively enforce (2.33). Note that (2.33) is effectively enforced by checking the smallest eigenvalue which is obtained cheaply without computing the whole eigen-structure. The

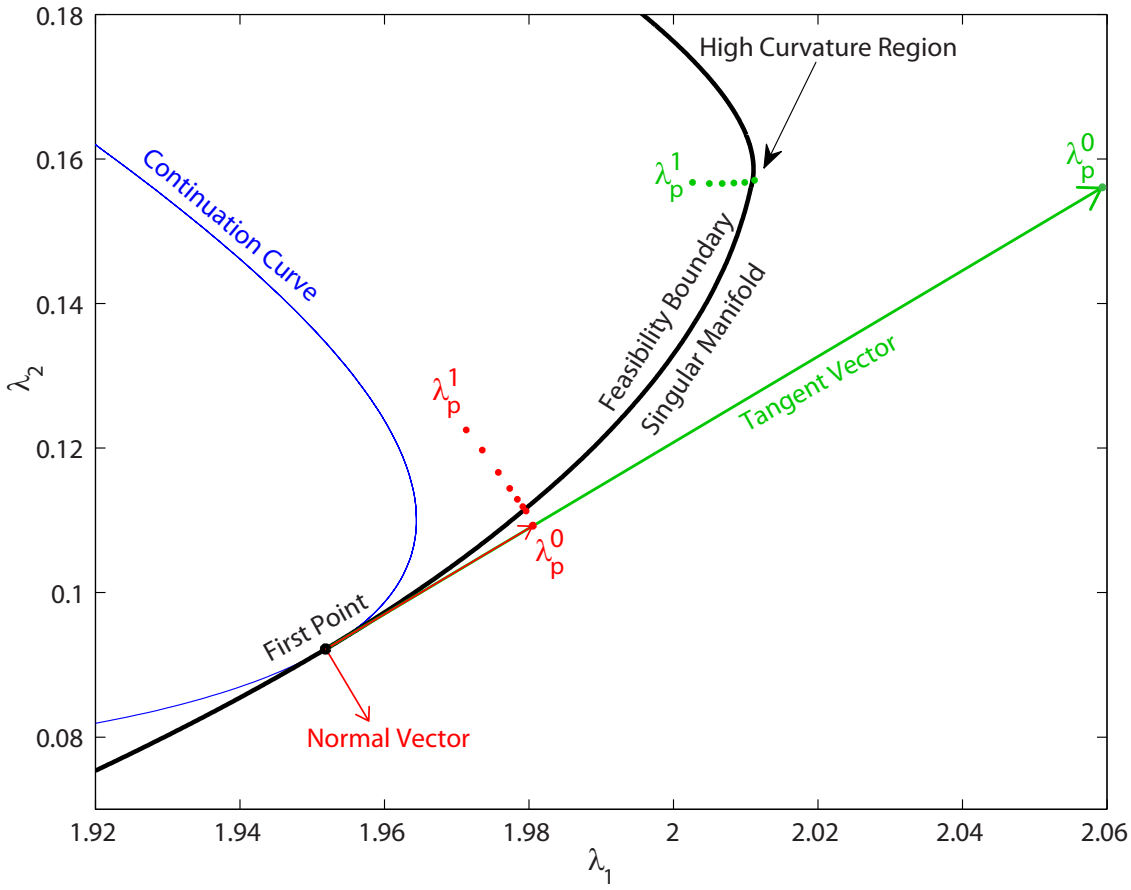

Figure 2.5: The typical process of obtaining successive points on the singular manifold of the feasibility boundary based on nonlinear least-squares estimation method

secant method, if the step size is small, results in the smallest eigenvalue being less than the specified tolerance. The condition (2.33) can be enforced more strictly by reducing this tolerance. However in all cases examined so far (including large networks such as the DTE/ITC system) smaller tolerances would only slow the process without any tangible improvement in the accuracy. If the solution to (2.32) does not meet the tolerance criteria, continuation method, based on the homotopy concept discussed in the previous section can be applied to move λ_p along the normal vector to further approach the singular manifold. The continuation starts from (z, λ_p) which satisfies (2.32) and frees parameter β where $\lambda_p^1 = \lambda_p^0 + \beta N$. Here N is the normal vector calculated based on the previous point on the singular manifold. In this way at each point along the continuation, the change in λ_p is along the normal vector. If based on the secant approximation the Newton's method does not converge to a solution which typically signifies non-existence of solution, nonlinear least squares estimation is used to find the nearest point on the boundary. However for an small step size in the range of $0.01 - 0.001$ this rarely happens. The smaller the step size

is, the less likely is the need for computationally more expensive nonlinear least squares method. However an step size that is too small can also slow the process. Hence a step size that has the optimal computational performance varies for each network and can be obtained empirically. With the appropriate choice of the step size τ, successive points are typically obtained within 1-2 iterations.The process for obtaining the singular segment of the boundary is depicted in Figure 2.6.

It should be noted that for types of parameters that cannot be stated explicitly in terms of power flow variables (i.e. voltage magnitudes and angles) such as line impedances or setpoints quantities, a secant method similar to (2.37) can be used to obtain λ_p. However, this prediction, most likely lies outside the feasible region which requires a more frequent application of nonlinear least squares estimation techniques. This makes the process of convergence to the successive points computationally less efficient.

Assume that $\lambda \in \mathbb{R}^n$ is the set of power flow parameters that can be expressed explicitly in terms of the states (i.e. active power injection at PQ and PV buses and reactive power injection at PQ buses) and contains the set of free parameters λ_p,

$$h(z, \lambda_p) = \lambda - k(z) = 0 \tag{2.39}$$

Then the nonlinear least squares state estimation problem to find (z, λ_p) from an initial estimate (z_0, λ_p^0) can be formulated as,

$$\text{minimize} \qquad ||e||^2 = e^\top e = \sum_{i=1}^{p} \gamma_i [\lambda_i^0 - k_i(z)]^2 + \sum_{i=p+1}^{n} \gamma_i [\lambda_i - k_i(z)]^2 \tag{2.40}$$

where $\gamma_i > 0$ is the penalizing factor corresponding to the ith element in λ which also contains the free parameters λ_p as its first p parameters. Here the penalizing factors corresponding to the fixed parameters of λ are chosen to be much larger than the penalizing factors corresponding to λ_p^0, the initial estimate of the free parameters. This difference in penalizing factors substantially reduces the mismatch in power flow equations (2.39) that correspond to fixed parameters while minimizing dist$(\lambda_p^0, \lambda_p(z))$, expressed as the sum of squares of the first p elements of $h(z, \lambda_p)$, i.e. the elements of the vector $\lambda_p^0 - \lambda_p(z)$.

This is essentially a cost minimization problem that can be solved by a standard Guass-Newton algorithm. Starting from an initial estimate for the minimum z_0, the Gauss-Newton iteration then can be expressed as,

$$z_{j+1} = z_j + (h_z^\top h_z)^{-1} h_z^\top X[\lambda - k(z)] \tag{2.41}$$

where X is the diagonal matrix of penalizing factors.

Notice that the diagonal elements in X corresponding to the power flow free parameters λ_p^0 are the key parameters for adjusting the rate of convergence to the boundary. γ_i corresponding to λ_p are chosen to be much smaller than γ_i corresponding to the fixed parameters of λ. As the Gauss-Newton method iterates and the estimated states move toward the boundary the smallest eigenvalue of the power flow Jacobian is checked and once it reaches below a certain tolerance the solution is declared to be on the boundary. It should be noted that checking the smallest eigenvalue is computationally much cheaper than obtaining the whole eigenstructure of the Jacobian. The rate of convergence is not quadratic and thus slower compared to Newton's method. This rate is clearly depicted in Figure 2.5 for exaggerated step sizes (in red and green) for the tangent vector. However in practice, usually it takes 1-3 iterations to reach the boundary (i.e. the smallest eigenvalue drops below the tolerance.) It is also argued in the literature that Gauss-Newton method may have a reduced region of convergence compared to Newton's method [40, 55, 56]. In the application of the method to cases studies so far, divergence has not been observed. Even in such cases the convergence of Gauss-Newton can be improved by different modifications such as the Levenberg-Marquardt algorithm, also known as the trust region method [55, 56].

2.5.2.2 Non-Singular Segment

The singular manifold may encounter limits of regulating devices at which point, the singularity condition (2.33) generally does not hold. The feasibility boundary, then is defined by the 1-manifold of the regulating device limit in the λ_p-parameter space, beyond which (2.32) has no solution that satisfies the limit. (2.32)-(2.33) is replaced by

$$h(z, \lambda_p) = 0 \tag{2.42}$$

$$q_j(z, \lambda_p) = L_j \tag{2.43}$$

where the function q_j, associated with a certain network controller, e.g. reactive power injection, is held fixed at its limit L_j. In the case of a tap position, a power flow variable itself, (2.43) is replaced by $z_j = L_j$. Here again, assuming $p = 2$, there are $n+1$ equations and $n + 2$ unknowns and the solution is a 1-manifold in the parameter and state space, i.e. in $\mathbb{R}^{n+2}$. This 1-manifold can be computed efficiently by the continuation method and mapped onto the parameter space.

It should be noted that the stability boundary would not remain on this manifold indefinitely. Either the singularity condition is encountered again which means that the singular

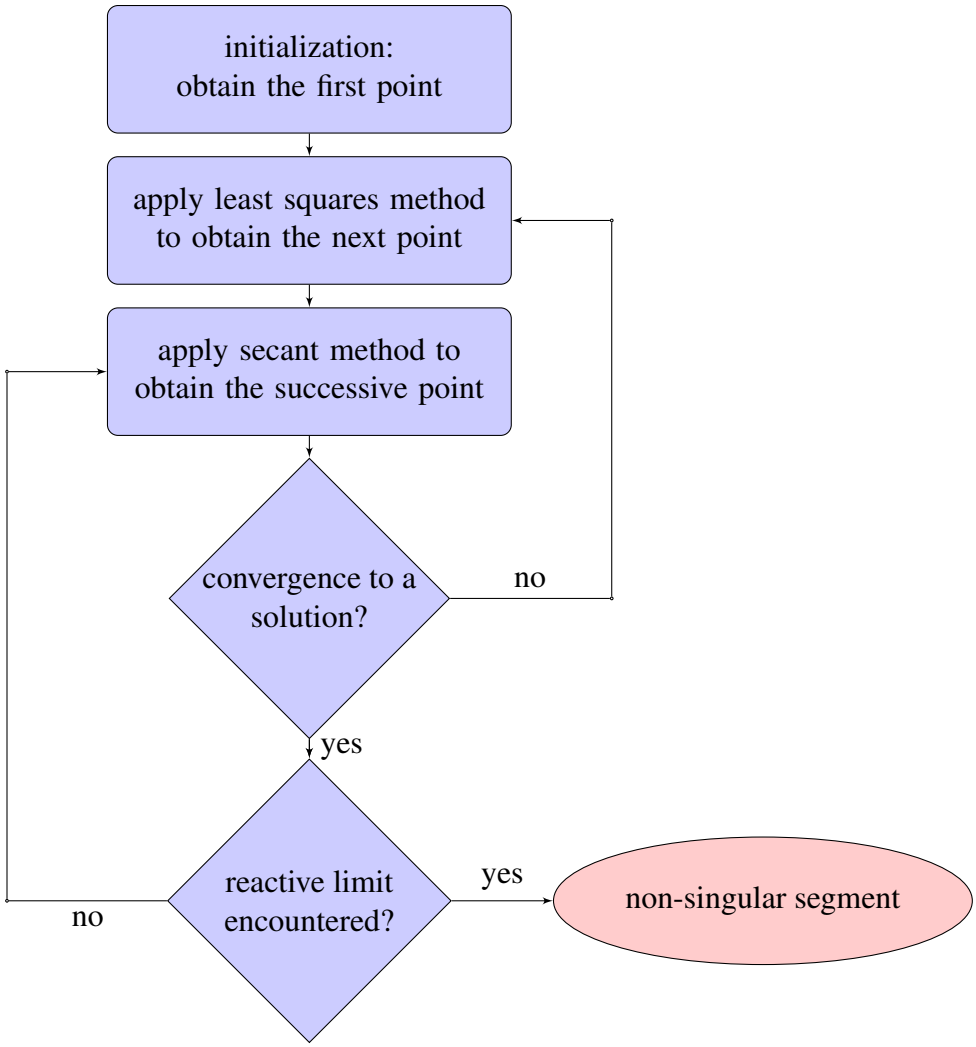

Figure 2.6: Flow chart showing the process of obtaining the singular branch of the feasibility boundary

manifold splits from the non-singular (limit-induced) manifold or another limit is encountered. In the first case, all that is needed is to repeat the procedures outlined in the previous subsection. The second case is less straightforward as there are the following three possibilities,

- The feasibility boundary continues on the newly encountered limit while the previous limit is enforced concurrently
- The feasibility boundary continues on the newly encountered limit while the previous limit is freed
- The feasibility boundary continues on the existing limit while the newly encountered limit changes status (either freed or enforced)

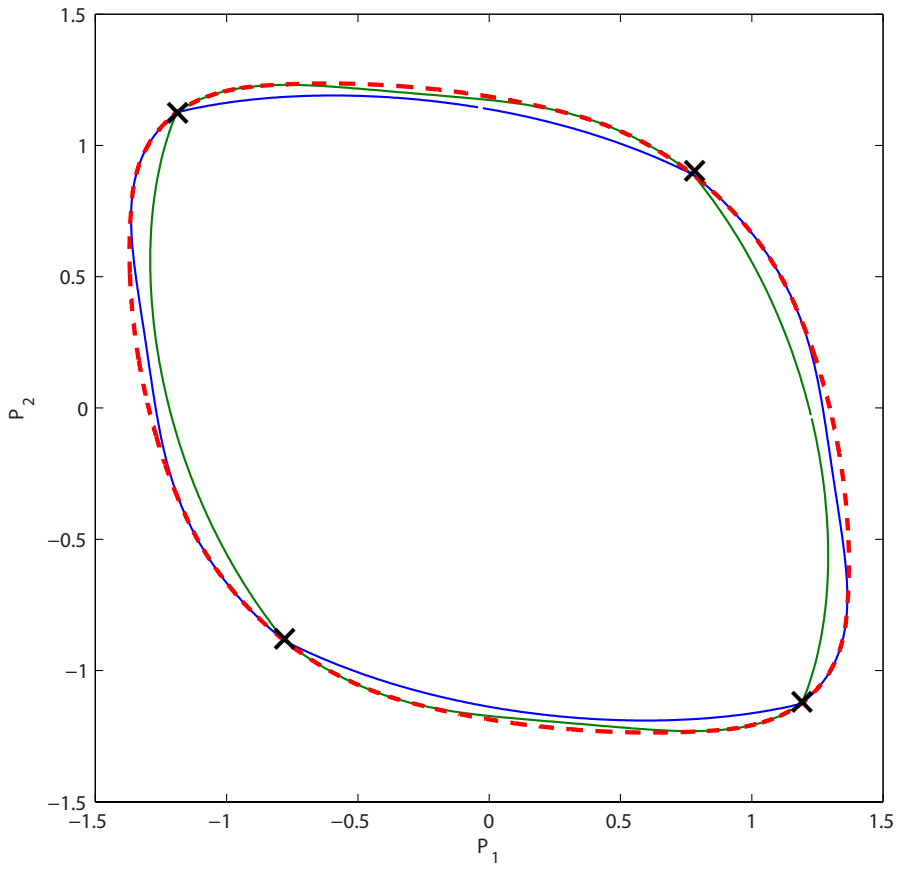

Figure 2.7: Non-singular and singular segments of the feasibility boundary for the three-bus system of Figure 2.10: The feasibility boundary continues on the newly encountered limit while the previous limit is enforced.

The method checks all these scenarios to find the one that correctly characterizes the subsequent segment of the feasibility boundary. The three possible scenarios are highlighted by the $\times$ symbol in Figures 2.7 through 2.9 corresponding to the three-bus system of Figure 2.10 with different reactive limits. The reactive limit contour corresponding to generators 1 and 2 for each case are shown in blue and green respectively. The feasibility boundary is shown as dashed red lines. Note that the non-singular segments of the boundary are distinguished from the singular segments by the overlap of the reactive limit contours (in blue or green) and the dashed red lines.

In Chapter 3 this method will be applied to the DTE/ITC system to compute the singular and non-singular segments of the boundary (associated with OLTC limits, synchronous generator reactive limits and the limits of the STATCOM devices at wind farms).

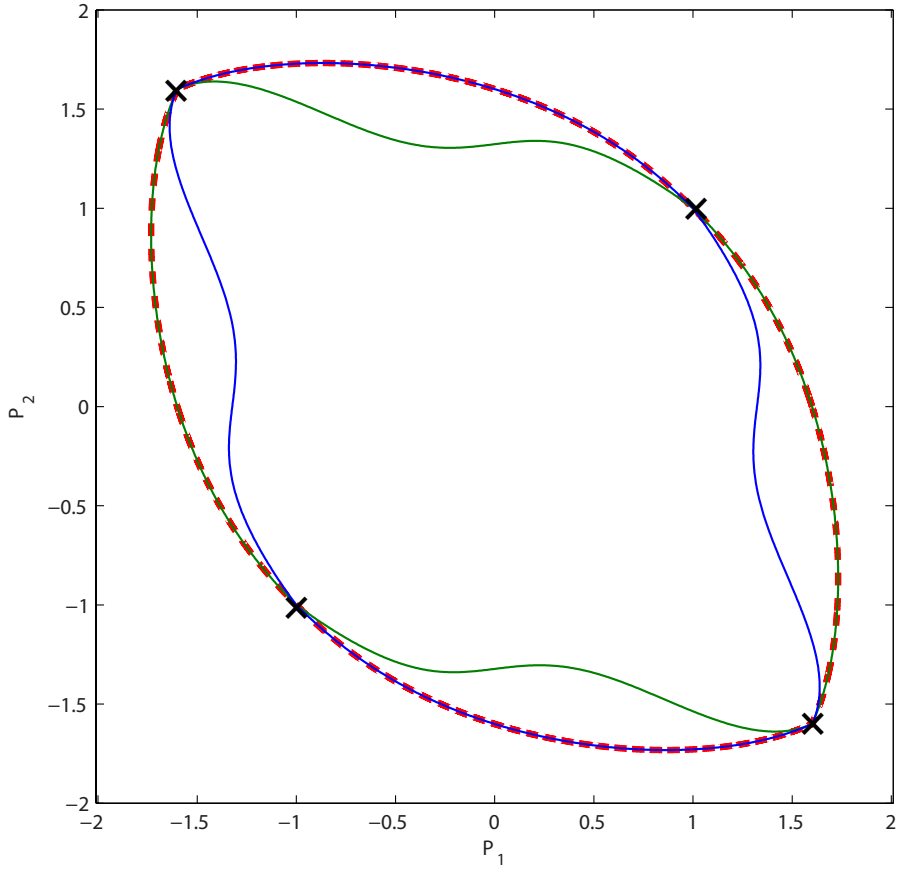

Figure 2.8: Non-singular and singular segments of the feasibility boundary for the three-bus system of Figure 2.10: The feasibility boundary continues on the newly encountered limit while the previous limit is freed.

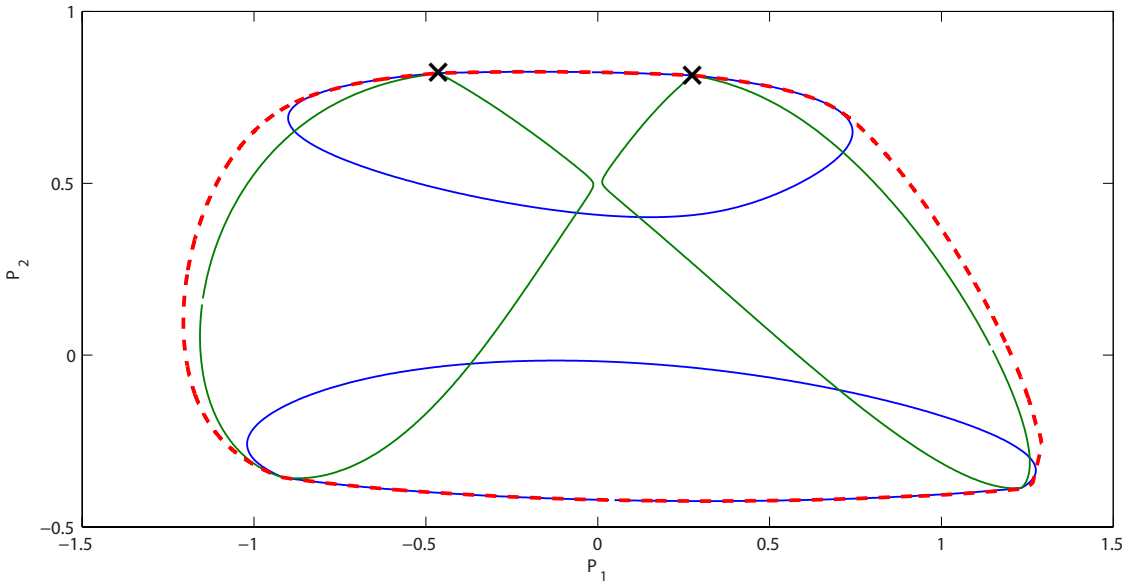

Figure 2.9: Non-singular and singular segments of the feasibility boundary for the three-bus system of Figure 2.10: The feasibility boundary continues on the existing limit while the newly encountered limit changes status (either freed or enforced).

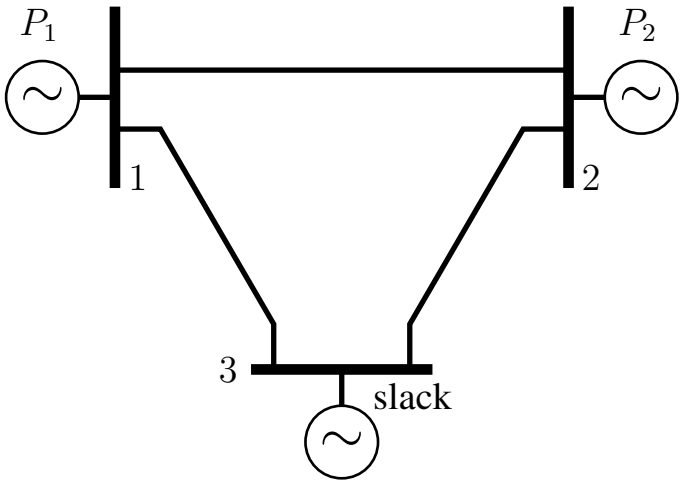

Figure 2.10: Three-Bus System

CHAPTER 3

Impact of Wind Generation on the DTE/ITC System Serving Eastern Michigan

3.1 Introduction

Due to lower connection costs, it is generally more economical to connect utility-scale variable generation, in particular wind farms, at sub-transmission levels (40-120 kV). In fact, in many cases it is unavoidable as only a lower voltage network is available. However, relative weakness of the sub-transmission network, characterized by low short-circuit ratios and high impedances [59], poses serious challenges for the large-scale integration of variable generation. In the case of wind power, its inherent variability can lead to unusual reactive power absorption and injection patterns. Since reactive power is closely coupled with voltage magnitudes and voltage regulating assets, wind power variations at multiple nodes may affect bus voltages and transformer tap positions in complicated and unexpected ways.

Many utilities require wind-farm operators to regulate the voltage at the point of interconnection (POI) to a setpoint value determined by the system operator. Nevertheless, varying power flow can cause voltage fluctuation at unregulated load buses that are sometimes located far from the POI. As voltage fluctuations can be problematic for consumers, utilities are required to install additional voltage regulating equipment. Varying power flow can also result in a higher frequency of on-load tap-changing (OLTC) operation of transformers that connect weak sub-transmission networks to the transmission system. As will be explored later in Chapter 5 this increase may significantly shorten the lifetime of these expensive devices.

The strict voltage regulation at POI and its corresponding reactive requirement which has to be provided by transmission system may also have a detrimental impact on the voltage security of the system. This becomes especially critical where wind generation

is connected at both sub-transmission and transmission levels. The circulation of reactive power through resistive feeders tends to increase network active power losses.

Therefore it is important to examine interactions between wind-farm voltage regulation and other, pre-existing voltage regulating equipment, such as tap-changing transformers, and coordinate their goals to achieve optimal and secure operation of the grid. Previous studies have shown for radial distribution feeders that voltage regulation at the POI tends to increase tap-changing operations [15]. However, many sub-transmission and distribution networks have a mesh structure. The presence of multiple wind injection nodes in a mesh network further complicates the impact of wind on voltages and taps. Existing techniques for analyzing power system response provide limited insights into the complex interactions between regulating devices and variable generation.

This chapter examines the impact of wind generation on the DTE/ITC system, which serves the eastern region of Michigan where wind farms are connected at both the sub-transmission and transmission levels. A section of the system with significant wind generation is depicted in Figure 3.1 where active power is delivered from central power plants to the 42 kV sub-transmission system (in black) through a 120 kV transmission loop that is highlighted in red. At the interconnection points, the lower voltage (42 kV side) is regulated by five tap changing transformers highlighted by red ellipses. Three sub-transmission wind generation nodes (WG_1, WG_2 and WG_3) are highlighted in blue each with a rated capacity of 50 MW. The three transmission wind injection nodes (WG_4, WG_5 and WG_6) each with a rated capacity of 100 MW and reactive compensation capability of ± 50 MVAr are highlighted in red. DTE the owner of sub-transmission and distribution networks requires wind farm operators to regulate the voltage at the point of interconnection to a given setpoint value, and this makes reactive power compensation[1] at the wind injection nodes indispensable.

Here the focus is primarily on the effect of reactive capability of the 42 kV wind injection nodes on the sub-transmission voltage profile, OLTC tap-changing operations, active power losses and the voltage stability margin. In section 3.2 sensitivity analysis, based on the power flow Jacobian, is applied to identify transformers that are most sensitive to wind generation variability at both sub-transmission and transmission levels. Later power flow continuation methods are also used to produce contour diagrams that allow more extensive investigations of the variables that are most sensitive to wind injections under different reactive capabilities at these nodes. Finally OLTC operations and network losses are obtained based on simulation of the DTE/ITC system for a month of wind generation and load data. In section 3.3, the impact of reactive compensation of sub-transmission wind generation on

[1] STATCOMs are often used to provide dynamic reactive support.

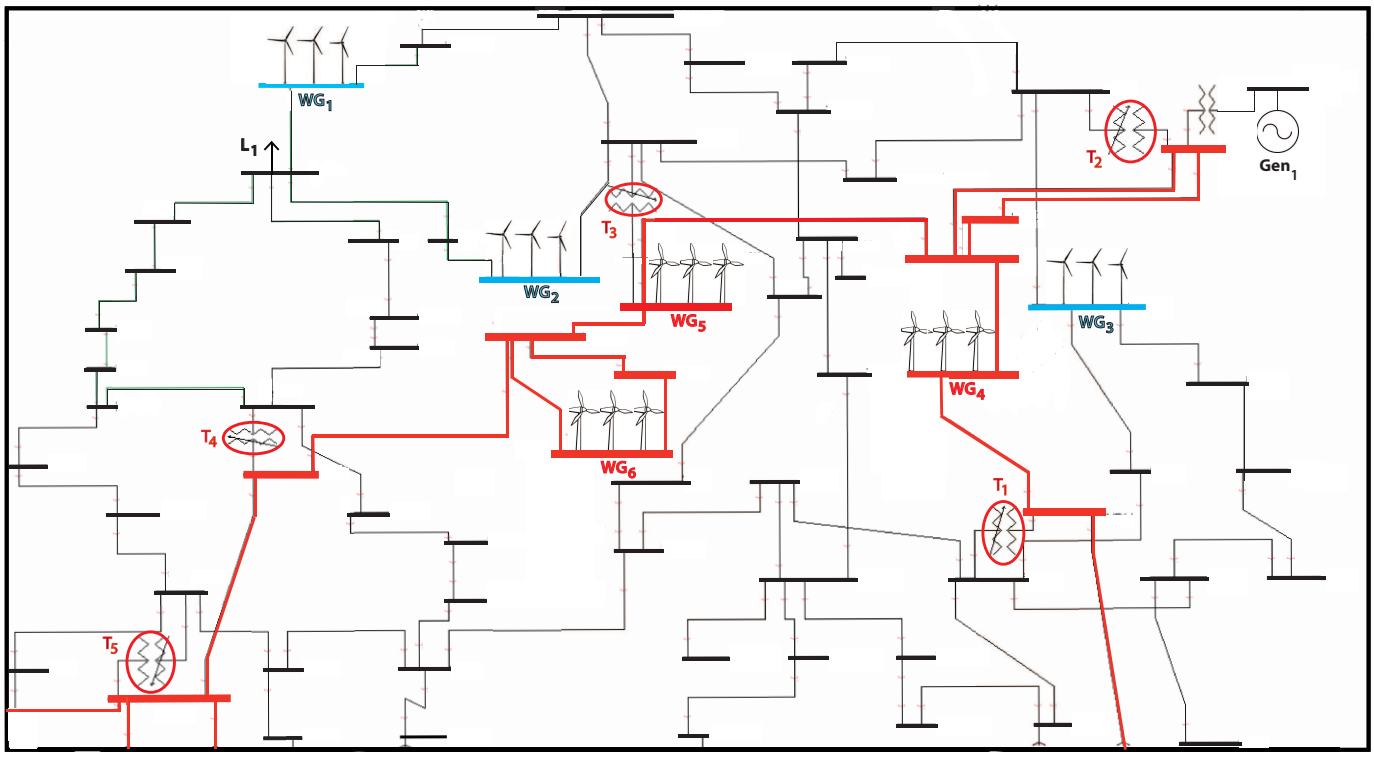

Figure 3.1: DTE/ITC wind development network

the voltage stability margin is examined.

3.2 Wind Generation Variability and the Impact on OLTC Operation

In order to gain insight on the impact of local reactive compensation on transformer tap operation and voltage magnitudes of adjacent nodes, this section contrasts the following two cases:

A. No reactive compensation capability at wind injection nodes.

B. Reactive compensation capability of ± 15 MVAr at each wind injection node.

As the size of wind farms are increasing, the case of no compensation is no longer permitted by the system operator. The reason is that voltage fluctuations caused by wind variability place enormous stress on voltage regulating equipment in distribution substations. Figure 3.2(a) shows the voltage contour diagram of load bus L_1 in the vicinity of the wind injection nodes. The region of interest, corresponding to the feasible range of wind

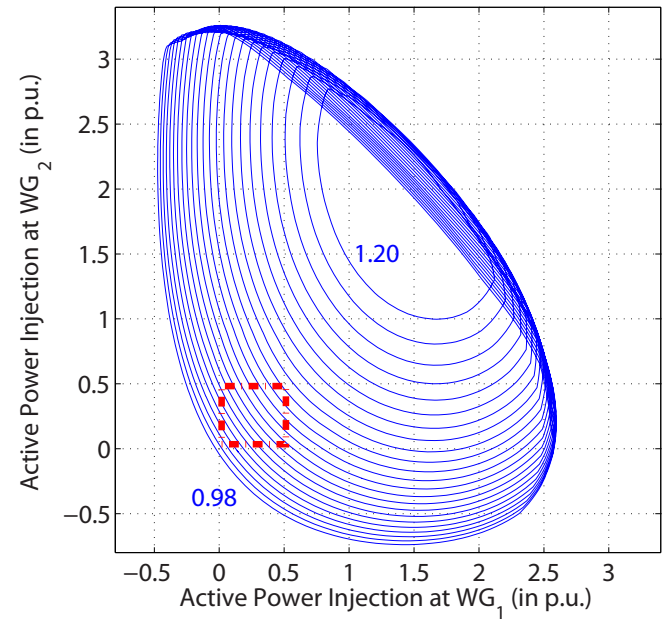

(a) No voltage regulation at the wind injection nodes: Global view

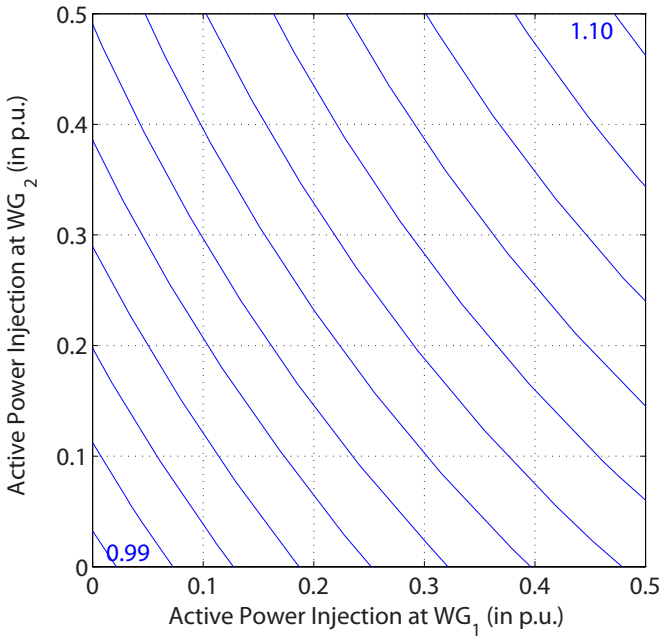

(b) No voltage regulation at the wind injection nodes: Region of interest

Figure 3.2: Contour diagrams of voltage magnitude at load bus L_1 for varying active power injections at wind nodes (no voltage regulation).

injection at each node, is highlighted in the red box, and an enlarged version is shown in Figure 3.2(b). As wind injection at the nodes simultaneously varies from 0 to 50 MW, voltage increases from 0.99 p.u. to 1.10 p.u. This voltage rise phenomenon, caused by wind-power injection on weak networks [4], has lead to stricter grid standards requiring large distributed-generation installations to operate in voltage control mode [2, 17]. Figure 3.3 shows voltage contours of the same bus for the case of ± 15 MVAr compensation and, as shown in Figure 3.3(b), the voltage fluctuation range is now reduced to 0.99-1.05 p.u. However as explained later even though the no-compensation case may appear extreme and unpractical, it is useful in the way it highlights the need for coordination between reactive compensation at wind injection nodes and transformer tap operation.

The transformer tap sensitivity values for the two cases mentioned above are presented in Tables 3.1 and 3.2 respectively. Here the three operating points of no wind, 40% and 80% wind output are considered, and it is assumed that wind outputs are 100% correlated. The latter two operating points correspond to medium and high wind generation respectively. It can be noticed that tap positions are in general more sensitive to wind injection in the case of ± 15 MVAr reactive compensation and that T_3 has the highest sensitivity values followed by T_4 and T_5. Furthermore, in the case of ± 15 MVAr reactive compensation, tap sensitivity is high at no wind, peaks at medium wind and drops to its lowest at high wind. This pattern is most visible for T_3 and T_4. In contrast, the no-compensation sensitivity values are highest at no wind and are almost zero at medium and high wind.

These values indicate which transformers and buses are most sensitive and at what range of wind injection. With that knowledge the contour diagrams of relevant variables (tap positions or voltage magnitudes) can be generated. Figure 3.4(a) shows the tap position contour diagram of T_3 which overall had the highest sensitivity values. By looking at the region of interest shown in Figure 3.4(b), one can see that at low to medium wind injection, tap contour lines (each corresponding to a tap step) are closely spaced whereas at higher wind outputs the tap position does not change at all. Contrasting Figures 3.3(b) and 3.4(b) reveals an interesting pattern. Regions of high tap and low voltage sensitivity almost entirely overlap. The reason for this will be explained analytically in Chapter 5 and lies in the reactive power flow through the OLTC transformer. Regulation of voltage at wind injection nodes require absorbtion of reactive power at the POI. Once the inductive limit of reactive compensation devices (STATCOMs or SVCs) are reached the variability in flow of reactive power through the upstream OLTC significantly declines but then the POI voltage magnitudes start to fluctuate in response to variation in wind generation.

Moreover there are discontinuities in the contour lines when injection is high at one node and low at the other. These somewhat symmetrical discontinuity points correspond to

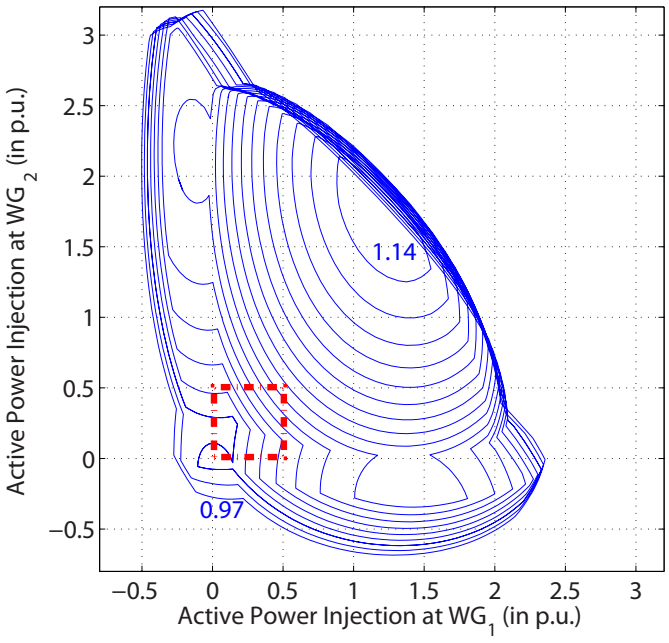

(a) -/+ 15Mvar compensation at wind injection nodes: Global view

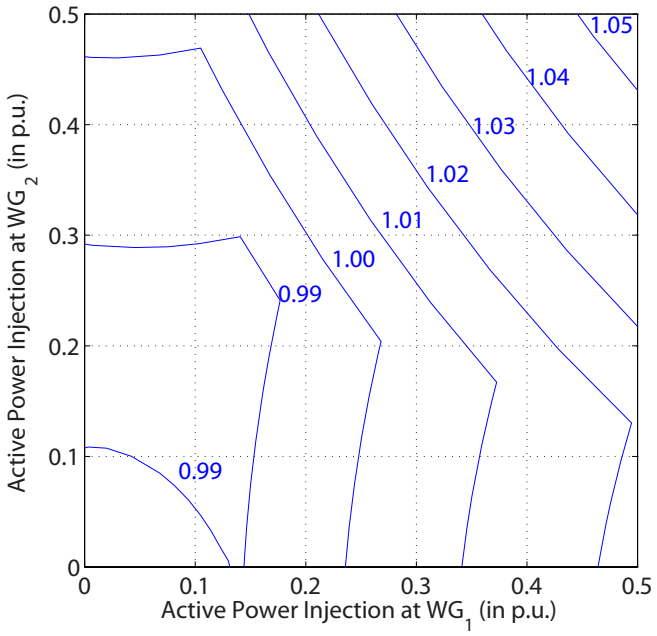

(b) -/+ 15Mvar compensation at wind injection nodes: Region of interest

Figure 3.3: Contour diagrams of voltage magnitude at load bus L_1 for varying active power injections at wind nodes (± 15 MVAr compensation).

Tap Step Sensitivities ($\frac{\text{step}}{\text{MW injection}}$)						
Operating Point	Injection Node	Transformer				
		T_1	T_2	T_3	T_4	T_5
No Wind Output	WG_1	-0.01	-0.03	-0.07	-0.08	0.00
	WG_2	-0.01	-0.01	-0.07	-0.06	0.00
	WG_3	-0.06	-0.07	-0.06	-0.00	0.00
40% Wind Output	WG_1	0.01	-0.01	-0.02	-0.03	0.01
	WG_2	0.01	0.00	-0.02	-0.02	0.02
	WG_3	0.01	0.01	-0.01	0.00	0.00
80% Wind Output	WG_1	0.02	0.00	0.00	-0.01	0.02
	WG_2	0.02	0.00	0.00	0.00	0.02
	WG_3	0.00	0.01	0.00	0.00	0.00

Table 3.1: Tap step sensitivities for the transformers highlighted in Figure 3.1. No reactive compensation at wind injection nodes.

Tap Step Sensitivities ($\frac{\text{step}}{\text{MW injection}}$)						
Operating Point	Injection Node	Transformer				
		T_1	T_2	T_3	T_4	T_5
No Wind Output	WG_1	0.04	0.04	0.10	0.12	0.08
	WG_2	0.05	0.04	0.16	0.10	0.06
	WG_3	0.09	0.08	0.08	0.02	0.03
40% Wind Output	WG_1	0.04	0.04	0.09	0.05	0.05
	WG_2	0.08	0.07	0.20	0.18	0.14
	WG_3	0.18	0.15	0.14	0.02	0.04
80% Wind Output	WG_1	0.03	0.01	0.02	0.03	0.06
	WG_2	0.03	0.02	0.03	0.03	0.06
	WG_3	0.04	0.02	0.02	0.01	0.01

Table 3.2: Tap step sensitivities for the transformers highlighted in Figure 3.1. Compensation of ± 15 MVAr at each wind injection node.

limits of reactive compensation at each injection node. As wind injection increases, reactive compensation devices absorb more reactive power until the inductive limit is encountered. As wind injection continues to increase, the voltage magnitude of the injection node and adjacent nodes starts to rise. Figures 3.5 and 3.6 show the contour lines corresponding to inductive limits of WG_1 and WG_2 superimposed on voltage magnitude and tap position diagrams respectively. The solution space is divided into four regions labeled A, B, C and D. In region A, both WG_1 and WG_2 are regulating. In region C, WG_2 has reached its inductive limit but WG_1 is still regulating, whereas in region D the situation is the reverse. In region B both WG_1 and WG_2 have reached their inductive limits. This latter region corresponds with where T_3 tap position stabilizes. According to the sensitivity values, this is also the case for all other transformers. The tap position contour diagram of T_3 for the case with no compensation, shown in Figure 3.7, also confirms, albeit in a negative way, the

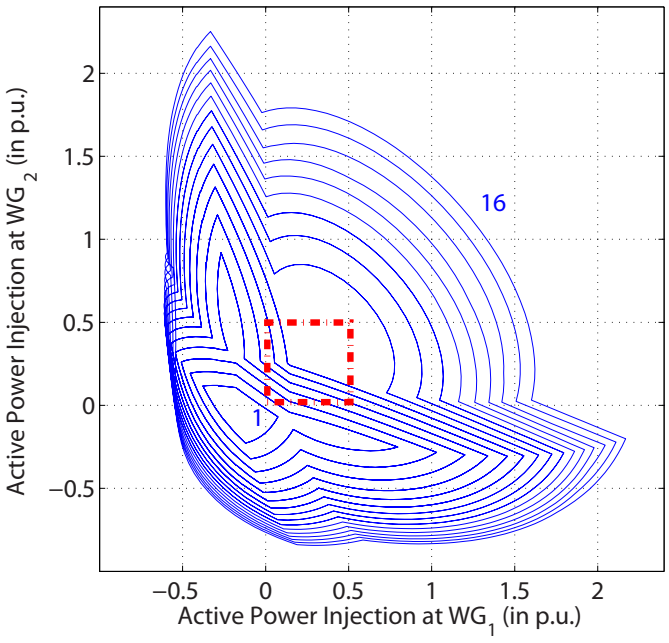

(a) -/+ 15Mvar compensation at wind injection nodes: Global view

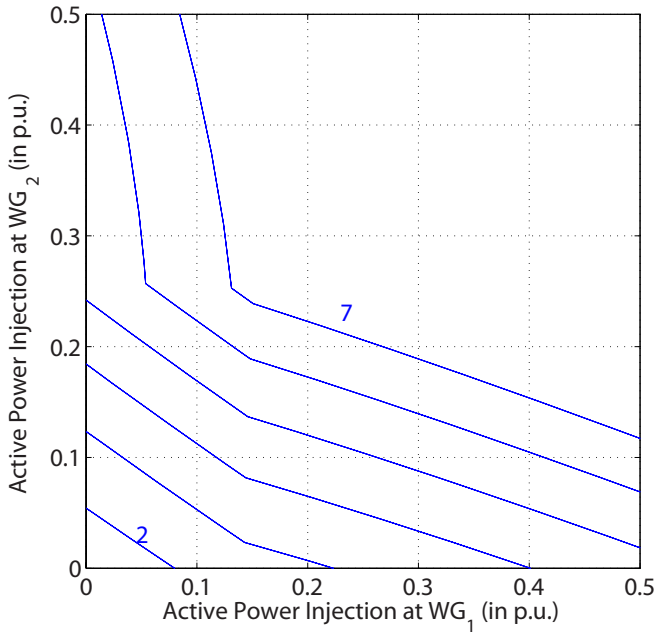

(b) -/+ 15Mvar compensation at wind injection nodes: Region of interest

Figure 3.4: Contour diagram of T_3 tap position for varying active power injections at wind nodes (± 15 MVAr compensation).

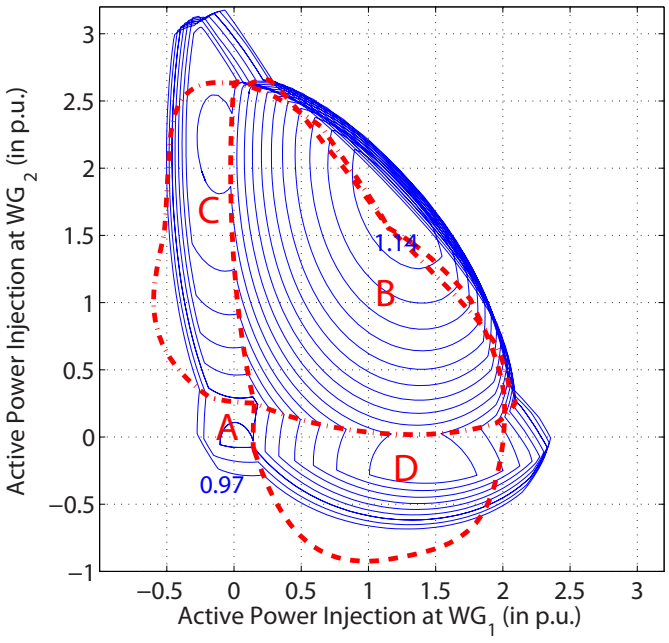

(a) Global view

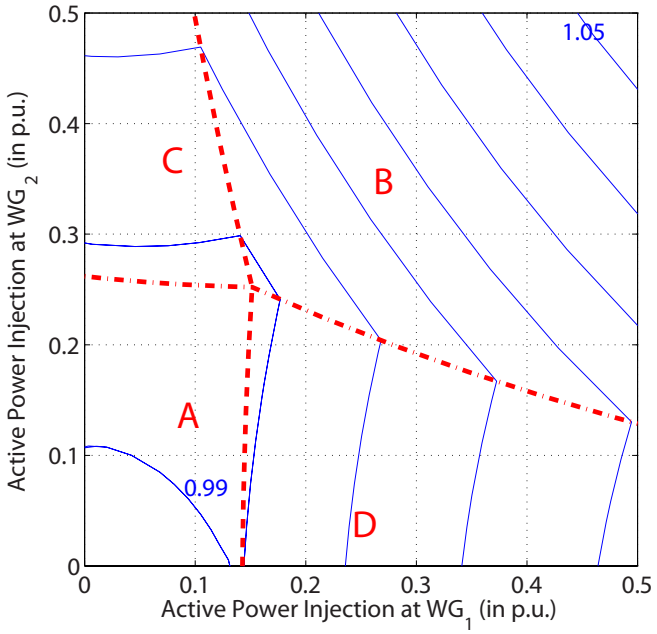

(b) Region of interest

Figure 3.5: Demarcation of the L_1 voltage magnitude contour diagram into the four regions determined by reactive compensation limits.

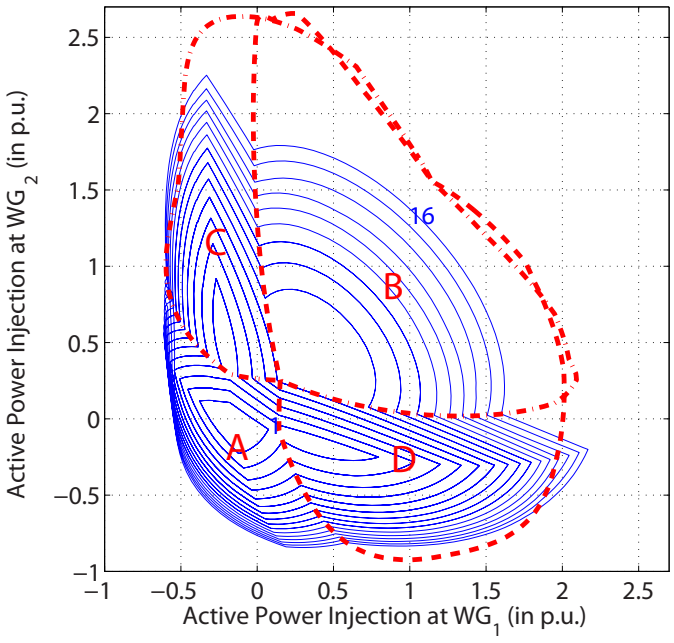

(a) Global view

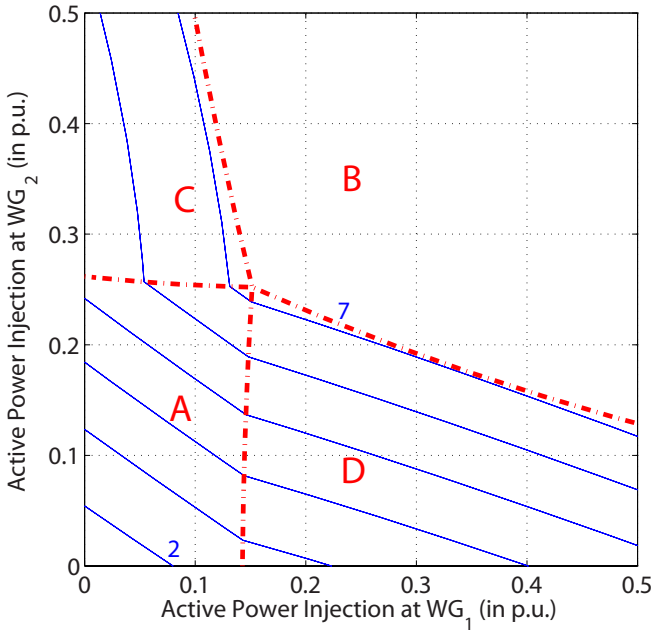

(b) Region of interest

Figure 3.6: Demarcation of the T_3 tap position contour diagram into the four regions determined by reactive compensation limits.

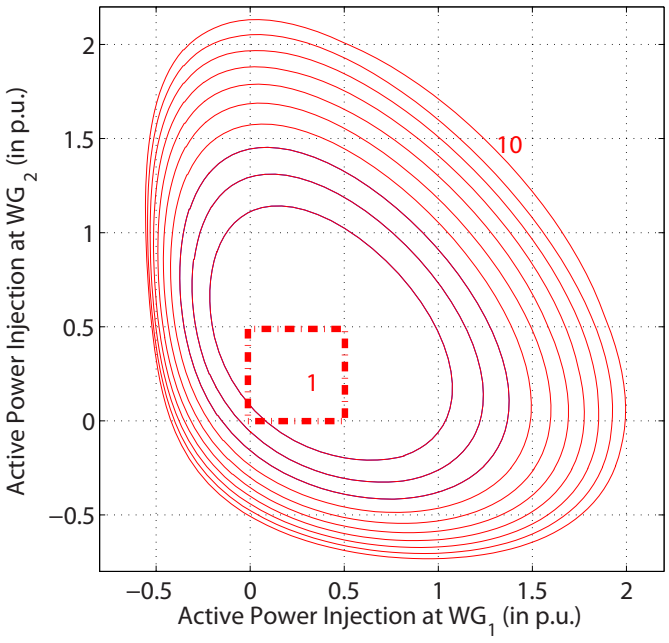

Figure 3.7: Contour diagram of T_3 tap position for varying active power injections at wind nodes (no voltage regulation).

observation that reactive compensation results in higher tap sensitivity. Therefore, in the absence of any voltage regulation at the injection nodes, tap position sensitivity is reduced.

However, before concluding that there exists a trade-off between voltage regulation at the injection nodes and tap change operation, one should investigate the actual tap-changing operation of transformers under normal operating conditions, prior to wind. This base case, where transformer taps are adjusted only in response to changes in the system load, must be compared with cases where variable wind is added, with and without local reactive compensation.

3.2.1 Wind Variability and Tap Change Operation Simulation

The previous section examined possible relationship between voltage regulation of wind injection nodes and sensitivity of the tap positions of the transformers that connect the sub-transmission and transmission systems. This will be explored further via simulation of the tap change operation of the five transformers in the DTE/ITC system.

The simulation is based on power flow code developed in Matlab and verified with commercial power flow programs. The simulation models tap position as a discrete variable. The power flow is executed every minute with updated load (P, Q) information for

Number of Monthly Tap Changes					
Simulation Cases	Transformer				
	T_1	T_2	T_3	T_4	T_5
No Wind	140	23	98	85	173
WG_1,WG_2 and WG_3: Each 50MW with no reactive compensation	78	25	133	112	175
WG_1,WG_2 and WG_3: Each 50MW and -/+15 Mvar compensation	360	350	511	456	442

Table 3.3: Number of monthly tap change operations for the transformers highlighted in Figure 3.1.

all buses in the network, and with minute-by-minute wind generation data. If the voltage of the bus that is regulated by a tap-changing transformer moves outside the deadband $(-\frac{1}{120}, +\frac{1}{120})$ p.u., centered on the voltage set-point, for two consecutive power flow executions (i.e. more than one minute) then the tap is adjusted accordingly (increased or decreased by a single step) to bring the voltage magnitude within the deadband. This models the actual tap-changing mechanism at DTE/ITC system, where the regulated voltage is allowed to deviate from the set-point by a certain margin ($\pm\frac{1}{120}$ p.u.) for a certain period of time (typically one minute) before the tap-change operation is triggered. This mechanism is designed to prevent small disturbances from triggering unnecessary tap-change operations.

The cases considered in the simulation study are as follows:

A. No Wind Injection.

B. Wind Injection at WG_1 , WG_2 and WG_3
(each with a rated capacity of 50 MW , no reactive compensation).

C. Wind Injection at WG_1 , WG_2 and WG_3
(each with a rated capacity of 50 MW, ± 15 MVAr compensation).

The simulations used load data for the DTE/ITC system, and wind generation data from three wind farms in Eastern Michigan, all with one minute resolution and for the same period. Wind generation is highly correlated between these three wind farms as seen in Figure 3.8 which shows wind generation profiles of these wind farms for a 10-day period. Figure 3.9 contrasts the load and wind generation variability over a month period. Table 3.3 gives the number of tap changes per month for the five cases. It can be seen that wind injection in general increases tap change operation. However this increase is significant when all sub-transmission wind-farms have local reactive compensation (voltage regulation).

Deeper insights can be obtained by considering the trend in the number of monthly tap change operations as the reactive compensation capacity at wind injection nodes increases. This is shown in Figure 3.10. As the reactive compensation increases, the number

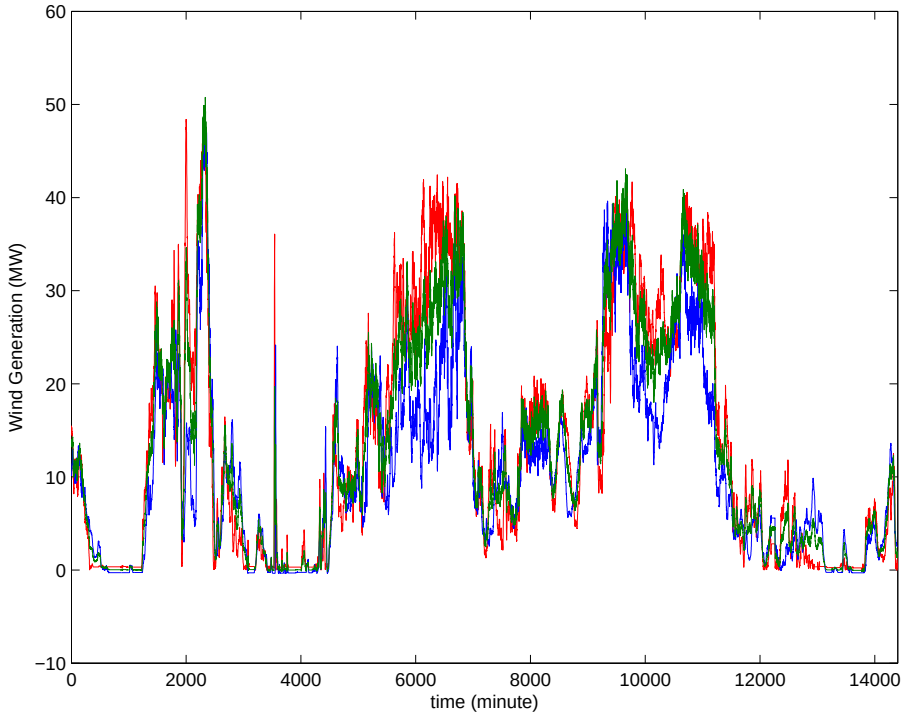

Figure 3.8: Wind generation profile of the DTE's 42kV wind farms for a 10-day period.

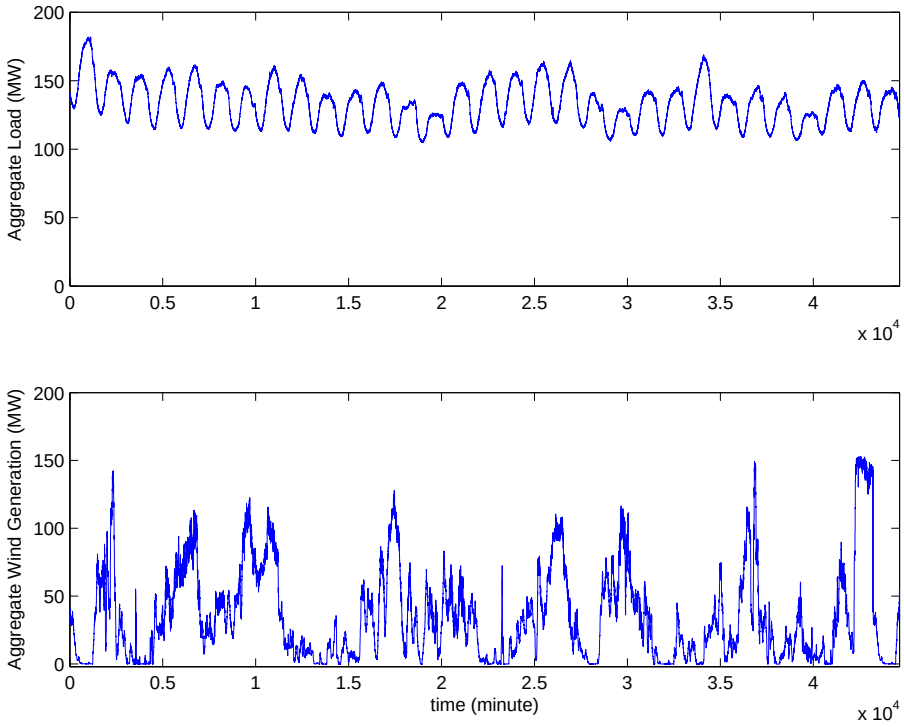

Figure 3.9: Aggregate load and wind generation profile of the DTE's 42kV sub-transmission network (for a typical month).

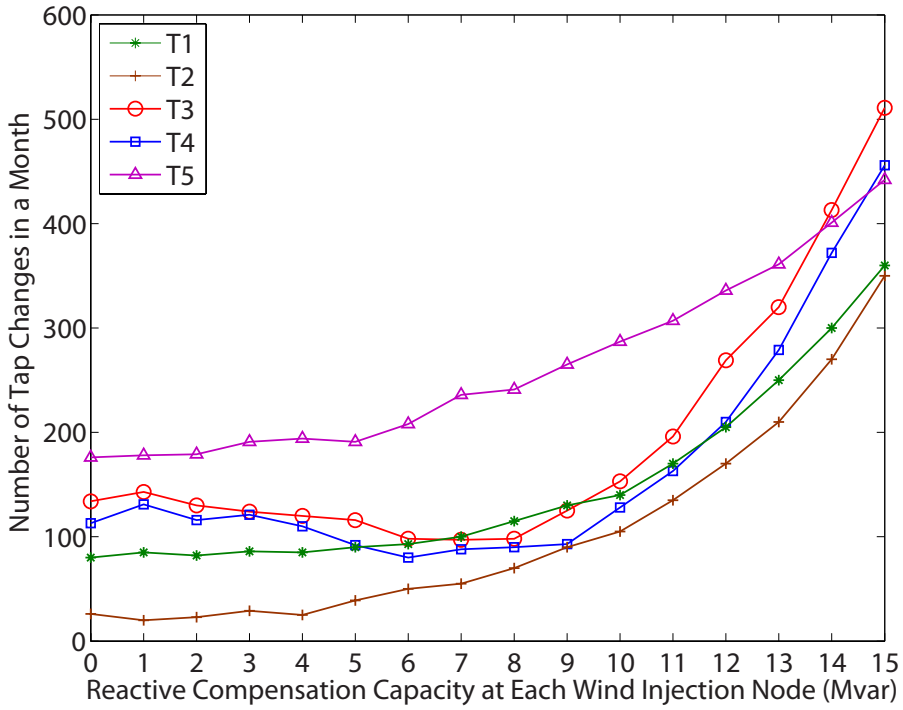

Figure 3.10: Number of monthly tap change operations of the five transformers for varying reactive compensation capacity at wind injection nodes.

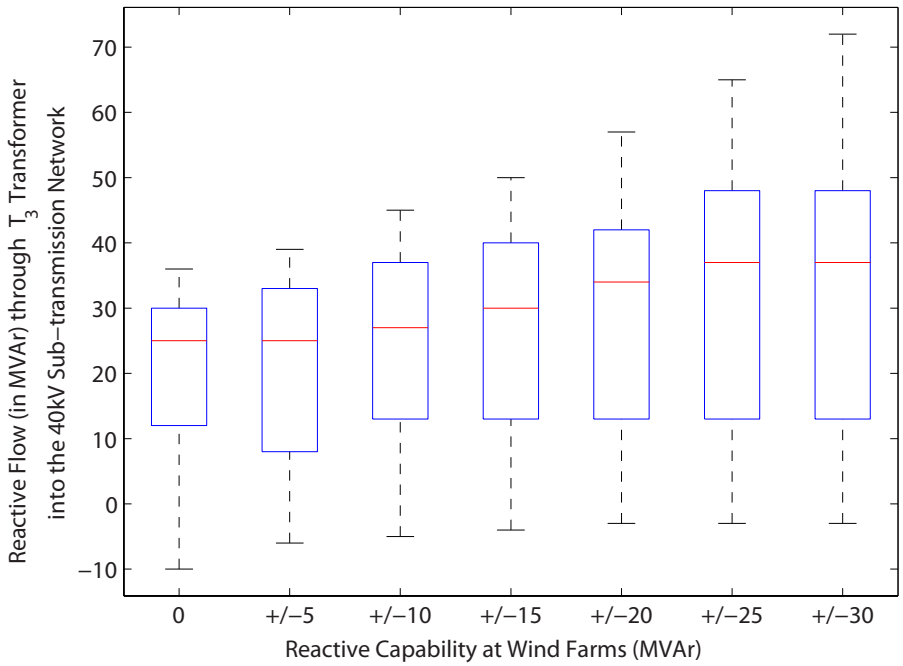

Figure 3.11: Statistics of reactive flow through T_3 transformer (minimum, maximum, 25% and 75% percentile and median)

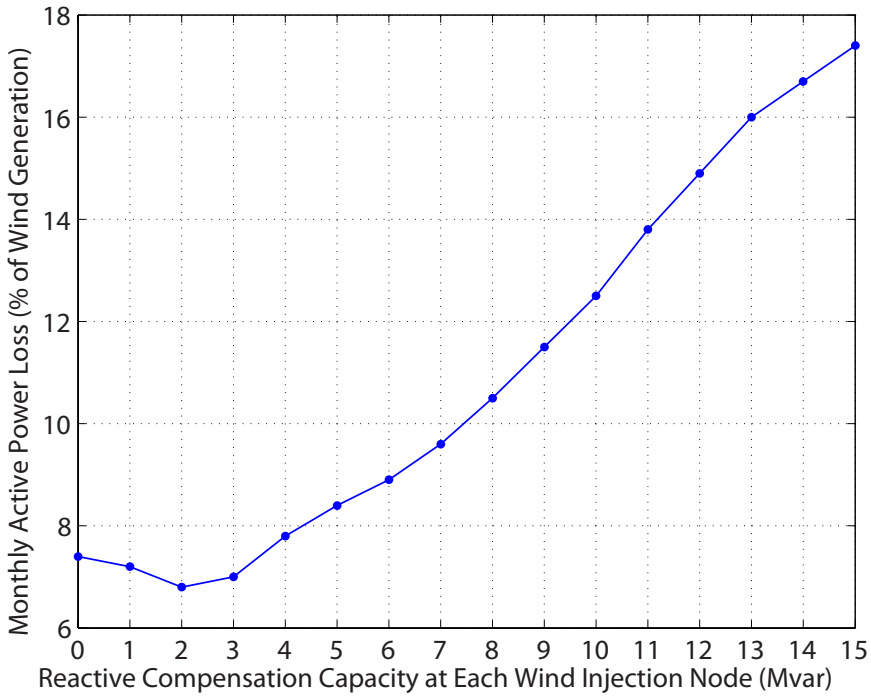

Figure 3.12: Active power loss as a percentage of monthly wind generation for varying reactive compensation capacity at wind injection nodes.

of monthly tap operations initially remains relatively constant before starting to increase significantly around ± 10 MVAr. At that point the sub-transmission network begins to draw large amounts of reactive power from the 120 kV transmission system. This is demonstrated in Figure 3.11 where the minimum, maximum, 25% and 75% percentile and median reactive flow into the sub-transmission network through T_3 transformer for a given month of data is plotted as reactive compensation capability of the three wind farms varies from 0 to ± 30MVAr. Before the voltage regulating devices reach their inductive limits (as wind injection increases), more and more reactive power is drawn from the transmission system. This flow of reactive power into the DTE's resistive sub-transmission network where the X/R ratios are in the range of 1-1.2 causes significant loss of wind generation (see Figure 3.12) especially at low-load high generation periods. This increase in reactive power flow also causes the voltage on the primary side of the tap-changing transformers to drop, so the transformers respond by raising taps. Figure 3.13 illustrates the impact of greater reactive compensation on the transmission system voltage. For higher wind power production, tighter voltage regulation at wind injection nodes and nearby load buses comes at the cost of greater voltage drop on the 120 kV transmission system.

Although voltage regulation at the point of wind interconnection is indispensable, the analysis presented here suggests that it has a detrimental effect on tap-changer operation

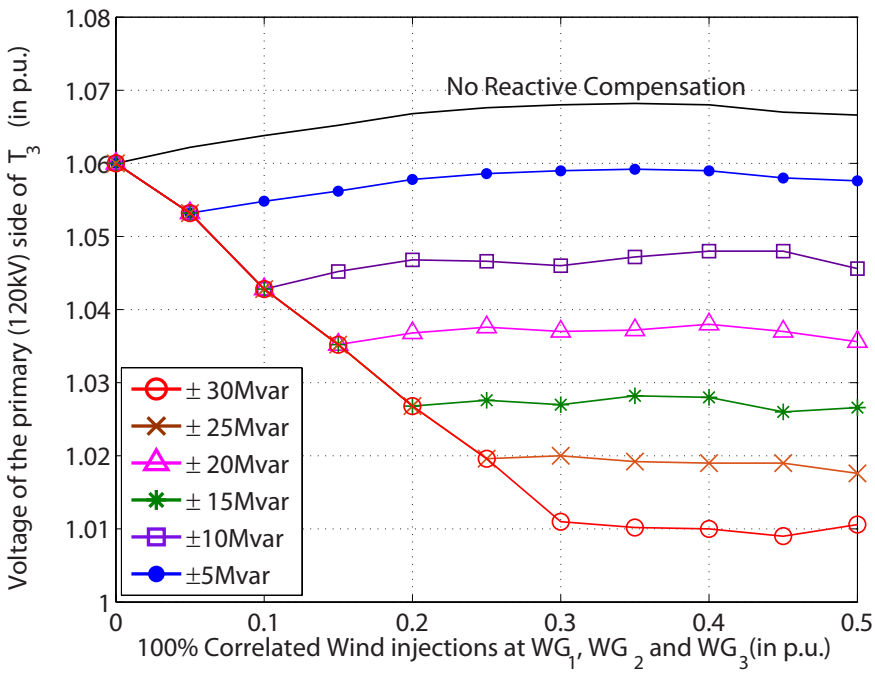

Figure 3.13: Voltage magnitude on the primary (120 kV) side of transformer T_3 for varying wind injection and different reactive compensation capacities.

for the transformers that connect the sub-transmission network (42 kV) to the transmission system (120 kV). Wind-farm voltage regulation tends to increase the sensitivity of tap position to wind power variations, and significantly increases the number of tap change operations. Consequently, the life of these expensive assets will be decreased, hindering the development of wind power in weak grids.

The simulation results presented here indicate that the tap positions of the 120/42 kV transformers tend to remain relatively constant when the voltage at wind injection nodes is not regulated. On the other hand, lack of voltage regulation at wind farms leads to unacceptable voltage fluctuations within the sub-transmission network which, as Figure 3.14 shows, burdens the OLTC transformers connecting the 42kV sub-transmission network to DTE's 13.2kV distribution feeders. No voltage regulation at the 42kV wind injection node results in a roughly 4-5 fold increase in the number of tap operations of the nearby distribution substation OLTC (at L_1) compared to the case of no wind injection. This highlights the importance of developing a coordinated voltage control scheme to reduce the OLTC operations of both sub-transmission and distribution transformers and active power losses in the sub-transmission network. These voltage control schemes along with theoretical

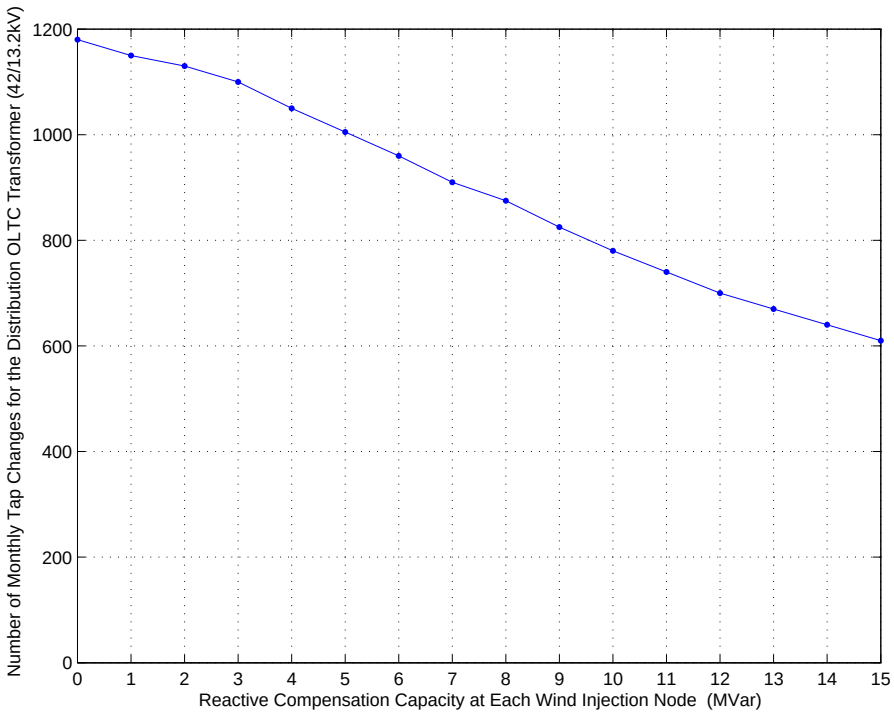

Figure 3.14: Number of monthly tap change operations for the 42/13.2kV distribution OLTC transformer at L_1 in Figure 3.1 for varying reactive compensation capacity at wind injection nodes

investigations of what truly causes tap operations are presented in chapter 5.

3.3 Impact of wind generation on the voltage stability of the DTE/ITC system

In the previous section the focus was solely on the issues associated with the sub-transmission wind generation. However in many utilities as in the DTE/ITC case, wind farms beyond a certain size are required to connect directly to the higher voltage network due to operational constraints such as line flow limits and losses. Figure 3.1 highlights three nodes on the ITC owned 120kV transmission network where large wind farms are connected. The key issue to be investigated here is that as wind generation reaches its peak across the system how the voltage stability margin, defined as distance to the feasibility boundary of the network is affected for different reactive compensation capabilities at sub-transmission wind injection nodes (i.e. WG_1, WG_2 and WG_3). For this purpose, it is assumed that transmission wind injection nodes have a reactive compensation capability of ± 50 MVAr and sub-transmission wind injection nodes has the following reactive capabilities,

1. No reactive capability.

2. ± 15 MVAr reactive compensation.

3. ± 30 MVAr reactive compensation.

4. ± 50 MVAr reactive compensation.

Using the method for computing the feasibility boundary discussed in Section 2.4, the parameter space is defined as the transmission generation index λ_t and sub-transmission generation index λ_s. Generation indices can be interpreted as capacities that can be installed at either sub-transmission or transmission levels with a fixed ratio. For example if the transmission capacity ratios are taken to be 1:2:3 (for WG_4, WG_5 and WG_6) as λ_t increases from 0 to 1, assuming full wind intensity, the injections at the three transmission wind farms reach 100MW, 200MW and 300MW. Here it is assumed that wind generation is perfectly correlated between wind farms which is a reasonable assumption given that wind outputs are highly correlated even over a distance of 1000km [60]. Alternatively generation indices can be interpreted as normalized wind generation where for example $\lambda_s = 0$ and $\lambda_s = 1$ correspond to no-wind and full-wind generation at the sub-transmission level.

The feasibility boundaries corresponding to the 4 cases of sub-transmission reactive compensation capability are shown in Figure 3.15. Note that as λ_s increases from 0, the generation at WG_1, WG_2 and WG_3 increases with a fixed ratio which here is chosen to be 1 but can be modified to represent the generation capacity ratios at these nodes. The same holds for λ_t with respect to WG_4, WG_5 and WG_6.

It can be seen in Figure 3.15 that at high levels of sub-transmission wind generation, the feasibility margin shrinks as the reactive capability is increased. This pattern with regard to reactive capability becomes less apparent at high transmission wind injection levels and ultimately reverses at the lower right region of Figure 3.15 where transmission wind injection is at it highest level and there is no sub-transmission wind injection. This is due to a combination of factors. First as λ_t increases the voltage magnitudes at the transmission system tend to decline. This in combination with reactive power flow into sub-transmission network pushes the OLTCs to their upper limit at which point the voltages across the 42kV network start to fall. This in turn alleviates the voltage rise issue and curbs the reactive requirement of the 42kV sub-transmission network. Hence OLTCs reaching their limits has a stabilizing impact on the DTE/ITC system by relieving the strain on the reactive reserves of the transmission system. Notice that in this section in contrast to the previous section, the tap variables are modeled as continuous which has no impact on the analysis presented here.

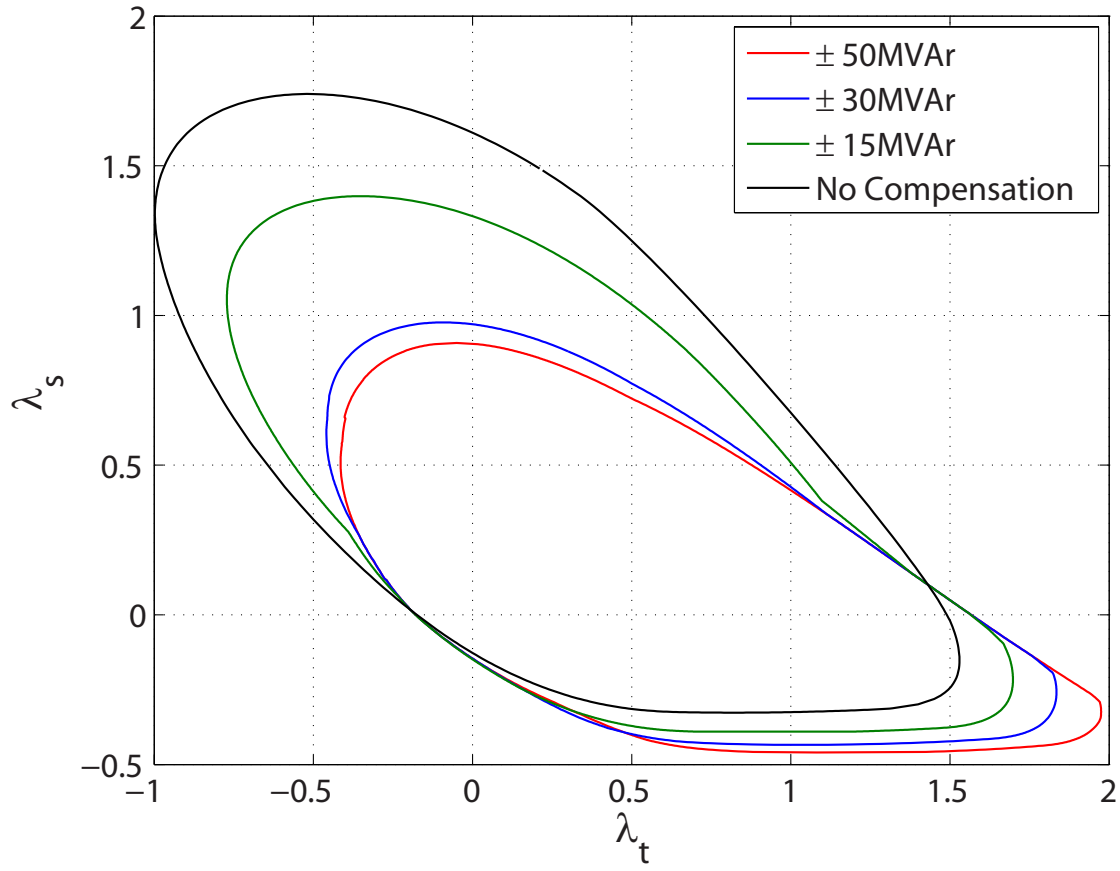

Figure 3.15: Power flow feasibility region for sub-transmission and transmission wind injection for varying reactive capabilities at DTE's sub-transmission wind generation nodes WG_1, WG_2 and WG_3.

Figures 3.16 and 3.21 contrast the singular and non-singular segments of the feasibility boundary for the two cases of no compensation and ± 50MVAr capability. Notice that in Figure 3.16 four different cross sections of the feasibility region are highlighted in blue dashed line. These cross sections correspond to fixed values of λ_s at $0.50, 1.00, 1.30$ and 1.70. The P-V curves associated with these cross sections are shown in Figures 3.17, 3.18, 3.19 and 3.20. It is clearly seen that as λ_s increases from 0.50 to 1.70 the voltage at L_1 bus increases significantly as expected by the fact that there is no reactive compensation capability at sub-transmission wind farms. The saddle-node and limit-induced bifurcations are contrasted in Figure 3.18 where the bifurcation corresponding to the positive value of λ_t is characterized by a discontinuity caused by WG_5 reaching its reactive limit. The bifurcation corresponding to the negative value of λ_t is characterized by singularity of power flow Jacobian where the tangent to the P-V curve $\frac{\partial V}{\partial \lambda_t}$ is vertical.

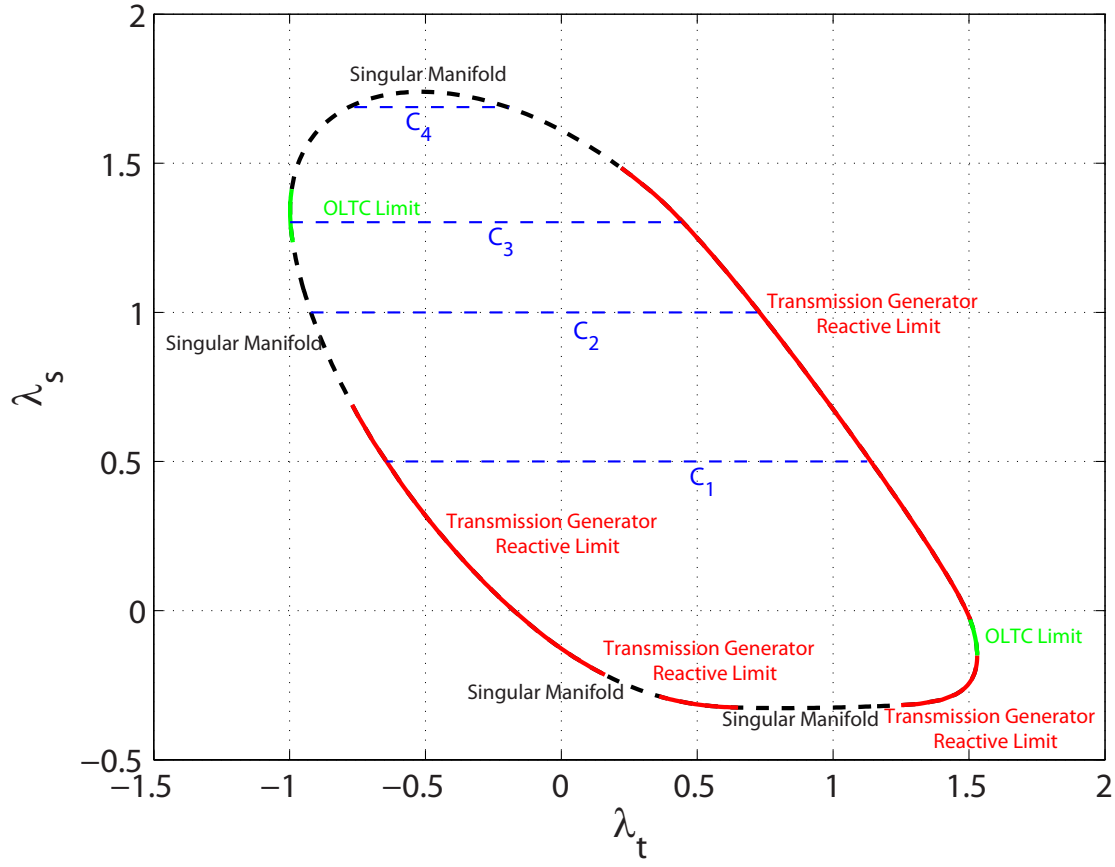

Figure 3.16: Power flow feasibility region for sub-transmission and transmission wind injection for zero reactive capability at DTE's sub-transmission wind generation nodes WG_1, WG_2 and WG_3. The segments of feasibility boundary demarcated by the reactive limits of transmission wind generation nodes (WG_4, WG_5 and WG_6) are in red. The segments demarcated by OLTC upper limits (1.10 p.u.) are in green. The singular segments are marked by dashed black lines.

It should also be noted that as the OLTC upper limits are increased, the feasibility region shrinks even further. This is shown in Figure 3.22. Theoretical investigations related to these phenomena are discussed in Chapter 4.

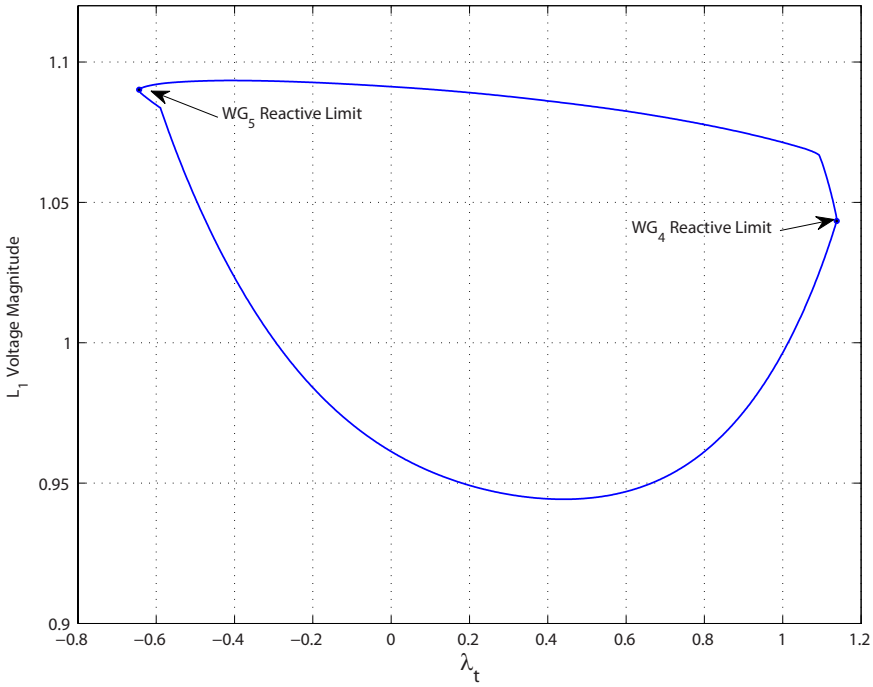

Figure 3.17: P-V curve corresponding to boundary cross section C_1 ($\lambda_s = 0.50$) for the case of no reactive capability at sub-transmission wind farms.

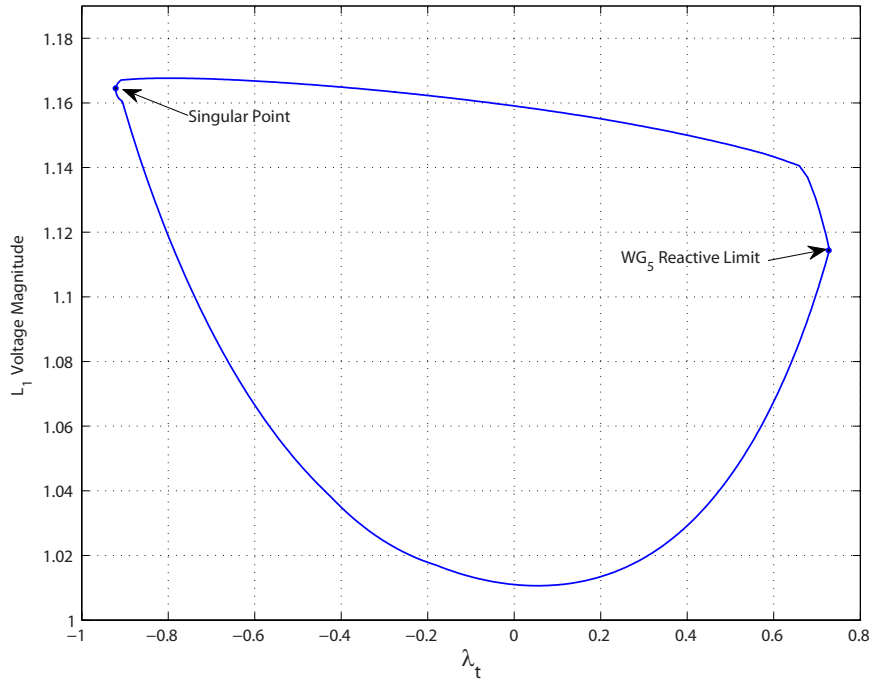

Figure 3.18: P-V curve corresponding to boundary cross section C_2 ($\lambda_s = 1.00$) for the case of no reactive capability at sub-transmission wind farms.

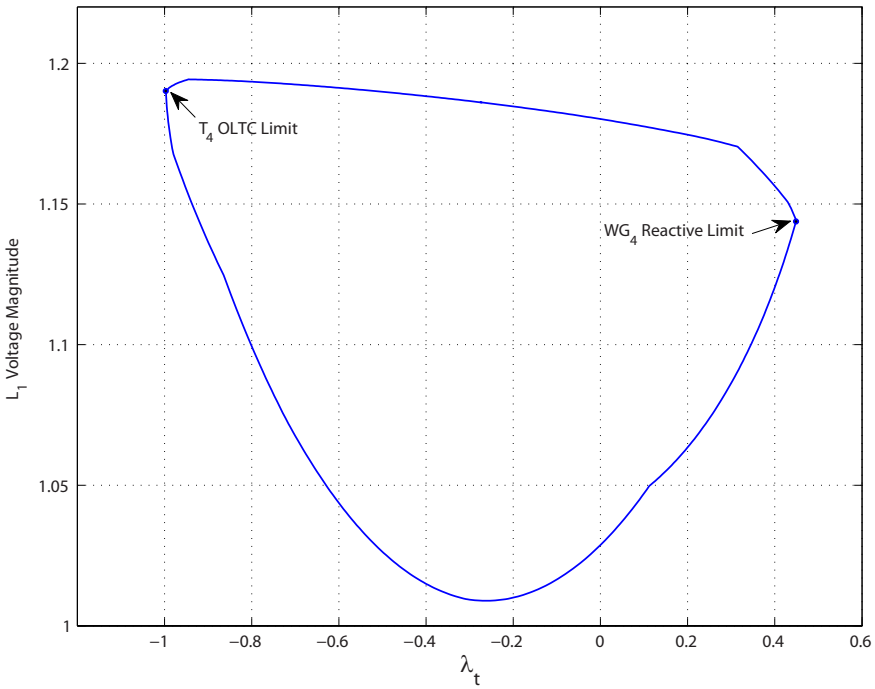

Figure 3.19: P-V curve corresponding to boundary cross section C_3 ($\lambda_s = 1.30$) for the case of no reactive capability at sub-transmission wind farms.

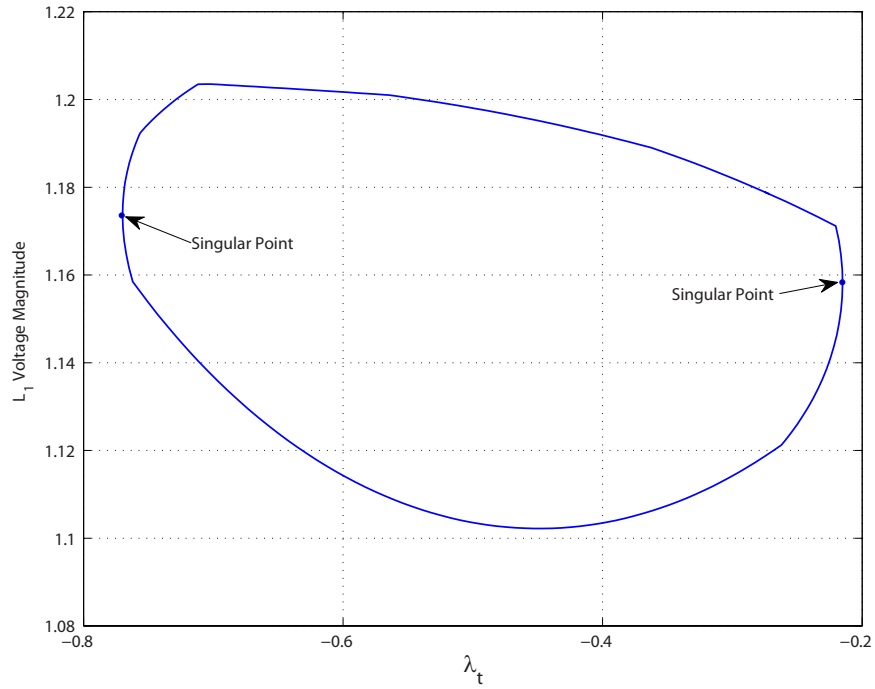

Figure 3.20: P-V curve corresponding to boundary cross section C_4 ($\lambda_s = 1.70$) for the case of no reactive capability at sub-transmission wind farms.

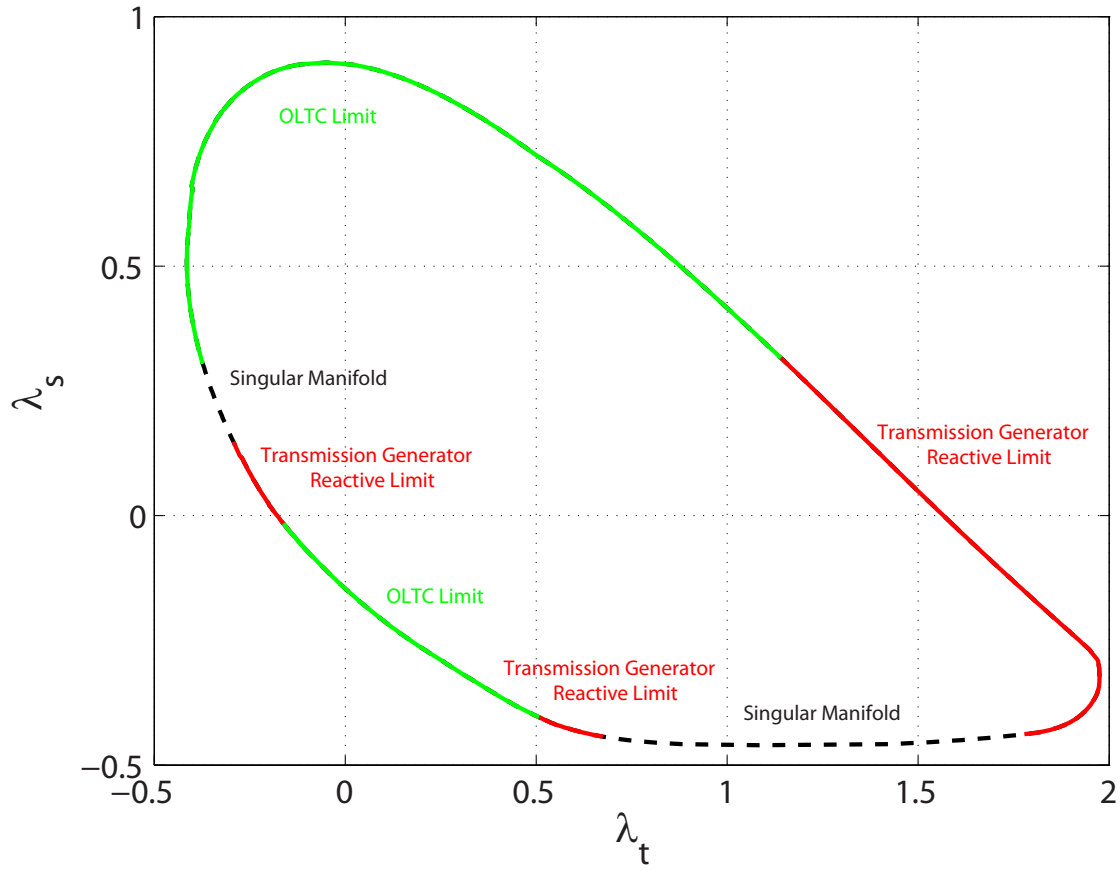

Figure 3.21: Power flow feasibility region for sub-transmission and transmission wind injection for ± 50 MVAr capability at DTE's sub-transmission wind generation nodes WG_1, WG_2 and WG_3. The segments of feasibility boundary demarcated by the reactive limits of transmission wind generation nodes(WG_4, WG_5 and WG_6) are in red. The segments demarcated by OLTC upper limits (1.10 p.u.) are in green. The singular segments are marked by dashed black lines.

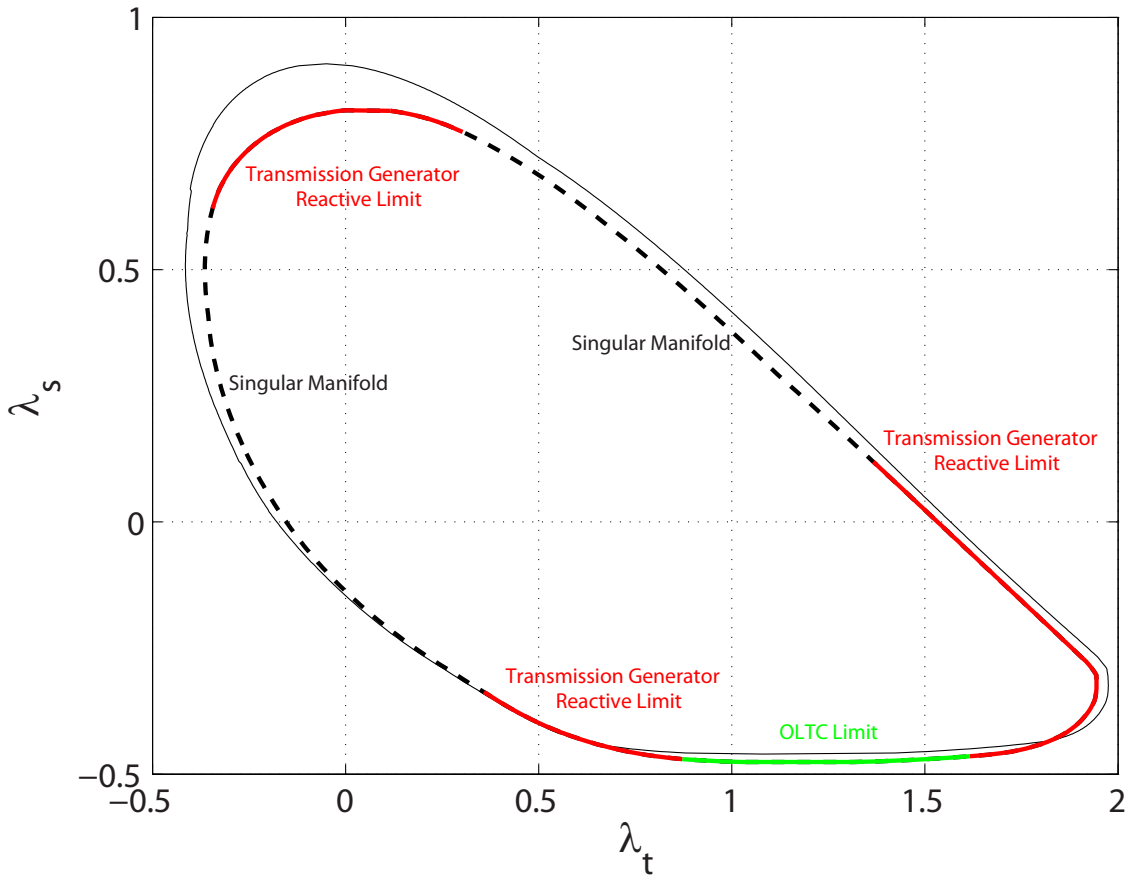

Figure 3.22: The case of ± 50 MVAr capability with enhanced OLTC limits (1.15 p.u.) contrasted with previous OLTC limits (1.10 p.u.) (solid black line).

CHAPTER 4

Integration of Variable Generation and the Impact on Structural Stability

4.1 Introduction

Wind and solar power are primarily integrated into what is referred to as weak grids characterized by lower (sub-transmission) voltage levels and high resistivity. Excellent wind resources are usually located where power infrastructure is not sufficiently developed. Even in the presence of stronger transmission networks, it is usually less costly and hence preferable from a developer's perspective to connect wind generation of appropriate size into lower voltage networks if grid codes allow.

In a typical transmission network where $\frac{X}{R} \approx 10$, and under normal operating conditions, there is a strong coupling between reactive power and voltage magnitudes, while the coupling between voltage magnitudes and active power is much weaker. As the network becomes resistive, these relations undergo a fundamental transformation and with it the typical paradigm of reactive compensation to support voltage levels across the network. Whereas in transmission networks active power injection tends to slightly suppress voltages requiring most synchronous generators to operate at lagging power factors close to unity, in resistive networks such an injection may induce *severe* voltage rise [4]. Consequently, strict voltage regulation at the point of wind interconnection may create an enormous reactive sink. Reactive reserves are primarily provided by the stronger transmission network. Therefore, the new reactive requirement of the resistive network, seen as reactive load at the point of connection to the transmission system, may impact the voltage stability margin.

A number of studies in recent years have simulated the impact of wind generation at distribution networks on the steady state operation of transmission systems and have come up with conflicting observations and suggestions. A study on the Irish grid using time series simulation suggests that voltage control mode as opposed to fixed power factor mode

of wind generators connected at the distribution level may enhance system voltage stability [61]. Another study simulating the impact of sub-transmission wind injections using IEEE 34-node test feeder argues that as wind injection increases the reactive demand on the transmission networks decreases and with it the negative impact of wind injection on voltage stability of the system [62]. A similar statement on the reduction of reactive power import from the transmission system is put forward, based on a "simple generic model", in a paper that analyzes the repercussions of distributed generation for transmission system operation [63]. Opposite conclusions are drawn in another simulation-based study using a 6-node test system. The simulation results are cited to argue that once wind injection exceeds the local demand, the stability margin (measured by Q-V method) shrinks and this is attributed to increased losses caused by reverse power flow toward the transmission system [64].

While these simulations offer some limited insight into their respective network configurations, the conclusions made are not universally valid. What is missing in the literature is an analytical investigation of network parameters illuminating the role of network resistivity and modes of voltage/reactive power control on the stability boundary of the system.

An exhaustive search of the available literature pinpoints only a single study that has explored this direction deeper. The study illustrates, using continuation power flow, the asymmetry in voltage stability boundaries between negative injection (load) and positive injection (generation) in resistive networks [65]. As a result of this asymmetry it is unlikely that active power injection into resistive networks, within the line flow constraints of the network, causes any voltage collapse per se. The more challenging question that this chapter seeks to answer is that how resistivity of a network connected to a stronger transmission network can impact the voltage stability margin of the entire system.

This chapter is organized as follows. Section 4.2 investigates the impact of resistance on the reactive requirement of a radial network. It, then, introduces two theorems that express the observations in analytical terms. Section 4.3 discusses the implications of these two theorems in the context of a generic transmission system with a radial branch modeling the sub-transmission/distribution network. Section 4.4 introduces the concept of *critical resistance*, discussing its significance for tuning the parameters of a radial resistive network as to minimize the impact of embedded generation on the structural stability of the power system. Section 4.5 applies insight obtained in the earlier sections to investigate the voltage stability impact of sub-transmission wind injection under different voltage control modes for the DTE/ITC system. In sections 4.4 and 4.5 continuation power flow (see section 2.3) is used to obtain Q-V curves, an established stability criterion in the power industry. In this method, a fictitious reactive load at a pilot transmission node is increased until either

saddle-node or limit-induced bifurcation is reached. The reactive power margin is, then, used a measure of voltage stability [66].

4.2 The Impact of Resistance

In order to investigate the question posed earlier regarding network resistivity and structural stability, a 4-bus network, shown in Figure 4.1, is considered that models transmission and sub-transmission/distribution networks, with the latter connected radially at an intermediate node (Bus 2). Embedded generation is connected at Bus 1 and its power output is exported to the transmission network at Bus 2. Load is modeled at Bus 3. The rest of the network is modeled as the infinite bus.

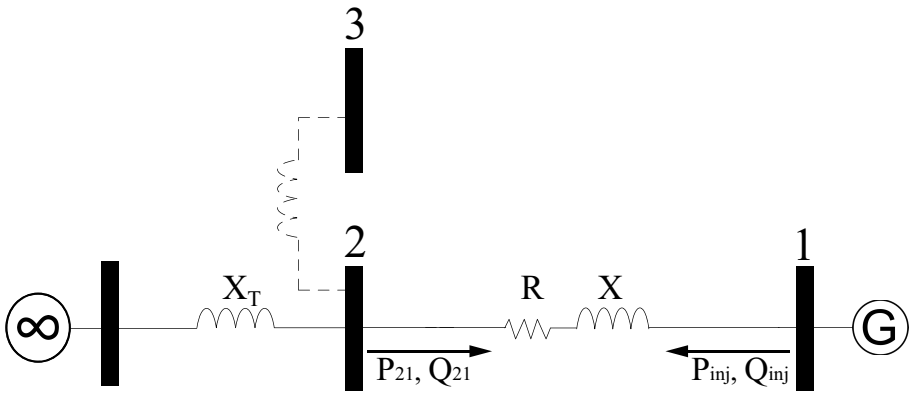

Figure 4.1: A generic power system with a resistive branch

Let us examine the distribution interconnection in isolation assuming that voltage at Bus 2 is fixed at 1.00 p.u. (this assumption is later relaxed) and study the changes in the reactive requirement of the distribution feeder as it becomes resistive (i.e. increasing R from zero to $\frac{R}{X} = 1$ while keeping X constant at 0.50 p.u.) for the following two modes:

1. Full voltage control at Bus 1 ($V_1 = 1.00$ p.u.)

2. No voltage control at Bus 1 (Unity p.f. $Q_1 = 0$)

Figure 4.2(a) shows a set of curves relating active power injection at Bus 1 (X-axis), to reactive power flow into the distribution feeder at Bus 2 (Y-axis), under full voltage control mode. Each curve corresponds to a value of R, starting with a perfect circle at $\frac{R}{X} = 0$, morphing into ellipses with increasing eccentricity as R increases and finally a line segment

(in red) at $\frac{R}{X} = 1$. At $\frac{R}{X} = 0$ a quadratic equation similar to (4.6), introduced later, can be derived for Q_{21} and P_{21} and reformulated as a circle with $P_{inj} = -P_{21}$. At $\frac{R}{X} = 1$ and given that $V_1 = V_2$, network is symmetrical with respect to Q_{21} and P_{inj} which explains the 45° slope of the red line passing through the origin in Figure 4.2(a). The fact that $P_{inj} = Q_{21}$ and thus are called symmetrical when $R = X$ and $V_1 = V_2$ can be easily inspected in the following equations that define the power flow in the radial network:

$$P_{inj} = \frac{R(V_1^2 - V_1 V_2 \cos(\delta_{12})) + X V_1 V_2 \sin(\delta_{12})}{R^2 + X^2} \tag{4.1}$$

$$Q_{21} = \frac{X(V_2^2 - V_1 V_2 \cos(\delta_{21})) - R V_1 V_2 \sin(\delta_{21})}{R^2 + X^2} \tag{4.2}$$

As indicated by arrow, for a given level of active power injection, the reactive requirement of the distribution network, Q_{21}, increases with increasing R. Thus the distribution network becomes more inductive relative to the transmission network.

Figure 4.2(b) shows the same set of curves under unity p.f. (no voltage control) mode. Starting with a perfect circle at $\frac{R}{X} = 0$, the curves are morphed into ellipses with increasing eccentricity as R increases. However, in contrast to the previous set of curves, the major radius of the ellipses also increases with R, enhancing the power transfer capability of the feeder in the positive direction, i.e. for active power injection (P_{inj}) at Bus 1. This is in line with the discussion of asymmetry in the loadability margin in [65]. As indicated by arrow, for a given level of active power injection, Q_{21} decreases with increasing R making it less inductive relative to the transmission network.

Next, the previous observations regarding the transformation that a network with embedded generation undergoes as it becomes resistive are formulated analytically by introducing the following two theorems:

Theorem 1 *For the network of Figure 4.1, where both V_1 and V_2 are fixed (regulated), $0 < P_{inj} < P_{max}$ and $R < R_{max}$ the following relations hold,*

(a) $\frac{\partial Q_{inj}}{\partial R} < 0$

(b) $\frac{\partial Q_{21}}{\partial R} > 0$

Where $P_{max} = \sqrt{\frac{4V_1^2V_2^2 - V_1^4}{4X^2}}$ and R_{max} is the largest real root of the following quartic equation,

$$R^4 - 2\alpha\beta R^3 + (\alpha^2\beta^2 + 2X^2)R^2 - X^2(\alpha^2 + \beta^2)R + X^4 = 0 \tag{4.3}$$

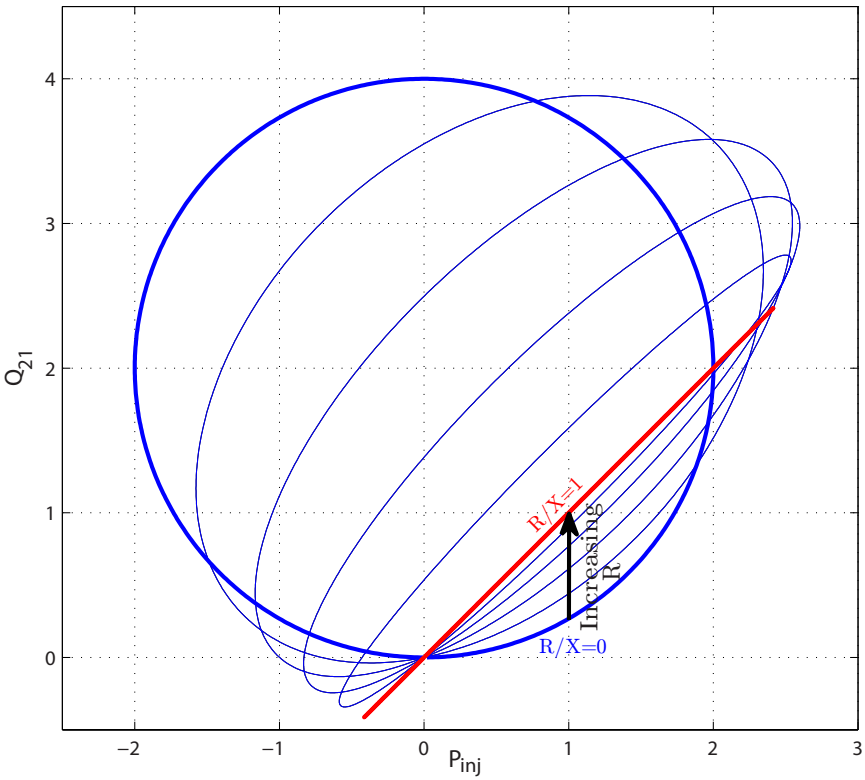

(a) Full voltage control at Bus 1 ($V_1 = 1.00$ p.u.)

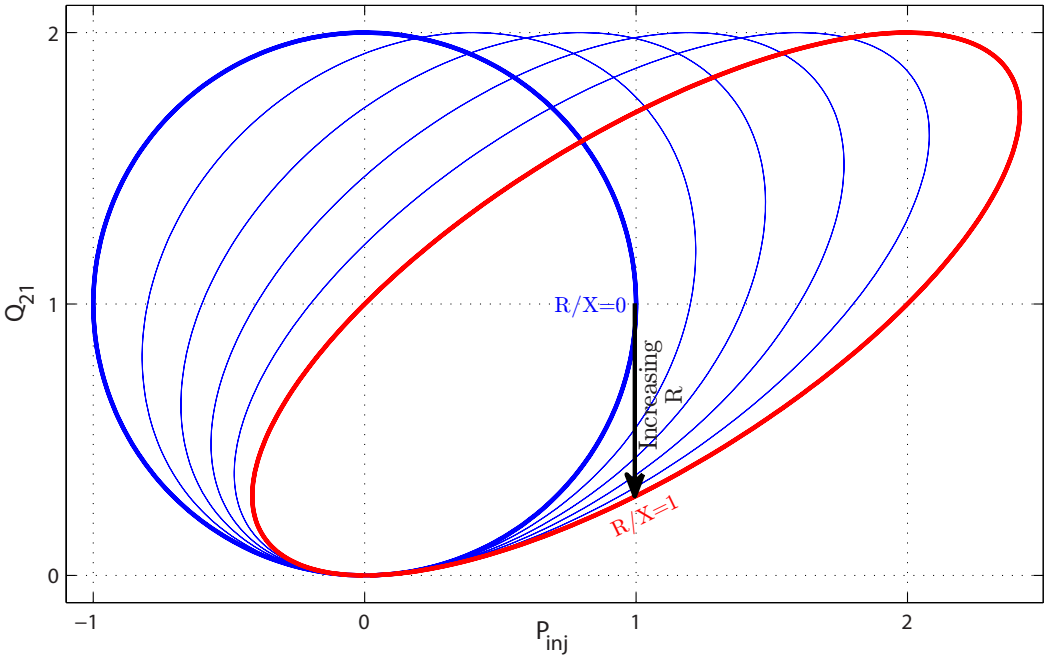

(b) No voltage control at Bus 1 (Unity p.f. $Q_1 = 0$)

Figure 4.2: $P_{inj} - Q_{21}$ diagrams

where $\alpha = \frac{V_1 - V_2}{\sqrt{P_{inj}}}$ *and* $\beta = \frac{V_1 + V_2}{\sqrt{P_{inj}}}$

Proof:

$$P_{inj} = \frac{R(V_1^2 - V_1 V_2 \cos(\delta_{12})) + X V_1 V_2 \sin(\delta_{12})}{R^2 + X^2} \tag{4.4}$$

$$Q_{inj} = \frac{X(V_1^2 - V_1 V_2 \cos(\delta_{12})) - R V_1 V_2 \sin(\delta_{12})}{R^2 + X^2} \tag{4.5}$$

Eliminating δ_{12} gives the following quadratic equation in terms of Q_{inj},

$$(R^2 + X^2)Q_{inj}^2 - 2XV_1^2 Q_{inj} + \zeta = 0 \tag{4.6}$$

$$\zeta = V_1^4 - 2RP_{inj}V_1^2 - V_1^2 V_2^2 + (R^2 + X^2)P_{inj}^2 \tag{4.7}$$

$$Q_{inj} = \frac{XV_1^2 - \sqrt{X^2 V_1^4 - (R^2 + X^2)\zeta}}{(R^2 + X^2)} \tag{4.8}$$

$$\frac{\partial Q_{inj}}{\partial R} = \frac{\gamma^{\frac{-1}{2}}(R\zeta + (R^2 + X^2)P_{inj}(RP_{inj} - V_1^2)) - 2RQ_{inj}}{R^2 + X^2} \tag{4.9}$$

$$\gamma = X^2 V_1^4 - (R^2 + X^2)\zeta \tag{4.10}$$

It can be easily checked that $\frac{\partial Q_{inj}}{\partial R} < 0$ for $R = 0$ when $P_{inj} > 0$. Setting $\frac{\partial Q_{inj}}{\partial R} = 0$ and rearranging in terms of R gives the quartic equation of (4.3). The largest real positive root of this equation determines the value of R beyond which $\frac{\partial Q_{inj}}{\partial R} > 0$. For part (b) note that $Q_{21} = Q_{loss} - Q_{inj}$ and hence comes the following identity,

$$\frac{\partial Q_{21}}{\partial R} = \frac{\partial Q_{loss}}{\partial R} - \frac{\partial Q_{inj}}{\partial R} \tag{4.11}$$

The reactive loss of the feeder can be expressed as,

$$Q_{loss} = \frac{X(V_2^2 - V_1^2 + 2(RP_{inj} + XQ_{inj}))}{R^2 + X^2} \tag{4.12}$$

$$\frac{\partial Q_{loss}}{\partial R} = \frac{2X(P_{inj} + X\frac{\partial Q_{inj}}{\partial R}) - 2RQ_{loss}}{R^2 + X^2} \tag{4.13}$$

Setting $\frac{\partial Q_{loss}}{\partial R} = 0$ gives the quartic equation of (4.3). Therefore, $R = R_{max}$ is the common root of $\frac{\partial Q_{loss}}{\partial R} = 0$ and $\frac{\partial Q_{inj}}{\partial R} = 0$ and hence the root of $\frac{\partial Q_{21}}{\partial R} = 0$. However, in contrast to $\frac{\partial Q_{inj}}{\partial R}$, $\frac{\partial Q_{21}}{\partial R}\ |_{R=0}$ is not necessarily positive for all $P_{inj} > 0$.

$$\frac{\partial Q_{21}}{\partial R} = \frac{2(XP_{inj} - RQ_{loss}) + (X^2 - R^2)\frac{\partial Q_{inj}}{\partial R}}{R^2 + X^2} \tag{4.14}$$

$$\left.\frac{\partial Q_{21}}{\partial R}\right|_{R=0} = \frac{2P_{inj} + X\frac{\partial Q_{inj}}{\partial R}}{X} \tag{4.15}$$

Setting $\frac{\partial Q_{21}}{\partial R}\ |_{R=0} = 0$ gives $P_{max} = \sqrt{\frac{4V_1^2V_2^2 - V_1^4}{4X^2}}$. For $P_{inj} \leq P_{max}$, $\frac{\partial Q_{21}}{\partial R}|_{R=0} \geq 0$ and changes sign at $R = R_{max}$. For $P_{inj} < 0$, the real roots of (4.3) are negative implying that for all positive values of R Theorem 1 does not hold.

Theorem 2 *For the network of Figure 4.1, where V_2 and Q_{inj} are fixed (hence V_1 is not regulated) and for $P_{inj} > 0$ and $R < R_{max}$ the following relations hold,*

(a) $\frac{\partial V_1}{\partial R} > 0$

(b) $\frac{\partial Q_{21}}{\partial R} < 0$

Where R_{max} is the largest real root of the following equation,

$$Q_{inj}^2R^2 - P_{inj}(2XQ_{inj} + V_2^2)R + X^2P_{inj}^2 = 0 \tag{4.16}$$

Proof:

Equation (4.6) can be rearranged in terms of V_1 as,

$$V_1^4 - (2(RP_{inj} + XQ_{inj}) + V_2^2)V_1^2 + \eta = 0 \tag{4.17}$$

$$\eta = (R^2 + X^2)(P_{inj}^2 + Q_{inj}^2) \tag{4.18}$$

The stable solution corresponds to the largest root of (4.17) and its derivative is given by,

$$\frac{\partial V_1^2}{\partial R} = P_{inj} + \frac{P_{inj}(XQ_{inj} + \frac{V_2^2}{2}) - RQ_{inj}}{\sqrt{(XQ_{inj} + RP_{inj} + \frac{V_2^2}{2})^2 - \eta}} \tag{4.19}$$

Setting $\frac{\partial V_1^2}{\partial R} = 0$ gives quadratic equation of (4.16). It can be checked that $\frac{\partial V_1^2}{\partial R}|_{R=0} > 0$ for $P_{inj} > 0$. For part(b) the derivative of (4.12) is given as,

$$\frac{\partial Q_{loss}}{\partial R} = \frac{2X(P_{inj} - \frac{\partial V_1^2}{\partial R}) - 2RQ_{loss}}{R^2 + X^2} \tag{4.20}$$

It can be checked that $\frac{\partial Q_{loss}}{\partial R} = 0$ gives the quadratic equation of (4.16).

$$\left.\frac{\partial Q_{loss}}{\partial R}\right|_{R=0} = \frac{P_{inj}}{X}(1 + \frac{(XQ_{inj} + \frac{V_2^2}{2})}{\sqrt{(XQ_{inj} + \frac{V_2^2}{2})^2 - X^2(P_{inj}^2 + Q_{inj}^2)}}) \tag{4.21}$$

It can be seen that $\frac{\partial Q_{loss}}{\partial R}\big|_{R=0} < 0$ for all positive P_{inj}. Hence $\frac{\partial Q_{loss}}{\partial R} < 0$ for $P_{inj} > 0$ and $R < R_{max}$. Since $\frac{\partial Q_{inj}}{\partial R} = 0$ in (4.11) part (b) is proved. The assumption of fixed V_2 can be relaxed in both theorems by replacing V_2 and X by V_∞ and $X' = X + X_T$ respectively. Notice that node 3 is disconnected throughout this analysis and the network is radial. For theorem 1 part(b), $\frac{\partial Q_{loss_X}}{\partial R}$ is a fraction of $\frac{\partial Q_{loss_{X'}}}{\partial R}$ and hence since $\frac{\partial Q_{\infty 2}}{\partial R} = \frac{\partial Q_{loss_{X'}}}{\partial R} - \frac{\partial Q_{inj}}{\partial R}$ is positive, $\frac{\partial Q_{21}}{\partial R} > 0$. For Theorem 2 part(b), $\frac{\partial Q_{loss_X}}{\partial R} < 0$ and hence $\frac{\partial Q_{21}}{\partial R} < 0$. Finally there is an interesting feature of the network that relates the quartic equation of (4.3) in Theorem 1 to the quadratic equation of (4.16) in Theorem 2. Both these equations correspond to the case of $P_{loss} = P_{inj}$. Hence at $R = R_{max}$, all the power injected into the resistive feeder is dissipated and $P_{21} = 0$. This shows that the stipulated relations in both theorems hold under reasonable operation conditions.

4.3 The Implications for Structural Stability

Before considering the implications of the two theorems for the structural stability of the 4-bus network, it is important to distinguish between two typical configurations of connection of lower-voltage sub-transmission/distribution networks to higher voltage sub-transmission/transmission systems. As noted earlier the OLTC mechanism effectively decouples the voltages of the two networks through tap-changing mechanism while the transformer is energized. A detailed discussion of the OLTCs in relation to variable generation in resistive networks is presented in Chapter 5. OLTCs are indispensable where there are sensitive (customer) nodes in the lower voltage network whose voltage profile should be maintained under all loading conditions. However, it is not uncommon to see fixed tap transformers at distribution levels. The fixed tap transformer has an off-load tap changer that can be manually adjusted only when the transformer is de-energized. These transform-

ers are significantly less costly, more reliable and have a simpler maintenance [7, 10]. This section contrasts the case of (OLTC) variable tap with the case of fixed tap in the context of power system structural stability. The transformer impedance in both cases is lumped into X, the inductance of the distribution feeder in Figure 4.3. Hence, there is an ideal transformer between the low and high voltage sides of Bus 2 that is shown as part of the distribution feeder in Figure 4.3.

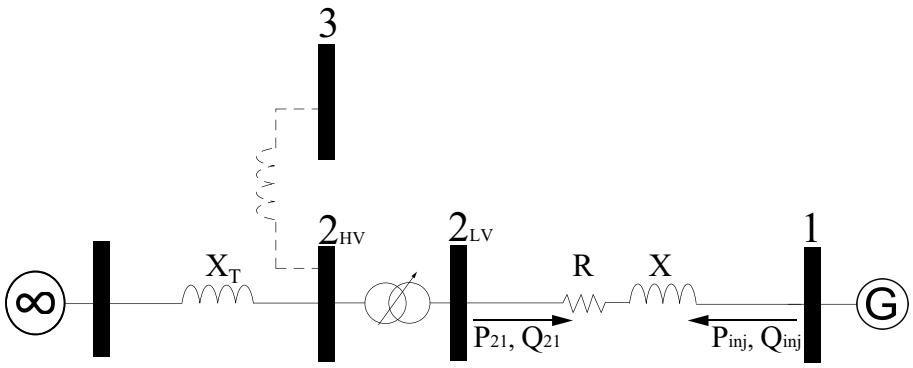

Figure 4.3: A generic power system with the lower voltage distribution network connected to the higher-voltage network through an OLTC transformer.

4.3.1 Variable Tap

Figure 4.4 shows the parameter space of P_{21} and Q_{21}, the active and reactive flows into the distribution network modeled as loads at Bus 2. The distribution side of Bus 2 is regulated to 1.00 p.u. and therefore transmission voltage variations does not affect the distribution network. This decomposes the network of Figure 4.3 into a three-bus transmission system and a two-bus distribution network. For the moment let us focus on the transmission system. The feasibility boundary (bifurcation manifold) is demarcated by the solid black curve. The line tangent to the curve at $P_{21} = 0$ and its normal vector are almost parallel to the X-axis and Y-axis respectively. Therefore, in the vicinity of line $P_{21} = 0$ the voltage stability margin is more sensitive to changes of the operating point along the Y-axis than the X-axis. This is due to the much stronger coupling between reactive power and voltage magnitudes at the transmission level. Now consider the distribution network Bus 1 has unlimited reactive capability and hence $V_1 = 1.00$ under all operating conditions. According to Theorem 1, as the network becomes more resistive, the reactive requirement of the distribution network, Q_{21}, increases. To illustrate the impact of network resistivity, three contours each corresponding to a value of $\frac{R}{X}$ with X constant at $0.50p.u.$ is obtained

by freeing P_{inj} and superimposed onto the parameter space of P_{21} and Q_{21}. Each contour is highlighted with a different color in the order shown (green, blue and red). Each thin black contour maps a fixed value of P_{inj} to values of $\frac{R}{X}$ that varies from 0 to 2. Notice that here the reactive capability is unlimited. To better illustrate the change in distance to bifurcation manifold and observe the trajectory of the operating points as, later, the reactive (voltage control) capability of wind injection node is restricted, the points corresponding to $P_{inj} = 0.60$ p.u are highlighted for each value of $\frac{R}{X}$. These points are shown as either solid or hollow circles depending on whether they are inside or outside the feasibility boundary of the reduced system.

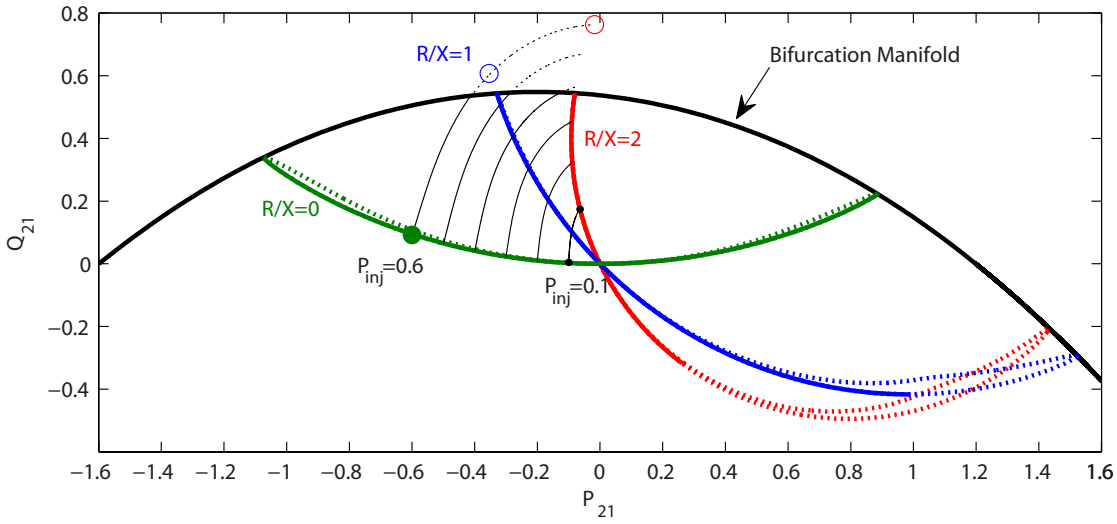

Figure 4.4: Variable tap (OLTC) case: Full voltage control

4.3.1.1 Increasing Resistivity Under Full Voltage Control

Increasing R has a two-fold impact. It increases, Q_{21}, as anticipated by Theorem 1, moving the operating point sharply toward the bifurcation manifold. It also increases P_{loss} and hence reduces the net active power injection into the transmission network at Bus 2, moving the operating point away from the bifurcation manifold along the X-axis. However the impact of the increase in Q_{21} dominates and the distance to bifurcation manifold is significantly reduced. Notice the hollow circles in Figure 4.4 corresponding to infeasible operating points at $\frac{R}{X} = 1, 2$. These operating points are perfectly feasible for the radial resistive network considered in isolation but once (P_{21}, Q_{21}) is modeled as load for the reduced system by eliminating the resistive feeder they are no longer feasible. Notice that the amount of active power that can be safely injected decreases significantly as R increases. As discussed later in the case of fixed tap, this is due to the fact that V_2, the voltage

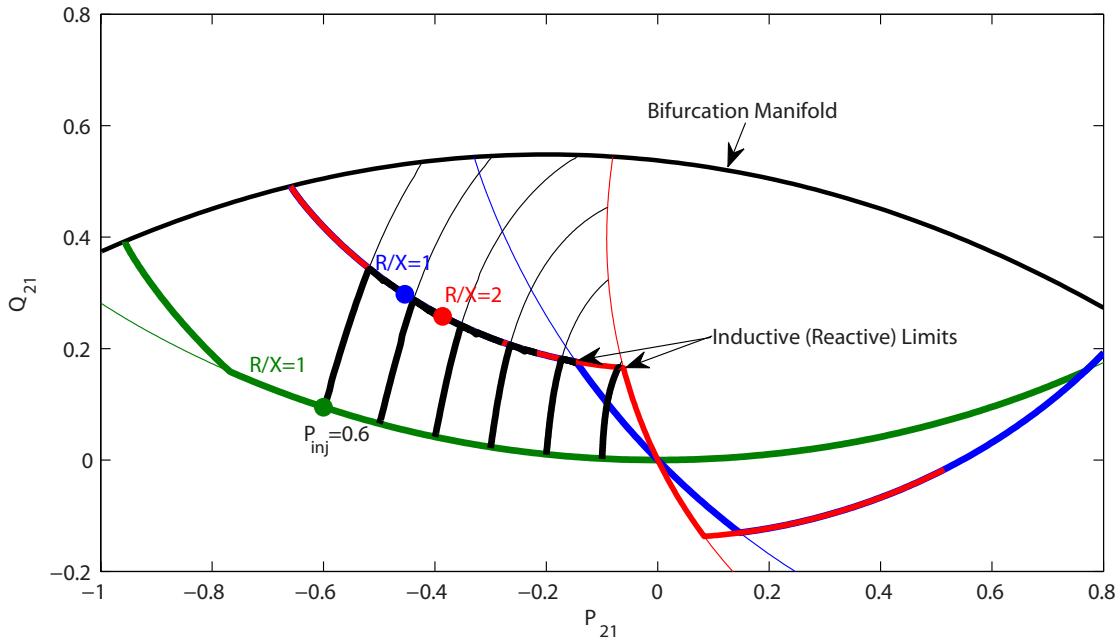

(a) Variable tap (OLTC) case: Limited voltage control

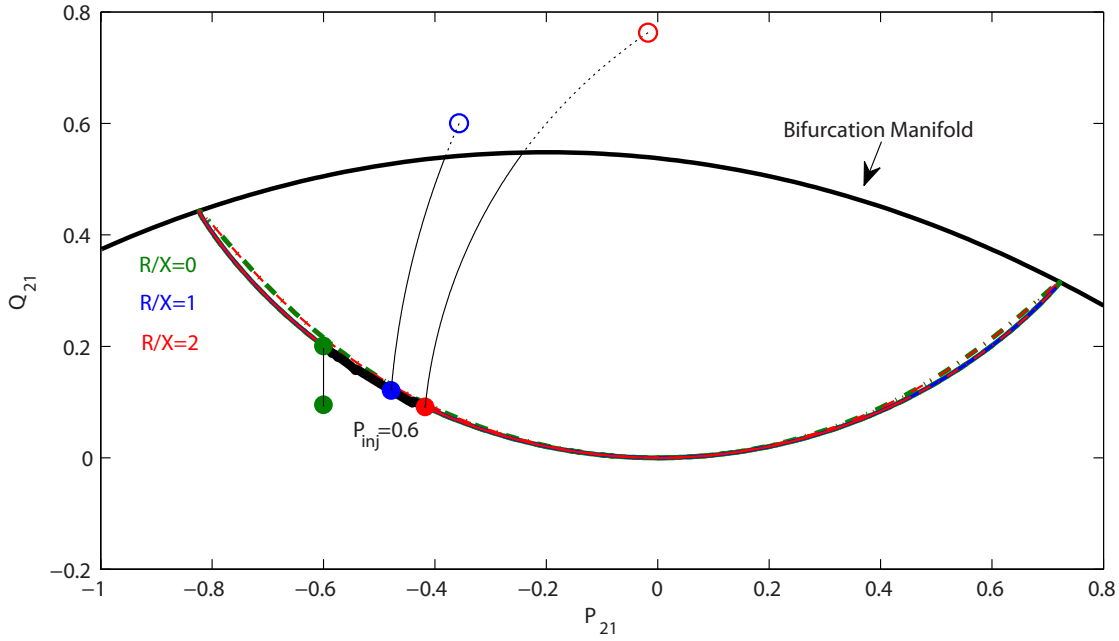

(b) Variable tap (OLTC) case: Unity p.f.

Figure 4.5: Transformation of Figure 4.4 as voltage control capability is restricted (a) until no voltage control at unity p.f. (b). Thin black lines in (b) show the movement of the previously infeasible operating points under full voltage control inside the feasibility region.

magnitude of Bus 2 (the distribution side), is regulated by OLTC.

4.3.1.2 Increasing Resistivity Under Limited Voltage Control

According to Theorem 1-(a), as resistivity increases, the reactive compensation at Bus 1, Q_{inj}, initially capacitive at small R, becomes increasingly more inductive. Figures 4.5(a) and 4.5(b) show the structural changes that occur as a result of enforcing reactive limit for Bus 1. The thicker black contours in Figure 4.5(a) corresponds to the limited reactive compensation contrasted with the full voltage regulation in Figure 4.4 (thin black lines in the background). Note that as long as voltage is regulated these contours overlap with the contours of the Figure 4.4. However when inductive limits are encountered, Q_{21} decreases as R increases, pushing the operating points away from the boundary. This transition from voltage regulation to fixed reactive compensation is shown at its extreme case of unity p.f. (no voltage regulation) in Figure 4.5(b) for the case of $P_{inj} = 0.60 p.u.$. Note that, here, the three contours of Figure 4.4 (in green red and blue colors) completely overlap. This can be explained by the fact that under unity p.f., i.e. when $Q_{inj} = 0$, as P_{inj} and R are freed the Q_{21} and P_{21} stay on the same algebraic curve whereas under full voltage control due to the coupling between P_{inj} and Q_{inj} as R and P_{inj} are freed Q_{21} and P_{21} admit values on a two-dimensional surface.

As the voltage control is restricted for the cases of $\frac{R}{X} = 1$ (blue) and $\frac{R}{X} = 2$ (red), the operating points move inside the boundary and at no voltage control as the network becomes more resistive the distance to bifurcation boundary increases (moving from the green dot to blue and then red dots). This is anticipated by Theorem 2-(b), which states that for fixed reactive compensation at Bus 1, as the network becomes more resistive, the reactive requirement of the distribution network, Q_{21}, decreases.

4.3.1.3 Impact of Reactive Capability of Wind Interconnection

Note that the bifurcation manifold is obtained based on the parameters of the transmission system and is particularly sensitive to changes in reactive load and voltages at other transmission nodes such as Bus 3. Thus, secure operation of the system requires a sufficiently large margin for reactive import into the distribution feeder (at Bus 2) from the transmission system. As seen in Figure 4.5(b), for *sufficiently resistive* distribution networks, restricting the reactive capability of Bus 1 moves the operating points away from this manifold and enhances the stability margin. As the size of reactive compensation at Bus 1 is reduced, larger amounts of active power can be injected into the distributed network and P_{loss} decreases considerably. This however, causes the resistive network voltage, V_1, to rise and as shown later, in the context of DTE/ITC system, could lead to severe overvoltages.

4.3.2 Fixed Tap

Figure 4.6 is similar to Figure 4.4 but corresponds to the case of fixed tap where the voltage of the distribution side of Bus 2 follows the voltage variations of the transmission system.

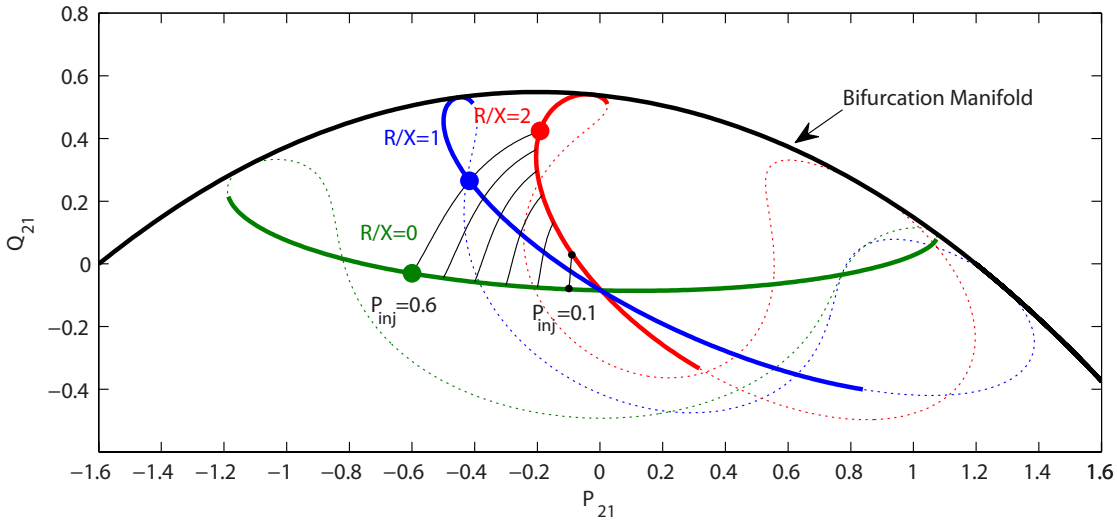

Figure 4.6: Fixed-tap case: Full voltage control

4.3.2.1 Increased Resistivity Under Full Voltage Control

Here, the fixed P_{inj} contours (in black), in contrast to the variable tap case, are squeezed inside the feasible region as R increases. This is due to the declining transmission voltages in response to the increasing reactive requirement of the distribution network as resistivity increases. Under fixed tap, a reduction in transmission voltages directly translate to suppression of distribution voltages which in turn mitigates the increase in reactive requirement. In fact, it can be demonstrated analytically that when Bus 1 is a reactive sink (i.e. $Q_{inj} < 0$), $\frac{\partial Q_{21}}{\partial V_2} > 0$. Hence there is an stabilizing effect, under fixed tap, which curbs the excessive reactive requirement of the network. This allows higher levels of active power to be securely injected at now stable operating points which would have been otherwise unstable under variable tap (OLTC) case. A more subtle difference between fixed and variable tap cases is the higher resistive loss of the latter. This is due to the fact that V_2 and hence the reactive flow through the resistive network are higher under variable tap whereas under fixed tap V_2 tends to drop as active power injection into the distribution feeder increases. This significantly restricts the flow of reactive power into the feeder and reduces the losses. In Chapter 5, it is shown analytically for a radial resistive network with embedded generation that active power loss is minimized when the flow of reactive power into the resistive

network is zero.

4.3.2.2 Increasing Resistivity Under Limited Voltage Control

Figures 4.7(a) and 4.7(b) show the structural changes that occur as a result of enforcing reactive limit for Bus 1. Similar to the case of variable tap and as anticipated by the theorems, as the resistivity increases the distance to the bifurcation manifold increases or decreases based on the voltage control mode.

4.3.2.3 Impact of Reactive Capability of Variable Generation Interconnection

Restricting the reactive capability of Bus 1, in the case of fixed tap, does enhance the stability margin and reduce P_{loss} for *sufficiently resistive* networks. However this restriction is not as critical to the stable operation of the system as it is for the variable tap (OLTC) case. Even the reduction in P_{loss} is not as significant as in the OLTC case. These differences between the fixed tap and OLTC cases are all due to the reduced reactive requirement of the resistive network when the distribution side voltage of Bus 2 is not held fixed. It is worth mentioning that the effect of OLTC on reducing the stability margin and increasing losses is highly dependent on its voltage setpoint (i.e. the distribution side of Bus 2) and that of the embedded generation node. As the OLTC setpoint is lowered the results of variable tap case approximate those of the fixed tap case. This is due to the fact that at lower OLTC voltage setpoints, the reactive requirement of the resistive network is curbed and hence the distance to the bifurcation boundary increases. Similarly increasing the setpoint of Bus 1, reduces the reactive requirement of the resistive network. In practice, however, in a large sub-transmission/distribution network there is little flexibility in controlling the OLTC setpoints which are chosen to keep the lowest voltage in the network above the lower voltage limit for all loading conditions [7, 67]. There are similar operational considerations, such as severe overvoltages, that limit the extent to which the wind injection node setpoints can be increased.

4.3.3 Asymmetry in Power Transfer Margin

Within the feasibility boundary of the transmission network (where P_{21} and Q_{21} are considered as loads), there are other bifurcations where the solid and dotted branches of the curves corresponding to each value of $\frac{R}{X}$ meet (much more noticeable in Figure 4.6 than in Figure 4.4). These bifurcations pertain to the 5 bus network of Figure 4.3 that models the distribution network and are caused by the resistive part of the system, i.e. the distribution

network, reaching its maximum power transfer capability as P_{inj} varies. This is an interesting example that when a more detailed model of a given power system is examined there might be voltage instabilities that otherwise are not considered in the reduced model (in this specific case when the distribution network is reduced to the transmission load, $P_{21} + jQ_{21}$ at Bus 2). As mentioned previously, network resistivity introduces asymmetry in power transfer margin between active power generation and consumption, expanding the transfer capability of power generation. For example in the fixed-tap case and under full voltage control as active power absorption at Bus 1 increases, the distribution network in Figure 4.3 reaches bifurcation at approximately $P_{inj} = -0.50 p.u.$ ($\frac{R}{X} = 1$) and $P_{inj} = -0.10 p.u.$ ($\frac{R}{X} = 2$). For active power injection into the distribution network, bifurcation occurs at approximately $P_{inj} = 1.00 p.u.$ ($\frac{R}{X} = 1$) and $P_{inj} = 1.30 p.u.$ ($\frac{R}{X} = 2$) . These bifurcation points would not be ever reached through increasing P_{inj}, without first violating thermal limits of the resistive feeder. The reason is that sub-transmission/distribution line capacities are often planned based on load profiles. Hence, in the case of active power injection these bifurcations are of no practical relevance. Thus here the focus has been on changes in the lower voltage network that impact the voltage stability of the reduced (i.e. transmission) system, through changes in P_{21} and Q_{21}.

4.4 The Concept of Critical Resistance

As already noted in Figures 4.5(a) and 4.7(a) and later Figures 4.5(b) and 4.7(b), restricting voltage control capability of the embedded generation node pushes the operating points away from the bifurcation manifold when the feeder is resistive (i.e.$\frac{R}{X} = 1, 2$). This is the opposite when the feeder is not resistive ($\frac{R}{X} = 0$) and the voltage stability margin is reduced by restricting the voltage control capability. As the feeder becomes resistive, the system undergoes a qualitative change with regard to the impact of reactive compensation on the voltage stability margin. The value of R at which this reversal occurs is designated as *critical*. This critical value is characterized by $Q_{inj} = 0$ and depends on P_{inj}. For $R > R_{cr}$ voltage control requires an inductive mode of reactive compensation, i.e. $Q_{inj} < 0$, whereas for $R < R_{cr}$ the reactive compensation is in a capacitive mode, i.e. $Q_{inj} > 0$.

Theorem 3 *For the network of Figure 4.3, where both V_1 and V_2 are fixed, the critical*

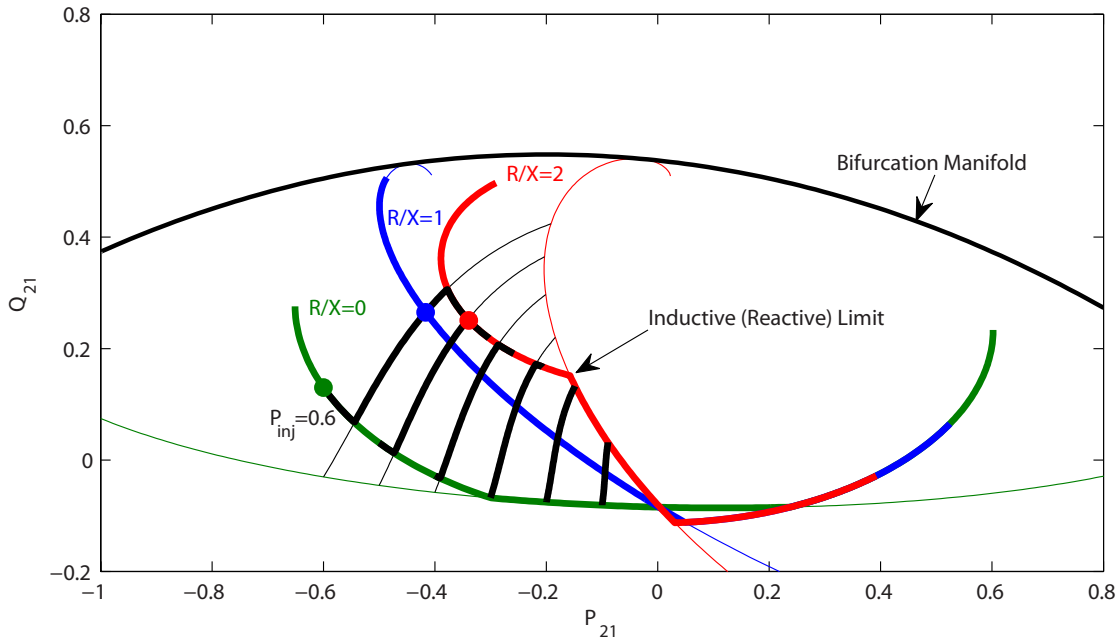

(a) Fixed-tap case: Limited voltage control

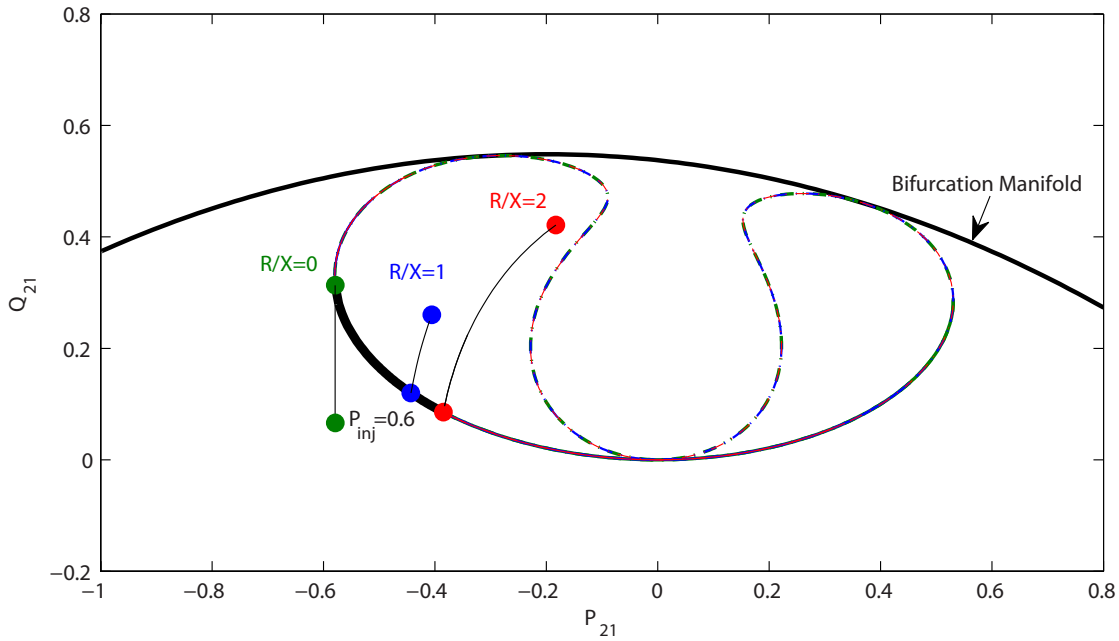

(b) Fixed-tap case: Unity p.f.

Figure 4.7: Transformation of Figure 4.6 as voltage control capability is restricted (a) until no voltage control at unity p.f. (b). Thin black lines in (b) show the movement of the operating points inside the feasibility region as the reactive (voltage control) capability is restricted .

resistance is given by,

$$R_{cr} = \max\{0, \frac{V_1^2 - \sqrt{V_1^2 V_2^2 - X^2 P_{inj}^2}}{P_{inj}}\} \tag{4.22}$$

Proof:
At R_{cr} by definition V_1 is regulated to its setpoint with no reactive compensation (i.e. unity p.f.). By setting $Q_{inj} = 0$ in (4.17) and rearranging in terms of R the following expression is obtained,

$$P_{inj}^2 R^2 - 2P_{inj}V_1^2 R + V_1^4 - V_1^2 V_2^2 + X^2 P_{inj}^2 = 0 \tag{4.23}$$

Eq. (4.23) has the following two roots $\frac{V_1^2 \pm \sqrt{V_1^2 V_2^2 - X^2 P_{inj}^2}}{P_{inj}}$. It can be checked that the root corresponding to Q_{inj} changing sign from positive to negative as R increases is given by $\frac{V_1^2 - \sqrt{V_1^2 V_2^2 - X^2 P_{inj}^2}}{P_{inj}}$.

For the network of Figure 4.1, when $V_1 = V_2 = 1.00p.u.$, $X = 0.50p.u.$ and $P_{inj} = 0.60p.u.$, R_{cr} is obtained as $0.08p.u.$ Figure 4.8 shows the $Q - V$ curves at Bus 3 (load), where $X_{23} = 0.2p.u.$, for $R = 0.02p.u. < R_{cr}$ (in green) and for $R = 0.20p.u. > R_{cr}$ (in red). Restricting the reactive capability of Bus 1, as anticipated by Theorem 3, increases the reactive margin of Bus 3 and hence enhances the stability margin for $R > R_{cr}$. This is the opposite for $R < R_{cr}$. Theorem 3 provides some insight on how embedded generation in resistive network impacts the voltage stability margin of the system. Note that R_{cr} increases as V_1 increases and V_2 decreases. This allows the network operator to increase R_{cr} toward the actual resistance of the feeder by adjusting setpoint parameters in order to mitigate the impact of active power injection on the voltage stability margin. This is in line with the discussion of the OLTC and the voltage setpoint of the POI in Section 4.3.1.

4.5 Sub-transmission Wind Injection: DTE/ITC System Case

Figure 4.9 shows a section of the DTE/ITC system with a meshed 42kV sub-transmission network (with line $\frac{R}{X}$ ratios ≈ 1). WG_1 and WG_2 wind farms, highlighted in blue, each with a rated capacity of 50MW are connected at the sub-transmission level. At the interconnection points of the transmission and sub-transmission networks, the lower voltage (42kV) side is regulated by five OLTC transformers highlighted by red ellipses. Typically sub-transmission utilities require the voltage at the point of wind interconnection to be strictly regulated instead of the once more common fixed power factor mode. This is mainly to minimize the impact of wind variability on the voltage profile of the distribution network (in this case 13.2kV) which is not shown in Figure 4.9. Figure 4.10 shows the Q-

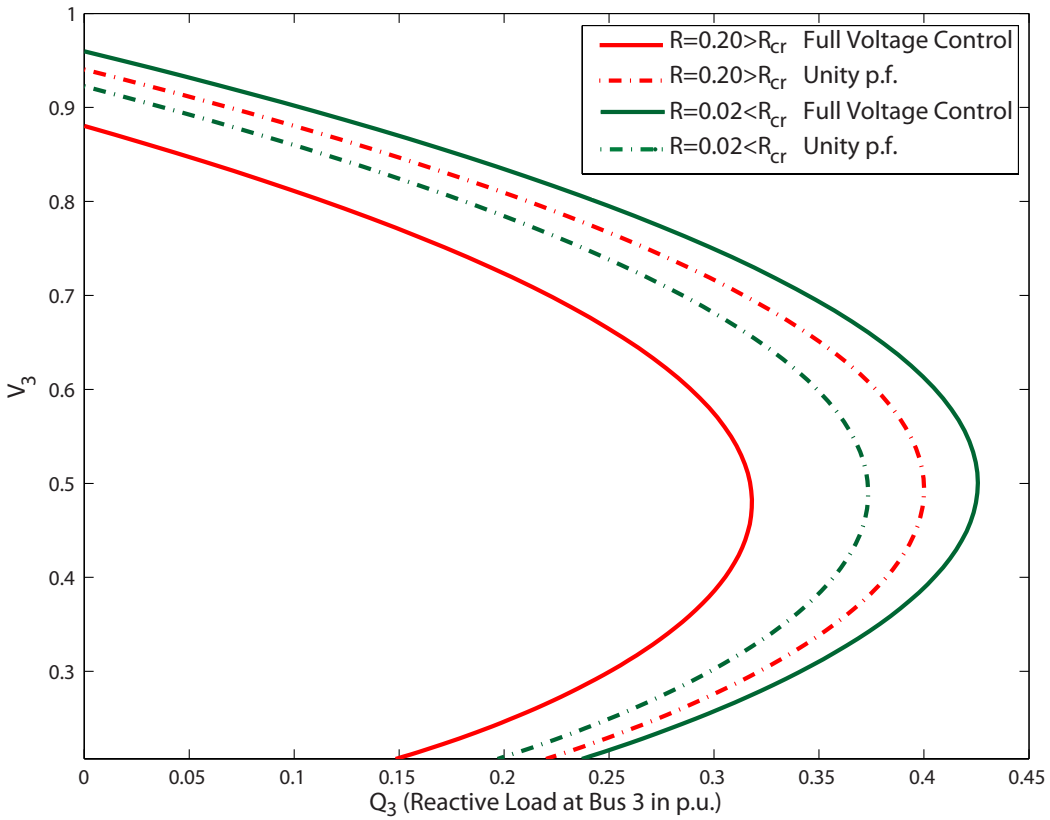

Figure 4.8: Q-V curves at Bus 3

V curves of a transmission bus that is highlighted with a variable reactor for the following four configurations of voltage control at WG_1 and WG_2 wind farms:

1. Unity p.f. ($Q_{inj} = 0$) (in black)
2. ± 10MVAr (in green)
3. ± 25MVAr (in blue)
4. Full Voltage Control (in red)

In line with the previously presented analysis, the case of unity p.f. results in the largest voltage stability margin as the reactive import from the 120kV transmission system is minimal. However this mode results in severe overvoltages (in the range of 1.15-1.25p.u.) at WG_1, WG_2 and their adjacent buses. Moreover, the case of no compensation is often not permitted as voltage fluctuations caused by wind variability place enormous stress on voltage regulating equipment in distribution substations. As the reactive capability of the wind nodes increases in response to the needs of the distribution substations, the voltage stability

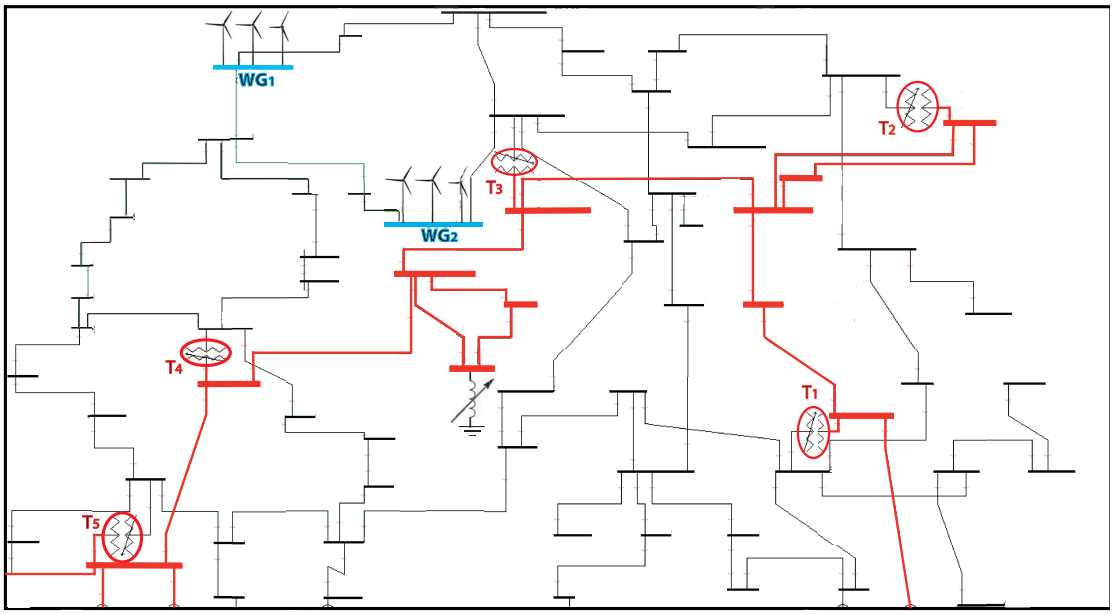

Figure 4.9: Wind development network: wind injection nodes (blue), the 120 kV transmission system and the 120/42 kV tap-changing transformers (red), the 42 kV sub-transmission network (black)

margin shrinks. However, the case of ± 25MVAr does not quite follow this pattern. Note that based on the Q-V criteria there is no difference between this case and the full voltage control in terms of impact on the voltage stability (bifurcation points overlap). This can be explained by the OLTC tap limits. Note that in the blue curve (± 25MVAr) there are two visually distinct discontinuities marked by $\circ$ symbol. As the fictitious reactive load increases, the 120kV voltages drop sending the OLTC taps toward their upper limits (first discontinuity). Once at their limits, the OLTC transformers become fixed tap and stop regulating the 42kV side voltages. With sub-transmission voltages decreasing, the voltage rise issue fades away and the reactive compensators at wind injection nodes come off their inductive limits (second discontinuity). The release of reactive limits explains why the solid blue curve overlaps with the red curve following the second discontinuity. In order to illuminate the role of OLTC limits, the Q-V curve corresponding to increased OLTC upper limits (effectively limitless) is shown for the last two configurations (dashed blue and red lines). The bifurcation points are reached at much lower reactive loads reducing significantly the voltage stability margins. Also, it is seen that, now, full voltage control has a lower margin compared to limited voltage control (± 25MVAr). Hence the OLTC limits are helpful in that they prevent an early voltage collapse as reactive loads on the transmission system increase.

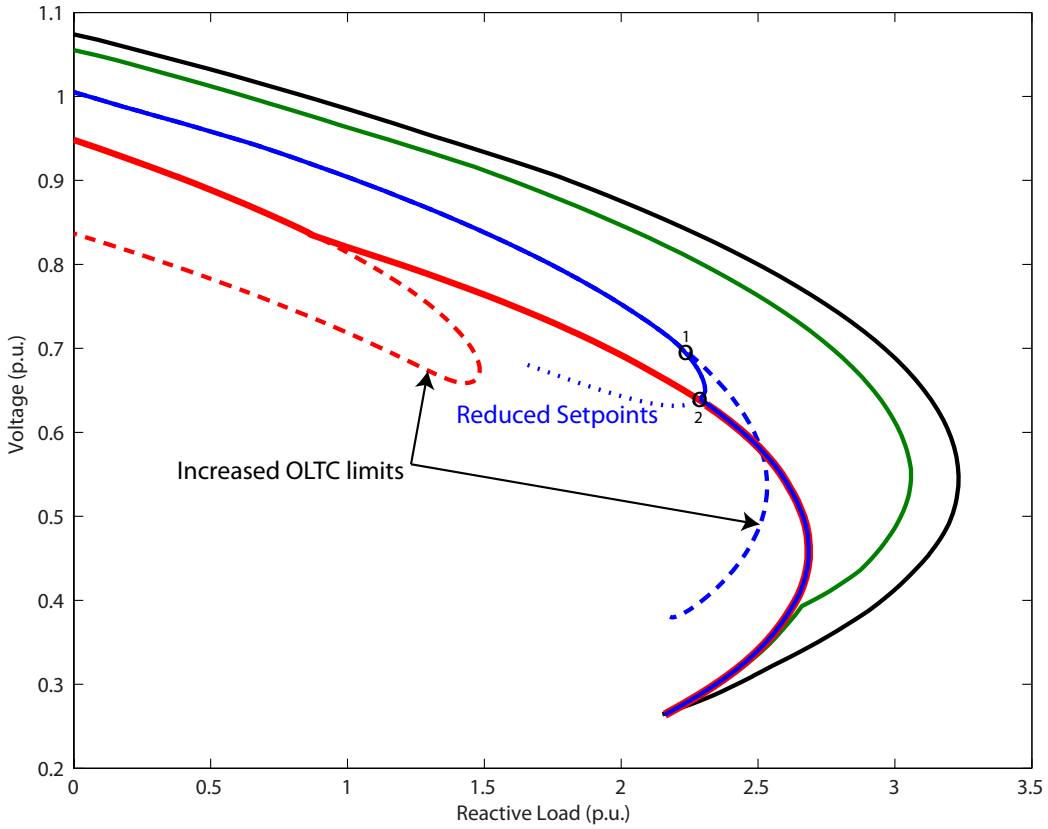

Figure 4.10: Q-V curves of a transmission bus that is highlighted in Figure 4.9 with a variable reactor

The voltage setpoints of wind injection nodes are even more critical in the voltage stability of the DTE/ITC system. Notice the dotted blue curve that corresponds to voltage setpoints of WG_1 and WG_2 reduced from 1.00 p.u. to 0.95 p.u. This curve overlaps with the solid blue curve up to $Q \approx 2.3$ which marks the second discontinuity related to inductive limits of reactive compensators at WG_1 and WG_2 which are located very close to one another appearing as virtually a single discontinuity in the Figure 4.10. This overlap is due to the fact that these curves are obtained under high wind generation output where the reactive compensators at the POIs are initially at their limits. For the solid blue curves corresponding to 1.00 p.u. setpoints, the reactive compensators come off the limit at the second discontinuity whereas for the dotted curve corresponding to setpoints of 0.95 p.u. saddle-node bifurcation is reached when reactive compensators are still at their inductive limits. This occurs even though the OLTC are effectively fixed tap and the 42kV voltages are declining and underlines the significance of voltage setpoint coordination between various regulating devices in resistive networks with large levels of wind and solar power penetration and limited active power consumption.

In this chapter it was demonstrated that wind power integration into resistive networks can negatively impact the structural stability of the system. It was proven analytically (in Theorem 1) that the reactive requirement of the lower voltage network increases, under active voltage regulation of the embedded generation node(s), as network resistivity increases. The reverse with regard to the reactive requirement of the resistive network was proven (in Theorem 2) for the case of fixed reactive compensation (no voltage regulation) at the embedded generation node(s). The implications of these analytical findings were explored on a generic transmission system to which a resistive branch is connected that models sub-transmission/distribution network. Finally, a real power system with sub-transmission wind injection was examined to verify the findings. It was noted that the impact on voltage stability is exacerbated by strict voltage control schemes that often require large reactive power absorbtion at the injection node(s). Voltage stability margin improves with restriction of the reactive capability of injection nodes. The crucial role of reactive limits, especially for OLTC transformers, in enhancing the structural stability of the power system was also highlighted. This is in sharp contrast to the transmission level where there is an established conception that reactive resources reaching their limits is a major contributor to voltage instability [68]. This conception is based on a large number of studies in 1990s that were inspired by major blackouts. These studies pinpoint insufficient reactive capabilities as the most common underlying cause of voltage collapse [69]. Here a new paradigm is explored that emerges from integration of significant generation capacities into resistive networks that traditionally have only served loads at high power factors. The coordination of voltage regulating devices in resistive networks from the structural stability perspective is an interesting area that can be the basis of future studies. This is however a complicated task as the more immediate daily operational aspects of sub-transmission wind injection including voltage rise, line losses, and the impact of generation variability on voltage regulating devices overshadows stability concerns when it comes to voltage setpoint coordination. These topics will be discussed in the following chapter.

CHAPTER 5

Voltage Control Schemes for Minimizing OLTC Operations and Network Loss

5.1 Introduction

Traditionally, voltage control schemes in sub-transmission and distribution networks are structured around transformers equipped with an on-load tap-changer (OLTC) sometimes assisted by mechanically-switched capacitor banks. These devices have managed to keep the voltage magnitudes within their acceptable limits as the flow of active power varies with loading conditions. At low penetration levels the impact of variability in wind and PV generation is hardly felt in the presence of comparable or even larger load variations. However as the size of variable generation grows in respect to local feeder demand, the varying bidirectional flow of active power in the feeders interferes with the operation of the OLTC transformers, the key voltage regulators in distribution and sub-transmission networks. For example, excessive tap changes have been recently observed in the San Diego Gas & Electric (SDG&E) service territory in distribution feeder transformers serving affluent neighborhoods along the coast. In this case, the culprit is the concentration of roof-top PV arrays in combination with daily coastal fog patterns and atypically low midday load due to mild temperatures. The SDG&E is seeking the enhancement of PV-inverter functionality with "Volt/VAr control" as a solution [70].

The OLTCs play the following key roles:

- Adjust the voltage profile of the lower voltage network as loading conditions vary.
- Buffer the lower voltage network against disturbances at the higher voltage network.
- Control the flow of reactive power especially in meshed sub-transmission networks.

Beside certain operational disadvantages such as sub-optimality of flux density and variability of transformer impedance, the indispensable contribution of OLTC also comes

at an increase in transformer cost and complexity and a reduction in network reliability [7]. According to an international survey on the failure of power transformers involving 7000 units (between 1968-1978) with maximum age of 20 years, OLTC failures accounted for 41% of substation transformer failures. 70% of these failures led to the forced outage of the transformer [10]. It should be noted that the yearly failure rates (i.e. the number of failed units to the number of units in service at any given year) were around 1-2%, which is quite low.

OLTC failures are primarily mechanical followed by electrical faults. Mechanical failures are related to springs, bearings, shafts, and drive mechanisms. Electrical faults are due to wear in contacts, insulation problems and burning of transition impedances [11]. In either case, the failure probability is directly linked to the frequency and range of tap-changing operations. The periodic maintenance of conventional oil-type OLTC is based on the time in service since last maintenance or the number of operations, whichever comes first [8]. The recently developed vacuum-type OLTC has replaced oil as an arc-quenching medium and the contact wear is reduced. However this innovation does not address the mechanical failures. The number of operations, in this more advanced type, is the sole indicator for the periodic maintenance and the life-time of the tap-changer. Based on the claims of two prominent manufacturers the vacuum-type OLTC has a lifespan of 300,000 to 1 million operations [8, 9]. Typically transmission and sub-transmission OLTCs have a lower frequency of operation than distribution OLTCs. Under current operating conditions (i.e. without high penetration of variable generation) OLTC daily operations are in the range of 20-140 [9] with transmission OLTCs typically changing tap position less frequently than sub-transmission and distribution OLTCs. This range of operation translates to a 10-120 year lifespan. This longevity combined with historically low rates of OLTC failures explains the general attitude of complacency among power utilities toward the management of these critical assets even as the penetration of wind and solar PV increases.

Nonetheless, in the past two decades a number of studies have explored the so-called off-line control of OLTCs and/or mechanically-switched capacitor banks (MSCs) in which the tap position and other switches are dispatched hourly typically a day in advance with the main goal of reducing network losses and maintaining the voltage profile within its allowable range as loading conditions vary [71, 72, 73, 74, 75]. Relying on load forecast, the day-ahead schedule of these electro-mechanical devices is obtained through dynamic programming [71, 72] or faster though less accurate heuristic methods [73, 74, 75] with a daily budget of switching operations as a constraint. A similar dynamic programming-based approach has been extended to voltage coordination of dispatchable and non-dispatchable DGs with OLTCs and capacitor banks. However there has been no treatment of generation

variability and its impact on OLTC operations and it is concluded that "DG can alleviate the impact of load demand variations on the grid" [76]. A somewhat similar approach is proposed for a coordinated voltage control of PV generation and an upstream OLTC with a key difference that in contrast to previous studies, the OLTC tap is programmed a day ahead based on hourly load and irradiance forecast, but *indirectly* through adjustment of voltage reference setpoints of OLTC and PV inverter the optimal value of which are obtained by interior point techniques [77]. The objective is to minimize tap changes and prevent OLTC from encountering its limits. However day-ahead irradiance forecasting would be quite inaccurate in terms of capturing variability due to clouds which is vitally important.

These methods are inappropriate for the coordination of voltage control devices in the presence of large-scale or concentrated variable generation for three reasons. First, variable generation at high penetration levels imprints distinctly different statistical characteristics in flow patterns than load variation does and can trigger switching on the scale of a minute. At such frequency of variation, finding the optimal schedule of tap positions even for an hour ahead through dynamic programming and other search methods would be impractical. What further complicates the issue especially in meshed networks with multiple OLTCs is the infamous "curse of dimensionality" which plagues similar recursive methods with backward induction as the number of states, in this case switching devices, increases [78].

Second, programming of OLTCs in advance requires disabling the Automatic Voltage Control (AVC) relays of the closed-loop feedback control. It is not uncommon at the transmission level for operators to control taps manually through remote control which requires disabling the AVC at least temporarily. However upon inquiry of industry practices on the control of OLTCs the author found that off-line programming of tap positions where the tap position is scheduled in advance, in contrast to real-time feedback control of OLTCs, is quite rare. In the few cases where such off-line schemes do exist, they are limited to LV transformers directly feeding certain industrial plants or at the customer end. These downstream OLTCs are unlikely to interfere with the voltage regulation of the upstream network. This rarity is noticed previously and is explained in terms of load forecast errors that make such dispatches unreliable and it is suggested that only MSCs be dispatched in an off-line fashion [75]. However the more fundamental issue is posed from a *robust control* perspective. If there are uncertainties in the network parameters or significant error in forecast such off-line schemes can lead to an unacceptable voltage profile in the network. This is especially pertinent to the case of stochastic power production which introduces significant uncertainty in the system. In the absence of a feedback control, small errors in the programming of high and medium-voltage OLTCs, especially in meshed (sub-transmission) configurations, may propagate throughout the network leading to unacceptable voltages

or shifting the tapping burden onto far more numerous downstream OLTCs that still have real-time feedback control.

Third, with the advent of power electronic devices such as STATCOM, the traditional role of MSCs in voltage control is undergoing a fundamental transformation. In modern configurations, capacitor banks are mainly used to shift the dynamic reactive support (i.e. STATCOM) band into a desirable region within which it can instantaneously adjust its reactive output in response to fast disturbances in the system (including those caused by variable generation) [79, 80]. In the legacy voltage control schemes where MSCs are still being utilized, the switching is either done manually and thus infrequently by the network operator or in an automated fashion with much longer time constants than those typical of OLTCs [81]. Moreover, the MSC switching-related failures, in contrast to OLTCs, are unlikely to disrupt power delivery. Hence despite the fact that MSCs are cheaper than STATCOMs and are still widely used, especially within the wind farm, there is little justification for including them and their switching frequency into a grid-level optimally coordinated voltage control scheme accommodating variable generation. In contrast to MSCs, there is no prospect, at least in the near future, for a similar economically viable power electronics based alternative for OLTCs. The closest scheme is the concept of electronic (thyristor-commutated) tap changing which has only found application in low-voltage transformers. There are a number of electronic OLTC designs for LV networks proposed in recent years, the viability of which have yet to be determined by industry [82, 83, 84, 85].

Controlling deadband has also been suggested for reducing tap operations due to load variations in the context of "multiple line drop compensation" schemes [86]. Although the closed-loop feedback control is active, the conflicting goals and the reported trade-off in voltage regulation performance will only be exacerbated in the presence of variable generation. Another coordinated control scheme exploits "slight deviation of the reference voltage from the desired value" to prevent unnecessary tap operations caused by capacitor switching transients [75]. The idea of active control of OLTC's voltage reference setpoint is also explored in the context of voltage rise caused by DG penetration and a number of simple coordinated control schemes are field-tested in distribution networks in Europe [87, 88]. However, the impact on the frequency of OLTC operations is either not considered [87] or has received only tangential treatment in the discussion of simulation results for a number of simple control modes [88].

The voltage reference setpoint is the most critical parameter in the closed loop control of OLTC in the sense that the voltage deviation is measured with respect to this setpoint. Therefore a control scheme that relies on frequent adjustment of the voltage setpoint value is potentially problematic as it may cause excessive tap operations. Due to the high sensi-

tivity of tap positions to AVC relay parameters such as deadband [7, 12], these parameter are not good candidates for incorporation into a fast-responding control scheme. The common parallel configuration of multiple OLTC transformers further complicates such control schemes as the AVC setpoint of parallel OLTCs need to be carefully tuned and coordinated [12]. In previously mentioned studies, the adjustments of these setpoints are done only periodically (say hourly) which would reduce the effectiveness of the control scheme to cope with rapid generation variability. On the other hand if the set-point is frequently adjusted, the question is posed as to what extent the OLTC fulfills its main task of regulating voltage. In the limit, the set-point could be changed so frequently that no tap change ever occurred. A centrally coordinated voltage control scheme has to rely on the forecast status of an inherently uncertain variable generation to minimize tap operations among other objectives. Even if technically feasible, real-time manipulation of the parameters of AVC relays such as deadband, voltage setpoint and time delay is unwise as it can either defeat the purpose of voltage regulation or incur excessive tap operations. This *does not* extend to off-line tuning of these parameters, for example, to better coordinate cascaded OLTCs and prevent redundant tap operations [89].

Currently most grid codes require utility-scale wind and PV plants to strictly regulate the voltage at the point of interconnection. This is typically achieved by installing dynamic reactive support in the form of STATCOM (or increasingly less commonly SVC) with instantaneously controllable setpoints and no switching cost. In the case of wind farms, this external reactive compensation by far exceeds the cumulative reactive capability of individual wind turbines [90]. Even small-scale PV generation is soon equipped with inverters that have "Volt/VAr control" capabilities [70]. In the presence of FACTS devices, an effective and robust voltage coordination scheme would rely on voltage setpoints of FACTS devices as the primary control input. This becomes more clear in the next section where we investigate the genuine cause of OLTC operations.

In recent years, a number of studies have examined the impact of variable generation on the frequency of (upstream) OLTC operations and have made some conclusions as to how to mitigate this impact through the proper choice of "Volt/VAr control" modes of DGs [14, 13] or a coordinated dispatch of reactive power [16]. The conclusions are based on simulation results of specific, typically radial, network configurations. It is suggested that "the number of OLTC operations and the voltage fluctuation in the system will be reduced significantly when the DG is operated at a constant voltage" [13] or "increasing the range of reactive power output of the DGs under voltage control mode" (as opposed to constant p.f.) would reduce the tap frequency [14]. This is contradicted by another study that observes an increased frequency of tap changing for the case of enhanced reactive

capability compared to the constant p.f. approach[15]. It is also claimed that, "in general, for distribution networks connected to external grids with, $X/R \leq 5$, no significant effect on the frequency of tap changes is seen due to introduction of wind power." [16]

This chapter shows that these conclusions are not valid "in general." It is assumed, in these studies [14, 13, 16, 15], that tap changing is caused by the variation of power flow through the OLTC transformer with no distinction between active or reactive power. A clarification on this subject is essential for the proper design of a voltage control scheme. These arguments are elaborated in section 5.2 which explores the relationship between active and reactive power flows through the OLTC transformer and tap sensitivity. In Section 5.3 the test network and tap models are discussed. Section 5.4 demonstrates the fundamental conflict between the frequency of tap operation of upstream (sub-transmission) and downstream (distribution) OLTCs in relation to generation variability and voltage/reactive power control. Section 5.5 explores the inherent limitation of local control schemes in addressing this conflict by examining the droop control methods of reactive power at the point of interconnection of variable generation. The droop control is based on a fictitious impedance the phase angle of which exhibits interesting properties and can be used as a tuning parameter. Section 5.6 introduces a centrally coordinated voltage control scheme that is based on model predictive control (MPC) strategies utilizing short-term forecasts of stochastic generation and an exhaustive search method to find the optimal voltage setpoint for a upcoming period. Section 5.7 introduces an equivalent mixed-integer optimization formulation that finds the same optimal control output but at a higher computational efficiency. Section 5.8 discusses the results of the implementation of the control scheme on the DTE/ITC system.

5.2 What induces tap change?

The generic model of an OLTC transformer is illustrated in Fig 5.1. It comprises an ideal transformer in series with impedance Z_{tr} that models the leakage reactance and the often negligible resistance of the coils [91]. The bulk power system as seen from the primary side of the transformer is represented by its Thevenin equivalent with a fixed magnitude voltage source and impedance, Z_{Th}.

Lumping Z_{Th} and Z_{tr} into Z_{eq}, the following relationship can be derived with some algebraic manipulation,

$$n^4|Z_{\text{eq}}|^2(P^2+Q^2)+n^2V_{\text{s}}^2(2(R_{\text{eq}}P+X_{\text{eq}}Q)-V_{\text{Th}}^2)+V_{\text{s}}^4=0 \tag{5.1}$$

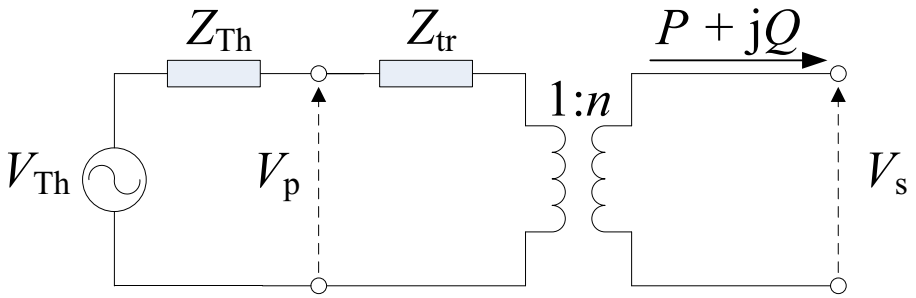

Figure 5.1: Generic Model of an OLTC Transformer

It should be noted that solutions to (5.1) only exist when $R_{\text{eq}}P + X_{\text{eq}}Q \leq V_{\text{Th}}^2/2$. Therefore the solution space boundary in the parameter space of (P, Q) is defined by the following line equation,

$$2(R_{\text{eq}}P + X_{\text{eq}}Q) - V_{\text{Th}}^2 = 0 \tag{5.2}$$

Holding V_s constant in (5.1), the sensitivity of tap position, n, with respect to P and Q, is given by,

$$\frac{\partial n}{\partial P} = \frac{-n^3|Z_{\text{eq}}|^2P - nV_{\text{s}}^2R_{\text{eq}}}{2n^2|Z_{\text{eq}}|^2(P^2+Q^2) + V_{\text{s}}^2(2(R_{\text{eq}}P + X_{\text{eq}}Q) - V_{\text{Th}}^2)} \tag{5.3}$$

$$\frac{\partial n}{\partial Q} = \frac{-n^3|Z_{\text{eq}}|^2Q - nV_{\text{s}}^2X_{\text{eq}}}{2n^2|Z_{\text{eq}}|^2(P^2+Q^2) + V_{\text{s}}^2(2(R_{\text{eq}}P + X_{\text{eq}}Q) - V_{\text{Th}}^2)} \tag{5.4}$$

The ratio of sensitivities of tap position to active and reactive power flow through the transformer is given by,

$$\eta = \frac{\frac{\partial n}{\partial P}}{\frac{\partial n}{\partial Q}} = \frac{P + \frac{(\frac{V_{\text{s}}}{n})^2R_{\text{eq}}}{|Z_{\text{eq}}|^2}}{Q + \frac{(\frac{V_{\text{s}}}{n})^2X_{\text{eq}}}{|Z_{\text{eq}}|^2}} \tag{5.5}$$

Notice that at no load, $\frac{V_s}{n} = V_{Th}$ and hence,

$$\frac{(\frac{V_s}{n})^2}{|Z_{eq}|} = \frac{V_{Th}^2}{|Z_{eq}|} = S_{sc\text{-}s} \tag{5.6}$$

Where $S_{sc\text{-}s}$ denotes the short circuit capacity of the network at the secondary terminal of the transformer. Under reasonable transformer loading conditions, $\frac{(\frac{V_s}{n})^2}{|Z_{eq}|} \approx S_{sc\text{-}s} \gg |P + jQ|$ and thus $\eta \approx \frac{R_{eq}}{X_{eq}}$.

Notice that Z_{eq} is dominated by Z_{tr} which is almost a pure inductance, especially for sub-transmission transformers and Z_{Th}, the Thevenin impedance of the bulk power system typically has a high X/R ratio so it is expected that $\frac{R_{eq}}{X_{eq}} \ll 1$. Hence, it is not the variation of active power flow through the transformer *per se* that induces tap change. This statement is based on the OLTC generic model and is independent of the grid. The fact that tap change primarily occurs due to variation of reactive power explains the observations made in Section 3.2 regarding the DTE/ITC network serving Eastern Michigan [6]. In that study which entailed simulation of a number of voltage regulation scenarios, it was noted that enforcing strict voltage control at the point of interconnection of wind farms in the 42kV sub-transmission network, which requires enhancing the reactive compensation capability (through STATCOMs or SVCs), would adversely affect the OLTC transformers that connect the 42kV network to the 120kV transmission system. This is because, under strict voltage control mode at POIs, as wind generation varies reactive power flow through the transformers varies too. Under unity p.f. mode, there is much less reactive flow variability through the upstream transformers as wind generation varies and hence OLTC operation frequency is significantly reduced.

Now we address the so-called reverse power flow through low-voltage distribution transformers where Z_{Th} may be sufficiently resistive to impart a less inductive character to Z_{eq} than what is typical in higher-voltage networks.

Eq. (5.1) can be rewritten as the equation of a circle,

$$(P + \frac{V_s^2 R_{eq}}{n^2|Z_{eq}|^2})^2 + (Q + \frac{V_s^2 X_{eq}}{n^2|Z_{eq}|^2})^2 = \frac{V_s^2 V_{Th}^2}{n^2|Z_{eq}|^2} \tag{5.7}$$

Figure 5.2 shows the circular diagrams for fixed values of tap position n and for $V_s = 1.00$p.u. The circles corresponding to maximum and minimum tap position are highlighted in red and blue colors respectively. Notice that the centers of circles corresponding to each

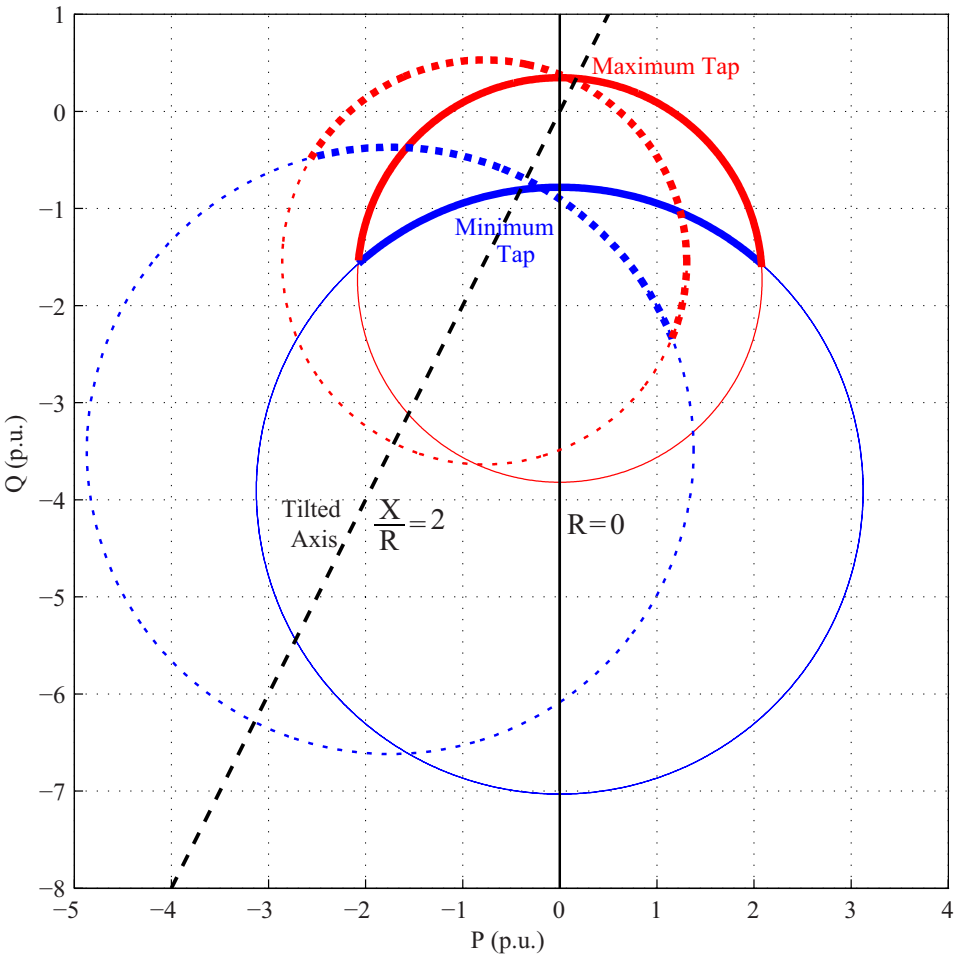

Figure 5.2: Tap contours (positive values of P and Q correspond to load)

tap position are collinear and the slope of the axis of collinearity is $\frac{X_{\text{eq}}}{R_{\text{eq}}}$. Hence when R_{eq} is negligibly small, the axis is perpendicular to the P axis and as R_{eq} increases this axis is tilted. As highlighted in Figure 5.3, these axes are hinging at the No Load point ($P = 0, Q = 0$). It is clear that as P varies, the rate of crossing the blue solid contours, corresponding to $R_{\text{eq}} = 0$, is small at least until very high transformer loading conditions are reached. At high loading conditions, the sensitivity of tap position to P increases slightly irrespective of the sign of P. However, as the axis tilts slightly due to increased resistivity of the upstream network, the sensitivity to active power flow toward the load is exacerbated as the transformer loading increases. Compare the red dashed contours in the regions $P \in$ [-0.4 -0.8] and $P \in$ [0.4 0.8] highlighted by dashed black lines. This clarifies the prevalent confusion on the impact of reverse power flow on tap changing frequency [13, 14, 16] and shows that fluctuations in the reverse active power flow do not affect the OLTCs as much as fluctuations in the normal active power flow toward the load do.

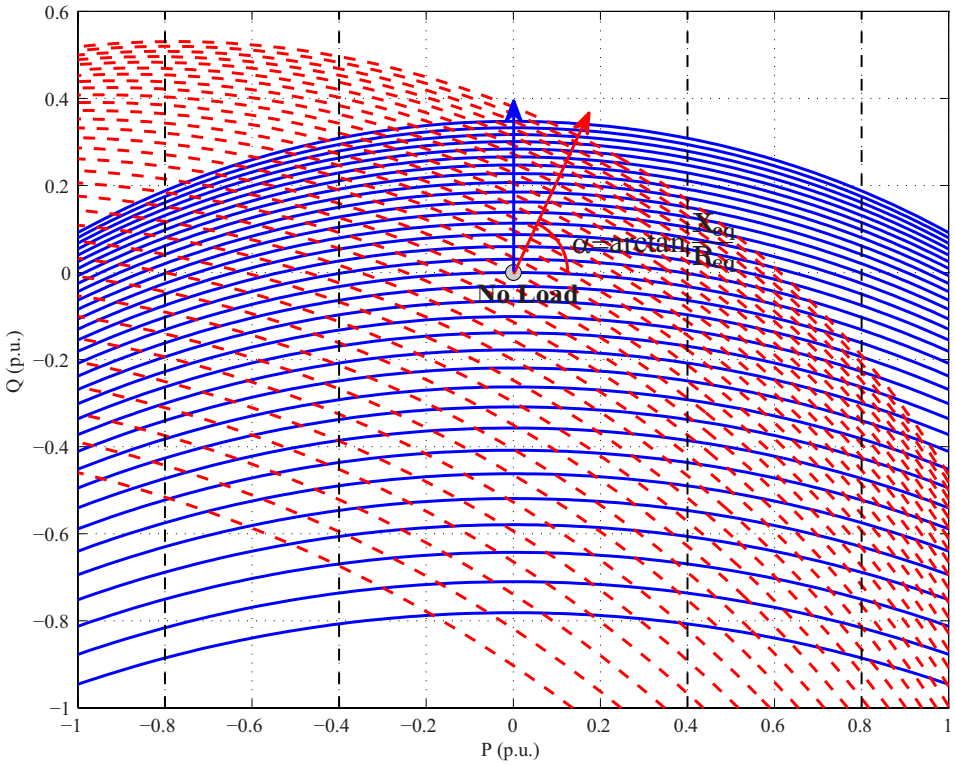

Figure 5.3: Tap contours (zoom)

5.3 Network and Modeling Assumptions

The specifications of a test network and the underlying OLTC regulation models are presented in this section. This simple test network captures much of the complexity of typical sub-transmission networks from the standpoint of voltage regulation and coordination of upstream and downstream OLTCs. In the following sections the effectiveness of the proposed voltage control schemes is evaluated through simulation of the interaction of generation variability, reactive compensation at the POI and the upstream and downstream OLTCs in the test network. Wind and PV generation and load data with a 1-minute resolution for a full year are used in these simulations. Samples of these data are shown previously in Figures 1.3, 3.8 and 3.9.

5.3.1 Generic Test Network Specifications

The test network is shown in Fig 5.4. Our goal is to devise an effective voltage control scheme that minimizes tap-changing operations of the sub-transmission OLTC connecting **Bus 2** and the transmission system and the distribution OLTC connecting **Bus 1** and **Bus**

d which serves the load $(P_{\mathrm{c}} + jQ_{\mathrm{c}})$ in the presence of variable generation (P_{g}). First we discuss the results of the droop control scheme and in subsequent sections present the evolution of a model predictive control scheme. Embedded in the MPC scheme is a method for active power loss reduction. Note that Bus 2 may also serve its own load or other feeders which are not considered in this study. Therefore its voltage is regulated to avoid any adverse impact on the voltage profile of the rest of the network as loading conditions vary.

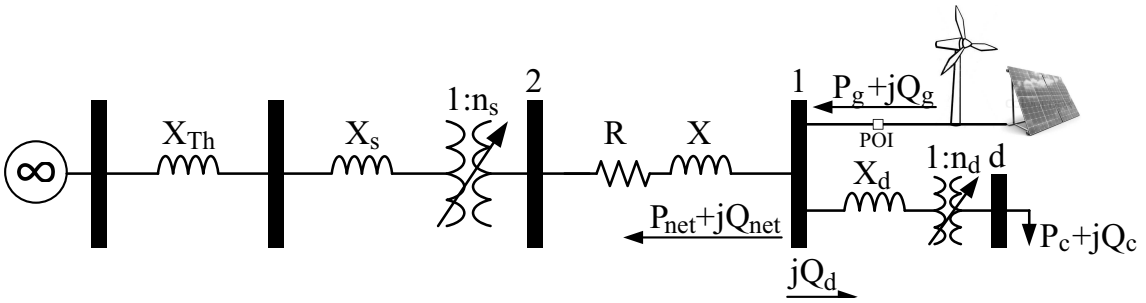

Figure 5.4: Test Network

Parameter Specification of the Test Network (Figure 5.4)		
Symbol	value (p.u.)	Description
X_{Th}	0.1	Thevenin equivalent impedance
X_{s}	0.2	Sub-transmission OLTC reactance
X_{d}	0.3	Distribution OLTC reactance
X	0.5	Sub-transmission line reactance
R	0.5	Sub-transmission line resistance
P_{g}	0.5 (peak)	Wind or PV Generation (variable)
Q_{g}	$[Q_{\mathrm{g}}^{\min}\ \ Q_{\mathrm{g}}^{\max}]$	Wind farm reactive compensation (controllable)
$Q_{\mathrm{g}}^{\max}$	0.4	Q_{g} upper limit
$Q_{\mathrm{g}}^{\min}$	-0.4	Q_{g} lower limit
P_{c}	0.2 (peak)	Active power consumption at distribution Bus d (variable)
$Q_{\mathrm{c}}^{\mathrm{peak}}$	0.1 (peak)	Reactive power consumption at distribution Bus d (variable)
V_{∞}	1	Infinite bus voltage magnitude
V_1^{sched}	1 or $[0.8\ 1.2]$	Bus 1 (Wind Generator) voltage setpoint (controllable)
V_2^{sched}	1	Scheduled voltage for Bus 2
V_d^{sched}	1	Scheduled voltage for Bus d
DB	$\pm\frac{1}{120}$	OLTC Deadband
T_s	0.1	Sub-transmission OLTC time constant
T_d	0.1	Distribution OLTC time constant

5.3.2 Tap models

The most common control mechanism for tap changing is for the AVC relay to detect OLTC-regulated bus voltage deviating outside a prescribed deadband and to either immediately initiate a tap change operation or start a timer to trigger an operation once the voltage stays outside the deadband for a certain time. If the voltage comes back within the deadband before the time delay has elapsed, the timer is reset, preventing an otherwise redundant operation.

As solid-state relays (SSRs) replace electromechanical relays (EMRs), new OLTC control capabilities emerge which enable the OLTC to correct sudden large voltage deviations more quickly [7]. This could be achieved either by making the time delay inversely proportional to the magnitude of deviation or by defining an ordinary differential equation (ODE) for tap based on the magnitude of voltage deviation and integrate the differential equation to trigger an operation once this integral exceeds a certain tolerance. To use these features which are particularly relevant in the presence of variable generation, the following ODE model which is a modified form of continuous tap models, proposed previously, for dynamic studies [92] is introduced,

$$\frac{dn}{dt} = \begin{cases} \frac{1}{T}(V - V_{\text{ref}} - DB) & \text{if } V - V_{\text{ref}} > DB \\ \frac{1}{T}(V - V_{\text{ref}} + DB) & \text{if } V - V_{\text{ref}} < -DB \\ 0 & \text{if } |V - V_{\text{ref}}| < DB \end{cases} \tag{5.8}$$

Notice that V is dependent on n by power flow *algebraic* equations and the derivative of n is dependent on V by the above *hybrid dynamical* equation. We designated this model *DBODE* to highlight its hybrid dynamical aspect. If the time constant, T, is chosen sufficiently small, the model approximates the commonly used tap change mechanism in DTE where any voltage deviation outside the deadband, no matter how small, would trigger a tap change. Note that in this model once the tap error $t_e = \int \frac{dn}{dt} dt$ exceeds a single tap step, tap operation is triggered and the tap error is reset to zero to avoid multiple tap operations. This particular instance of the *DBODE* model is henceforth referred to as discrete model or simply *DB* to distinguish it from the case where tap derivative, proportional to voltage deviation, is integrated over time. Throughout this chapter all simulations involving tap-change use the discrete (DB) model which is obtained by setting $T = 0.1min$ in (5.8).

5.4 Pareto Distribution Curve

This section demonstrates, in the context of the test network of Fig 5.4, the fundamental conflict between the frequency of tap operation of upstream (sub-transmission) and downstream (distribution) OLTCs in relation to generation variability and voltage/reactive power control.

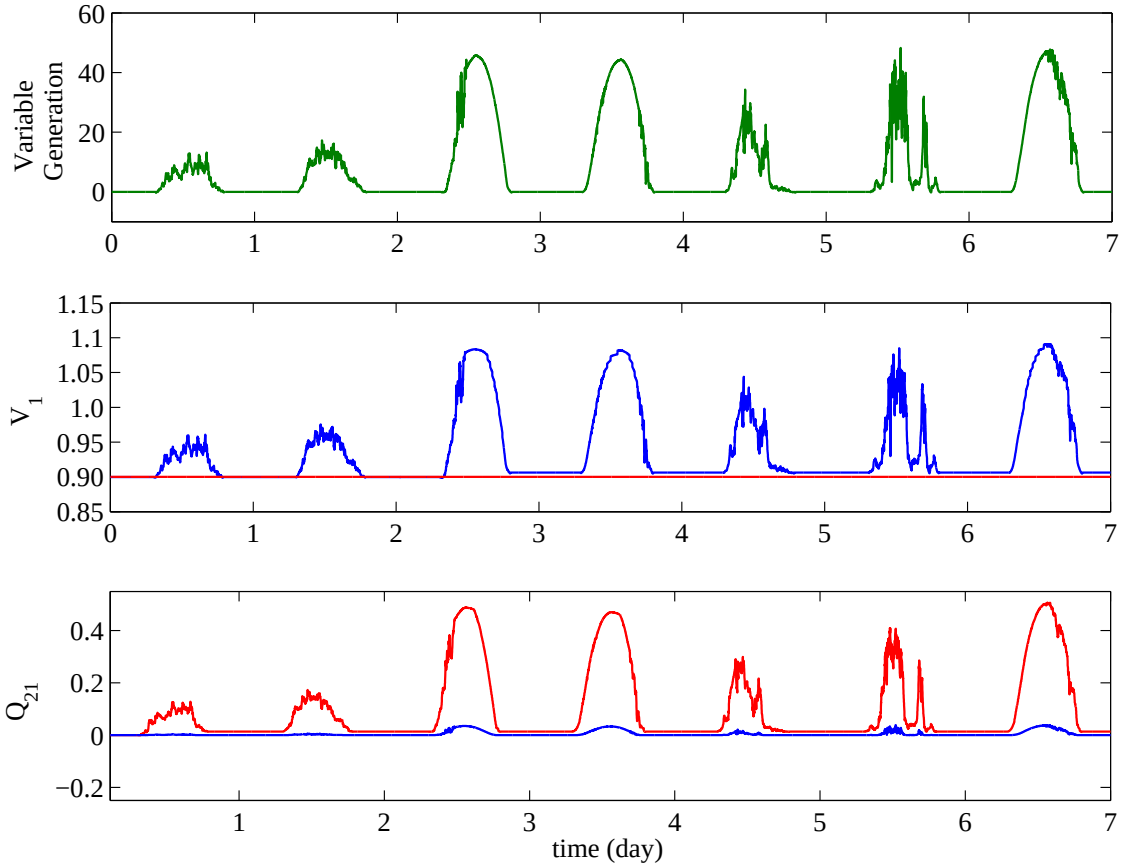

Figure 5.5: Voltage-Reactive Flow duality

Figure 5.5 shows variation of PV generation on the scale of a minute over the course of a week (in green). For the case of no Volt/VAr control capability at POI, the voltage variation of Bus 1 (in blue), where PV power is injected into the network, perfectly resembles the variation of PV generation. The corresponding reactive flow into the sub-transmission network Q_{21} which passes through the upstream (sub-transmission) transformer (also in blue), on the other hand, is almost constant. As explained previously, this means that in the absence of reactive power absorbtion at the POI, the sub-transmission OLTC is not adversely affected by generation variability. However the lack of voltage regulation of Bus 1 to which the primary side of the distribution transformer is connected, results in high

frequency of downstream OLTC operations.

The situation is reversed for the case of strict voltage regulation at Bus 1 which requires significant reactive power absorption at the POI at peak generation. This reactive power has to be provided by the transmission system and flows through the sub-transmission transformers. The voltage is constant whereas Q_{21}, reactive flow into the sub-transmission network almost perfectly follows generation variability (in red). This shifts the burden on to the upstream OLTC and significantly reduces the distribution OLTC operations as its primary voltage is now held constant.

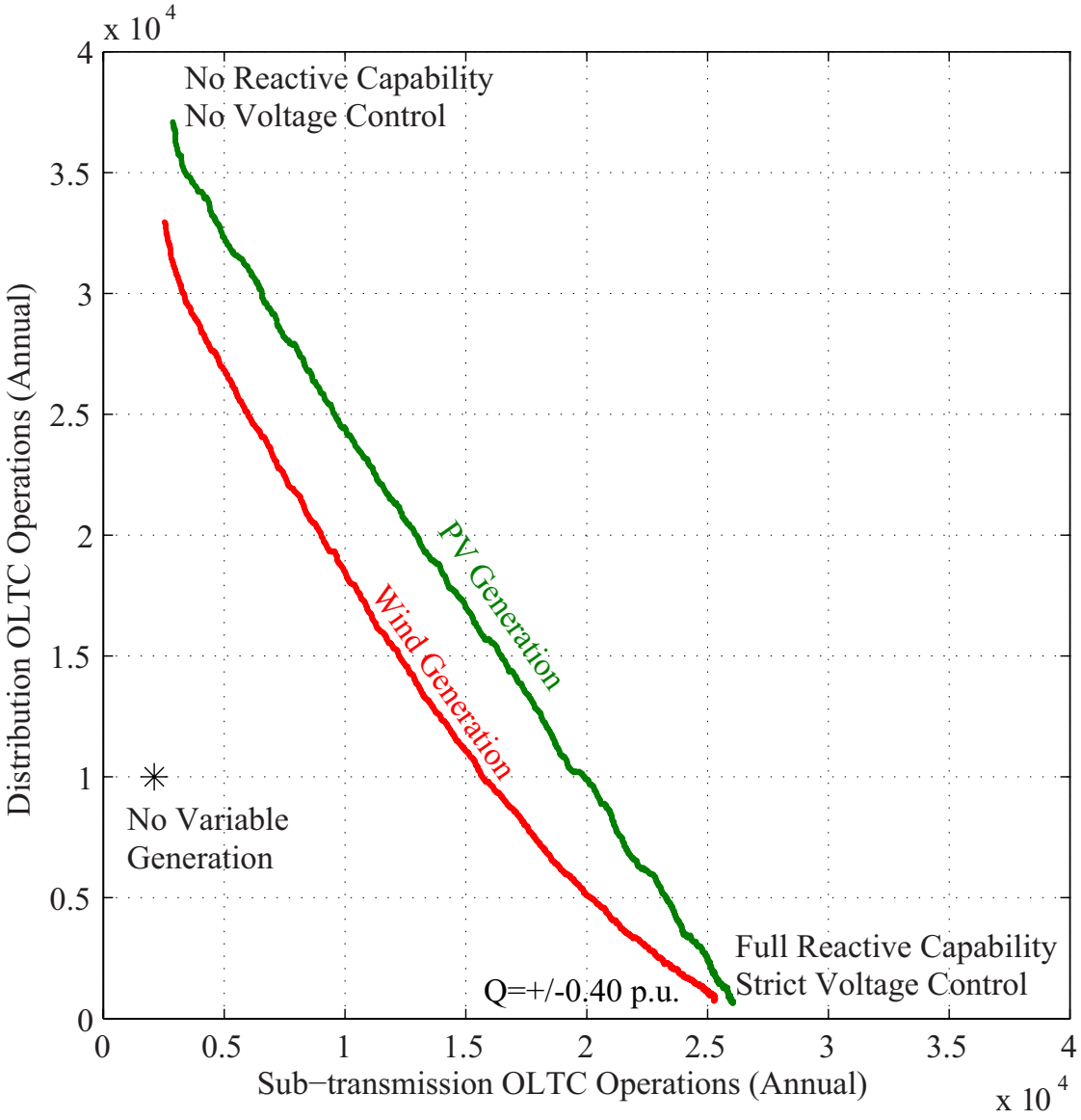

Figure 5.6: Pareto curve (voltage set-point at Bus 1 is 1.00)

Hence, generation variability in resistive networks impacts the upstream and downstream OLTCs in opposite ways, depending on the Volt/VAr control mode. This conflict is illustrated in Fig 5.6 which plots annual sub-transmission versus distribution OLTC operations for varying ranges of reactive compensation capability at Bus 1, starting at zero capability (unity p.f.) to ± 0.40p.u. for both PV and wind generation. As the reactive capability at POI is enhanced incrementally, the number of distribution operations declines gradually, shifting the burden onto the sub-transmission OLTC. These curves are designated *pareto* in the sense that this is the best that can be achieved under standard voltage control strategies. Notice that the annual OLTC performance anywhere on the *pareto* curves is significantly worse than the case of no generation variability, shown in Figure 5.6, where the tap changes are solely due to the variation of load. The simulation on the generic test system of Figure 5.4 with actual load and generation data highlights, once again, the scale of the problem faced by utilities that integrate large-scale wind and solar PV projects.

The previously cited studies on the impact of wind and PV generation on tap frequency [13, 14, 15, 16, 77] have only considered upstream OLTCs and endorsed various voltage control modes or coordination schemes based on configuration of their respective networks. The author could only find one study that involved downstream OLTC and, as expected, it advocated a control scheme based on enhanced reactive capability of the inverter to mitigate the adverse effect of PV variability observed under unity power factor mode [93]. As of now, no study has pointed out this fundamental conflict let alone suggested ways to mitigate it.

Next section demonstrates the inherent limitation of *local* voltage control schemes in addressing the conflict embodied in *pareto* curves.

5.5 Droop Control Scheme

The concept of *droop* has its origins in primary frequency control as a mechanism for coordination of generating units in response to load variations. Without proper droop configurations of frequency to power output, generators would be in a constant state of conflict with each other to share the load mismatch and may lose synchronism and trip out. Reference [94] discusses in detail the classical droop scheme. The scheme is particularly appealing due to its simplicity, robustness and the fact that it is solely dependent on locally measured signals and does not involve communication between individual generators.

Droop schemes are occasionally used for multiple generators that are sharing the same terminal to better coordinate the voltage control and reactive compensation among these units. With the advent of microgrids, the concept of droop has been used extensively in

the realm of voltage control to coordinate the parallel operation of generators and voltage source convertors and prevent excessive circulation of reactive power [95, 96]. Among various voltage droop schemes that have been proposed in recent years, the fictitious impedance based droop is preferred for resistive networks due to the strong coupling of voltage magnitudes with both active and reactive power flows [96]. In this method, the reactive power at the inverter terminal is controlled indirectly through the voltage regulation of a fictitious bus that is connected to the terminal through a fictitious impedance. The magnitude and angle of this impedance and the voltage setpoint of the fictitious bus are all parameters that can be tuned for each inverter for a more effective coordination of adjacent DGs. Figure 5.7 shows this scheme in the context of the modified version of the test network introduced earlier. Notice that the fictitious bus here is Bus F. Q_G^* the reactive power output at the POI is determined based on strict voltage regulation of Bus F (instead of Bus 1). The fictitious setup (inside the dashed box) and its controller assume that variable generation passes through the fictitious impedance ($R_{\text{droop}} + jX_{\text{droop}}$) and based on that the droop voltage controller computes Q_G^* to regulate the voltage of Bus F. This Q_G^* is then injected at the POI.

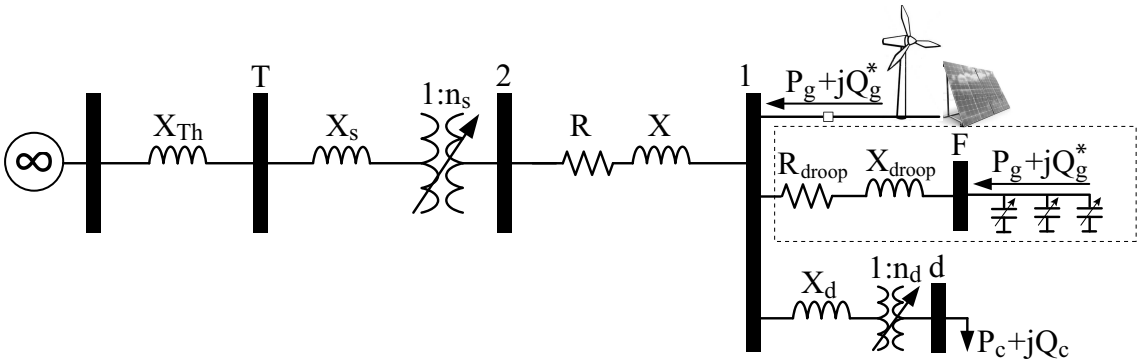

Figure 5.7: Fictitious-Impedance Droop Scheme

This scheme is implemented for the test network of Figure 5.4 for both wind and PV generation. The performance is illustrated in Figures 5.8-5.9. Note that for each performance curve, the reactive power limits are held constant at ± 0.40 p.u. and the only varying parameter is the size of the fictitious droop impedance. For purely resistive droop impedance the initial reduction in sub-transmission OLTC operations is quite dramatic (see the black curve in Figures 5.8 and 5.9). However the effectiveness rapidly declines as the size of the fictitious droop impedance is increased. As the impedance becomes more inductive (i.e. its angle is increased) the improvement in sub-transmission is more persistent but results in higher distribution OLTC operations (see the red and yellow curves in Figures 5.8 and 5.9). This is expected with droop because the terminal (i.e. Bus 1) voltage has an increasingly wider range of variation as the fictitious impedance gets larger and explains the

inherent limitation of uncoordinated local voltage schemes. This limitation becomes even more apparent in larger sub-transmission networks with mesh configurations where the distribution substations are not necessarily in the immediate vicinity of embedded generation nodes.

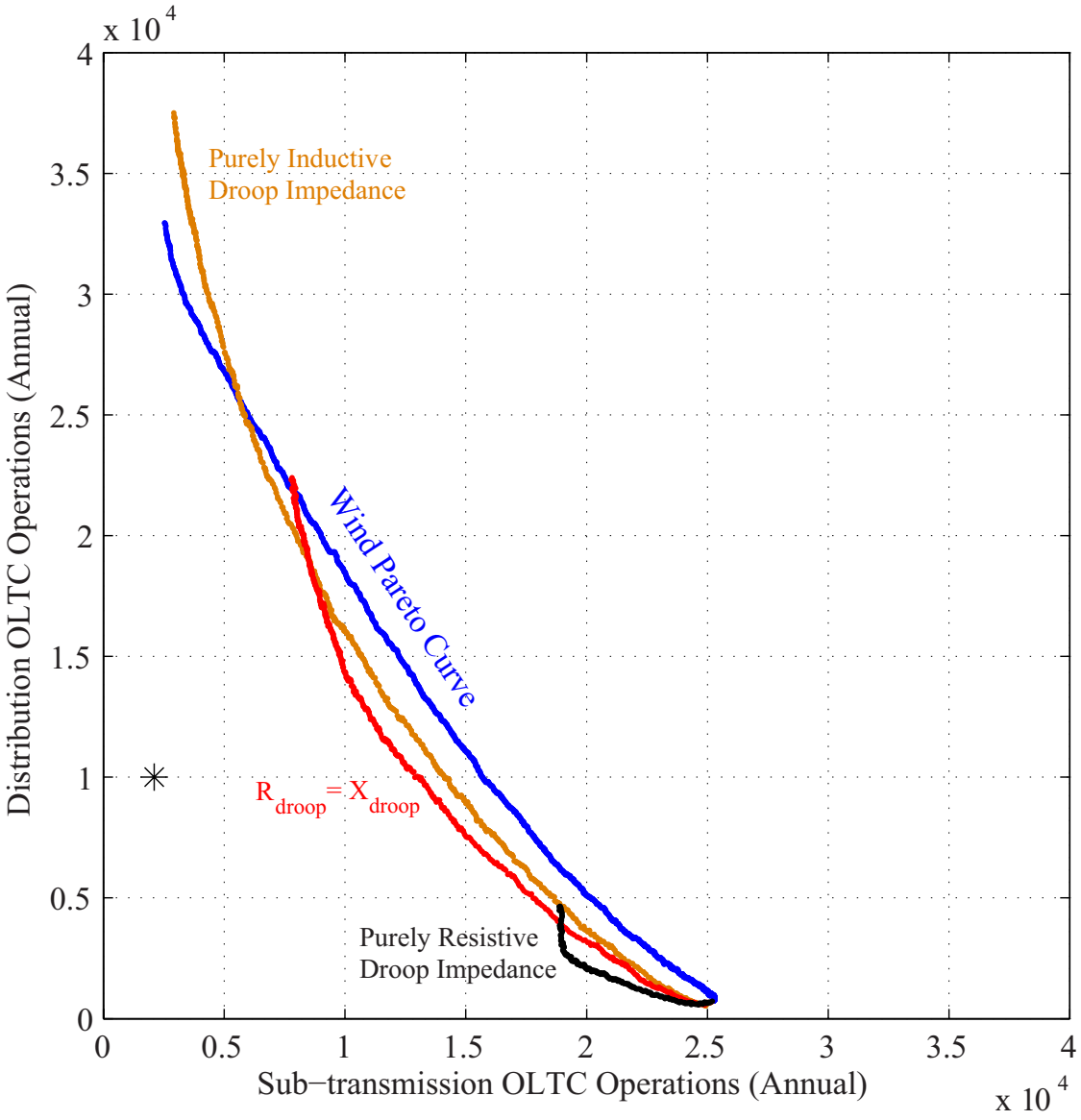

Figure 5.8: Wind Generation Droop Control (Zero droop is at the lower right corner)

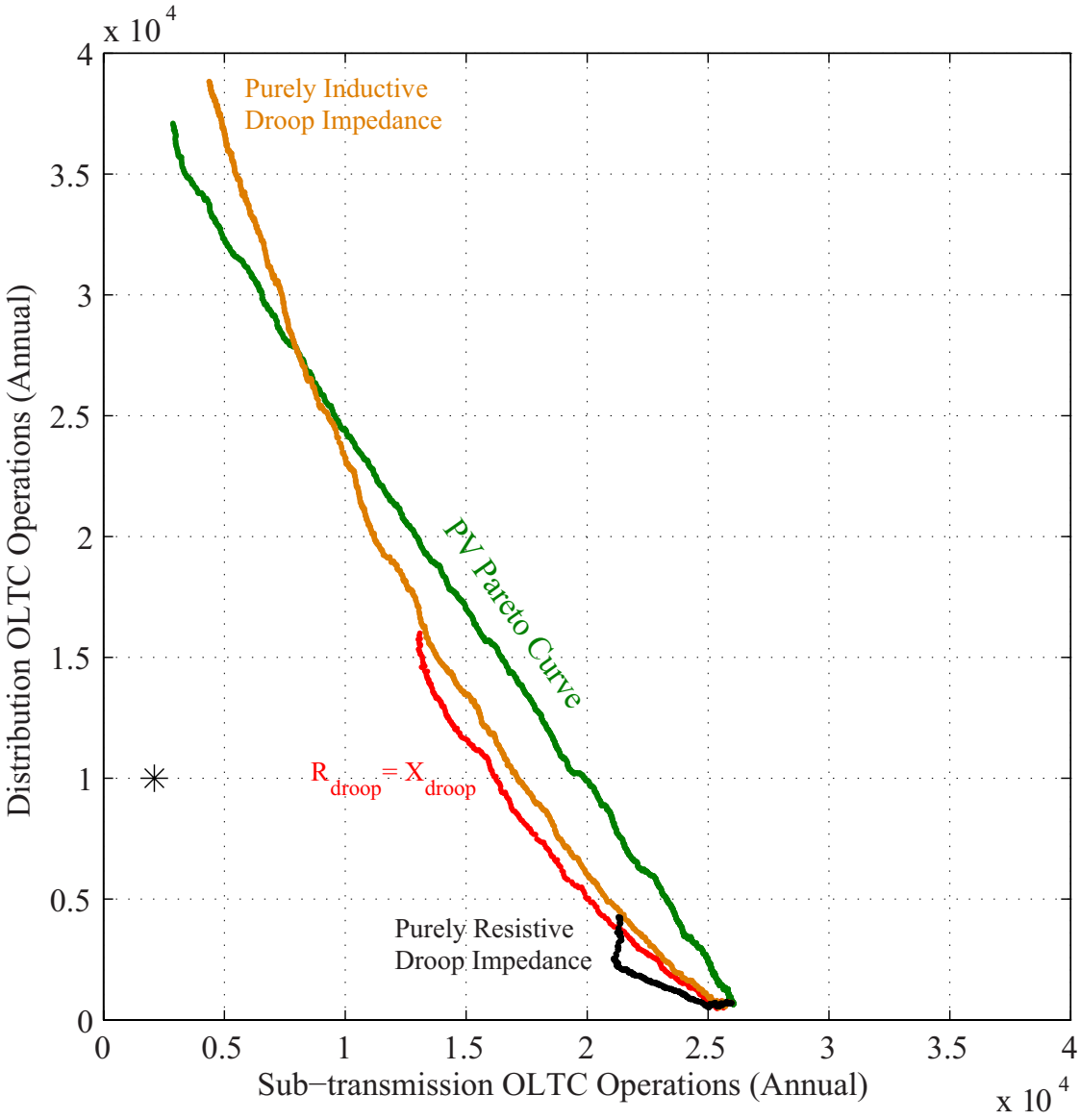

Figure 5.9: PV Generation Droop Control (Zero droop is at the lower right corner)

5.6 Model Predictive Control Scheme

This section presents the evolution of a model predictive control scheme to achieve the conflicting objectives of minimizing the tap-changing operations of the sub-transmission OLTC and the distribution OLTC of the test network (Figure 5.4) in the presence of wind generation (P_g). Embedded in the control scheme is a method for active power loss reduction.

The scheme and the embedded algorithms are based on a series of discretized mappings that relate the control output (voltage setpoint of Bus 1) to OLTC operations, network loss and reactive flow into the resistive network (Q_{21}) over varying time horizons. Later we will introduce an equivalent mixed-integer optimization formulation which finds the same optimal control output but at a higher computational efficiency.

The efficacy of such a scheme depends on the availability of accurate generation forecast with high temporal resolution over lead times of 10-120 minutes. It is expected that as the horizon of the forecast period increases, the forecast accuracy suffers. So for example any 1-minute resolution forecast for the next 60 minutes tends to be more accurate for more immediate intervals (say the first 30 minutes) than for later intervals (say the second 30 minutes). However as explained later the most forecast-sensitive component of the scheme is the fine-tuning process which relies on the forecast with lead times of 2-10 minutes. For the longer horizon that is used only to obtain an initial estimate for the voltage setpoint of POIs, forecast errors are unlikely to have tangible impact on the performance of the scheme.

Historically, forecasting methods have developed for the needs of energy markets with the focus on forecasts with hourly resolution. However, with generation variability coming to the forefront of integration issues for utilities, the research focus is shifting toward short term forecasting with high temporal resolution. Wind power forecasts with temporal resolutions from 5 to 15 minutes are currently used in optimizing reserve allocation and controlling wind power fluctuations at offshore wind farms [97]. For higher temporal resolution (1-5 min) forecasts of wind power, Markov-switching Autoregressive (MS-AR), among other time series analysis models, are proposed as a significant improvement over persistence method [97]. These purely statistical models use recently observed values of wind and other variables to predict wind speed or power over the next few time steps. The accuracy of these models can be enhanced for longer time horizons by incorporating meteorological data and numerical weather prediction (NWP) methods [97, 98]. For similar PV generation forecast, a combination of statistical and NWP methods are used [99].

5.6.1 The Control Strategy

Voltage setpoint of Bus 1 to which variable generation is connected can be adjusted and held fixed for time windows of varying length to reduce the number of tap changes of the sub-transmission and distribution OLTCs. Suppose we want to minimize the tap operations over a given interval of t minutes by adjusting the setpoint of V_1 prior to the start of that interval. The most straightforward method is to fix the setpoint at a particular value and

run the successive power flows at every minute with updated wind or PV generation and load forecasts for the next t minutes and record the number of OLTC tap changes, network loss and other variables of interest. Once this is repeated for a sufficiently dense set of set-points in the feasible range, a discrete approximation of a generally non-convex function is available that maps the V_1 setpoint to the number of tap operations, network loss and other quantities that may be drafted into the optimization framework. These mappings can be used to obtain an optimal setpoint, that minimizes both distribution and sub-transmission OLTC operations, for that time window. The voltage setpoint is adjusted at the beginning of the time window to its optimal value and remains constant until the end of it. Later an equivalent norm-zero optimization problem is introduced based on sensitivity factors of the power flow Jacobian matrix that achieves the same objective. Notice that in the case of *DBODE*, tap error from the previous interval is considered as an input for the current interval. However through the simulations in this chapter the discrete (*DB*) model is assumed where the tap error is set to zero after each voltage excursion outside the deadband. At time t, the power flow is solved based on the current tap positions $n_s(t)$, $n_d(t)$, generation $P_g(t)$ and load $(P_c(t), Q_c(t))$ to obtain the voltages $V_2(t)$ and $V_d(t)$. If voltages are outside the deadband, then the tap positions for the next minute $n_s(t+1)$, $n_d(t+1)$ are adjusted by one tap step. This processes is repeated throughout the simulation interval. It should be noted that it takes 10-15 seconds for the mechanical switching to complete once the tap-change is triggered [7]. Hence for the DB model used in this chapter the 1 minute time step of simulation is sufficiently large for tap changing operation. The only exogenous inputs into the system for a given time window, for which an optimization problem is formulated and solved, are the variable generation output and load. The process of mapping setpoint to tap operations is only implemented for a single scenario of generation and load during the period.

A basic algorithm that incorporates loss reduction for a time window of 20 minutes is illustrated in Figure 5.10. Here the blue plot is a discrete mapping of voltage setpoint to the sum total of distribution and sub-transmission tap operations. As explained in the previous paragraph obtaining the total number of tap changes for a given time window requires the knowledge of exogenous variables, i.e. generation and load, during that time window. The green plot is the discrete mapping for the loss. The set of voltage setpoint values that result in minimum OLTC operations is obtained as,

$$V_{sp} = \{0.992, 0.993, 0.994, 0.995, 0.998, 0.999, 1.000, 1.001, 1.002, 1.003\}$$

but the optimal value is chosen as 1.003 since it has the lowest loss. We call this method of

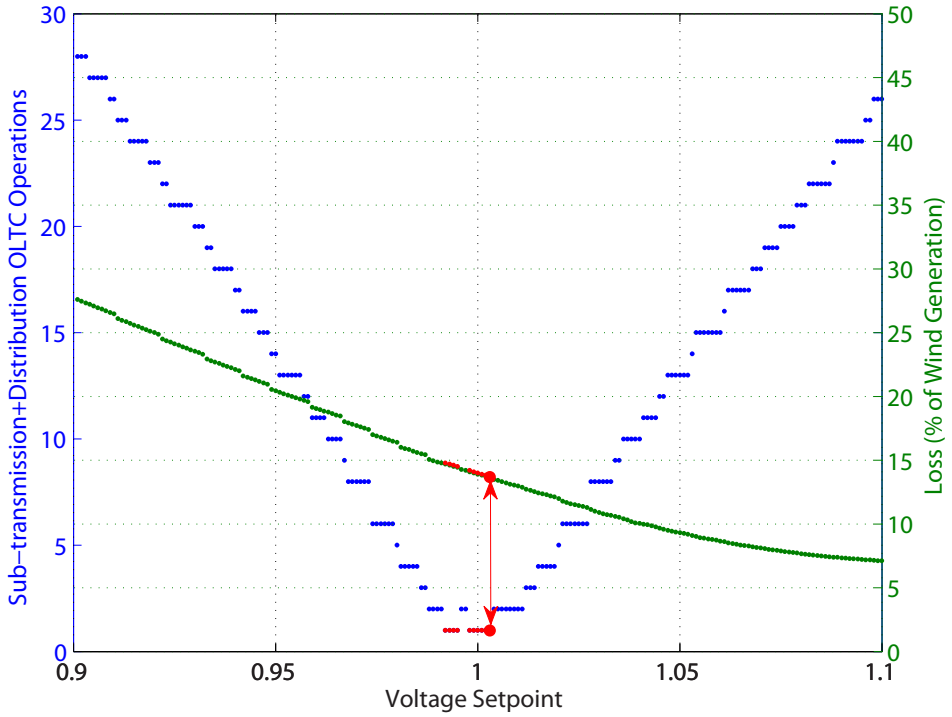

(a) Discrete mappings of voltage setpoint to OLTC operations (blue) and Loss (green) for a 20 min time window

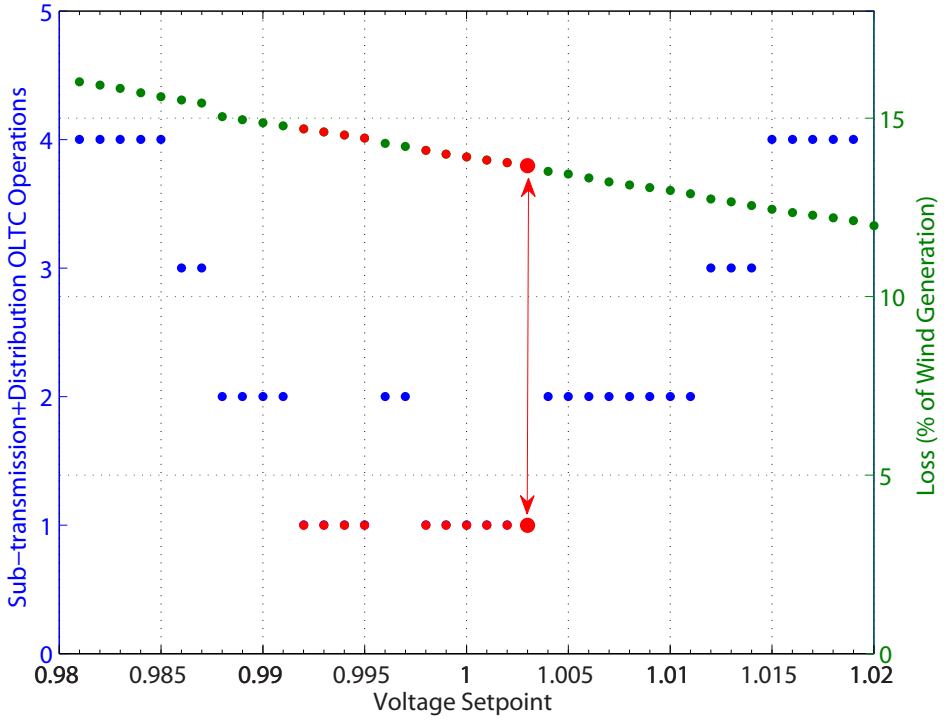

(b) A typical set of setpoint values that results in minimum OLTC operations are highlighted in red.

Figure 5.10: Basic Loss Reduction Scheme

using loss as a *tie-breaker* the **Basic Loss Reduction (BLR)** scheme. Later we introduce the **Enhanced Loss Reduction (ELR)**.

As a next step toward the development of the MPC scheme let us investigate how the length of a time window affects the minimization of OLTC operations. The length of time windows are chosen to be larger than the resolution of the generation and load data and are much larger than the time constant $T = 0.1$ in (5.8). The simulation is implemented for a one-minute time step but the optimal setpoint value is determined and held constant for the time window. As shown in Figures 5.11-5.12, for shorter time windows (of $1, 2, 5, 10, 20$ minutes) the reduction in sub-transmission OLTC operations is more significant. This is due to the increasing capability of the voltage setpoint at Bus 1 to follow wind or PV power variations as the length of time windows shrink. The improvement in sub-transmission operations comes at the cost of increasing distribution OLTC operations. This is especially evident in Figure 5.11 (for the case of wind generation) at time windows of 1 and 2 minutes.

Note, however, that the longer time windows are special cases of shorter time windows. This means that longer time window performance can be replicated by running shorter time windows and enforcing a constant setpoint value across these shorter time windows. This is the critical aspect of the model predictive control scheme, namely the fine tuning process, that is to be discussed shortly.

But how for example voltage control over a 2 hour time window can be enforced based on the implementation of voltage control for all the 5 minute time windows that span this 2 hour window?

Assume that at any given instance we can look 2 hours ahead and obtain the setpoint that minimizes the OLTC operations (with BLR) for that time window. Having obtained this optimal value, if we then allow 5 minute adjustment of the setpoint around the original (2 hour) optimal setpoint we can reproduce the results corresponding to the 5 minute window. Here we assume that these adjustments can be made over the entire feasible range of the voltage setpoint. By reducing the range around the optimal setpoint to which the new setpoint can be adjusted on a 5 minute basis we can move the OLTC reduction performance toward that of 2 hour. The 2 hour time window performance corresponds to the case where the upper and lower limits of the feasible range are set equal to the original (2 hour) optimal setpoint (i.e. 5 minute adjustments have to pick the optimal setpoint as the only feasible point) (See Figures 5.13-5.14). It should be noted that the fine-tuning (shorter) time window has to be significantly shorter than the longer time horizon to realize a larger spectrum for the composite OLTC operation reduction performance (this spectrum is depicted by red circles in Figures 5.13-5.14). So we can have combinations of 5/60, 5/120,10/60,10/120 or even 1/120 minutes. If we choose shorter fine-tuning time windows we can better follow

the variability of generation and thus the OLTC performance can move closer to that end of the spectrum that corresponds to low sub-transmission and high distribution OLTC operations. In Figure 5.13 the total number of sub-transmission and distribution tap operations appears to be constant for all time windows (except for the 1 minute time window). This is not the case in Figure 5.14 where the black dots do not fall into a perfect line and the 1 minute time window is not an exception. While the general pattern of performance with respect to the length of time widows is explained above, it is difficult to determine whether these more specific patterns are caused by some inherent variation regime for wind or PV solar generation. This difficulty is partly due to the discrete nature of the tap changing mechanism and the large scale of the simulation. However these interesting patterns need to be investigated for larger sets of generation and load data in future studies.

In order to control the outcome of the OLTC operation reduction performance (i.e. the ratio of distribution to sub-transmission OLTC operations) we can adjust three parameters:

1. *Length of the time horizon* over which the behavior of OLTCs in response to the control output (i.e. the voltage setpoint that is to be held fixed over the entire time window) is predicted.

2. *Length of the time window* over which the behavior of OLTCs in response to fine-tuning the voltage setpoint around the original voltage setpoint of the horizon is predicted.

3. *Range of feasible setpoint values* centered at the model predicted optimal setpoint within which we can *fine tune* the setpoint over the time window (say 5 minute).

Figures 5.13-5.14 show the performance of the control scheme with respect to the pareto curve for horizon length of 2 hr and fine-tuning time window of 5 minutes as the fine-tuning range increases from a restricted range (a single setpoint) to the full range. As highlighted by the black circles, increasing the horizon or time window lengths shifts the burden of tap-changing onto the sub-transmission OLTC whereas increasing the range has the opposite effect and reduces the sub-transmission operations at the expense of distribution operations. Note that this logic is already present in the pareto curve of Figures 5.6. As the reactive capability of the wind injection node is restricted, both the frequency and range of voltage fluctuations for Bus 1 increases. This shifts the burden onto the distribution transformer. These processes are illustrated in Figures 5.15 and 5.16 where the voltage at Bus 1 and the reactive power flow from Bus 2 to Bus 1 are shown in response to PV generation (load $P_c + jQ_c$ is not considered) over a week period for the following three cases:

1. No Voltage Control at Bus 1 (blue)

2. Full Voltage Control at Bus 1 (red)

3. Proposed Coordinated Voltage Control at Bus 1 (black) with horizon and window lengths of 120min and 20min and full range of voltage setpoints

Figure 5.17 shows the sub-transmission and distribution OLTC tap positions corresponding to the above cases. For no voltage control case sub-transmission OLTC operates only a few times whereas the distribution OLTC incurs around 880 tap operations. For the full voltage control case sub-transmission OLTC incurs 800 operations whereas distribution OLTC does not tap at all. The proposed control scheme results in roughly 100 operations for sub-transmission and 300 operations for the distribution transformer. As can be seen in the figure, the proposed scheme reduces high frequency tap position fluctuations in response to voltage fluctuation at Bus 1 while the voltage setpoint roughly follows generation variability.

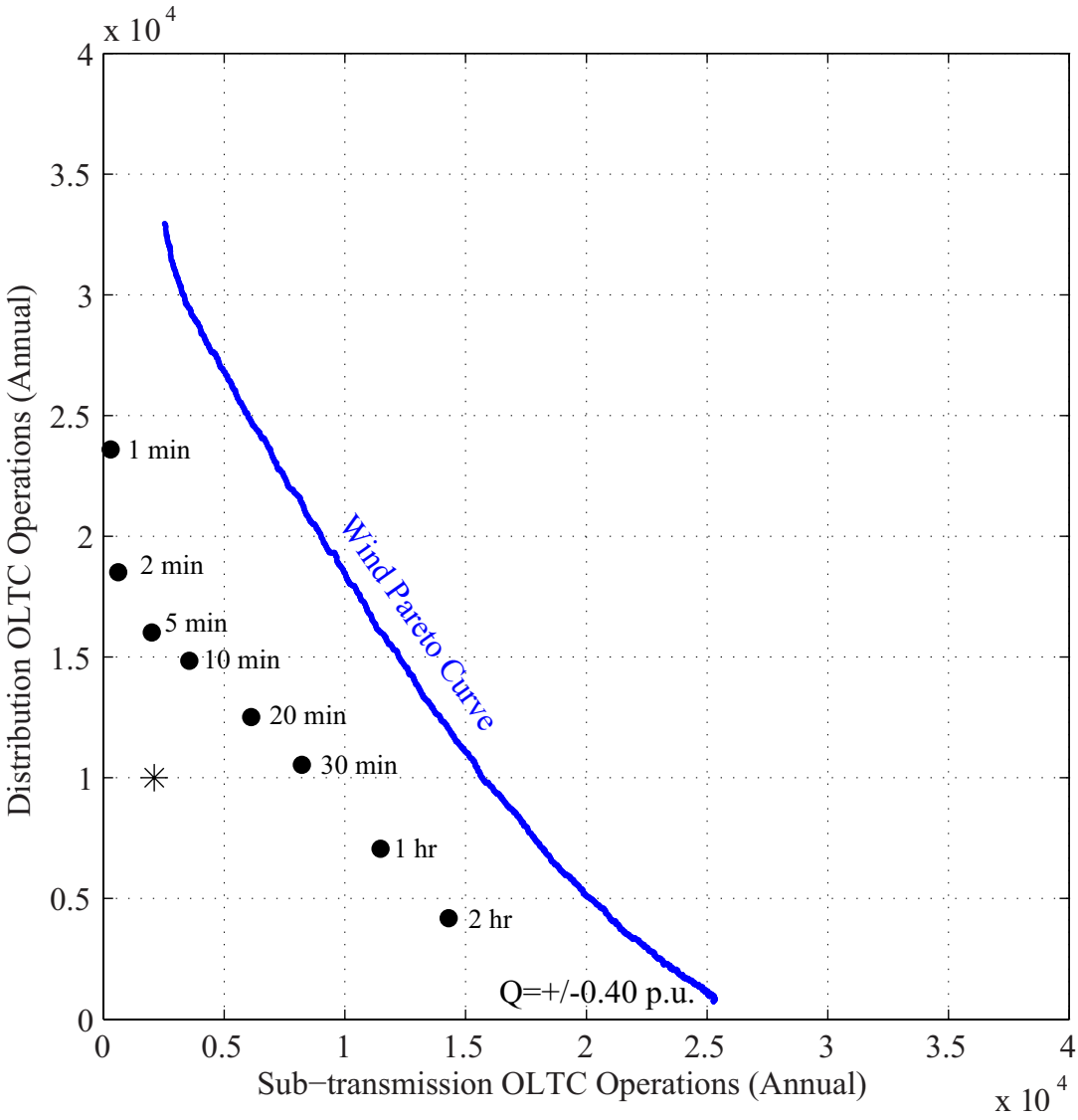

Figure 5.11: Reduction of OLTC operations for the varying time windows of voltage set-point control (Wind generation)

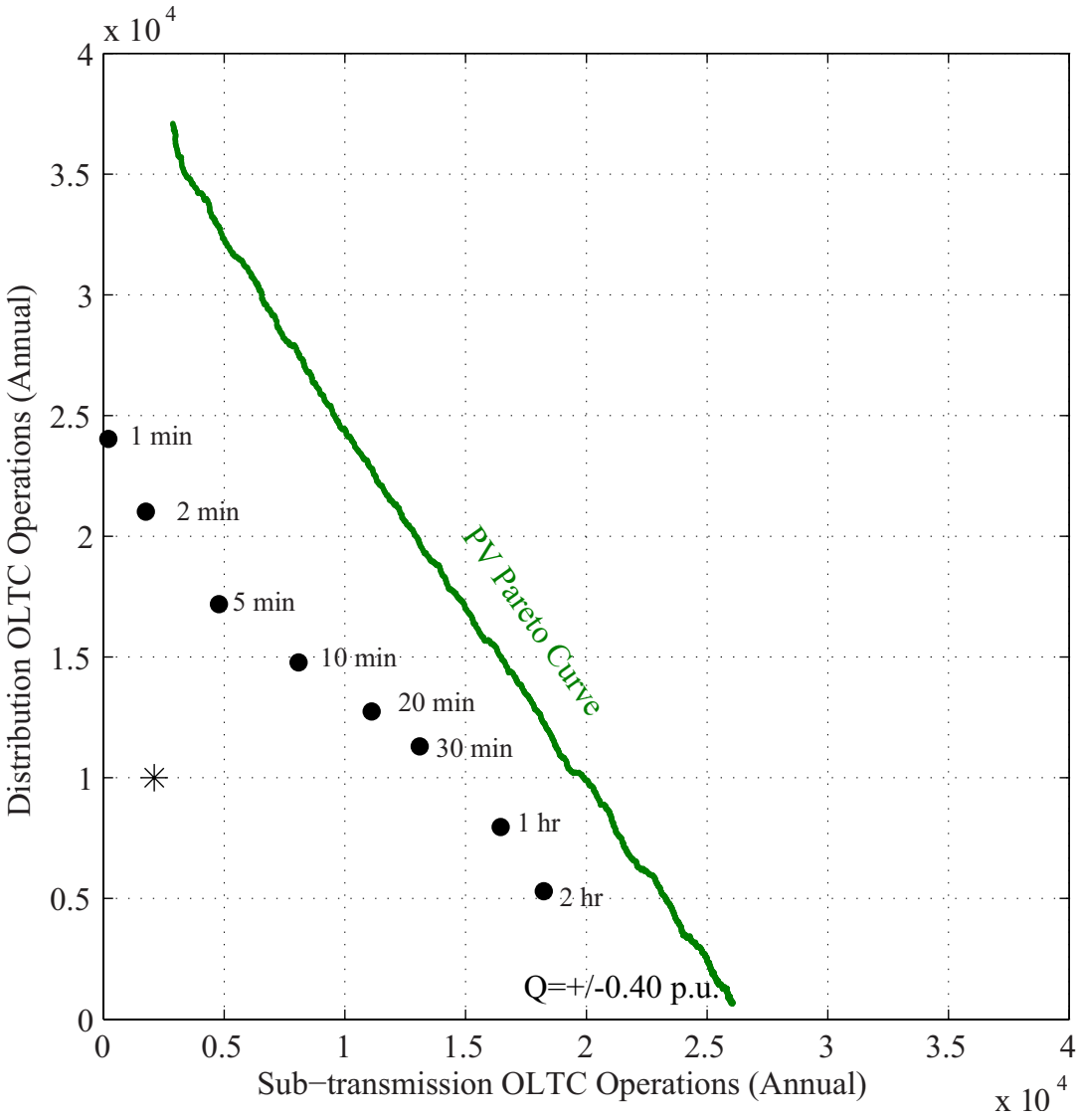

Figure 5.12: Reduction of OLTC operations for the varying time windows of voltage set-point control (PV generation)

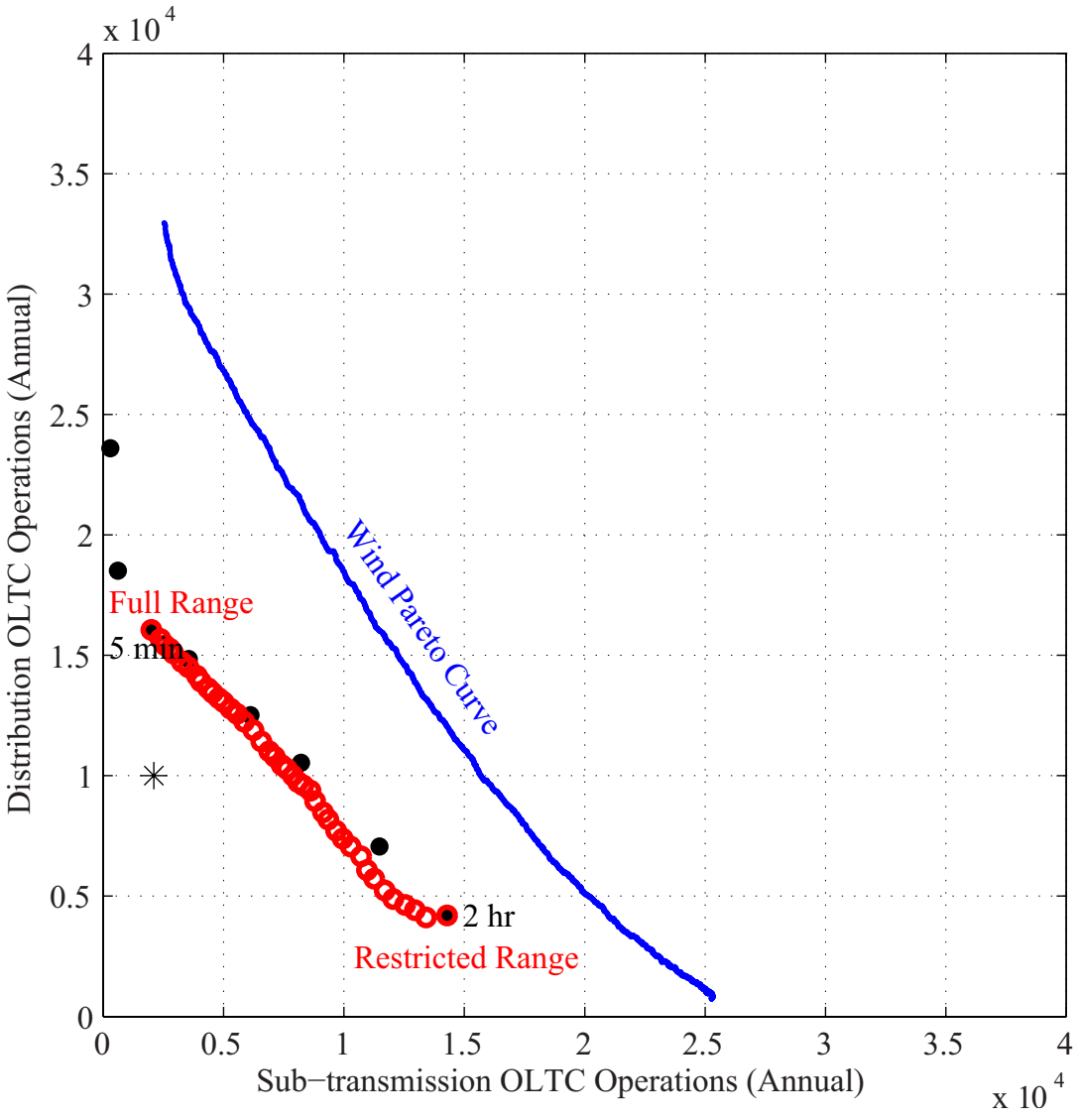

Figure 5.13: Red circles correspond to the varying feasible ranges for *fine-tuning every 5 minutes* around the 2hr optimal setpoint (Wind generation)

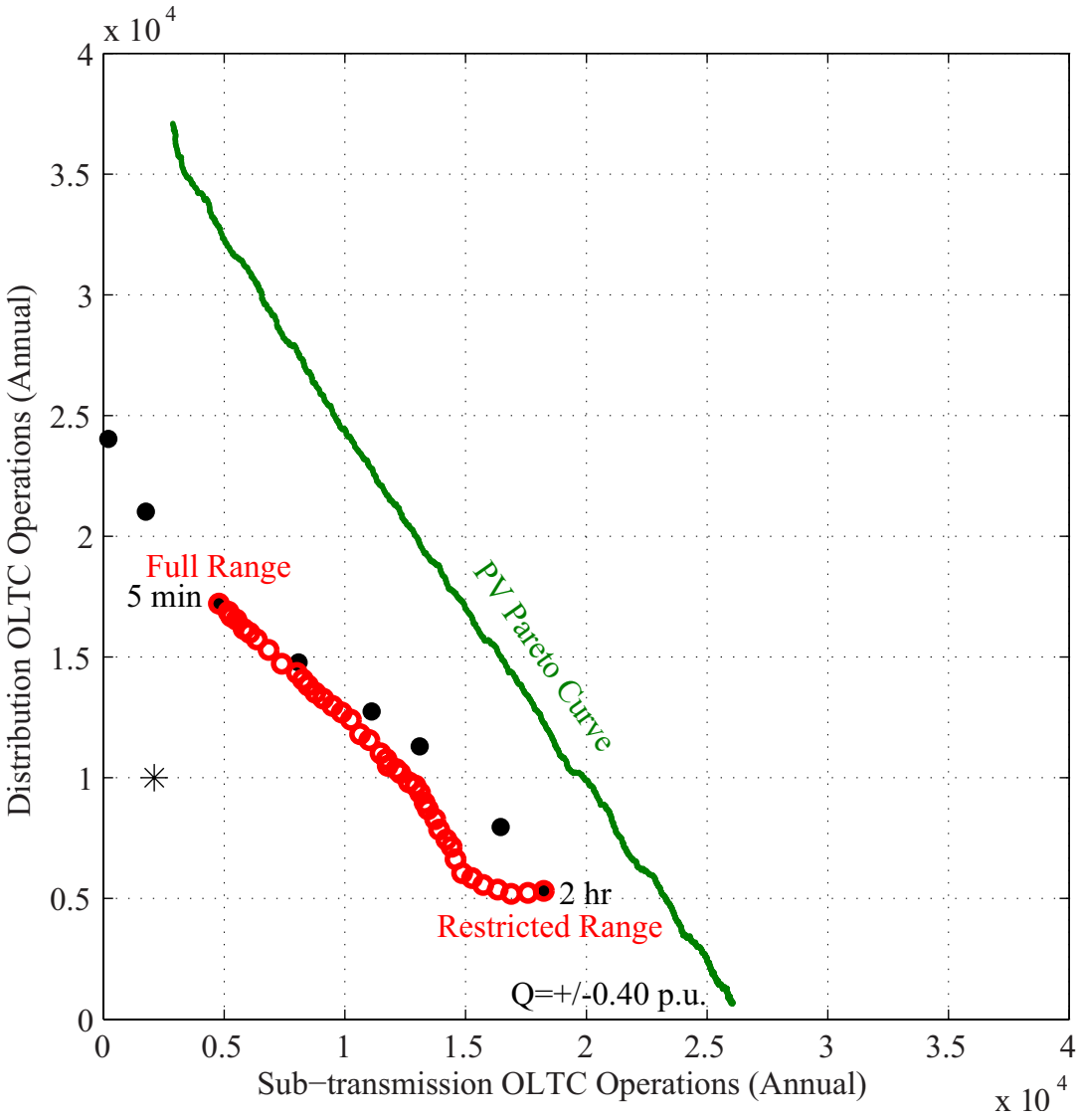

Figure 5.14: Red circles correspond to the varying feasible ranges for *fine-tuning every 5 minutes* around the 2hr optimal setpoint (PV generation)

5.6.2 Comparison with a moving horizon MPC method

Here the performances of proposed MPC method in Section 5.6.1 is compared with a moving horizon MPC formulation where a single voltage setpoint is computed for the horizon but only enforced for the first time step after which a new setpoint for a new horizon is computed. It should be noted that computing a distinct setpoint value for each time step of a horizon in an MPC scheme requires an optimization formulation of the form discussed in

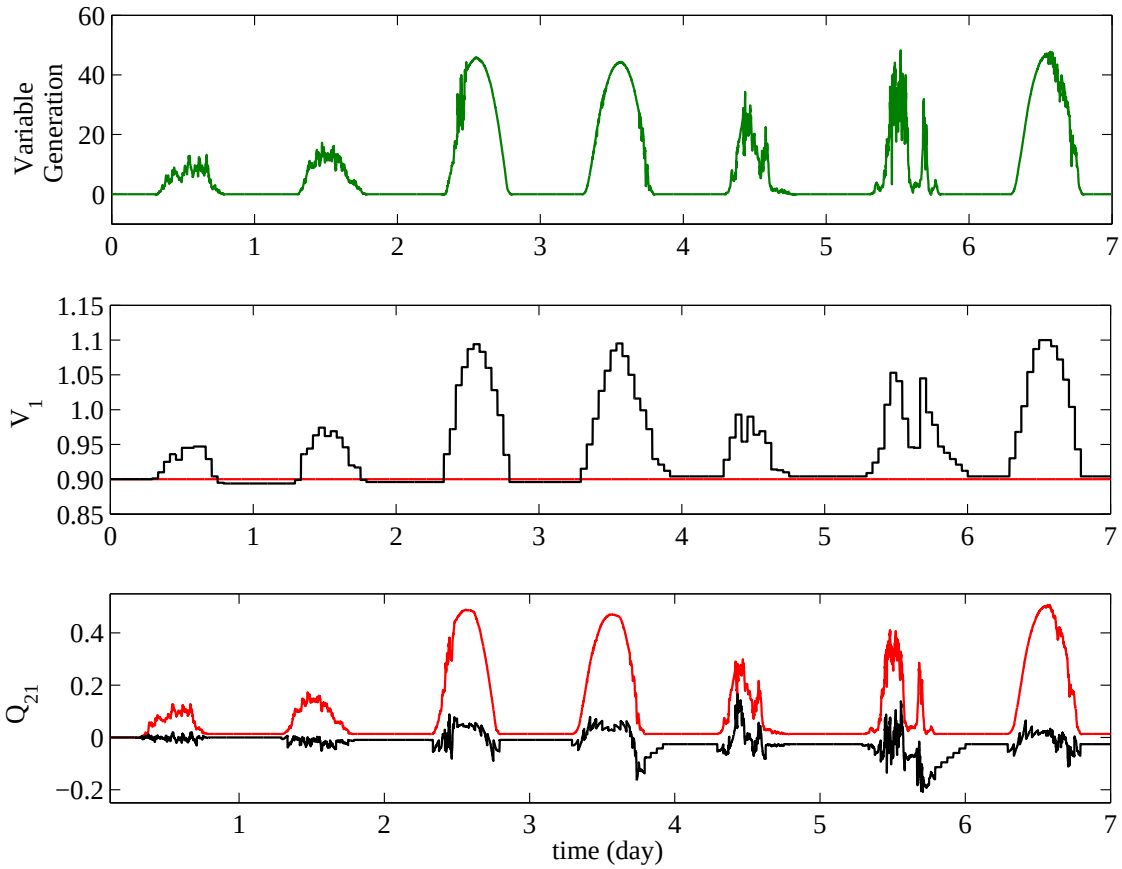

Figure 5.15: Comparison of the proposed voltage control scheme (black) with full voltage control (red)

Section 5.7.

The moving horizon method steps as applied to the optimal voltage control problem are as follows:

1. Choose a horizon, say 120 minutes.
2. Choose a time-step, say 5 minutes.
3. Determine an optimal set-point that remains constant for all time-steps in the horizon.
4. Implement the set-point for the first time step (5 minutes).
5. Move the horizon along by one time-step (5 minutes) and repeat the process.

Notice that the optimal set-point in step 3 is obtained by enumeration. This means that for each time horizon the system dynamics is simulated based on generation and load data and the number of tap operations and the network loss is recorded. This simulation is repeated for each setpoint value in the discretized feasible range. The setpoint that minimizes

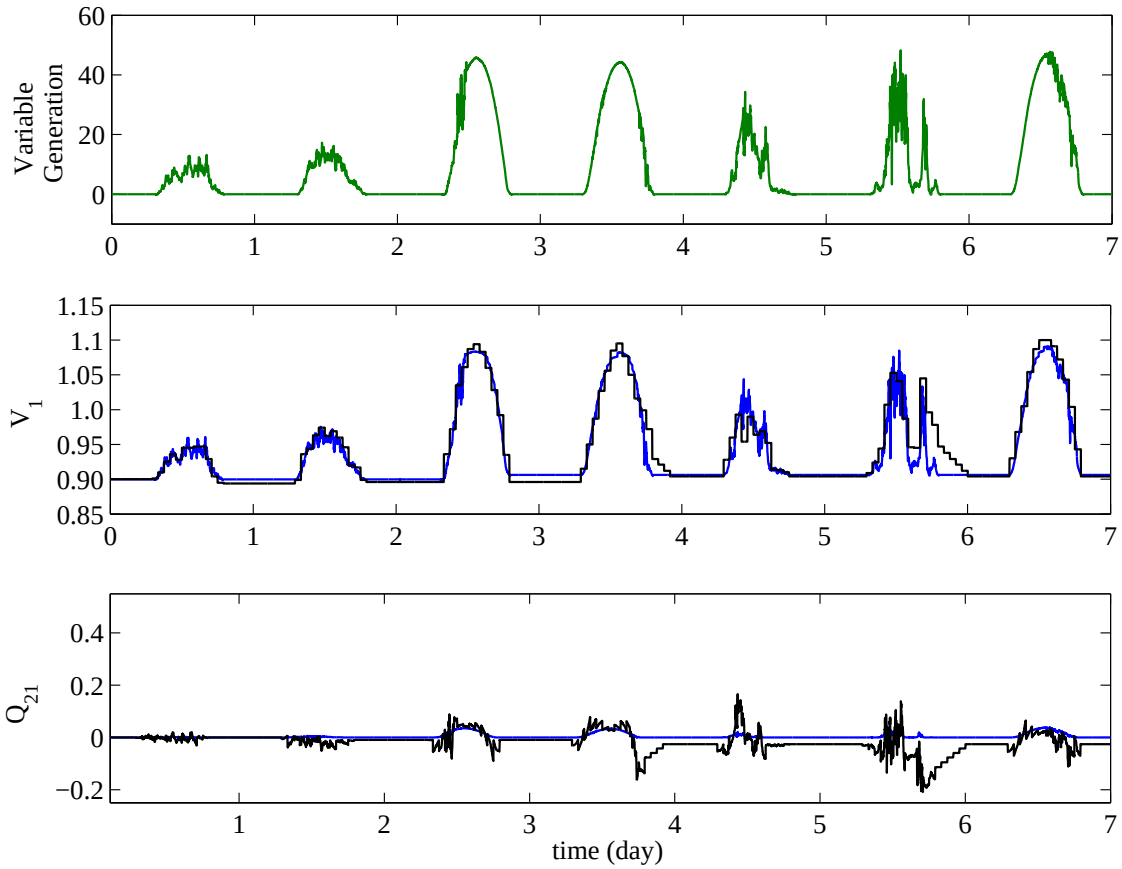

Figure 5.16: Comparison of the proposed voltage control scheme (black) with no voltage control (blue)

the weighted sum of OLTC operations is declared optimal for that time horizon. Also the horizon and time step lengths are chosen based on simulation and observation and thus empirically. This combination and similar combinations such as 120/30, 120/20 and 120/10 have better performances compared to other combinations. This superior performance is likely related to the statistical characteristics and patterns of variability of wind and solar generation as well as load.

Figure 5.18 shows the results for a 120 minutes horizon and the 6 time steps of 5, 10, 20, 30, 60 and 120 minutes are shown as black circles. The choice of horizon and time-step lengths are based on empirical observations. However, here, a longer horizon of 120 minute is chosen as it is more effective in reducing the number of distribution operations. For example a 120/5 combination results in an annual figures of 1.0×10^4 and 6×10^3 tap operations for the distribution and sub-transmission OLTCs. For a 20/5 combination these figures are 1.5×10^4 and 5×10^3. The performance of the proposed method in Section 5.6.1 is shown in red circles. As the control parameter (the fine-tuning range) changes the

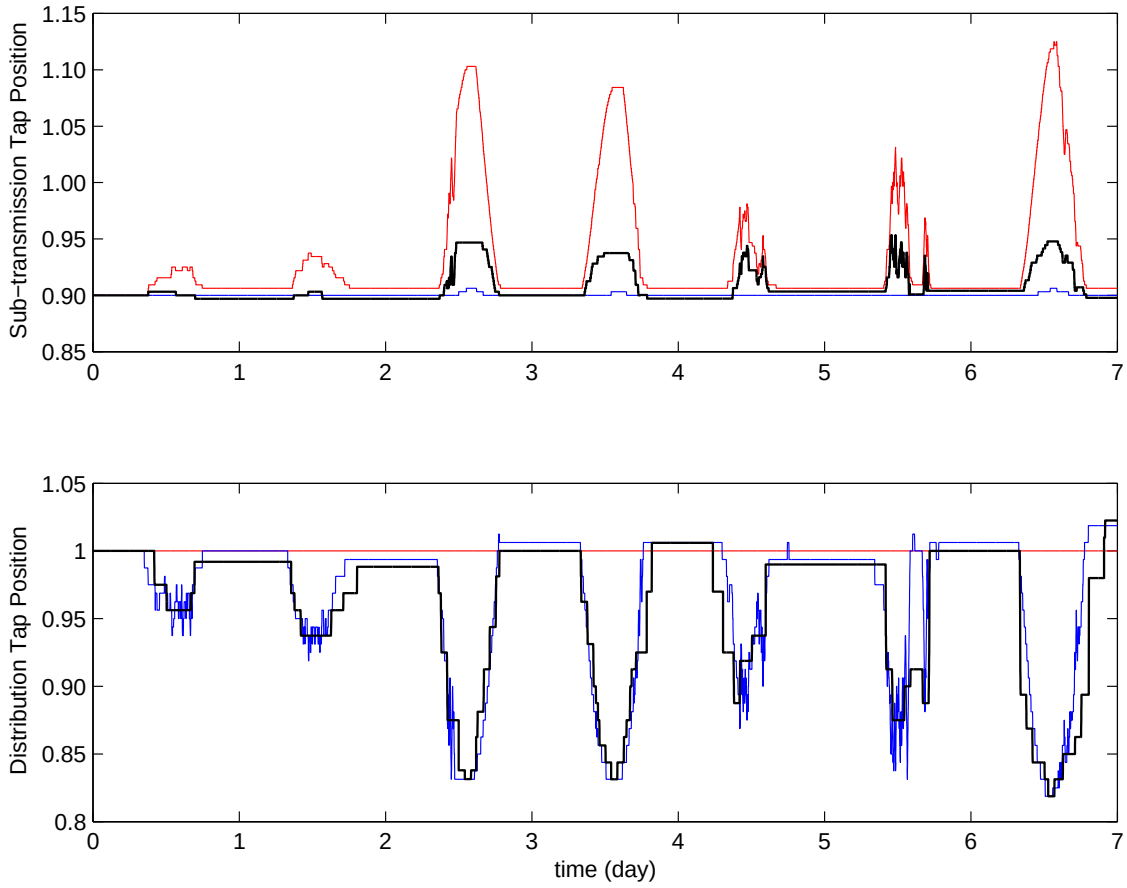

Figure 5.17: Comparison of tap operations between the no voltage control (blue), full voltage control (red) and the proposed coordinated voltage control scheme (black)

proposed MPC method makes a smooth and continuous transition between the two end of the spectrum whereas in the moving horizon MPC scheme there is an uneven change in the performance between adjacent time steps. So for example the results of 120/5 and 120/4 combinations are not necessarily close. In other words as time steps change from 5 to 10 minutes in one minute increments there is not a smooth transition from the OLTC reduction performance corresponding to 5 minute to that corresponding to 10 minute.

As seen in Figure 5.18 this particular version of moving horizon MPC strategy is not as effective in reducing the sub-transmission operations as the proposed fine-tuning MPC method. It can not follow generation variability as effectively as the proposed method. The reduction in the distribution operations is really small (1.0×10^4 versus 1.1×10^4 annual operations for the 120/5 combination). Among reasons for inferior performance of this moving horizon MPC scheme is the very weak dynamic coupling from one time step to the other in terms of tap error in (5.8). If there had been a significant tap error, passed from one time step to another, the moving horizon strategy would have performed

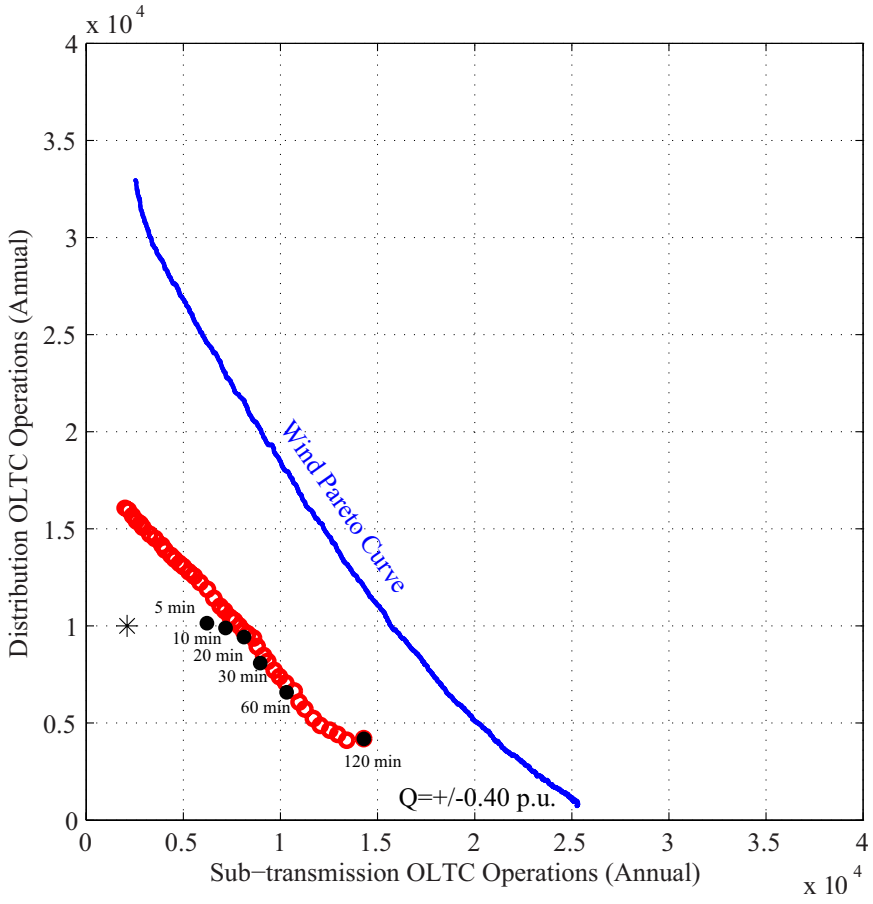

Figure 5.18: Red circles correspond to the varying feasible ranges for *fine-tuning every 5 minutes* around the 2hr optimal setpoint (Wind generation). Black circles corresponding to varying time-step lengths for the conventional moving horizon MPC.

better. However in discrete tap model or even continuous tap model with reasonable time constants T, there is little dynamic coupling between adjacent time steps. Other moving horizon MPC formulations may outperform this strategy.

5.6.3 A More Effective Drafting of Network Losses

In a resistive network, loss reduction is an indispensable feature of any voltage coordination scheme. Due to the strong coupling of both active and reactive power flows with node voltages and in the presence of active power variations, voltage regulation may entail massive flows of reactive power throughout the network. This could lead to unacceptably high active power losses.

Among the previously mentioned studies which have introduced optimization schemes

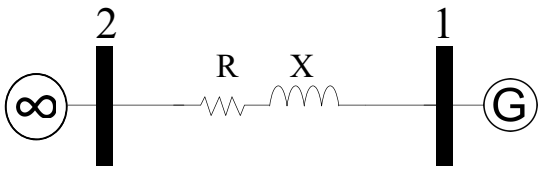

Figure 5.19: Two-bus network

for minimizing the number of tap-changing operations of OLTC transformers in vicinity of DGs some have considered a fixed weight factor to incorporate the loss into the objective function [16, 76]. The problem with such an approach is that (1) loss and number of tap-changing operations are two different quantities and (2) loss is continuous whereas switching operations are discrete.

Hence, any optimization formulation that relates these two quantities through fixed weighting factors tend to be suboptimal in the sense that under various conditions either the switching operation or the loss may be over- or under-penalized. In such cases a small improvement in loss or tap-changing operations may come at a much greater cost in terms of the other quantity. In fact for such problems, it is often possible to find a different set of weight factors that improves both the number of tap-changing operations and the loss. This is due to the non-convexity and discrete nature of the optimization. Therefore the outcome may be very sensitive to the choice of weight factors. However the set of weight factors that results in the optimal outcome is not known *a priori* and the methods introduced in [16, 76] provide no insight on how to find it. Even if the appropriate set of weights can somehow be obtained for a given time horizon of the problem, the often multi-horizon nature of the optimization may require the weight factors to be adjusted at each optimization interval. For example in the proposed voltage control scheme a particular set of weights may be more appropriate for low generation variability whereas a different set of weights may be more fit for periods of high variability. This is still an open question as how these weights should be adjusted as the generation variability regime or the parameters of the voltage control scheme such as the horizon length change. This adaptive nature of the weight factors further complicates the problem.

Unlike methods that use fixed weights for incomparable quantities, we are drafting the loss reduction into the control strategy without using weight factors. Before introducing the method, we state the following theorem:

Theorem 4 *For the network of Figure 5.19 where V_2 is fixed, $\frac{\partial P_{loss}}{\partial V_1} = 0$ (the active power*

loss is locally minimum with respect to V_1) if and only if the following condition holds:

$$Q_{21}(V_1) = 0 \tag{5.9}$$

Proof:

$$P_{loss} = \frac{R(V_2^2 - V_1^2 + 2(RP_1 + XQ_1))}{R^2 + X^2} \tag{5.10}$$

$$Q_{21} = \frac{X(V_2^2 - V_1^2) + 2RXP_1 + (X^2 - R^2)Q_1}{R^2 + X^2} \tag{5.11}$$

Q_1 is itself also a function of V_1:

$$Q_1 = \frac{XV_1^2 - \sqrt{X^2V_1^4 - (R^2 + X^2)\zeta}}{(R^2 + X^2)} \tag{5.12}$$

Where,

$$\zeta = V_1^4 - 2RP_1V_1^2 - V_1^2V_2^2 + (R^2 + X^2)P_1^2 \tag{5.13}$$

Now by substituting for Q_1, one can check that both $Q_{21} = 0$ and $\frac{\partial P_{loss}}{\partial V_1} = 0$ reduce to the following quadratic polynomial in terms of V_1^2:

$$R^2V_1^4 - (R^2 + X^2)(2RP_1 + V_2^2)V_1^2 + (X^2 - R^2)P_1^2 + X^2(2RP_1 + V_2^2)^2 = 0 \tag{5.14}$$

It should be noted that the unity p.f. at the point of injection ($Q_1 = 0$) has been substituted for $\frac{\partial P_{loss}}{\partial V_1} = 0$ in at least one recent study [16]. However, this condition for a resistive network could be a highly inaccurate substitute for minimum loss. The often sizable reactive loss, exacerbated by the network resistivity, causes these two conditions to diverge. However $Q_{21} = 0$ is under all conditions a precise substitute for minimum loss.

The strategy of the enhanced loss reduction is to allow OLTC operations to drive the operating point as closely as possible toward the $Q_{21} = 0$. This is achieved in the fine-tuning process described earlier in Section 5.6.1. For the fine-tuning interval of, say, 1 minute, we intentionally allow the OLTC operation to be suboptimal by 1 (or 2) operation(s) if that re-

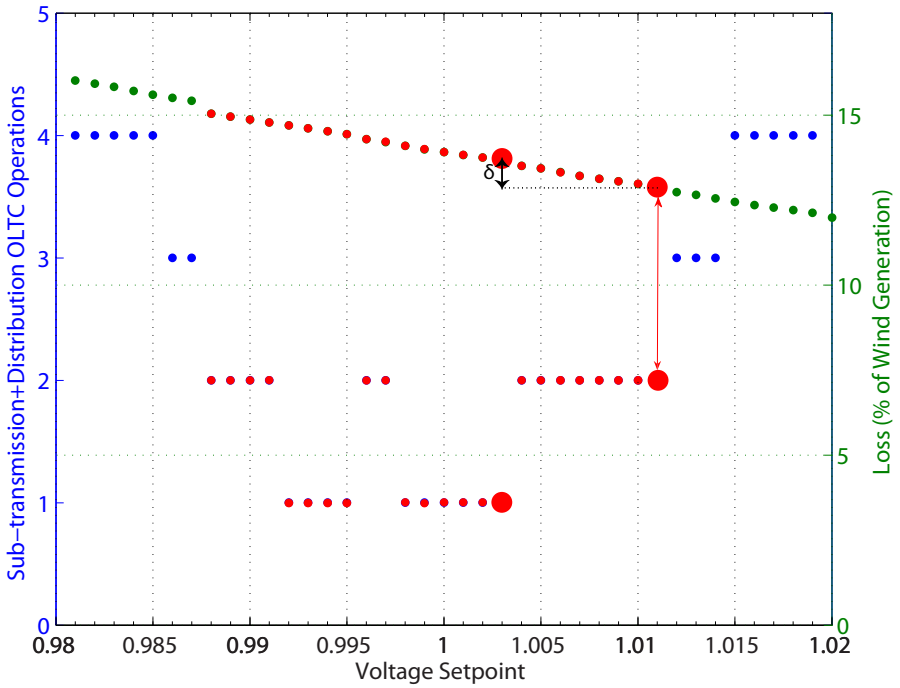

Figure 5.20: Enhanced Loss Reduction: Excess OLTC operation is allowed if $\delta \geq \delta_{loss}$

sults in loss reduction of δ_{loss} compared to BLR. This algorithm is illustrated in Figure 5.20 which is the same case discussed earlier in the context of BLR (see Figure 5.10(b)). Here δ, the loss reduction resulted from allowing one excess operation is greater than a particular δ_{loss}. If the condition $\delta \geq \delta_{loss}$ cannot be satisfied then no excess tap is allowed.

With δ_{loss} chosen at the right order of magnitude which is a relatively wide range of values, the ELR scheme significantly reduces network loss while incurring only a small increase in OLTC operations. For example for the test network of Figure 5.4, δ_{loss} chosen in the range of $0.5 - 2.0\%$ of generation over the period of optimization, say 10 minutes, can reduce the network losses by 5% of the actual generation over the entire period of a year. Figure 5.21 highlights the performance of the loss reduction scheme (in blue) compared to the case where the absolute minimum OLTC operations is chosen. Note that the Q_{21} is driven to zero (as predicted by Theorem 1) with only a few excess tap operations (each tap operation causes a step drop in Q_{21}) whereafter the voltage setpoint follows the wind variations and the number of tap changes are exactly the same between the two cases. This is because the voltage setpoint exactly follows the same generation variability but in different regions. For example in one case the voltage setpoint may vary around 1.00 p.u. and in the other case it may vary around 1.05 p.u. However in both cases the reactive power flow through the upstream transformer is effectively constant. Figure 5.21 correspond to

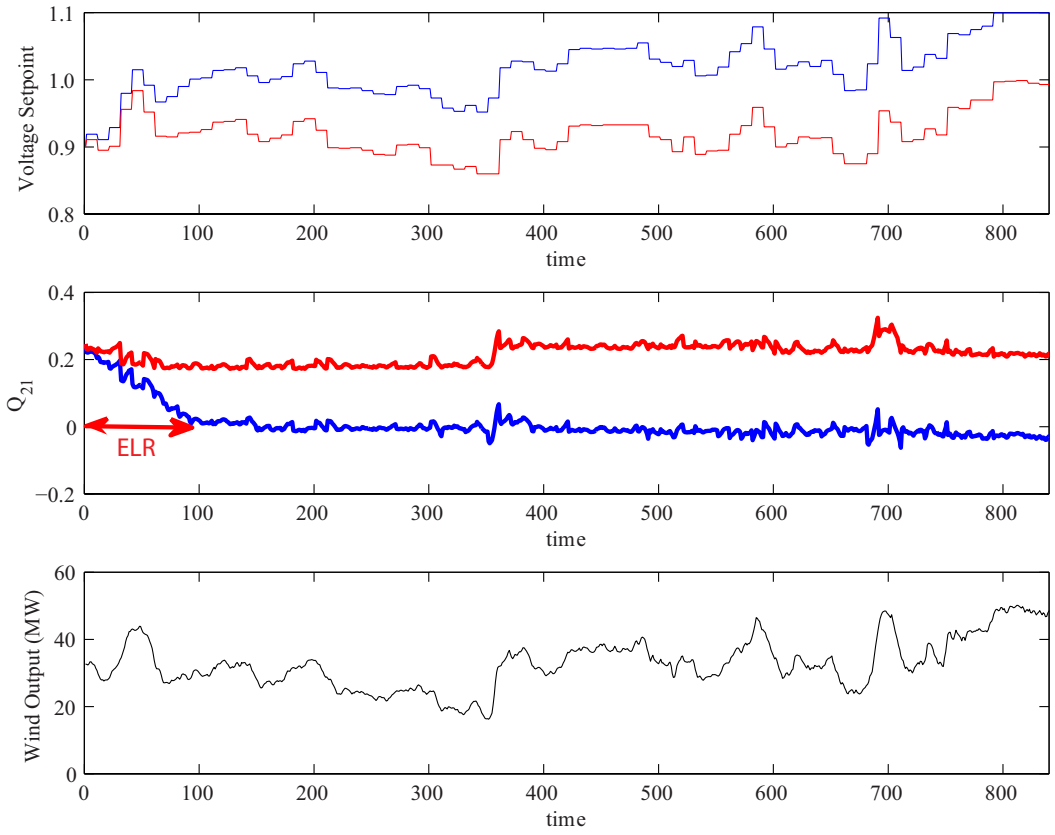

Figure 5.21: Enhanced Loss Reduction (blue) versus Basic Loss Reduction (red)

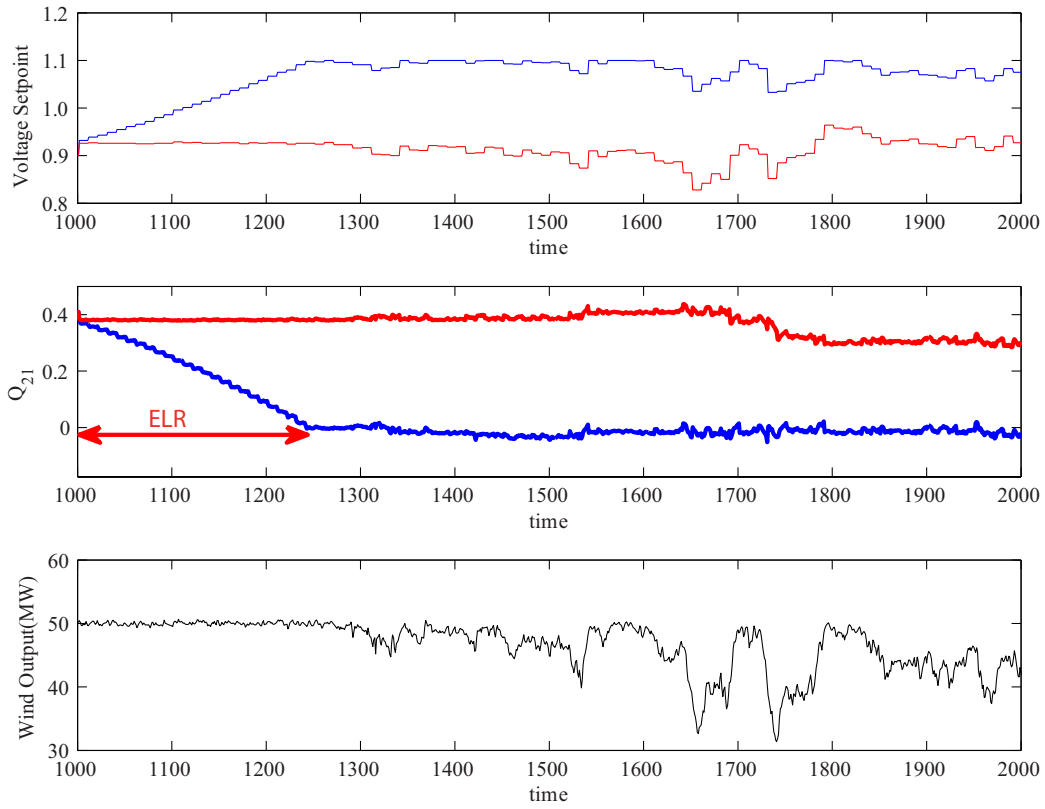

Figure 5.22: Enhanced Loss Reduction (blue) versus Basic Loss Reduction (red)

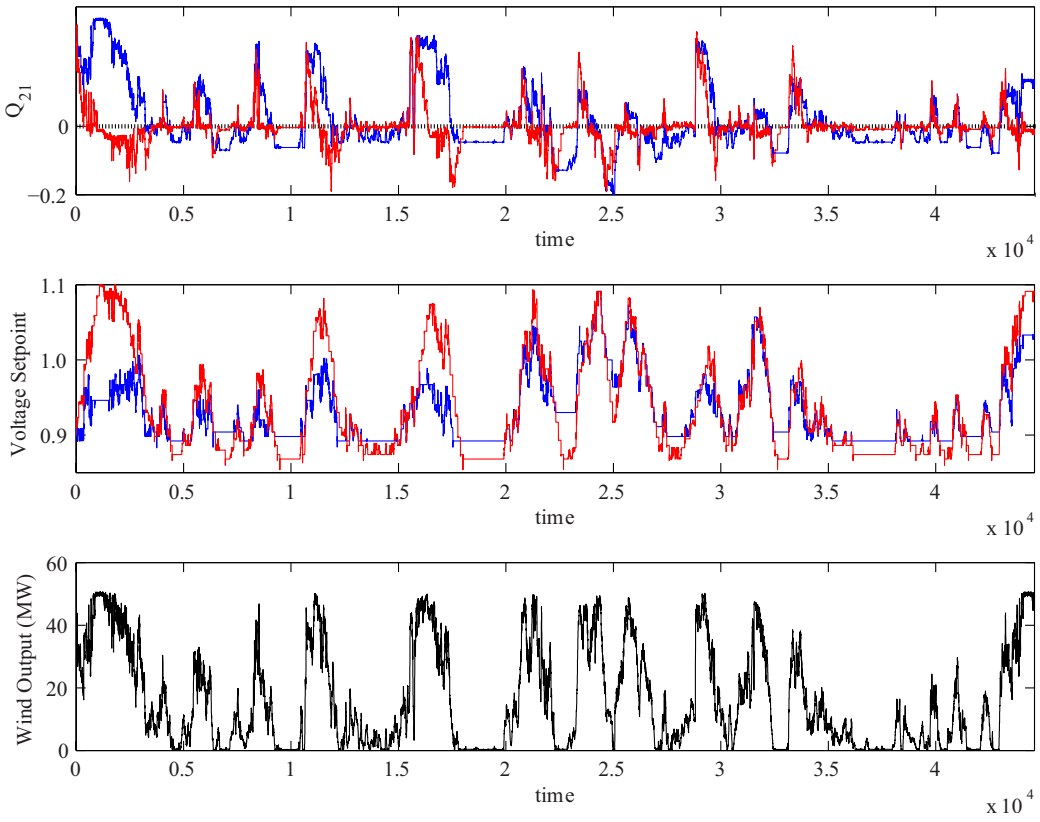

Figure 5.23: ELR (red) versus BLR (blue) in terms of reactive flow into the network

a highly variable wind output. Figure 5.22 shows the same process but for the case of steady wind output. Here the tap changes are more visible and correspond to downward drops in the Q_{21}. It should be stressed that the performance is not sensitive to the choice of δ_{loss} within a wide range of values which can be determined empirically in advance as it is expected to vary for different operating systems. This phenomenon is explained by Theorem 4 that relates loss minimization to the reactive flow into resistive network. In fact the tendency of Q_{21} to move toward zero is a corollary of choosing setpoint in a way as to reduce losses by allowing excess tap. If δ_{loss} is too large the control scheme restricts the capability of OLTCs to drive the operating point toward $Q_{21} = 0$ resulting in higher loss. This is understood by analyzing Figure 5.20. Note that here by allowing an excess tap operation, the setpoint can be changed from $1.003p.u.$ to $1.011p.u.$ and this results in loss reduction roughly equal to 1% of wind generation for the optimization period. Had δ_{loss} been set to a much higher value no excess tap would have occurred and the losses would have been much higher. At the other extreme, a value of δ_{loss} that is too small would allow excessive distribution OLTC operations for an insignificant reduction in loss. This is due to the high sensitivity of the distribution tap to voltage setpoint which is the primary side voltage of the distribution transformer. Anywhere far from these two extremes the performance of the control scheme is almost identical in terms of reduction in OLTC operations and network loss. With this approach, not only the sensitivity of the outcome to the choice of weight factors has been reduced but also a clear relation between the tap change and the loss reduction is established. The network operator can decide on a lower bound on loss reduction below which excess OLTC tap operation(s) are not justified. Therefore, the issue of arbitrary decision-making process is averted. In Figures 5.21 and 5.22, similar mechanism for loss reduction depicted in Figure 5.20 with δ_{loss} chosen as 1% of generation, is applied for every single time window over the course of optimization.

Figure 5.23 contrasts the performance of ELR and BLR on the flow of reactive power into the network. Note especially that Q_{21} is much closer to zero in ELR (red) versus BLR (blue). This saves an additional 6% of the generation, that would have been lost in the BLR case (blue) whereas the increase in tap operations, sub-transmission and distribution combined, is only 3%. This slight increase once translated into economic terms (extended life-time of OLTCs) is negligible in contrast to the economic benefits of enhanced efficiency of power delivery. This relationship between the reactive flow and the loss which was investigated earlier plays an important role in the formulation of the optimization problem in the next section.

5.7 Optimization

As a first step toward formulation of an optimization problem for the control scheme, we need to find an appropriate substitute for the loss in the objective function. Unlike the network of Figure 5.19 or the generic test network of Figure 5.4, it is not generally possible to find an explicit function for loss in terms of controllable parameters. However, one can expect that the relationship between reactive flow into a resistive network and loss as stated in the theorem holds in general. This relationship has already been suggested for the DTE/ITC system in Section 3.2.1 and is in agreement with the observations made later in Section 5.8. A more conclusive statement requires further investigation in the context of larger networks. Figure 5.24 shows the OLTC operations, loss and the Euclidian norm (2-norm) of the reactive flow into the sub-transmission network, $||Q_{21}||_2$, as a function of voltage setpoint for the network of Figure 5.4 for a 30 minute time window. Notice that as observed in Figure 5.24 the 2-norm of the reactive flow for that time window, with appropriate scaling, is almost a linear approximation for the loss. The discontinuity at $V_{sp} = 1.01$ is due to the fact that the reactive power flow during that time window changes sign and hence the 2-norm starts to increase and with it the network loss. The linear assumption is due to the constant sensitivity factors that relate network variables such as voltage magnitudes and reactive power flows to voltage setpoints of variable generation nodes. The optimization formulation relies on the observation that these factors are almost constant and hence are independent of the operating conditions. This is a reasonable assumption when the system is operating far away from its loadability limits where nonlinearity of power flow equations is most evident. As demonstrated in chapter 4, this assumption has strong justification for the case of active power injections into sub-tranmission/distribution networks where the distance to saddle-node bifurcation is substantially increased as a result of high resistivity of feeders. Furthermore observations based on the DTE/ITC system strongly support this assumption.

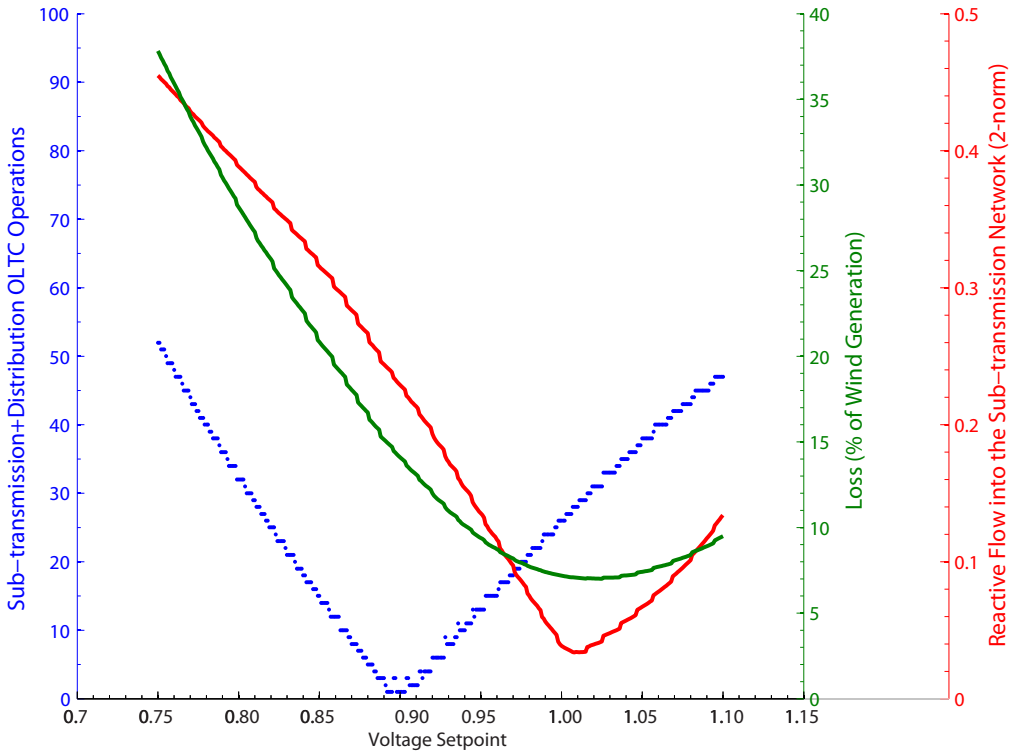

Figure 5.24: Reactive Flow into Resistive Network as a Substitute for Loss

5.7.1 Discrete (DB) Tap Model with BLR

The previous results are all based on obtaining a map between the voltage setpoint and the number of OLTC operations and network loss. Such a map is highly non-convex and requires an exhaustive search to determine its image which is then used to find the globally optimal voltage setpint that minimizes OLTC operations and active power loss corresponding to a given time window. Alternatively this exhaustive search problem can be formulated as a mixed-integer problem where the task of finding the global solution is relegated to heuristic-based algorithms utilized by mixed-integer programming (MIP) solvers in Gurobi or CPLEX. This formulation does not change the complexity of the problem but makes the process of obtaining the solution more efficient by relying on commercially developed solvers. As explained later this efficiency comes at the expense of accuracy which is slightly affected due to non-constant sensitivity factors. Below is a mixed-integer formulation that minimizes tap change occurrences and reactive flow into the network (a surrogate for loss).

$$\overset{*}{V}_{\text{sp}} = \underset{V_{\text{sp}}}{\operatorname{argmin}} \sum_{k=1}^{t} |s_{\text{st}}^{(k)}| + \sum_{k=1}^{t} |s_{\text{d}}^{(k)}| + a||\vec{Q}_{21}||_2 \tag{5.15}$$

subject to:

$$L_{\text{st}}^{(i)} = \Delta_{\text{st}}^{(i)} + DB + \frac{\partial V_2}{\partial n_{\text{st}}} \sum_{k=1}^{i-1} s_{\text{st}}^{(k)} + \frac{\partial V_2}{\partial n_{\text{d}}} \sum_{k=1}^{i-1} s_{\text{d}}^{(k)}, \forall\, i = 1...t \tag{5.16}$$

$$U_{\text{st}}^{(i)} = \Delta_{\text{st}}^{(i)} - DB + \frac{\partial V_2}{\partial n_{\text{st}}} \sum_{k=1}^{i-1} s_{\text{st}}^{(k)} + \frac{\partial V_2}{\partial n_{\text{d}}} \sum_{k=1}^{i-1} s_{\text{d}}^{(k)}, \forall\, i = 1...t \tag{5.17}$$

$$\Delta_{\text{st}}^{(i)} = V_2^{(0)} - V_2^{\text{sched}} + \frac{\partial V_2}{\partial P_{\text{g}}}(P_{\text{g}}^{(i)} - P_{\text{g}}^{(0)}) + \frac{\partial V_2}{\partial V_{\text{sp}}}(V_{\text{sp}} - V_{\text{sp}}^{(0)}) \tag{5.18}$$

$$s_{\text{st}}^{(i)} L_{\text{st}}^{(i)} \leq \epsilon L_{\text{st}}^{(i)},\ \forall\, i = 1...t \tag{5.19}$$

$$s_{\text{st}}^{(i)} U_{\text{st}}^{(i)} \leq -\epsilon U_{\text{st}}^{(i)},\ \forall\, i = 1...t \tag{5.20}$$

$$L_{\text{d}}^{(i)} = \Delta_{\text{d}}^{(i)} + DB + \frac{\partial V_d}{\partial n_{\text{st}}} \sum_{k=1}^{i-1} s_{\text{st}}^{(k)} + \frac{\partial V_{\text{d}}}{\partial n_{\text{d}}} \sum_{k=1}^{i-1} s_{\text{d}}^{(k)}, \forall\, i = 1...t \tag{5.21}$$

$$U_{\text{d}}^{(i)} = \Delta_{\text{d}}^{(i)} - DB + \frac{\partial V_{\text{d}}}{\partial n_{\text{st}}} \sum_{k=1}^{i-1} s_{\text{st}}^{(k)} + \frac{\partial V_{\text{d}}}{\partial n_{\text{d}}} \sum_{k=1}^{i-1} s_{\text{d}}^{(k)}, \forall\, i = 1...t \tag{5.22}$$

$$\Delta_{\text{d}}^{(i)} = V_{\text{d}}^{(0)} - V_{\text{d}}^{\text{sched}} + \frac{\partial V_{\text{d}}}{\partial P_{\text{g}}}(P_{\text{g}}^{(i)} - P_{\text{g}}^{(0)}) + \frac{\partial V_{\text{d}}}{\partial V_{\text{sp}}}(V_{\text{sp}} - V_{\text{sp}}^{(0)}) \tag{5.23}$$

$$s_{\text{d}}^{(i)} L_{\text{d}}^{(i)} \leq \epsilon L_{\text{d}}^{(i)},\ \forall\, i = 1...t \tag{5.24}$$

$$s_{\text{d}}^{(i)} U_{\text{d}}^{(i)} \leq -\epsilon U_{\text{d}}^{(i)},\ \forall\, i = 1...t \tag{5.25}$$

$$Q_{21}^{(i)} = Q_{21}^{(0)} + \frac{\partial Q_{21}}{\partial P_{\text{g}}}(P_{\text{g}}^{(i)} - P_{\text{g}}^{(0)}) + \frac{\partial Q_{21}}{\partial V_{\text{sp}}}(V_{\text{sp}} - V_{\text{sp}}^{(0)}) + \frac{\partial Q_{21}}{\partial n_{\text{st}}} \sum_{k=1}^{i-1} s_{\text{st}}^{(k)} + \frac{\partial Q_{21}}{\partial n_{\text{d}}} \sum_{k=1}^{i-1} s_{\text{d}}^{(k)}$$
$$, \forall\ i = 1...t \tag{5.26}$$

t : Length of the time window
$\vec{S}_{\text{st}} = [s_{\text{st}}^{(1)}, ..., s_{\text{st}}^{(t)}]$: Vector of sub-transmission tap changes ($s_{\text{st}} \in \{-1, 0, 1\}$)
$\vec{S}_{\text{d}} = [s_{\text{d}}^{(1)}, ..., s_{\text{d}}^{(t)}]$: Vector of distribution tap changes ($s_{\text{d}} \in \{-1, 0, 1\}$)
$\vec{Q}_{21}$: Vector of reactive power flow into the resistive feeder from Bus 2 toward Bus 1
$V_{\text{sp}}^{(0)}$: Voltage setpoint prior to the beginning of the time window
$\Delta_{\text{st}}^{(i)}$: Voltage error at sub-transmission OLTC regulated bus (Bus 2) at time i
$L_{\text{st}}^{(i)}$: Value of the voltage magnitude at sub-transmission OLTC regulated bus (Bus 2) relative to the lower band at time i
$U_{\text{st}}^{(i)}$: Value of the voltage magnitude at sub-transmission OLTC regulated bus (Bus 2) relative to the upper band at time i
$\Delta_{\text{d}}^{(i)}$: Voltage error at distribution OLTC regulated bus (Bus d) at time i
$L_{\text{d}}^{(i)}$: Value of the voltage magnitude at distribution OLTC regulated bus (Bus d) relative to the lower band at time i
$U_{\text{d}}^{(i)}$: Value of the voltage magnitude at distribution OLTC regulated bus (Bus d) relative to the upper band at time i
a: scaling constant so that $a||\vec{Q}_{21}||_2 \ll 1$
ϵ: a small constant so that $\epsilon \ll |L_{\text{st}}^{(i)}|, |U_{\text{st}}^{(i)}|$

Notice that (5.32) through (5.36) form the block of constraints related to the sub-transmission OLTCs and (5.37) through (5.41) form the block of constraints related to the distribution OLTCs. These block can be replicated to represent multiple transformers. Also notice that throughout this section we have considered fixed setpoint for a given time window. However this optimization can be extended to represent a sequence of optimal setpoint for each time step within a given time window by the following modifications in (5.18), (5.23) and (5.26):

$$\Delta_{\text{st}}^{(i)} = V_2^{(0)} - V_2^{\text{sched}} + \frac{\partial V_2}{\partial P_{\text{g}}}(P_{\text{g}}^{(i)} - P_{\text{g}}^{(0)}) + \frac{\partial V_2}{\partial V_{\text{sp}}}(V_{\text{sp}}^{(i)} - V_{\text{sp}}^{(0)}) \tag{5.27}$$

$$\Delta_{\text{d}}^{(i)} = V_{\text{d}}^{(0)} - V_{\text{d}}^{\text{sched}} + \frac{\partial V_{\text{d}}}{\partial P_{\text{g}}}(P_{\text{g}}^{(i)} - P_{\text{g}}^{(0)}) + \frac{\partial V_{\text{d}}}{\partial V_{\text{sp}}}(V_{\text{sp}}^{(i)} - V_{\text{sp}}^{(0)}) \tag{5.28}$$

$$Q_{21}^{(i)} = Q_{21}^{(0)} + \frac{\partial Q_{21}}{\partial P_{\mathrm{g}}}(P_{\mathrm{g}}^{(i)} - P_{\mathrm{g}}^{(0)}) + \frac{\partial Q_{21}}{\partial V_{\mathrm{sp}}}(V_{\mathrm{sp}}^{(i)} - V_{\mathrm{sp}}^{(0)}) + \frac{\partial Q_{21}}{\partial n_{\mathrm{st}}}\sum_{k=1}^{i-1} s_{\mathrm{st}}^{(k)} + \frac{\partial Q_{21}}{\partial n_{\mathrm{d}}}\sum_{k=1}^{i-1} s_{\mathrm{d}}^{(k)}$$
$$, \forall\, i = 1...t \tag{5.29}$$

Notice that in the above constraints V_{sp} is replaced by $V_{\mathrm{sp}}^{(i)}$. This change as insignificant as it may appear, substantially increases the computational complexity of the mixed-integer formulation and therefore the fixed setpoint version of the problem which is still a reasonably complicated formulation is implemented instead.

The key part of the optimization is comprised of the constraints (5.16) and (5.17) for the sub-transmission OLTCs and (5.19) and (5.20) for the distribution OLTCs where the OLTC controlled voltage magnitudes are related, through sensitivity factors, to the OLTC AVR deadband, variable generation output and voltage setpoint (decision variable) and discrete tap changes. Figure 5.25 shows how the signed magnitudes of L and U determine the tap adjustment from the given set of possibilities ($s \in \{0, -1, 1\}$). These constraints are designated *asymptotic* due to the role of epsilon which enforces the constraints as it approaches zero [100]. These relations are explained in Table 5.1.

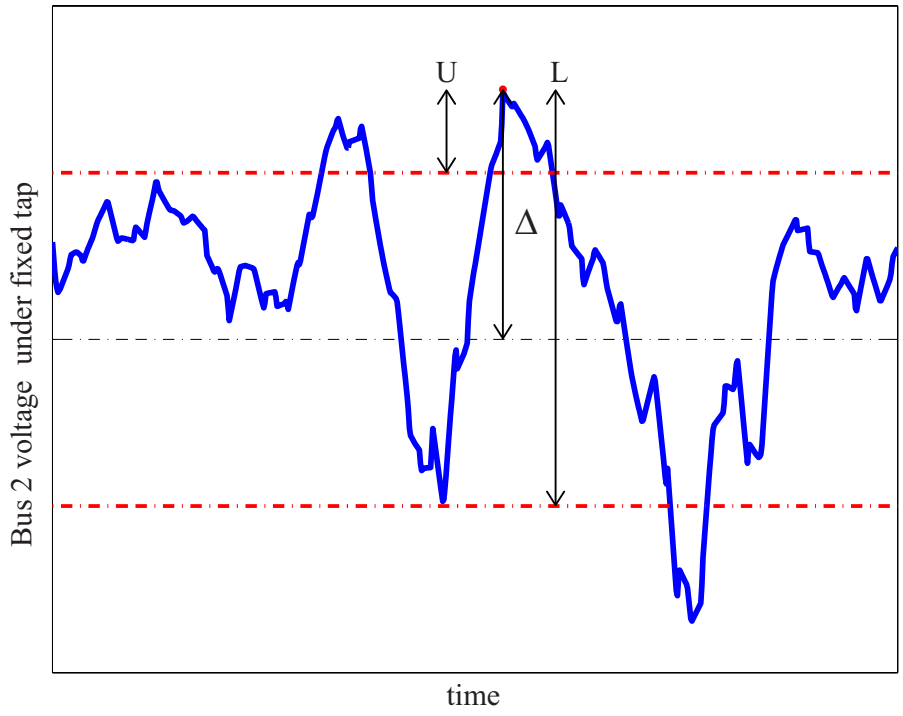

Figure 5.25: Asymptotic Constraints

The above MIP formulation has been implemented for the test network with annual

$sL \leq \epsilon L$	$0 \leq U \leq L \rightarrow s = -1$
$sU \leq -\epsilon U$	$U \leq 0 \leq L \rightarrow s = 0$
	$U \leq L \leq 0 \rightarrow s = 1$

Table 5.1: Asymptotic Constraints

wind and PV generation data and the results are shown in Figures 5.26 -5.27 as green squares corresponding to varying time windows of 1 minute to 2 hours. The green squares do not perfectly overlap the black dots obtained through exhaustive search. However, the optimal voltage setpoint profile and the corresponding tap operations are strikingly similar. To better illustrate the effectiveness of the MIP method, the comparison between the two methods for the case where voltage setpoint is adjusted every 10 minutes to reduce the number of tap operations over the period of a month is presented in Figure 5.28. The blue graph is the trajectory of the actual optimal setpoint obtained by mapping the setpoint to the number of tap operations. This mapping is obtained by exhaustive search which requires repeated simulations that solve nonlinear power flows. The red graph shows the trajectory obtained by estimating the optimal voltage setpoint for every 10 minutes based on Mixed-Integer programming. This is computationally less intensive and can be scaled up and implemented effectively for larger systems. However it does not *perfectly* replicate the trajectory of the exhaustive search and the results are slightly suboptimal.

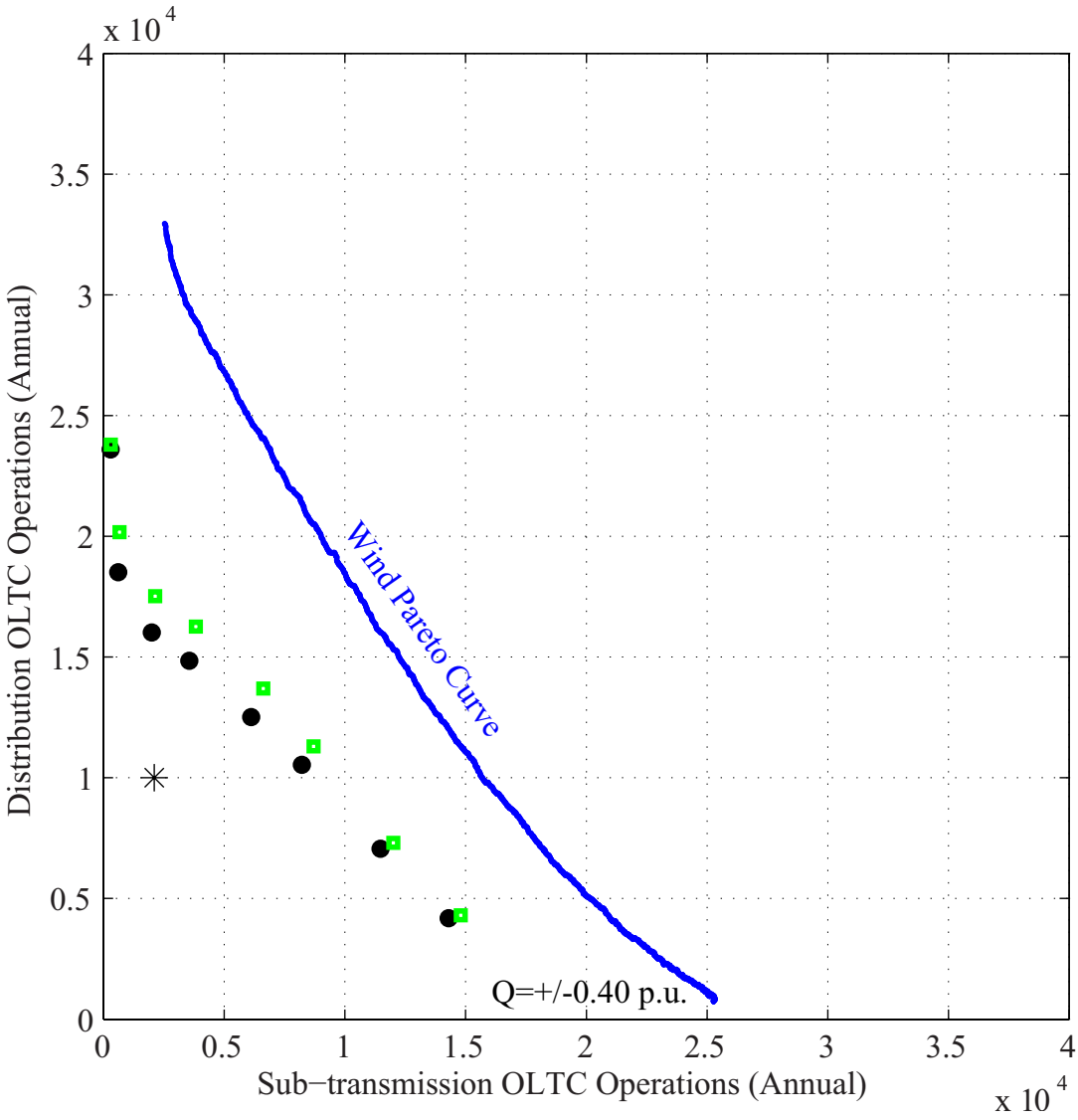

Figure 5.26: OLTC operation reduction performance: Comparison between exhaustive search and MIP formulation (Wind generation)

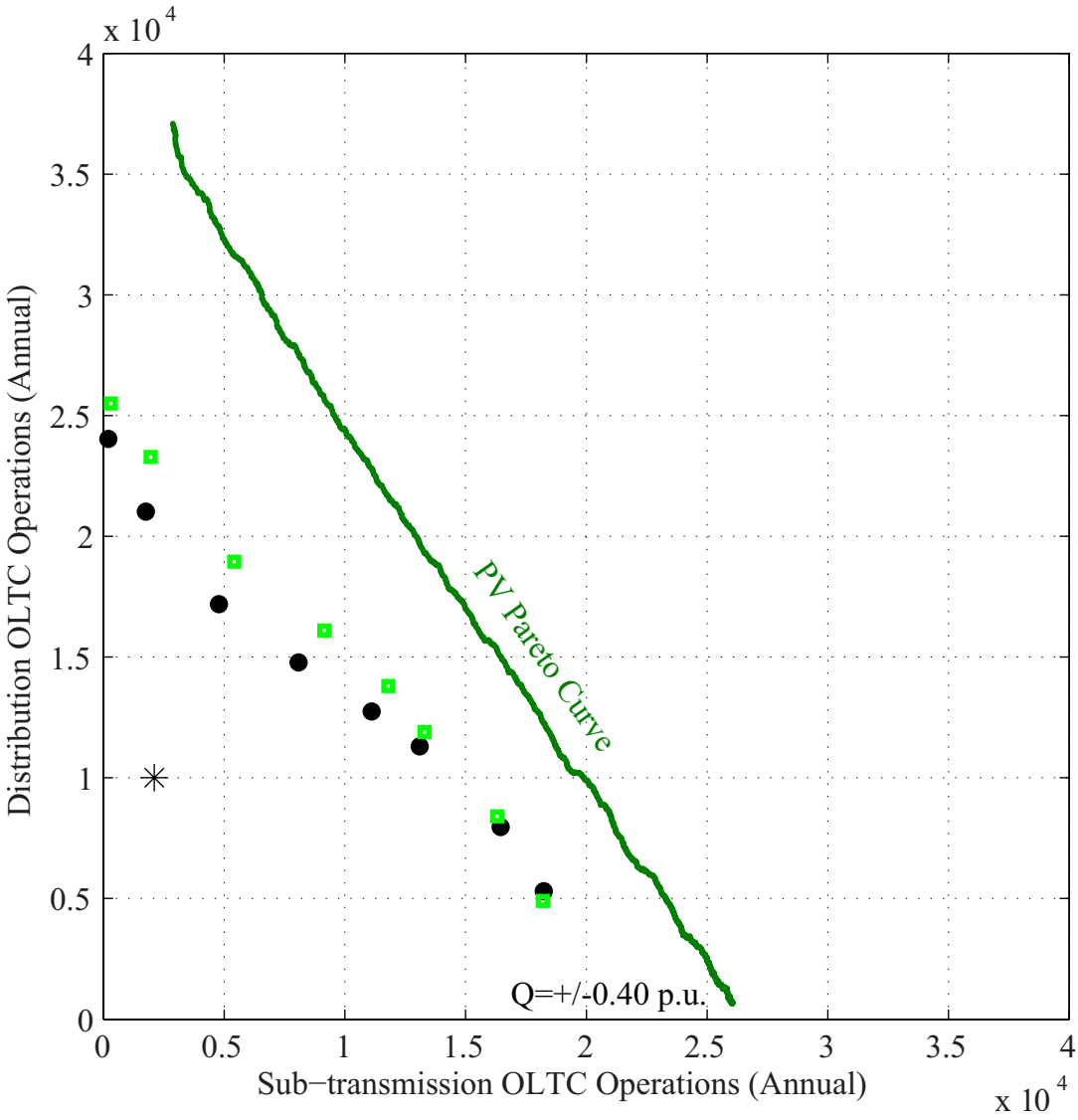

Figure 5.27: OLTC operation reduction performance: Comparison between exhaustive search and MIP formulation (PV generation)

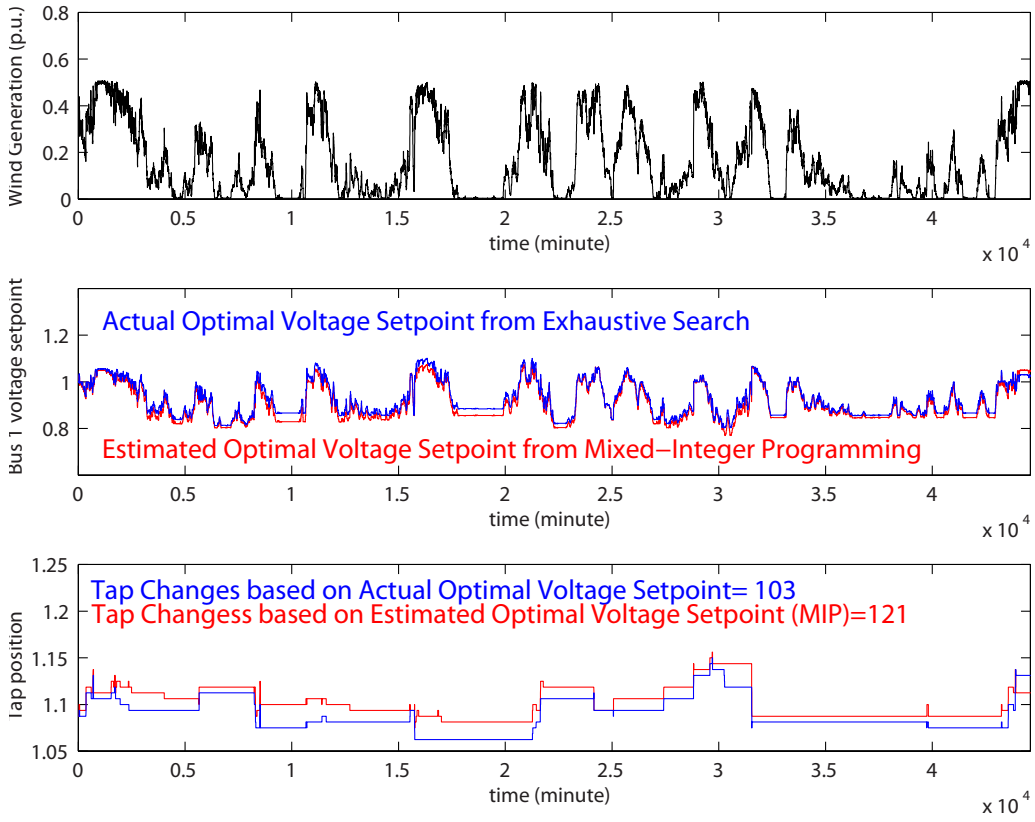

Figure 5.28: Comparison between Exhaustive Search and Mixed-Integer Optimization

The reason for this slight inaccuracy of the mixed-integer optimization results compared to the exhaustive search can be explained through analyzing Figure 5.29(a). The mapping of voltage setpoint to the number of tap operations obtained by exhaustive search is in blue color. The discrete plot in red color shows the feasible region that the MIP formulation sees for a typical 10 minute time window. Notice that in contrast to the blue plot, the red plot is not explicitly computed. The feasible region in red is an estimate of the actual mapping in blue and, as seen in the detail (Figure 5.29(b)), does not perfectly overlap the actual mapping. The occurrence of such cases, though infrequent, explains why tap reduction of MIP based voltage control is slightly sub-optimal. These infrequent cases occur due to the fact that sensitivity factors used in the MIP formulation are not perfectly constant and vary slightly as the loading and generation conditions vary. The more robust a system is (in terms of short circuit capacity), the more rigid the sensitivity factors are. This issue is resolved in the case of DTE/ITC system where the sensitivity factors are much more rigid, under normal load and generation conditions, compared to those of the test network of Figure 5.4.

A comment should be made on the striking efficiency of the MIP solvers used in Gurobi in finding the global solution. As Figure 5.29(a) shows, the feasible region is highly non-convex. Nonetheless a close examination of a fairly good number of cases where there were discrepancies between the exhaustive search and MIP solutions, revealed no instance where the MIP had failed to obtain the global solution of its feasible region. The feasible region for the MIP formulation was obtained by fixing the voltage setpoint (the decision variable) at a predefined value and solving the control variables of the MIP optimization problem (i.e. the number of operation for each OLTC). As this setpoint value changes in small increments the feasible region seen by the MIP problem is mapped (see the red dots in Figure 5.29(b)). However as noted above, this feasible region is not perfectly similar to the feasible region of the original problem due to sensitivity factors that are not perfectly constant.

5.7.2 Discrete (DB) Tap Model with ELR

Solving the previous problem, we obtain $\overset{*}{V}_{\text{sp}}^{\text{B}}$, $\vec{S}_{\text{st}}^{\text{B}}$, $\vec{S}_{\text{d}}^{\text{B}}$ where B denotes the BLR solution. Now having these three parameters, the following constraint is added to the previously stated MIP formulation to obtain the ELR solution,

$$||Q_{21}^{\text{B}}||_2 - ||Q_{21}||_2 \geq \delta_q \tag{5.30}$$

Where Q_{21}^{B} is obtained by substituting V_{sp}, $\vec{S}_{\text{st}}$ and $\vec{S}_{\text{d}}$ in constraint (5.42) by their respective values from the BLR step (i.e. $\overset{*}{V}_{\text{sp}}^{\text{B}}$, $\vec{S}_{\text{st}}^{\text{B}}$, $\vec{S}_{\text{d}}^{\text{B}}$). The ELR problem is then given as,

$$\overset{*}{V}_{\text{sp}} = \underset{V_{\text{sp}}}{\operatorname{argmin}} \sum_{k=1}^{t} |s_{\text{st}}^{(k)}| + \sum_{k=1}^{t} |s_{\text{d}}^{(k)}| + a||\vec{Q}_{21}||_2 \tag{5.31}$$

subject to:

$$L_{\text{st}}^{(i)} = \Delta_{\text{st}}^{(i)} + DB + \frac{\partial V_2}{\partial n_{\text{st}}} \sum_{k=1}^{i-1} s_{\text{st}}^{(k)} + \frac{\partial V_2}{\partial n_{\text{d}}} \sum_{k=1}^{i-1} s_{\text{d}}^{(k)}, \forall\, i = 1...t \tag{5.32}$$

$$U_{\text{st}}^{(i)} = \Delta_{\text{st}}^{(i)} - DB + \frac{\partial V_2}{\partial n_{\text{st}}} \sum_{k=1}^{i-1} s_{\text{st}}^{(k)} + \frac{\partial V_2}{\partial n_{\text{d}}} \sum_{k=1}^{i-1} s_{\text{d}}^{(k)}, \forall\, i = 1...t \tag{5.33}$$

$$\Delta_{\text{st}}^{(i)} = V_2^{(0)} - V_2^{\text{sched}} + \frac{\partial V_2}{\partial P_{\text{g}}}(P_{\text{g}}^{(i)} - P_{\text{g}}^{(0)}) + \frac{\partial V_2}{\partial V_{\text{sp}}}(V_{\text{sp}} - V_{\text{sp}}^{(0)}) \tag{5.34}$$

$$s_{\text{st}}^{(i)} L_{\text{st}}^{(i)} \leq \epsilon L_{\text{st}}^{(i)},\ \forall\, i = 1...t \tag{5.35}$$

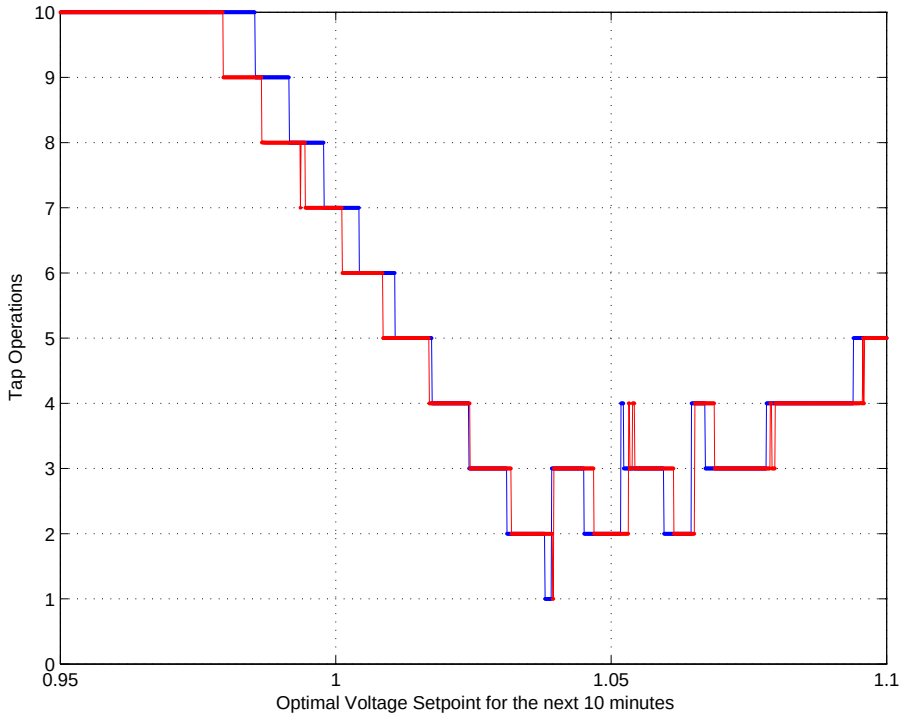

(a) mapping voltage setpoint to number of tap operations for a 10 min time window

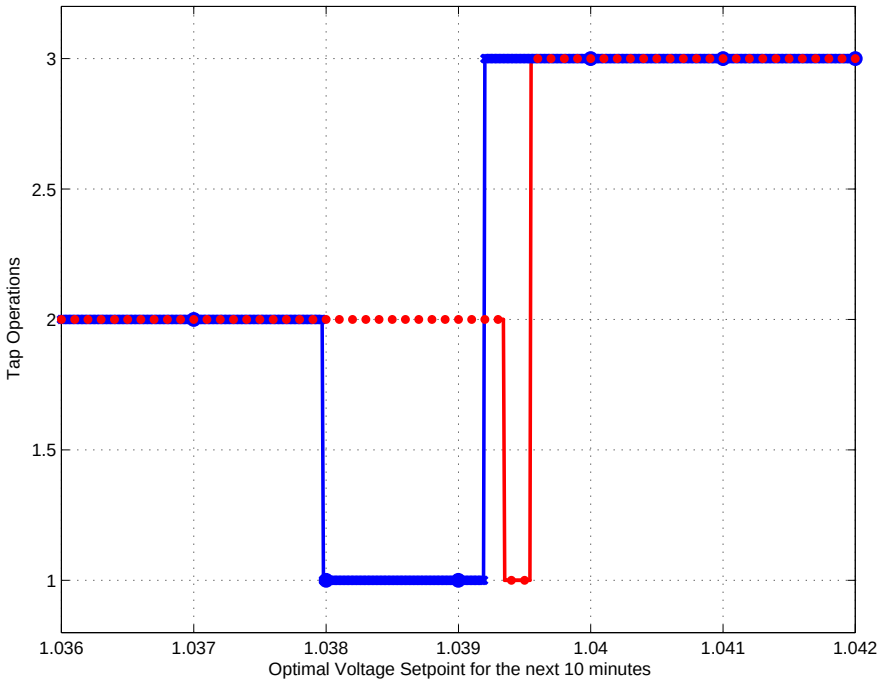

(b) zoom around the globally optimal setpoints (red dots corresponds to fixed setpoints that map the MIP feasible region).

Figure 5.29: Comparison between Exhaustive Search (blue) and Mixed-Integer Optimization (red). The optimal setpoint region in the MIP formulation is highlighted by a solid red line.

$$s_{\text{st}}^{(i)} U_{\text{st}}^{(i)} \leq -\epsilon U_{\text{st}}^{(i)},\ \forall\, i = 1...t \tag{5.36}$$

$$L_{\text{d}}^{(i)} = \Delta_{\text{d}}^{(i)} + DB + \frac{\partial V_d}{\partial n_{\text{st}}} \sum_{k=1}^{i-1} s_{\text{st}}^{(k)} + \frac{\partial V_{\text{d}}}{\partial n_{\text{d}}} \sum_{k=1}^{i-1} s_{\text{d}}^{(k)}, \forall\, i = 1...t \tag{5.37}$$

$$U_{\text{d}}^{(i)} = \Delta_{\text{d}}^{(i)} - DB + \frac{\partial V_{\text{d}}}{\partial n_{\text{st}}} \sum_{k=1}^{i-1} s_{\text{st}}^{(k)} + \frac{\partial V_{\text{d}}}{\partial n_{\text{d}}} \sum_{k=1}^{i-1} s_{\text{d}}^{(k)}, \forall\, i = 1...t \tag{5.38}$$

$$\Delta_{\text{d}}^{(i)} = V_{\text{d}}^{(0)} - V_{\text{d}}^{\text{sched}} + \frac{\partial V_{\text{d}}}{\partial P_{\text{g}}}(P_{\text{g}}^{(i)} - P_{\text{g}}^{(0)}) + \frac{\partial V_{\text{d}}}{\partial V_{\text{sp}}}(V_{\text{sp}} - V_{\text{sp}}^{(0)}) \tag{5.39}$$

$$s_{\text{d}}^{(i)} L_{\text{d}}^{(i)} \leq \epsilon L_{\text{d}}^{(i)},\ \forall\, i = 1...t \tag{5.40}$$

$$s_{\text{d}}^{(i)} U_{\text{d}}^{(i)} \leq -\epsilon U_{\text{d}}^{(i)},\ \forall\, i = 1...t \tag{5.41}$$

$$Q_{21}^{(i)} = Q_{21}^{(0)} + \frac{\partial Q_{21}}{\partial P_{\text{g}}}(P_{\text{g}}^{(i)} - P_{\text{g}}^{(0)}) + \frac{\partial Q_{21}}{\partial V_{\text{sp}}}(V_{\text{sp}} - V_{\text{sp}}^{(0)}) + \frac{\partial Q_{21}}{\partial n_{\text{st}}} \sum_{k=1}^{i-1} s_{\text{st}}^{(k)} + \frac{\partial Q_{21}}{\partial n_{\text{d}}} \sum_{k=1}^{i-1} s_{\text{d}}^{(k)}$$
$$, \forall\, i = 1...t \tag{5.42}$$

$$||Q_{21}||_2 \leq ||Q_{21}^{\text{B}}||_2 - \delta_q \tag{5.43}$$

This problem is simply infeasible if there does not exists a $\vec{Q}_{21}$ that is less than the initial $\vec{Q}_{21}^{\text{B}}$ by δ_q.

5.8 Implementation of the Voltage Control Scheme on the DTE/ITC System

This section discusses the simulation results of the implementation of the proposed voltage control method that was introduced in Section 5.6.1 on the DTE/ITC system (Figure 5.30). Wind is injected into the sub-transmission network at WG_1 and WG_2. Each of these two wind farms have a rated capacity of 50MW. The simulation spans a full year and involves annual wind and load data (1-minute resolution) for all the load buses in the system both at the 42kV and 120kV levels. As shown in Figure 3.8 wind data is highly correlated. There are 5 sub-transmission OLTCs highlighted in red ellipses in Figure 5.30. The distribution OLTC is modeled at L_1 and connect the 42kV bus to the 13kV distribution feeder. A discrete (DB) tap model is adopted with $T = 0.1$ in (5.8). The pareto curve is obtained for the distribution and sub-transmission OLTC operations and illustrated in Figure 5.31. Note that the sub-transmission OLTC operation is the average for T_1, T_2, T_3, T_4 and T_5 transformers in Figure 5.30. The MPC results based on varying time horizons of 5, 10, 20, 30, 60 minutes are also shown as black circles. The optimal setpoint is obtained based

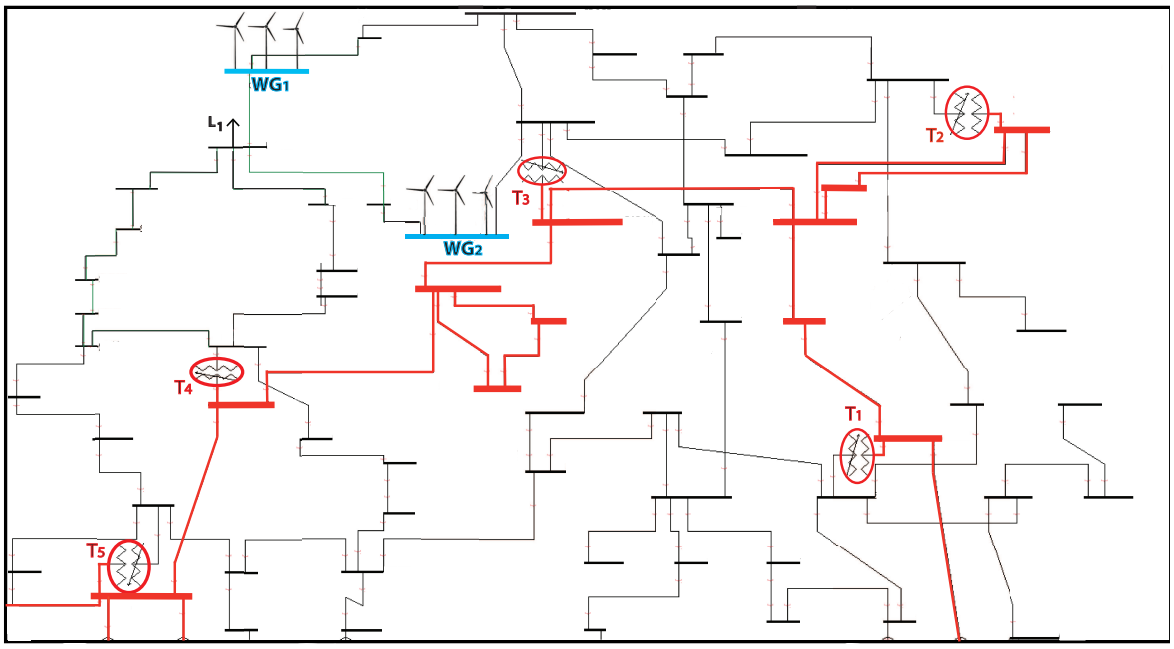

Figure 5.30: DTE 42kV sub-transmission wind development network

on exhaustive search of the image of the mapping from the voltage setpoints of WG_1 and WG_2 to the weighted sum of OLTC operations at distribution (L_1) and sub-transmission substations (T_1 through T_5). The proposed fine-tuning MPC results is shown in Figure 5.32. The improvement by implementing the coordinated voltage control is most noticeable for the most sensitive OLTC transformer that is T_3. Figures 5.33 and 5.34 are similar to Figures 5.31 and 5.32 with the difference that the x-axis is the number of T_3 OLTC operations. The OLTC operation reduction for T_3 is somewhere between 30% to 80% relative to the case of full voltage control. The reduction in L_1 distribution OLTC is between 80% to 90% compared to the case of no voltage control. The loss reduction is also significant especially compared to the case of full voltage control. The coordinated voltage control scheme restricts the losses to between 8% to 15% of the wind generation whereas in the absence of a coordinated voltage control this figure rises to between 11% to 27%. This stresses the significance of voltage coordination for loss reduction in resistive networks with variable generation.

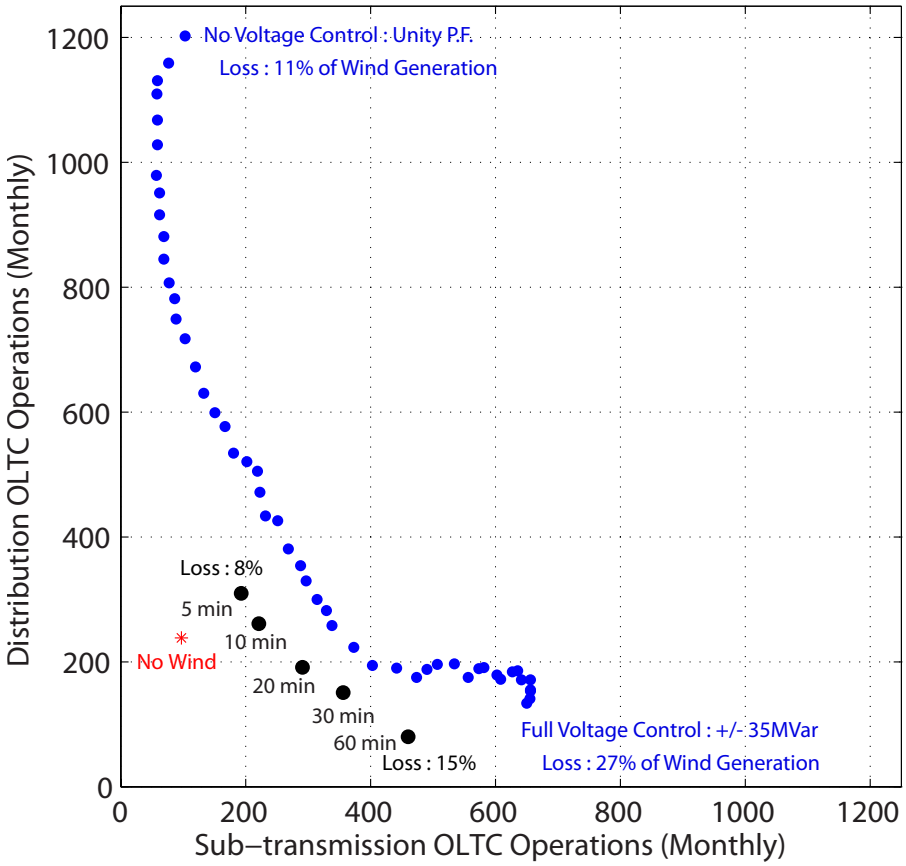

Figure 5.31: Pareto curve and Network Losses (Sub-transmission OLTCs Operation Averaged for T_1, T_2, T_3, T_4 and T_5 in Figure 5.30)

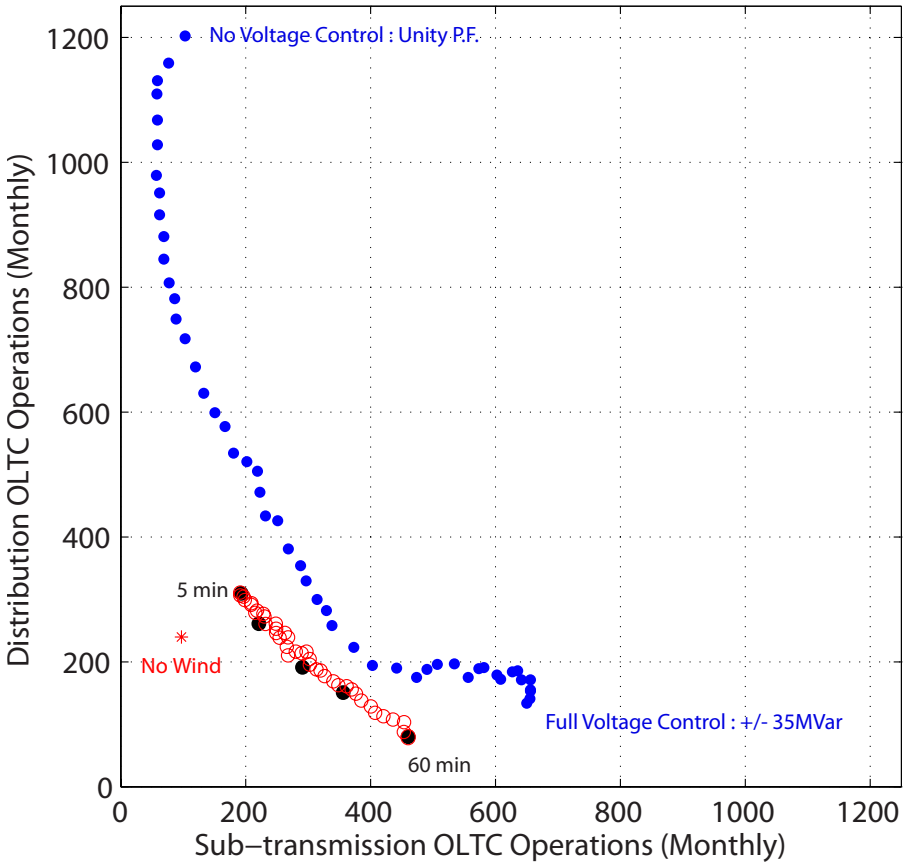

Figure 5.32: Red circles correspond to the varying feasible ranges for *fine-tuning every 5 minutes* around the 1hr optimal setpoint. (Sub-transmission OLTCs Operation Averaged for T_1, T_2, T_3, T_4 and T_5 in Figure 5.30)

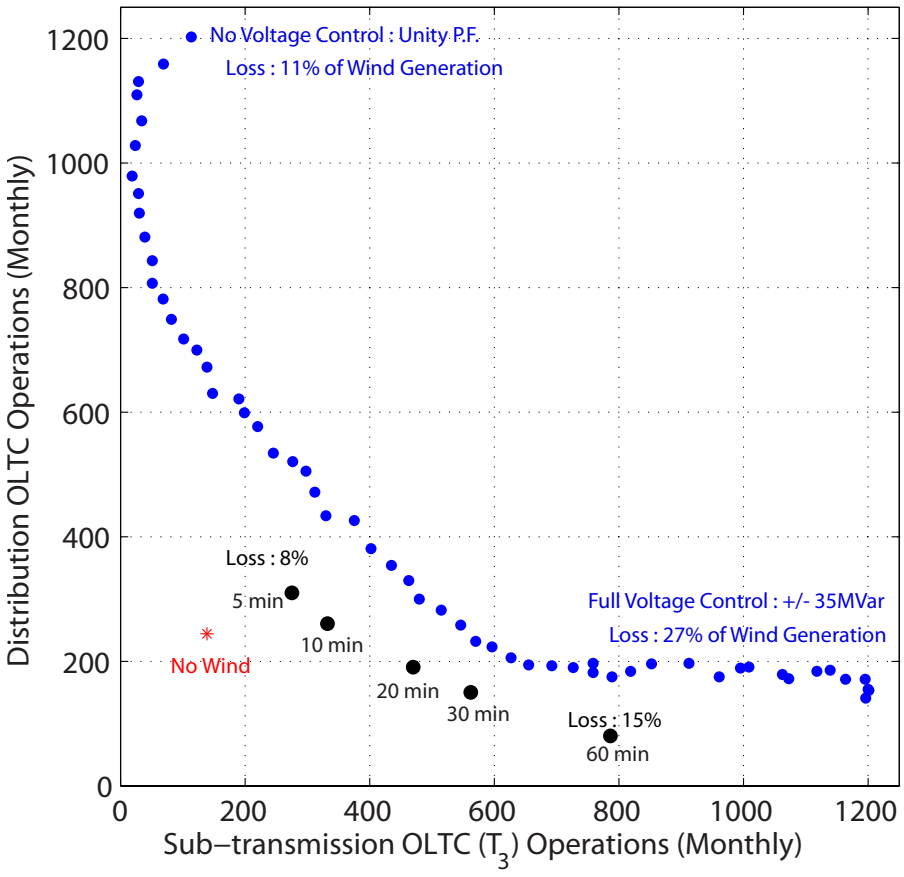

Figure 5.33: Pareto curve and Network Losses (x-axis shows only T_3 OLTC Operations)

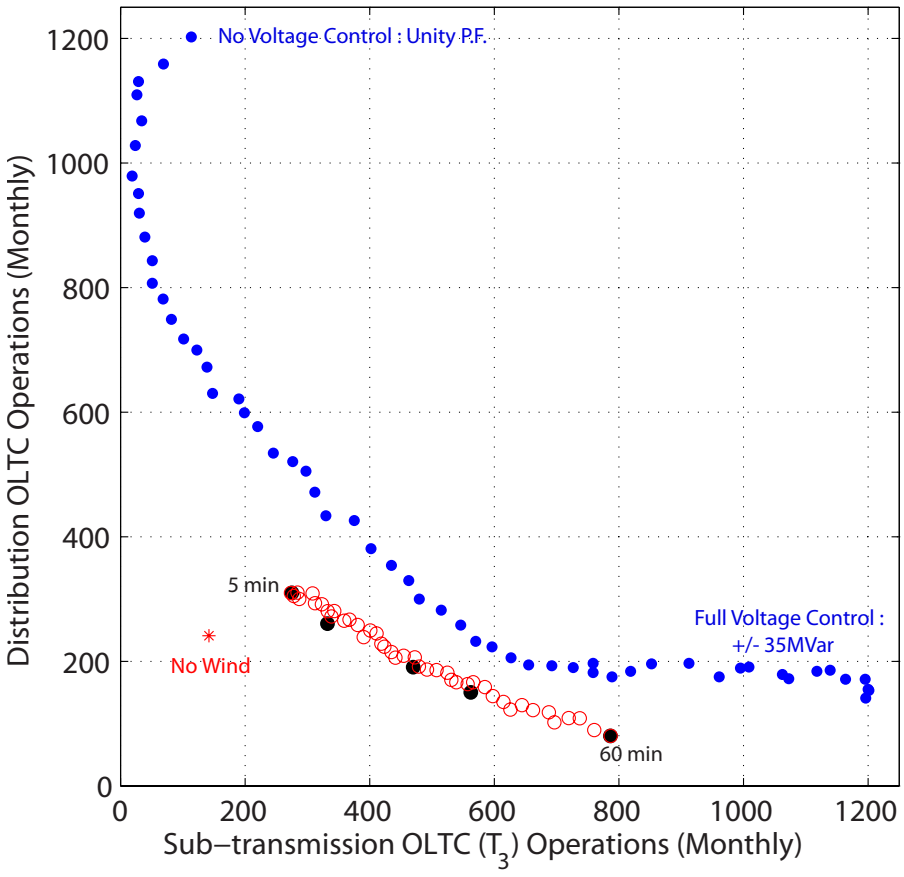

Figure 5.34: Red circles correspond to the varying feasible ranges for *fine-tuning every 5 minutes* around the 1hr optimal setpoint. (x-axis shows only T_3 OLTC Operations)

CHAPTER 6

Conclusions

6.1 Summary of Findings

The goal of this thesis was to investigate the impact of variable generation connected to resistive networks on the voltage regulation, active power losses and the structural stability of the power system. In Chapter 2 the concept of continuation power flow was revisited and applied to the study of wind generation variability. It was shown that this method can be a powerful tool to visualize the global behavior of certain key variables such as voltage magnitudes and tap positions in response to generation variability. The concept of sensitivity factors from the power flow Jacobian was also extensively used as part of either quadratic or mixed-integer programming to formulate a range of optimization problems that incorporate the generation variability in the context of either line congestion or hybrid dynamics of OLTC devices. Later, a computationally efficient method for obtaining the power flow feasibility boundary was introduced which enabled visualization of the segments of boundary corresponding to both saddle-node and limit-induced bifurcations. The relationship between the feasibility boundary and the voltage stability boundary was clarified by reviewing a number of influential studies published in the past four decades. These concepts were utilized in the ensuing analysis (in Chapter 3,4 and 5).

Chapter 3, devoted to the study of the impact of wind generation on the DTE/ITC (120/42/13.2kV) system serving Eastern Michigan, demonstrated that there exists a close relationship between voltage/reactive power control mode of wind farms on one hand and the OLTC operations, network losses and transmission voltage security of the system on the other hand.

Next through rigorous analytical investigations this thesis addressed a prevalent misconception regarding the impact of reactive compensation capability on the voltage stability of the system. It was demonstrated through visualizing the feasibility boundaries in Chapter 3, and later analytically in Chapter 4, that as the size of reactive compensation associated

with embedded generation in resistive networks increases, the voltage stability margin of the system is reduced and hence the structural stability of the system is negatively affected. This is in sharp contrast with the prevalent conception, originated from inductive transmission systems, that reactive compensation enhances the voltage stability.

Later another prevalent confusion on the relationship between OLTC tap operations and generation variability was addressed in Chapter 5. It was established analytically that there exists a relationship between reactive power flow variations and increased OLTC operations. This had already been observed through simulation in Chapter 3 for the DTE/ITC system. This thesis also demonstrated both analytically and through simulation that active power loss is minimized when the reactive power flow (from the inductive transmission system) into the resistive network is curtailed.

The relationship between the voltage magnitude at the point of interconnection of variable generation and reactive power flow from the transmission system into the resistive network was established in Chapter 5. This formed the basis of a model predictive voltage control strategy that anticipated the generation variability in short time horizons (5-60 minutes) and adjusted and held constant the voltage setpoint over successive time windows to follow the generation variability while filtering out high frequency variations. This effectively curtailed reactive power flow into the resistive network with the following benefits:

1. Sub-transmission (upstream) OLTC operations were significantly reduced
2. Active power losses were significantly reduced
3. The strain on the reactive reserves of the transmission system was mitigated with beneficial impact on the structural stability of the system

These benefits are realized at the expense of increased OLTC operations of the distribution (downstream) substations. These OLTC transformers, which in the case of DTE/ITC system, regulate the 13.2kV radial distribution networks are highly sensitive to changes in the voltage profile of the 42kV network caused by frequent adjustments of the voltage setpoints of wind farms connected to the 42kV network.

Finally a mixed-integer formulation was proposed as an equivalent to the exhaustive search method for finding the optimal setpoint for a given time window that minimizes OLTC operations and network loss. This formulation models the hybrid nature of OLTCs through *asymptotic constraints*. The formulation was implemented and validated in Gurobi for a simple test network. It was observed that Gurobi MIP solvers are very effective in finding the global solution (i.e the optimal voltage setpoint) to a highly non-convex map between the voltage setpoint and the number of OLTC operations and reactive flow into

the resistive network. The effectiveness of the proposed control was demonstrated for the DTE/ITC system where both the OLTC operations and the network loss were significantly reduced compared to standard voltage control configurations (with fixed voltage or unity p.f. modes).

6.2 Future Work

This thesis highlights a number of research directions in areas that have been neglected in recent years. One such area is the structural stability of power system and bifurcation theory. The concept of power flow feasibility boundary is central to the voltage stability studies in power systems. Although numerous studies were published in 1990s on power transfer capability and bifurcation so far the computation of the power flow feasibility boundary of large-scale networks (with its reactive limit segments), as a direct measure for assessing the voltage stability, has not been developed due to the difficulties explained in this thesis. Instead various proximity indices to this boundary have been introduced typically based on the Jacobian eigenvalues or singular values. However computing and visualizing the feasibility boundaries is becoming more relevant with the increasing penetration of highly variable generation. Improving the speed of the computation of the feasibility boundary can lead to efficient real-time tools that enable the system operator to monitor the voltage stability margin of the system as the state of the system changes rapidly due to stochastic generation across the system.

Another interesting area that flows out of this work is the application of mixed-integer programming concepts to hybrid control of tap-changing transformers. This was started in this thesis for the discrete tap model of OLTC transformers using MIP techniques. However the hybrid dynamics associated with DBODE tap models are much more complicated to capture using MIP techniques. It was noticed that commercial solvers are very effective in obtaining the global solution to the highly non-convex problems that involve switching events over a time horizon. It would be interesting to investigate how MIP formulations scale up to larger networks with a large number of OLTCs and controllable setpoints.

BIBLIOGRAPHY

[1] "Global Trends in Renewable Energy Investment 2014", Annual Report Published by the Frankfurt School-UNEP Collaborating Centre for Climate & Sustainable Energy Finance (FS-UNEP), April 2014 [Online].

[2] T. Ackermann (Editor), *Wind Power in Power Systems*, 2nd Edition, Wiley, 2012.

[3] T. Gonen, *Electric Power Distribution Engineering*. 3rd Edition, CRC Press, 2014.

[4] C.L. Masters, "Voltage rise: the big issue when connecting embedded generation to long 11 kV overhead lines", *IEE Power Engineering Journal*, vol. 16, no. 1, February 2002, pp. 5-12.

[5] S. Repo, H. Laaksonen, P. Jarventausta, O. Huhtala, and M. Mickelsson, "A case study of a voltage rise problem due to a large amount of distributed generation on a weak distribution network," Power Tech Conference Proceedings, 2003 IEEE Bologna , vol.4, no., pp.6 pp. Vol.4,, 23-26 June 2003.

[6] S.S. Baghsorkhi and I.A. Hiskens, "Impact of wind power variability on sub-transmission networks", *Proceedings of the IEEE Power and Energy Society General Meeting*, San Diego, CA, July 2012.

[7] M. J. Heathcote, *The J & P Transformer Book: A Practical Technology of the Power Transformer*, 13th Edition, Elsevier, 2007.

[8] D. Dohnal, "On-Load Tap-Changers for Power Transformers A Technical Digest", Maschinenfabrik Reinhausen (MR) Publication, Regensburg, 2009 [Online].

[9] "Type VRLTC load tap changer: Installation and maintenance guide", ABB Document, 2014 [Online].

[10] CIGRE Working Group 05, "An International Survey on Failures in Large Power Transformers in Service, *Electra*, No.88, 1983

[11] C. Bengtsson, "Status and trends in transformer monitoring", *IEEE Transactions on Power Delivery*, vol.11, no.3, pp.1379-1384, July 1996.

[12] L. Grigsby (Editor-in-chief), *Electric Power Engineering Handbook*. CRC Press, 2001.

[13] F.A. Viawan, "Voltage control and voltage stability of power distribution systems in the presence of distributed generation", PhD Thesis, Department of Energy and Environment, Chlamers University of Technology, Gteborg, 2008.

[14] J. O'Donnel, "Voltage management of networks with distributed generation", PhD Thesis, School of Engineering and Electronics, University of Edinburgh, 2007.

[15] P.M.S. Carvalho, P.F. Correia and L.A.F. Ferreira, "Distributed reactive power generation control for voltage rise mitigation in distribution networks", *IEEE Transactions on Power Systems*, vol. 23, no. 2, May 2008, pp. 766-772.

[16] S. Salih, P. Chen and O. Carlson, "The effect of wind power integration onthe frequency of tap changes of a substation transformer", *IEEE Transactions on Power Systems*, vol. 28, no. 4, pp.4320-4327 2013.

[17] "Interconnection Requirements for Variable Generation", NERC Report, Sept. 2012, [online].

[18] T. Van Cutsem, and C. Vournas, *Voltage Stability of Electric Power Systems*, Kluwer Academic Publishers, 1998.

[19] I.A. Dobson, et al.,"Chapter 2: Basic Theoretical Concepts," in *Voltage Stability Assessment: Concepts, Practices and Tools*, IEEE-PES, 2002.

[20] Fink, S., Mudd, C., Porter, K., Morgenstern, B., "Wind energy curtailment case studies: May 2008May 2009", NREL report no. SR-550-46716.

[21] L. Bird,J. Cochran,and X. Wang, "Wind and Solar Energy Curtailment: Experience and Practices in the United States", NREL, 2014.

[22] H. K. Trabish, "Why Arent Those Wind Turbines Turning?", Greentech Media, March 24, 2011 [Online].

[23] B. Kirby, J. Van Dyke, C. Martinez and A. Rodriguez, "Congestion ManagementRequirements, Methods and Performance Indices", ORNL/TM 2002, Oak Ridge National Laboratory, Oak Ridge TN, June 2002.

[24] P. Nefzger, U. Kaintzyk and J.F. Nolasco, *Overhead Powerlines: Planning, Design, Construction*, Springer, 2003.

[25] S.S. Baghsorkhi and I.A. Hiskens, "Analysis tools for assessing the impact of wind power on weak grids", *Proceedings of the IEEE International Systems Conference*, Vancouver, Canada, March 2012.

[26] J.D. Glover, M.S. Sarma and T.J. Overbye, Power System Analysis and Design, 5th Edition, CL-Engineering, 2012.

[27] D.S. Bernstein, *Matrix Mathematics: Theory, Facts, and Formulas*, 2nd Edition, Princeton University Press, 2009.

[28] J. Peschon, D.S. Piercy, W.F. Tinney and O.J. Tveit, "Sensitivity in power systems", *IEEE Transactions on Power Apparatus and Systems*, vol. PAS-87, no. 8, August 1968, pp. 1687-1696.

[29] M.M. Begovic and A.G. Phadke, "Control of voltage stability using sensitivity analysis", *IEEE Transactions on Power Systems*, vol. 7, no. 1, February 1992, pp. 114-123.

[30] F. Capitanescu, T. Van Cutsem, "Unified sensitivity analysis of unstable or low voltages caused by load increases or contingencies", *IEEE Transactions on Power Systems*, vol. 20, no. 1, February 2005, pp. 321-329.

[31] N. Flatabo, O. Fosso, R. Ognedal, and T. Carlsen, "A method for calculation of margins to voltage instability applied on the Norwegian system for maintaining required security level", *IEEE Transactions on Power Systems*, vol. 8, no. 3, August 1993, pp. 920-928.

[32] L. Soder, "Estimation of reduced electrical distribution losses depending on dispersed small scale energy production", in *Proceedings 12th Power Systems Computation Conference*, vol. 2, Zurich, Switzerland, 1996, pp. 1229-1234.

[33] C.B. Garcia and W.I. Zangwill, *Pathways to Solutions, Fixed Points and Equilibria*, Prentice Hall, Englewood Cliffs, NJ, 1981.

[34] R. Seydel, *Practical Bifurcation and Stability Analysis*, 3rd Edition, Interdisciplinary Applied Mathematics, Vol. 5, Springer-Verlag, 2010.

[35] G.B. Price, "A generalized circle diagram approach for global analysis of the transmission system performance" *IEEE Transaction on Power Apparatus and Systems*, Vol. PAS-103, No. 10, October 1984, pp. 2881-2890.

[36] V. Ajjarapu and C. Christy, "The continuation power flow: a tool for steady state voltage stability analysis", *IEEE Transactions on Power Systems*, vol. 7, no. 1, February 1992, pp. 416-423.

[37] I.A. Hiskens and R.J. Davy, "Exploring the power flow solution space boundary", *IEEE Transactions on Power Systems*, Vol. 16, No. 3, August 2001, pp. 389-395.

[38] M. Chertkov, M. Stepanov, F. Pan, and R. Baldick, "Exact and efficient algorithm to discover extreme stochastic events in wind generation over transmission power grids", *Proceedings of the 50th IEEE Conference on Decision and Control*, Orlando, FL, December 2011, pp. 2174-2180.

[39] K. Purchala, L. Meeus, D. Van Dommeln and R. Belmans, "Usefulness of DC power flow for active power flow analysis", *Proceedings of the IEEE Power and Energy Society General Meeting*, San Francisco, CA, July 2005.

[40] J. Nocedal and S.J. Wright , *Numerical Optimization*, Springer, 2006.

[41] S.M. Chan and V. Brandwajn, "Partial matrix refactorization", *IEEE Transactions on Power Systems*, Vol. 1, No. 1, February 1986, pp. 193-199.

[42] V.A. Venikov, V.A. Stroev, V.I. Idelchick, and V.I. Tarasov, "Estimation of electrical power system steady-state stability in load flow calculations," *IEEE Transactions on Power Apparatus and Systems*, vol.94, no.3, pp.1034-1041, May 1975.

[43] P.W. Sauer and M.A. Pai, "Power system steady-state stability and the load-flow Jacobian," *IEEE Transactions on Power Systems*, vol.5, no.4, pp.1374-1383, Nov. 1990.

[44] I. Hiskens and P. Reddy, "Switching-induced stable limit cycles," *Nonlinear Dynamics*, vol.50, pp.575-585, 2007.

[45] V.I. Arnold, *Geometrical Methods in the Theory of Ordinary Differential Equations*, (Translation from Russian), Springer-Verlag, 1983.

[46] D.C. Tarraf, and H.H. Asada, "On the nature and stability of differential-algebraic systems," *Proceedings of the 2002 American Control Conference*,vol.5, pp.3546-3551 2002.

[47] P.W. Sauer, B.C. Lesieutre and M.A. Pai, "Maximum Loadability and Voltage Stability in Power Systems", *International Journal of Electrical Power and Energy Systems*, vol. 15, pp.145-154 1993.

[48] A.A. Andronov and L.S. Pontryagin, *Systemes Grossiers*, Dokl. Akad. Nauk., SSSR, 14, pp.247-251, 1937.

[49] A.A. Andronov, A.A. Vitt and S.E. Khaikin, *Theory of Oscillators*, (Translation from Russian), Pergamon Press, 1966.

[50] Y.V. Makarov,Dong Zhao-Yang and D.J. Hill, "On Convexity of Power Flow Feasibility Boundary," *IEEE Transactions on Power Systems* , vol.23, no.2, pp.811-813, May 2008.

[51] Venkatasubramanian, V.; Schattler, H.; Zaborszky, J.; , "Local bifurcations and feasibility regions in differential-algebraic systems," *IEEE Transactions on Automatic Control*, vol.40, no.12, pp.1992-2013, Dec 1995.

[52] Dobson, I.; Lu, L.; , "Voltage collapse precipitated by the immediate change in stability when generator reactive power limits are encountered," *IEEE Transactions on Circuits and Systems I: Fundamental Theory and Applications*, vol.39, no.9, pp.762-766, Sep 1992.

[53] Y. Kataoka and Y. Shinoda "Voltage stability limit of electric power systems with generator reactive power constraints considered", *IEEE Transactions on Power Systems*, vol. 20, no. 2, pp.951-962 2005.

[54] N. Higham, *Accuracy and Stability of Numerical Algorithms*, SIAM, 2002.

[55] K. Levenberg, "A Method for the Solution of Certain Non-Linear Problems in Least Squares". *Quarterly of Applied Mathematics* 2: 164168, 1944.

[56] A. Bjork, *Numerical Methods for Least Squares Problems*, SIAM, Dec. 1996.

[57] D.K. Molzahn, "Application of Semidefinite Optimization Techniques to Problems in Electric Power Systems," Ph.D. Dissertation, University of Wisconsin-Madison, Department of Electrical Engineering, August 2013.

[58] D.K. Molzahn, J.T. Holzer, B.C. Lesieutre, and C.L. DeMarco, "Implementation of a Large-Scale Optimal Power Flow Solver Based on Semidefinite Programming," *IEEE Transactions on Power Systems*, vol. 28, no. 4, pp. 3987-3998, November 2013.

[59] C.L. Wadhwa, *Electrical power systems*, 4th Edition, New Age Publishers, 2006, pp. 727-728.

[60] P. Miskelly, "Wind farms in Eastern Australia: recent lessons", Energy & Environment, 23 (8), pp. 12331260, 2012.

[61] Vittal, E.; O"Malley, M.; Keane, A., "A Steady-State Voltage Stability Analysis of Power Systems With High Penetrations of Wind," *IEEE Transactions on Power Systems* , vol. 25, no.1, pp.433-442, Feb. 2010

[62] Ha, L.T.; Saha, T.K., "Investigation of power loss and voltage stability limits for large wind farm connections to a subtransmission network," *Power Engineering Society General Meeting, 2004. IEEE* , pp.2251-2256 Vol.2, June 2004

[63] J. A. Pecas Lopes, N. Hatziargyriou, J. Mutale, P. Djapic, and N. Jenkins, "Integrating distributed generation into electric power systems: A review of drivers, challenges and opportunities," *Electric Power System Research*, vol. 77, no. 9, pp. 1189-1203, July 2007.

[64] Le, H.T.; Santoso, S., "Analysis of Voltage Stability and Optimal Wind Power Penetration Limits for a Non-radial Network with an Energy Storage System," *Power Engineering Society General Meeting, 2007. IEEE* ,pp.1,8, 24-28 June 2007

[65] Nikolaidis, V.C.; Tsouris, N.A.; Vournas, C.D., "Continuation Power Flow Incorporating Dispersed Generation," *Power Tech, 2007 IEEE Lausanne* , pp.573,578, 1-5 July 2007

[66] "Voltage Stability Criteria, Undervoltage Load Shedding Strategy, and Reactive Power Reserve Monitoring Methodology", Prepared by Reactive Power Reserve Work Group (RRWG),Technical Studies Subcommittee, Western Electricity Coordinating Council, May 1998 [Online].

[67] I. Leisse, O. Samuelsson, J. Svensson, "Coordinated voltage control in distribution systems with DG - control algorithm and case study" , *CIRED Workshop*, Lisbon, May 2012.

[68] C. Taylor ,"Modelling of Voltage Collapse Including Dynamic Phenomena", International Conference on Large High Voltage Electric Systems. Study Committee 38. CIGRE Task Force 38.02.10. December 1992.

[69] O. Alizadeh Mousavi, R. Cherkaoui, "Literature Survey on Fundamental Issues of Voltage and Reactive Power Control, October 2011 [Online].

[70] John McDonald, "Solar Power Impacts Power Electronics In The Smart Grid", *Power Electronics Magazine*, August 2013.

[71] F.-C. Lu and Y.-Y. Hsu, "Reactive power/voltage control in a distribution substation using dynamic programming," *IEE Proceedings of Generation, Transmission and Distribution*, vol.142, no.6, pp.639,645, November 1995.

[72] R.-H. Liang and C.-K. Cheng, "Dispatch of main transformer ULTC and capacitors in a distribution system," *IEEE Transactions on Power Delivery* , vol.16, no.4, pp.625,630, 2001.

[73] Y. Liu, P. Zhang and X. Qiu, "Optimal reactive power and voltage control for radial distribution system," *IEEE Power Engineering Society Summer Meeting*, vol.1, no., pp.85-90 vol. 1, 2000.

[74] Z. Hu, X. Wang, H. Chen and G. A. Taylor, "Volt/VAr control in distribution systems using a time-interval based approached", *Proc. Inst. Elect. Eng., Gen. Transm. Distrib.*, vol. 150, 2003.

[75] J.-Y. Park, S.-R. Nam and J.-K. Park, "Control of a ULTC Considering the Dispatch Schedule of Capacitors in a Distribution System," *IEEE Transactions on Power Systems* , vol.22, no.2, pp.755-761, 2007.

[76] Y.-J. Kim, S.-J. Ahn, P.-I. Hwang, G.-C. Pyo and S.-I. Moon, "Coordinated Control of a DG and Voltage Control Devices Using a Dynamic Programming Algorithm," *IEEE Transactions on Power Systems*, vol.28, no.1, pp.42,51, 2013.

[77] Y.P. Agalgaonkar, B.C. Pal and R.A. Jabr "Distribution Voltage Control Considering the Impact of PV Generation on Tap Changers and Autonomous Regulators," *IEEE Transactions on Power Systems*, vol.29, no.1, pp.182-192, Jan. 2014.

[78] W. B. Powell, *Approximate Dynamic Programming: Solving the Curses of Dimensionality*, 2nd Edition, Wiley, 2011.

[79] J. Martnez, P. Rodriguez, P.C. Kjar and R. Teodorescu, "Design and coordination of a capacitor and on-load tap changer system for voltage control in a wind power plant of doubly fed induction generator wind turbines", *Wind Energy*, vol. 15, issue 4, pp.507-523, 2012.

[80] A. Oskoui, B. Mathew, J. Hasler, M. Oliveira, T. Larsson, A. Petersson and E. John, "Holly STATCOM - FACTS to Replace Critical Generation, Operational Experience," *Proceedings of the IEEE PES Transmission and Distribution Conference and Exhibition*, 2005/2006, 21-24 May 2006.

[81] J.J. Paserba, D.J. Leonard, N.W. Miller, S.T. Naumann, M.G. Lauby, F.P. Sener, "Coordination of a distribution level continuously controlled compensation device with existing substation equipment for long term VAr management," *IEEE Transactions on Power Delivery*, vol.9, no.2, pp.1034-1040, 1994.

[82] P. Wood, V. Bapat and R. P. Putkovich, "Study of improved load-tap-changing for transformers and phase-angle regulators: Final report, EPRI, Rep. EL-6764, 1990.

[83] J. Faiz and B. Siahkolah, *Electronic Tap-changer for Distribution Transformers*, Springer, 2011.

[84] S.M. Garcia, J.C.C Rodriguez, J.A Jardini, J.V. Lopez, A.I. Segura, and P.M.M Cid, "Feasibility of Electronic Tap-Changing Stabilizers for Medium Voltage Lines: Precedents and New Configurations," *IEEE Transactions on Power Delivery*, vol.24, no.3, pp. 1490-1503, July 2009.

[85] P. Bauer and S. W. H. deHaan, "Electronic tap changer for 500 kVA/10 kV distribution transformers: Design, experimental results and impact in distribution network", *Proc. IEEE IAS*, vol. 2, pp.1530-1537 1998.

[86] J.-H. Choi; S.-I. Moon, "The Dead Band Control of LTC Transformer at Distribution Substation," *IEEE Transactions on Power Systems*, vol.24, no.1, pp.319-326, 2009.

[87] H.Y. Li and H. Leite, "Increasing distributed generation using automatic voltage reference setting technique," *Proceedings of the IEEE Power and Energy Society General Meeting*, Pittsburgh, PA, July 2008.

[88] M. Stifter, B. Bletterie, H. Brunner, D. Burnier, H. Sawsan, F. Andren, R. Schwalbe, A. Abart, R. Nenning, F. Herb, and R. Pointner, "DG DemoNet: experiences from Volt/VAr control field trials and control algorithm advancements," *IEEE PES International Conference and Exhibition on Innovative Smart Grid Technologies (ISGT Europe)*, Berlin, 2012.

[89] M. Larsson, *Coordinated voltage control in electric power systems*, PhD Thesis, Dept. Ind. Elect. Eng. Automat., Lund Inst. Technol. 2000.

[90] E. Camm, M. Behnke, O. Bolado, M. Bollen, M. Bradt, C. Brooks, W. Dilling, M. Edds, W. Hejdak, D. Houseman, S. Klein, F. Li, J. Li, P. Maibach, T. Nicolai, J. Patino, S. V. Pasupulati, N. Samaan, S. Saylors, T. Siebert, T. Smith, M. Starke, and R. Walling, "Reactive power compensation for wind power plants," *in Proceedings of the IEEE PES General Meeting*, Calgary, Alberta, July 2009.

[91] P. Kundur, *Power System Stability and Control*, McGraw-Hill, 1994.

[92] P.W. Sauer and M.A. Pai, "A Comparison of Discrete vs Continuous Dynamic Models of Tap -Changing - Under - Load Transformers," *Proceedings of Bulk Power System Voltage Phenomenon III*, Davos, Switzerland 1994.

[93] R. Aghatehrani and A. Golnas, "Reactive power control of photovoltaic systems based on the voltage sensitivity analysis," *Proceedings of the IEEE Power and Energy Society General Meeting*, San Diego, CA, July 2012.

[94] J. Machowski, J. Bialek and J. Bumby, *Power System Dynamics: Stability and Control*, 2nd Edition, Wiley, 2008.

[95] C.K. Sao, and P.W. Lehn, "Control and Power Management of Converter Fed Microgrids," *IEEE Transactions on Power Systems*, vol.23, no.3, pp.1088-1098, 2008.

[96] Nikos Hatziargyriou, *Microgrids: Architectures and Control*, Wiley, 2014.

[97] P.-J. Trombe and P. Pinson , "High-resolution forecasting of wind power generation with regime-switching models and off-site observations,"2012 [online].

[98] G. Giebel, "The State of the Art in Short-Term Prediction of Wind Power, A Literature Overview," 2nd Edition, ANEMOS, 2011 [online].

[99] J. Kleissl, *Solar Energy Forecasting and Resource Assessment*, Academic Press, 2013.

[100] S. Howison, *Practical Applied Mathematics: Modelling, Analysis, Approximation*, Cambridge University Press, 2005.